Evaluation of URANS and DES Predictions of Vortical Flows over Slender Delta Wings

Lucy Schiavetta M.Eng

Department of Aerospace Engineering
University of Glasgow

February 2007

Thesis submitted to the Faculty of Engineering
in fulfillment of the requirements for the
degree of Doctor of Philosophy

Abstract

This thesis presents a study of vortical flows and vortex breakdown over slender delta wings. The formation of leading edge vortices over a slender delta wing provide advantageous aerodynamic characteristics at low velocities and angles of incidence. However, as the incidence of the planform is increased these vortices are affected by changes in the flow behaviour, which causes them to become unstable and breakdown into an incoherent form. This vortex breakdown is detrimental to the aerodynamic characteristics of the wing and can cause instability of the aircraft. Due to this adverse effect, it is important to understand the behaviour of such flows. Computational fluid dynamics is one method which, due to the development of numerical methods and the rapid advances in computer technology, is becoming increasingly valuable for the analysis of vortical flows and vortex breakdown and this thesis assesses the use of CFD to predict these types of flows. To perform this assessment two test cases are considered under different flow regimes. The first test case considers transonic flow and is investigated using steady state calculations and the second test case considers the unsteady subsonic behaviour of the flow.

The behaviour of the flow over slender delta wings under transonic conditions is highly complex. With the occurrence of a number of shocks in the flow, vortex breakdown is abrupt and the overall behaviour is quite different to that for subsonic flow. To consider this, the flow over a 65^o sharp leading edge delta wing is analysed for a transonic Mach number of $M = 0.85$ at two incidences: $\alpha = 18.5^o$ and 23^o. A Boussinesq based RANS turbulence model is used which has been modified for vortical flows. The flow solutions are compared to existing experimental data and show good agreement for the cases considered and a number of shock systems within the flow are identified. However, a discrepancy with the experimental data is shown where the critical incidence for the onset of vortex breakdown on the wing is under-predicted. A sensitivity study of the flow to a number of computational factors, such as turbulence model and time accuracy, is undertaken. However, it is found that these parameters have little effect on the overall behaviour of the transonic flow and the occurrence of vortex breakdown. From analysis of the solutions, it is determined that the onset of vortex breakdown is highly dependent on the vortex strength and the strength and location of the shocks in the flow. The occurrence of a critical relationship between these parameters is suggested for vortex breakdown to occur and is used to explain the discrepancies between the computational and experimental results based on the under-prediction of the vortex core axial velocity.

The second test case considers the unsteady behaviour of the vortex flow and vortex breakdown. Downstream of the vortex breakdown the flow is highly unsteady with many different phenomena occurring for varying frequencies. This unsteady behaviour can interact with the surface of the wing or with other surfaces of an aircraft, which can cause fatigue or stability issues. However, this behaviour is still a subject, which is a challenge for numerical methods, such as CFD. New approaches to turbulence modelling, such as detached eddy simulation (DES) have been proposed which allow for greater realism of the numerical predictions. However, this increase in accuracy comes with a considerable increase in computational expense compared to traditional turbulence modelling. Both DES and Unsteady Reynolds Averaged Navier-Stokes (URANS) turbulence methods are considered to predict the unsteady vortical behaviour. Calculations using DES are initially considered and the predicted behaviour and resolution of the flow are analysed. Both temporal and spatial refinement are considered and the effect that each of these factors have on the flow behaviour is examined. A number of unsteady flow features and their corresponding frequencies are identified from the solutions. From comparison with existing DES calculations and experimental data it is determined that the DES solutions are spatially under-resolved and are not able to capture the majority of the turbulent scales in the flow. However, it is also noted that the flow immediately downstream of breakdown is not dominated by turbulence and many low frequency coherent structures are found to occur. Therefore, it is concluded that URANS methods may be capable of accurately predicting this flow behaviour.

To consider this proposal two URANS turbulence models were used for the prediction of the flow for the same test case. The models chosen use two different approaches to model the turbulence in the flow. A linear Boussinesq

based model with a modification for vortex flow and a non-linear model based on an explicit algebraic Reynolds stress formulation are used. Again, the effects of both temporal and spatial refinement on the flow behaviour were considered. The relative behaviour of each model in predicting the unsteady flow behaviour was analysed with respect to the treatment of the turbulence in the vortex flow. It was found that each model predicted very similar behaviour. The URANS results were then compared to the DES solutions of the previous investigation to evaluate the relative behaviour. From this comparison it was determined that the URANS turbulence models were able to predict the dominant features of the low frequency phenomenon present in the vortex system and in the post-breakdown region. It was then concluded that the URANS models were suitable for predicting the unsteady behaviour of the flow at a considerable reduction in computational cost.

Declaration

The author hereby declares that this dissertation is a record of work carried out in the Department of Aerospace Engineering at the University of Glasgow during the period of October 2003 to February 2007. This dissertation is original in content except where otherwise stated.

Lucy Schiavetta

February 2007

Acknowledgements

Firstly, I would like to thank my supervisor Prof. Ken Badcock for all the guidance and advice throughout the course of this project and for providing me with many opportunities to develop my research skills outwith the CFD Lab. One of these opportunities allowed me to contribute to the NATO RTO AVT-113 Task Group, which was a very enjoyable, interesting and useful experience and I would like to thank all those involved in the group. Particularly, I would like to thank Okko Boelens, Willy Fritz, Russ Cummings and Scott Morton for the data they provided me with, all their help and for answering my many emails, and Prof. Hummel for his encouragement and enlightening discussions.

I must also thank BAE Systems who have sponsored this project and particularly, Mike Henshaw and Dominic Amor for their help and support during my industrial placement.

I would also like to express my gratitude to all the researchers past and present I have been fortunate to work and socialise with. It has made this project all the easier working in an enjoyable environment. I'd like to thank past CFD lab members Punit, Abdul, Dave L and Romy, particularly for helping me so much when I was the "new girl" and for their continuing help and support when I wasn't. I'd also like to thank Joe, Dave S, Yoh and Giangi for their friendship and ability to keep me laughing.

I would like to thank my family for their support and encouragement throughout the years, for never doubting I could do it and for telling me so when I needed to hear it. Their unswerving faith in me has been a source of strength again and again. Finally, I would like to thank Adriano, for his support and patience, despite being in the same situation and without whom I'd probably never have gotten this far.

Publications

Conference Papers

L.A Schiavetta, O.J Boelens and W. Fritz. **Analysis of Transonic Flow on a Slender Delta Wing Using CFD** *24th AIAA Applied Aerodynamics Conference*, San Francisco, June 5-8th 2006, Paper AIAA-2006-3171

L.A Schiavetta, K.J Badcock and R.M Cummings. **Comparison of DES and URANS for Unsteady Vortical Flows over Delta Wings** *45th AIAA Aerospace Sciences Meeting and Exhibit*, Reno, 8-11 January 2007, Paper AIAA-2007-1085

Presentations

L.A Schiavetta. **VFE-2 Facet: Progress Report**
Presented at NATO RTO AVT-113, *"Understanding and Modelling Vortical Flows to Improve the Technical Readiness Level for Military Aircraft"*, Task Group Technical Meeting, Budapest, Hungary, April 2005

L.A Schiavetta. **VFE-2 Facet - Progress Report and CFD Results Comparison**
Presented at NATO RTO AVT-113, *"Understanding and Modelling Vortical Flows to Improve the Technical Readiness Level for Military Aircraft"*, Task Group Technical Meeting, Granada, Spain, October 2005

L.A Schiavetta, O.J Boelens and W. Fritz. **Analysis of Transonic Flow on a Slender Delta Wing using CFD**
Presented at NATO RTO AVT-113, *"Understanding and Modelling Vortical Flows to Improve the Technical Readiness Level for Military Aircraft"*, Task Group Technical Meeting, Amsterdam, The Netherlands, May 2006

L.A Schiavetta, and R. Cummings. **VFE2 Facet: Further Transonic Analysis and Comparisons**
Presented at NATO RTO AVT-113, *"Understanding and Modelling Vortical Flows to Improve the Technical Readiness Level for Military Aircraft"*, Task Group Technical Meeting, Vilnius, Lithuania, Oct 2006

L.A Schiavetta. **Unsteady Vortical Flows using CFD**
Presented to BAE Systems, Advanced Technology Center, Sowerby, Filton, Bristol, UK, April 2006
Also Presented to Qinetiq, Farnborough, UK, April 2006

Contents

List of Figures

List of Tables

Nomenclature

Symbols

a_{ij}	Anisotropic component of Reynolds stress tensor
$a_{ij}^{(ex)}$	Extra anisotropic component of Reynolds Stress tensor for NLEVM model
a_{ij}^{SGS}	Subgrid scale anisotropic component of Reynolds stress tensor
$\mathbf{a}$	Anisotropic 2nd order tensor
c	Chord length/characteristic length
c_r	Root chord length
c_{b1}, c_{b2}, c_{v1}	Model constants for Spalart-Allmaras model
c_{w1}, c_{w2}, c_{w3}	Model constants for Spalart-Allmaras model
c_v	Specific heat at constant volume
c_p	Specific heat at constant pressure
d	Distance from wall
$\tilde{d}$	Variable used in Spalart-Allmaras model for DES formulation
d_{min}	Minimum distance from wall
e	Specific internal energy
f	Frequency, Hz
f_i	Body forces
f_{β^*}	Closure coefficents for $k-\omega$ model
f_{v1}, f_{v2}, f_w	Model functions for Spalart-Allmaras model
g, r	Model functions for Spalart-Allmaras model
ℓ	Characteristic turbulent eddy length scale
ℓ_o	Characteristic length of largest turbulent scales
k	Turbulent kinetic energy
k_T	Heat transfer coefficient
k_r	Residual kinetic energy
p	Pressure
q_i	Heat flux vector
q_i^t	Turbulent heat flux vector
r	Ratio of the magnitude of the strain rate tensor to the magnitude of the vorticity $r = S/\Omega$
r_c	Radius of vortex core at point of maximum swirl velocity
s	Local semi-span
t	Time
t	Pseudo time
u_i	Instantaneous velocity vector
$\bar{u}_i$	Time averaged velocity vector
$\tilde{u}_i$	Mass averaged velocity vector
$\hat{u}_i$	Filtered velocity vector
u_i'	Turbulent fluctuating velocity
u_i''	Mean flow fluctuating velocity
u_i'''	Fluctuating velocity from Favre averaging
u_i^{SGS}	Subgrid scale velocity
$u(\ell)$	Characteristic velocity scale
u_o	Characteristic velocity of largest turbulent scales

u_η	Kolmogorov velocity scale
u	Velocity in x-direction
v	Velocity in y-direction
w	Velocity in z-direction
y^+	First cell distance from wall
x_i	Position vector
x, y, z	Cartesian coordinates
x/c_r	Non-dimensional streamwise location
x_{tr}	Location of forced transition line
y/s	Non-dimensional spanwise location
z/c_r	Non-dimensional normal location

C_D	Drag coefficient
C_{DES}	DES model coefficient
C_L	Lift coefficient
C_N	Normal force coefficient
C_μ^{eff}	Effective eddy viscosity coefficient for NLEVM model
C_K	Kolmogorov constant
C_τ	Model constant for NLEVM model
C_p	Pressure coefficent
C_s	Smagorinsky constant
E	Total energy
$E(\kappa)$	Energy spectral density
$\mathbf{F}$	Flux vector in the x-direction
$\mathscr{F}$	Fourier Transform
$\mathbf{G}$	Flux vector in the y-direction
G	Filter function
$\mathbf{H}$	Flux vector in the z-direction
H	Total enthalpy
$\mathbf{I}$	Identity matrix
$II_\Omega, II_S, III_S, IV, V$	Invariants of strain-rate and rotation tensors
M	Mach number
M_1, M_2	Mach numbers defined upstream and downstream of shock surface
M_N	Mach number normal to shock surface
N	Number of samples in signal
$N, N_c, P_1, P_2, D, c_1', c_1, f_1$	Functions for NLEVM formulation
N_{DNS}	Required grid size for DNS calculations based in turbulent Reynolds number
P	Pressure
P_1, P_2	Pressures defined upstream and downstream of shock surface
P_ω	Production term in ω equation
$P_{\omega_{new}}$	Modified production term in ω equation
P_k	Production term in k equation
Pr	Prandtl number
$\mathbf{Q}_{i,j,k}$	Turbulent Flux residual
$\mathbf{R}_{i,j,k}$	Flux residual
$\mathbf{R}^*_{i,j,k}$	Unsteady Flux residual
R	Specific gas constant
$R_{\Phi(t)}$	Auto-correlation function of general variable $\Phi(t)$
Re	Reynolds number $Re = U_\infty c/\nu$
Re_T	Turbulent Reynolds number $Re_T = k^{1/2}\ell/\nu$
Ro	Rossby Number $Ro = U_{axial}/U_0$
S	Magnitude of vorticity; Magnitude of strain-rate tensor $(2S_{ij}S_{ij})^{1/2}$
S_{ij}	Strain-rate tensor
S^*_{ij}	Strain-rate tensor for compressible flow
$\hat{S}$	Local deformation rate
$\hat{S}_{ij}$	Filtered strain-rate tensor
$\bar{S}_{ij}$	Mean strain-rate tensor

$\mathbf{S}$	Normalised strain-rate tensor
St	Strouhal number, non-dimensional frequency $St = fc/U_\infty$
St_N	Nquist non-dimensional frequency
T	Temperature; Non-dimensional sample rate
T_o	Reference Temperature
U_∞	Freestream velocity
$\langle U_i \rangle$	Stationary mean velocity vector
U_i	Mean flow velocity vector
U_{max}	Maximum flow velocity
U_θ	Swirl/Tangential velocity
U_{axial}	Vortex core axial velocity
U_{local}	Local velocity magnitude
$\mathcal{V}_{i,j,k}$	Cell volume
$\mathbf{W}$	Vector of conserved variables

Greek Symbols

α	Angle of incidence
α	Model constant for $k-\omega$ model
α_{cr}	Critical incidence for vortex breakdown
β_n	Model coefficients for NLEVM model
β, β^*	Closure coefficents for $k-\omega$ model
γ	Ratio of specific heats, $\gamma = c_p/c_v$
δ_{ij}	Kronecker delta, $\delta_{ij} = 1$ if $i = j$ and $\delta_{ij} = 0$ if $i \neq j$
ε	Dissipation per unit mass
$\varepsilon_{i,j,k}$	Alternating symbol
η	Kolmogorov length scale
κ	Non-dimensional wavenumber; Von Kármán constant, $\kappa = 0.41$
λ	Wavelength
μ	Molecular viscosity
μ_o	Reference molecular viscosity
μ_T	Turbulent eddy viscosity
μ_{SGS}	Subgrid scale (or Smagorinsky) eddy viscosity
ν	Kinematic viscosity, $\nu = \mu/\rho$
$\tilde{\nu}$	Spalart-Allmaras equation working variable, $\tilde{\nu} = \nu_T/f_{v1}$
ν_T	Turbulent kinematic eddy viscosity, $\nu_T = \mu_T/\rho$
ν_{SGS}	Subgrid scale kinematic eddy viscosity
ρ	Density
$\bar{\rho}$	Time-averaged density
σ, σ^*	$k-\omega$ model constants
τ	Non-dimensional time; Swirl ratio; Turbulent time scale
τ_o	Characteristic time of largest turbulent scales
τ_η	Kolmogorov time scale
$\tau(\ell)$	Characteristic time scale
$\Delta\tau$	Non-dimensional time step
τ_{ij}	Viscous stress tensor
τ_{ij}^R	Reynolds stress tensor
τ_{ij}^{SGS}	Subgrid scale stress tensor
ϕ	Level of turbulence resolved by LES
χ	Model function for Spalart-Allmaras model
ω	Dissipation per unit turbulence kinetic energy
ω	Angular frequency
ω_i	Vorticity vector

Δ	Filter Width
$\Delta_x, \Delta_y, \Delta_z$	Cell dimensions in x, y, z directions
Δ_o	Optimal cell dimension

Δ_{max}	Maximum cell dimension
Λ	Sweep angle
Φ	General variable
Ω	Magnitude of rotation tensor $(2\Omega_{ij}\Omega_{ij})^{\frac{1}{2}}$
$\mathbf{\Omega}$	Normalised rotation tensor
Ω_{ij}	Rotation tensor
$\tilde{\Omega}_{ij}$	Mean rotation tensor

Acronyms

AMR	Adaptive Mesh Refinement
BILU	Block Incomplete Lower Upper
CAD	Computer Aided Design
CFD	Computational Fluid Dynamics
CFL	Courant-Fredrich-Lewy number
DES	Detached Eddy Simulation
DFT	Discrete Fourier Transform
DNS	Direct Numerical Simulation
FFT	Fast Fourier Transform
GUI	Graphical User Interface
JSF	Joint Strike Fighter
LDV	Laser Doppler Velocimetry
LE	Leading Edge
LES	Large Eddy Simulation
NASA	National Aeronautics and Space Agency
NLEVM	Non-Linear Eddy Viscosity Model
NTF	National Transonic Facility
PIV	Particle Image Velocimetry
PSD	Power Spectral Density
PSP	Pressure Sensitive Paint
RANS	Reynolds Averaged Navier Stokes
RLE	Round Leading Edge
RMS	Root Mean Square
RSM	Reynolds Stress Model
SA-DES	Spalart-Allmaras Detached Eddy Simulation
SARC	Spalart-Allmaras with Rotation Correction
SGS	Sub-Grid Scale
SLE	Sharp Leading Edge
SST	Shear Stress Transport
SSTDES	Shear Stress Transport Detached Eddy Simulation
TE	Trailing Edge
TNT	Turbulent Non-Turbulent
UAV	Unmanned Aerial Vehicle
UCAV	Unmanned Combat Aerial Vehicle
URANS	Unsteady Reynolds Averaged Navier-Stokes
VBD	Vortex Breakdown
VFE-1	1st international Vortex Flow Experiment
VFE-2	2nd international Vortex Flow Experiment
XLES	eXtra Large Eddy Simulation

Subscripts

∞	Freestream conditions
n	Current time-step
$n+1$	Next time-step
rms	Root mean square value

T	Turbulent quantities

Superscripts

i	Inviscid component
k_m, k_l, l_m, l_l	Time levels of variables in spatial discretisation
v	Viscous component

Chapter 1

Introduction

1.1 Overview

Delta wings were introduced to reduce the effects of compressibility such as the transonic drag rise. However, it was also found that these planforms were suitable for low speed flight and could produce lift at angles of incidence much larger than traditional swept wings [1]. This increased lift and improved aerodynamic characteristics allows greater agility, particularly at low speeds, and the design of many complex configurations have been centred around the use of such planforms.

The additional lift is due to the flow separating at the leading edges of these wings at low incidences and being convected downstream by the freestream velocity. The convection of this flow results in the production of coherent vortical structures, which exist above the leading edge and contribute to the lift force generated by the wing. However, as incidence is increased these structures become unstable and breakdown into an incoherent form. This reduction in the coherence of the flow structure over the wing has been found to have detrimental effects on the aerodynamic characteristics of the wing and may cause a sudden and unexpected aerodynamic instability of the aircraft. This is particularly true for transonic velocities where interactions between shockwaves and the flow over the wing can cause sudden changes in behaviour. Due to the ability of these structures to have both beneficial and detrimental effects on the aerodynamics of aircraft, a great deal of research and development has been carried out over the years to consider and improve the behaviour of the wings for a range of flight conditions.

From early research, it was noted that the flow over the delta wing was not steady in nature, particularly when the leading edge vortices suffered breakdown into a turbulent state [4]. This unsteadiness has been found to further complicate an already complex flow behaviour. Through interactions with the wing surface and other aircraft appennages such as the tailplane, this results in aeroelastic effects occurring on the aircraft, which can cause fatigue and, in the most severe cases, results in catastrophic failure. This type of behaviour was found, quite recently, to occur on the F-18A, where the vortices created from the leading edge extensions of the wings were found to breakdown upstream of the vertical fins of the aircraft at moderate angles of incidence as shown in Figure 1.1. This unsteady flow was then found to interact with the tailplane structure causing a buffeting effect. This was found to cause premature fatigue of the vertical fins and may affect the control surface of the aircraft, both of which will have serious effects on the stability and performance of the aircraft during rapid manoeuvres.

Therefore, it is clear that understanding the behaviour of this unsteady forcing is crucial to enable the alleviation of any structural responses which may exist. This type of unsteady flow is known as buffet and is a issue for all aircraft configurations which incorporate swept edges in their design. This is particularly important for complex fighter configurations such as the F-16XL, EuroFighter and for the design of future configurations. This need is further compounded by the emergence of new UAV and UCAV technologies, which are tending toward planforms where vortical behaviour will play a large role. This means that the need for a more complete understanding of the unsteady behaviour of vortical flows is becoming increasingly important.

The increased flight envelope of many of these aircraft has resulted in many manoeuvres being executed at transonic velocities. As mentioned above, this introduces the presence of shockwaves, which interact with the leading edge vortices. Generally, shocks appear due to localised supersonic regions and as the flow behaviour changes, say with an increase in incidence, the location and strength of the shocks present in the flow will change. This can have a significant effect on the overall flow behaviour and, as a result effect the performance of the aircraft whilst carrying out manoeuvres in this flight regime. Due to this, it is important to understand the overall behaviour of the

Figure 1.1: NASA F-18 HARV at $\alpha = 20^o$ with smoke visualisation showing vortex created by leading edge extension and vortex breakdown interacting with aircraft tailplane

flow and any interactions which occur between the shock and the vortical flow, in order to avoid significant loss of lift due to a sudden breakdown of the coherent vortex caused by the presence of shocks on the wing.

Traditionally, these issues were considered using experimental techniques, with large scale wind tunnel tests being carried out to determine the behaviour of the flow for various flight regimes. However, with the development of computational methods and the rapid advances in computer technology, computational fluid dynamics (CFD) has emerged as an increasingly useful tool in the understanding of aerodynamic flow behaviours. The use of CFD to compliment experimental testing in both research and industrial design processes is being increasingly realised by scientists and engineers in both fields. CFD reduces the need for expensive, large scale testing programs by allowing indication of regions of interest in the flow regimes before testing commences. CFD also allows many situations which cannot be examined in wind tunnels, such as more realistic flight conditions and scenarios, to be considered.

However, it is very unlikely that CFD will ever replace experimental testing, particularly as the nature of turbulence is still not fully understood. A great deal of research has been carried out in recent times to create models to allow the accurate simulation of a turbulent flow. However, many of these methods are based on empiricism or statistical methods and have limits to their accuracy. Many high fidelity methods have also been proposed, which directly solve the governing equations of fluid flow. However, these methods are particularly expensive in computational resources and are not in widespread use, particularly for realistic engineering flows. Therefore, the application of turbulence models and treatments within CFD and their ability to accurately predict interesting aerodynamic flow behaviours is a factor which needs to be addressed for all types of flows.

Before outlining the main objectives of this thesis and the work carried out during this project, it is necessary to provide an introduction to the behaviour of vortical flows over slender, sharp-edged delta wings and to consider the application of CFD to resolve this behaviour.

1.2 Vortical Flows over Slender Delta Wings

1.2.1 Leading Edge Vortices

As fluid passes over a sharp-edged delta wing, set at an incidence, α, the flow separates along the sharp leading edge and together with the separating boundary layer from the lower surface forms free-shear layers. These shear layers curve upward and curl in on themselves to create two counter-rotating vortices over the upper surface of the wing. As the shear layer returns to the surface of the wing, it induces a span-wise flow in the direction of the leading edge. If and when this flow meets an adverse pressure gradient it will separate again from the surface creating secondary vortices. In some cases this process can occur again below the secondary vortices creating tertiary separations. The overall behaviour is shown in Figure 1.2. The primary and secondary separation and attachment lines on the wing surface, which are created by the stream surfaces of the flow impinging on the surface, and the surface streamlines, which flow from attachment lines toward separation lines are shown.

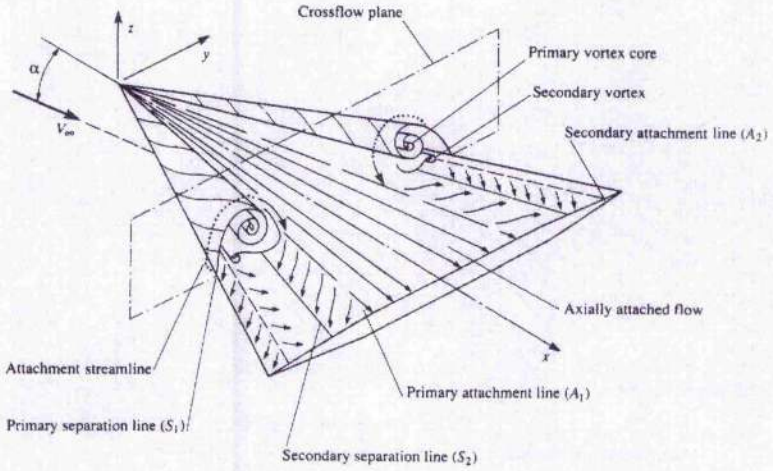

Figure 1.2: Schematic of the subsonic behaviour of the flow over a delta wing at incidence (from Ref. [1])

Also clear from Figure 1.2 is the increasing diameter of the vortex cores with distance from the apex. There have been many experimental and numerical investigations into the behaviour of vortices. Earnshaw [36] proposed that the vortex may be split into three main regions: the shear layer, the inviscid rotational core and the viscous subcore. The shear layer, as mentioned above, is created at the leading edge of the wing and feeds vorticity into the inviscid rotational region by curling in on itself. As the shear layer moves upward and over the wing, smaller substructures are found to occur within its structure [37, 38, 39, 40], which cause an increase in thickness as the distance from the leading edge increases. These substructures will be detailed in a later section. The inviscid rotational region which makes up the bulk of the vortex, contains the viscous subcore at its centre. A schematic of this behaviour is given in Figure 1.3.

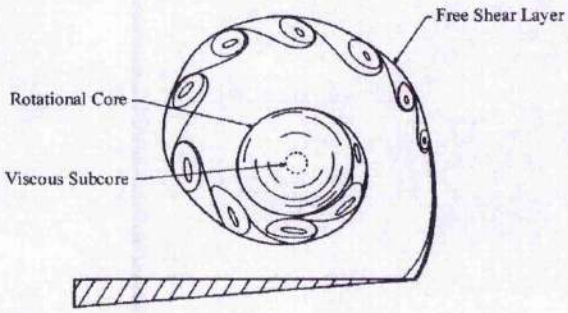

Figure 1.3: Structure of a leading edge vortex (from Ref. [2])

Other investigations have determined that there are a number of parameters which are important in describing the behaviour of the primary vortex, these include the circulation, vorticity and both swirl (tangential) and axial velocities [13, 41, 42]. Each of these variables have been found to vary with distance from the vortex core and, as such, the regions mentioned above can be defined from their behaviour. For example, the viscous-subcore may essentially be defined as the region in between the two extremes of swirl velocity, i.e the region where the swirl velocity changes sign. Figure 1.4 shows the distributions of swirl and axial velocities through the vortex core taken from experiments by Pagan and Solignac [3], with the three regions defined.

It is clear that as the viscous-subcore is approached, the axial velocity increases. This profile is similar to that of a swirling jet. The flow is in fact accelerating along the core and it is clear from the profile that the maximum axial velocity is approximately 2.5 times the freestream velocity. It has been found in other experiments by Payne *et al.* [41] and Mitchell [13] that the axial velocity can reach velocities up to three times the freestream velocity conditions. The maximum value reached within the vortex core is dependent on the incidence as shown in Figure 1.4 and also on the sweep angle of the wing. It was found by Wentz and Kohlman [7] that the vortex strength, which is related to circulation and vorticity amongst other parameters, also increases with increasing incidence.

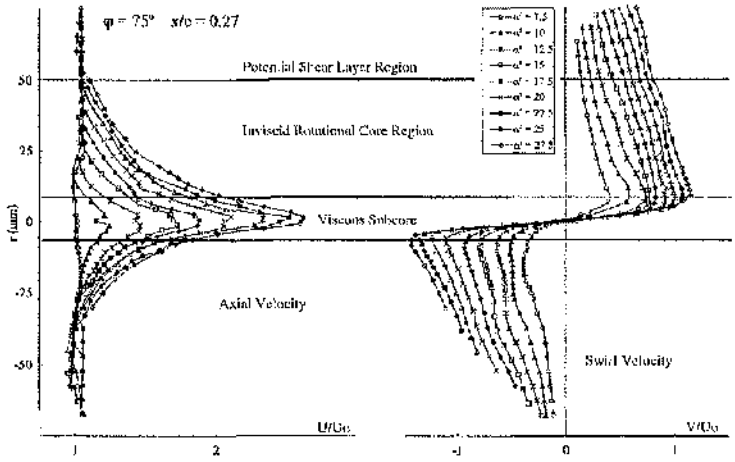

Figure 1.4: Profiles of swirl and axial velocity through a vortex core, detailing the three main vortex regions (adapted from Ref. [2], originally from Ref. [3])

Wentz and Kohlman also showed that the strength of the vortex is dependent on the sweep angle of the delta wing, such that as the sweep angle is increased the vortex strength decreases. This was further considered by Hemsch and Luckring [43], who determined an analytical relationship to relate the sweep angle and vortex strength. The location of the vortices has also been found to be dependent on the angle of incidence and the sweep angle of the wing. From a number of experiments [44, 45, 46], it has been found that with increasing incidence, the vortex core moves inboard and further away from the wing surface. Increasing the sweep angle was also found to move the primary vortices inboard and closer to the surface of the wing.

Due to the majority of the vortex behaving in an inviscid or potential manner and the fact that the primary separation is fixed to the sharp leading edge, it is generally accepted that the effect of Reynolds number on the behaviour of the primary vortex is negligible. This was confirmed in an experiment carried out by O'Neill *et al.* [44] on a series of 60^o and 70^o delta wings where the vortex trajectory was investigated for a range of Reynolds numbers, with only a very small difference being observed. However, other aspects of the flow are affected by Reynolds number, in particular the secondary and tertiary separations and the behaviour of the shear layer.

The secondary and tertiary vortices are less intense than the primary leading edge vortices and occur due to the separation of the crossflow as described previously. The location of the secondary separation is determined by the type of boundary layer, either laminar or turbulent, over the wing, which in turn is determined by the Reynolds number. Due to a greater susceptibility to adverse pressure gradients, the laminar separation occurs earlier and therefore further inboard on the delta wing surface. This means that a transition from a laminar to turbulent flow on a delta wing may be indicated by an outboard inflection of the secondary separation line. Generally, these smaller vortices affect the primary vortex by moving its position inboard and lifting it up off the surface of the wing [39, 47]. The size and strength of the secondary and tertiary vortices are also determined by the behaviour of the boundary layer. In work carried out by Hummel [48], it was found that for a laminar boundary layer and separation, the formation of the secondary and subsequent vortices, due to the spanwise pressure gradients, causes a peak in the surface pressure distribution greater than that of the primary vortex. This peak occurred in the vicinity of the separations outboard of the primary vortex. It was also found, in comparison, that for turbulent boundary conditions and separation that this peak is relatively flat and thus, less than the peak caused by the primary separation.

Due to the highly rotational nature of the flow within the vortex core which causes a region of high vorticity, the local static pressure is relatively low. As the primary vortex is situated in relatively close proximity to the wing surface, the impingement of the vortex on the surface results in a region of low pressure on the wing [49, 50, 51]. This suction force was investigated in the work by Polhamus [52], who split the lift of a sharp edged delta wing into two components, potential and vortex lift. The vortex lift is the contribution to the overall lift created by the suction of the leading edge vortices. Due to this extra component of lift, the presence of the leading edge vortices are generally beneficial to the performance of delta wings.

1.2.2 Vortex Breakdown

At some point, under the influence of external and internal instabilities, an abrupt change in the the vortex core occurs. The vortex core expands, the axial flow stagnates and downstream, the flow becomes highly unsteady and turbulent in nature. This process is known as vortex breakdown. Initially, at a low incidence, breakdown does not occur over the wing and may occur downstream of the trailing edge. However, with increasing incidence, the breakdown position moves upstream and crosses the trailing edge at a critical angle. Further increases in incidence, cause the location of breakdown to move further upstream on the wing until it reaches the apex, where the wing is said to be stalled.

From vortex tube experiments, Faler and Leibovich [53] detailed many different forms of vortex breakdown. However, Lambourne and Bryer [4], who studied the vortex breakdown process in detail, noted that two main types occur in flows over delta wings: bubble and spiral breakdown. Both types of breakdown are shown over a delta wing in Figure 1.5. Bubble breakdown exhibits an axisymmetric behaviour and is generally characterised by the occurrence of a stagnation point on the vortex core axis with a region of reversed flow downstream. The remaining outer flow passes over this bubble as a bluff body before being entrained into a region of turbulent flow downstream. For spiral breakdown, Lambourne and Bryer [4] suggested that three stages occurred. A deceleration of the vortex core, an abrupt "kink" in the vortex core, where the vortex filament spirals around a stagnant flow region and, finally, a further breakdown into large-scale turbulent flow downstream. A schematic diagram of this behaviour is shown in Figure 1.6 The spiral form of breakdown is generally much more common over slender delta wings. However, both these types of breakdown behaviour were found to occur in the experiments carried out more recently by Payne *et al.* [41, 54] for a series of delta wings with various sweep angles at a range of angles of incidence. Bubble bursts have also been found to occur occasionally in computational investigations [5].

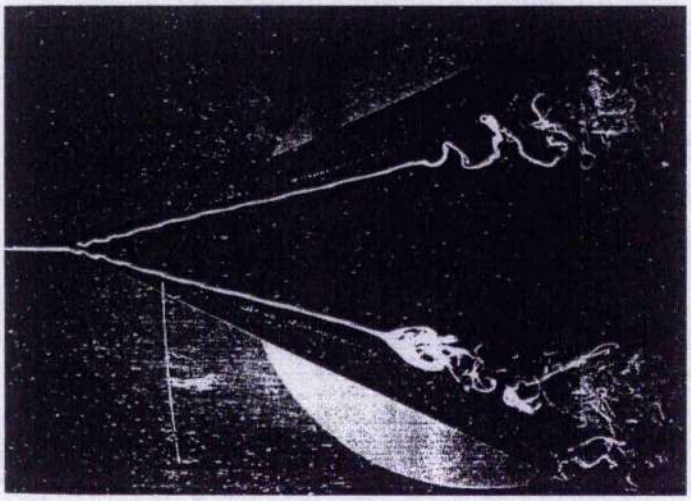

Figure 1.5: Leading edge vortices and types of vortex breakdown over a 65^o delta wing. The upper vortex exhibits the spiral form of breakdown and the lower vortex shows the bubble type (from Ref. [4])

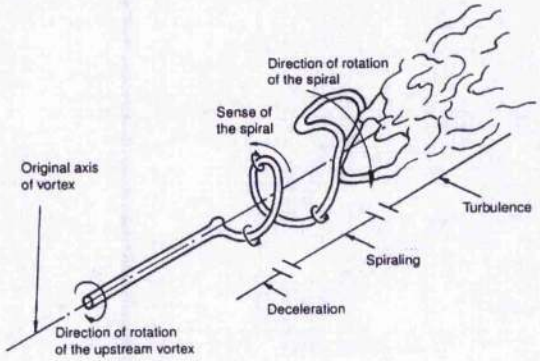

Figure 1.6: Spiral vortex breakdown occurring over delta wings (adapted in Ref. [5] from Ref. [4])

Evidence of the spiral structure was found from the experimental investigation by Klute *et al.* [6, 55] for a 75^o delta wing at an incidence of 40^o. The visualisation was performed in a water tunnel facility through the use of Digital PIV techniques on a 2-dimensional plane through the vortex core. The helical form of breakdown was witnessed by considering streamlines on a plane through the vortex core region as shown in Figure 1.7. The foci of the streamlines, calculated from the velocity field on the measurement plane, indicate the location where the helical structure intersects the plane and were found to occur in a staggered pattern. This view of the helical nature of vortex breakdown was also found in the instantaneous vorticity PIV results of Özgören *et al.* [56] and by Towfighi and Rockwell [57], again using PIV techniques.

Similar details of the spiral breakdown behaviour were witnessed in the computational investigation by Visbal [10] on a 75^o delta wing at a Mach number of $M = 0.2$, Reynolds number of 9.2×10^3 and for a range of angles of incidence, $17^o \leq \alpha \leq 34^o$. It was found, for this low Reynolds number, that the time-averaged view of the spiral structure displayed characteristics of an axisymmetric bubble type breakdown. However, in the instantaneous results and through streakline visualisations, the spiral form was clear. The behaviour of the spiral was also captured on a plane through the vortex core and a number of flow variables were plotted to visualise its structure. In a plot using contours of vorticity, the spiral structure was observed, suggested by small staggered regions of opposite sign vorticity. This was confirmed by the use of streamlines on the same plane which exhibited clear foci in the regions of the concentrated vorticity in a similar manner to the results of Klute *et al.* [6, 55] described above.

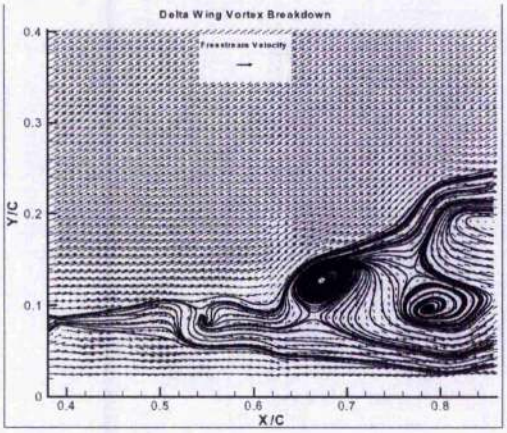

Figure 1.7: Instantaneous evidence of the spiral nature of breakdown $\tau = 0.037$, shown on a plane through the vortex core (from Ref. [6])

There have been many investigations into the movement and sensitivity of vortex breakdown to internal and external parameters both over delta wings and within vortex tubes. From these investigations, many theories have been proposed to explain the cause of vortex breakdown, which include an analogy to a 2-dimensional boundary layer, hydrodynamic instability and critical state (wave) theories which are explained in detail in Délery [49], Hall [50] and Escudier [58]. Much work has also been carried out on the theory that a critical parameter or relationship exists at which stagnation and mass disorganisation occurs in the flow. These criteria are generally based on internal parameters such as the swirl velocity, axial velocity and adverse pressure gradient and include, a critical value of swirl ratio (or Rossby number), based on critical states theory and stability of the vortex [46, 59, 60], a critical value of helical angle [61, 62], a switch in sign of the azimuthal vorticity [57, 63] and a critical value of circulation [64].

It has been found that there are a large number of external factors which also have an important effect on the behaviour of breakdown. These include, an external adverse pressure gradient [65], which was found to move the position of breakdown upstream, geometric effects such as the inclusion of centre-bodies or sting geometries [66, 67], sweep angle and leading edge properties [68, 69] and the proximity of wind tunnel walls [70, 71]. In the investigation by Wentz and Kohlman [7], the effect of the sweep angle on the critical incidence at which breakdown occurs over the wing was determined. It was found that with increasing sweep angle the onset of vortex breakdown could be delayed for sweep angles lower than approximately 75^o. This is shown in Figure 1.8.

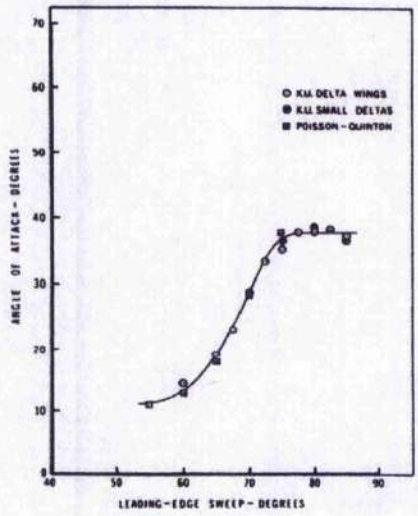

Figure 1.8: Effect of sweep angle on the occurrence of vortex breakdown at the trailing edge (from Ref. [7])

In a recent review by Jobe [72], the position and movement of vortex breakdown over 65^o delta wings is studied. The study details and collates the results gathered from many different investigations carried out over the years on various delta wing geometries for incompressible flow. Experimental, computational and empirical data was considered for a range of flow conditions. There is a large scatter of data for the range of angles of incidence tested. Some of this scatter is attributed to differences in leading edge geometry and centre-bodies. However, even among the investigations carried out on very similar geometries there are differences, which may be attributed to the unsteadiness of the vortex position (which can oscillate with an amplitude of $20\% c_r$ [8]) or to the way in which the point of breakdown is determined. However, a general trend was obvious from all the data for increasing incidence. Examples of this can be seen in Figure 1.9.

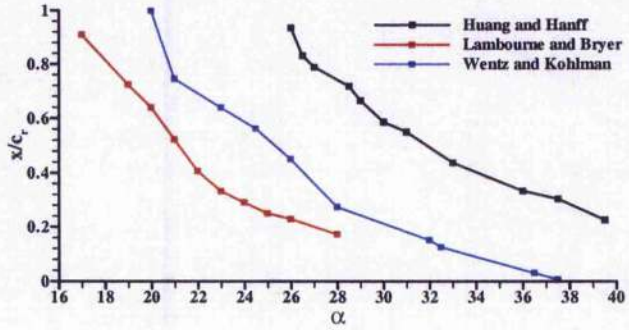

Figure 1.9: Movement of vortex breakdown over a 65^o delta wing with increasing incidence (data from Ref. [8])

The data shown is from three well-known experiments by Huang and Hanff [8] on a wing with sharp, symmetric, 10^o bevelled leading edges and a wing centre-body, Lambourne and Bryer [4] on a wing with no centre-body and a flat leeward surface and Wentz and Kohlman [7] on a wing with 15^o symmetrically bevelled leading edges and again no centre-body. From these results, it can be seen that for subsonic, incompressible flows that the movement of vortex breakdown upstream is relatively gradual for the 65^o delta wing. These three experiments also help to demonstrate the relevant conclusions of the review, namely that the position of breakdown is delayed downstream by the addition of a symmetric centre-body and also by an increase in lower surface bevel angle. A number of attempts have been made to correlate breakdown results and to determine an analytical relationship which will quantify the position of vortex breakdown considering a number of the influential parameters, mostly geometric. These were briefly summarised and tested on a large database of results by Gursul [73]. Unfortunately, none of the relationships allowed for a collapse of the data to a single line and thus the relationships were not deemed to be useful.

The occurrence of vortex breakdown has been found to have a pronounced influence on the aerodynamic characteristics of swept wings. In particular, there is a significant effect on the creation of lift on the wing. As mentioned

previously, the leading edge vortices cause an increased suction on the upper surface of the wing, which creates vortex lift. The theory which describes this contribution was proposed by Polhamus [52] and is based on a leading edge suction analogy which does not require knowledge of the behaviour of the leading edge vortex system, only assuming that the flow reattaches on the upper surface. However, as pointed out in the review of Lee and Ho [9], Polhamus' theory is not valid when vortex breakdown occurs over the wing and so is limited in the complete analysis of lift generation over delta wings. It was discovered in investigations by Wentz and Kohlman [7], O'Neill *et al.* [44] and Johari and Moreira [74] that for wings with sweep of more than 70°, that the point at which breakdown passes over the trailing edge coincides with the occurrence of maximum lift. This implies that vortex breakdown is detrimental to the production of lift. However, for wings with sweep angles below 65°, maximum lift does not occur until breakdown is almost at the apex of the wing and the wing is close to stall. Therefore, it can be assumed that the relationship between the occurrence of vortex breakdown and the generation of lift is highly complex and that other factors are important, such as sweep angle and vortex strength.

It has been generally thought that with increasing sweep angle, that the contribution of vortex lift increases [7, 9]. However, there is also compelling evidence that in fact the opposite is true. In a paper by Hemsch and Luckring [43], Polhamus' theory is considered and manipulated to provide a relationship between the change in sweep angle and the vortex lift. This was achieved by considering the non-linear part of the vortex lift and its relationship to a change in sweep angle. It was found from this investigation that with increasing sweep angle that the contribution of vortex lift decreases. It also showed that the overall contribution of non-linear lift increases with increasing sweep angle, therefore although the overall contribution of the vortex lift has decreased with increasing the sweep, the amount of non-linear lift generated has increased. This may help to explain the differences in relationship between the point of maximum lift and the point at which breakdown crosses the trailing edges for the wings described above, as it may be suggested that the linear production of lift is not as susceptible to the effects of breakdown.

In an investigation by Earnshaw and Lawford [75], the lift coefficient against incidence for a number of delta wings with various sweep angles was plotted. The results are shown in Figure 1.10. It is apparent from this graph that the lift characteristics of the 65° and 70° swept wings are the most favourable. It is also clear that with decreasing sweep angle the magnitude of C_L is reduced along with the angle at which it occurs. At first this may appear to dispute the results of Hemsch and Luckring [43], however, with consideration of the vortex breakdown characteristics over lower swept wings, this may be due to the theory not accurately predicting the full lift generated over the wings.

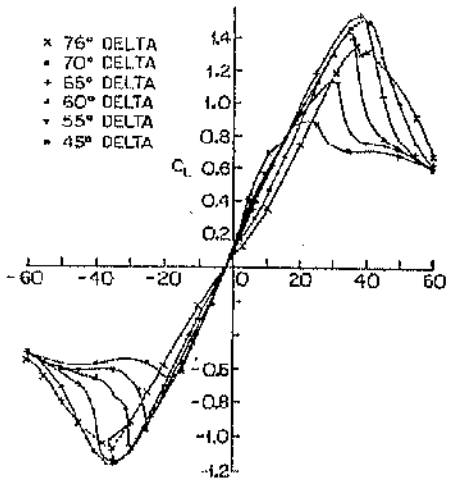

Figure 1.10: Lift coefficient vs angle of incidence for different sweep angles [9]

1.3 Unsteady Aspects of Delta Wing Vortical Flows

1.3.1 Vortex and Vortex Breakdown Instabilities

The occurrence of vortex breakdown causes an increase in the unsteadiness in the flow over delta wings. In the investigation carried out by Earnshaw and Lawford [75], it was found that as the breakdown location crossed the

trailing edge of the wing, there was a significant increase in the fluctuations of the measured normal force coefficient. Coherent fluctuations due to breakdown have also been witnessed in surface pressure readings [76] over delta wings and from vortex tube experiments [77, 78]. In the study conducted by Gursul [79], it is concluded that the fluctuations downstream of the breakdown location are caused by a hydrodynamic instability which manifests itself in the first helical mode. This was determined from the measurements taken by two pressure transducers situated in the flow downstream of breakdown. The helical mode instability, which is determined to occur over delta wings with various leading edge sweep angles, is described as a helix of the rotating vortex core filament. The sense of this helix is found to be in the opposite direction to the vortex rotation upstream of breakdown. However, the whole structure also rotates, with the same sense as the vortex core. This is, therefore, a description of the spiral mode of breakdown, which was described in Section 1.2.2 and shown in Figure 1.6. As stated, this is the most commonly witnessed mode of breakdown over delta wings. Through the analysis of the unsteady measurements it was found that a dominant frequency could be associated with the helical mode instability, which reduced with increasing incidence and decreasing sweep angle. For all delta wings tested, this frequency was found to occur in the range $St \approx 0.5 - 2$. It was also determined that the frequency of the instability decreased with increasing streamwise location i.e. along the vortex axis, suggesting that the pitch of the helix is increasing, therefore, the spiral is being stretched downstream.

In the computational investigation by Visbal [10] on a 75^o delta wing, discussed in Section 1.2.2, the unsteady nature of the spiral breakdown is also considered and analysed. As mentioned, a plane through the vortex core was considered and the instantaneous spiral structure was indicated by staggered regions of opposite sign vorticity. From this plane, the increase in radius and pitch of the helical configuration, mentioned by Gursul [79], was found. The development and movement of the helix was also witnessed through a number of consecutive instants, as the regions of vorticity were found to move downstream. Spectral analyses were carried out on the pressure signals measured under the vortex breakdown region. From the power spectral density (PSD) plots of the data, it was found that a number of dominant peaks occurred. The largest peak for the majority of the data, taken at different positions on the wing and at different angles of incidence, was centred around a non-dimensional frequency of approximately $St = 3.2$. This was suggested to correspond to the frequency of the rotation of the spiral structure. It was noted, however, that this frequency increased slightly with increasing incidence, due to the upstream progression of the breakdown location. Other peaks which were noted to occur in many of the results had non-dimensional frequencies of approximately $St = 1.3$ and 2.0. No suggestions were made to the cause of these peaks. From further consideration of the overall behaviour of the spectral data with increasing incidence, it was observed that with increasing incidence, and therefore stronger breakdown, the frequency response broadens.

This unsteady structure was also considered experimentally by Klute *et al.* [55], discussed in the previous section. From the instantaneous velocity calculated on a plane through the vortex core, the downstream progression of the streamline foci was witnessed, indicating the rotation of the spiral breakdown, as mentioned above. The foci were also found to be accelerating downstream at different rates, suggesting that the radius and wavelength of the spiral increases. This is in agreement with the findings of both Gursul [79] and Visbal [10]. The time histories of streamwise velocity, taken from the DPIV data at a number of points downstream of the breakdown location, were analysed using PSD techniques. From the analyses at a constant streamwise location from the breakdown location, a number of dominant frequencies were found at approximately $St = 0.44$, 1.72 and 2.78, with the $St = 1.72$ consistently exhibiting the highest energy at all points considered. Further analysis at varying streamwise locations downstream of breakdown showed that with increasing distance from breakdown, the dominant frequency of the flow decreased. This was attributed to the increase of the radius and wavelength of the spiral mentioned above. This dominant frequency for the helical mode instability ($St \approx 1.7$) was also captured in the inviscid computational results of Görtz [23]. The calculations were carried out on a 70^o delta wing at 27^o incidence and with Mach number $M = 0.2$. This frequency was calculated from flow visualisations where the period of one rotation of the breakdown spiral was observed to be approximately 0.008 seconds.

As well as the unsteadiness within the vortex breakdown region there is also unsteadiness in the location of vortex breakdown. In the computational study by Visbal [10], described above, a high amplitude, low frequency oscillation was found to occur due to the motion of the breakdown location. This is shown in Figure 1.11. It is clear that the large scale amplitude of the breakdown oscillation is approximately $9\%c_r$. The corresponding non-dimensional frequency of this oscillation was found to be $St \approx 0.075$. A higher frequency, low amplitude oscillation was also found, however the resolution of this was not sufficient to allow the frequency to be determined. This unsteady behaviour has also been found to occur in experimental investigations, such as Huang and Hanff [8], Garg and Leibovich [77], Payne *et al.* [41], Lowson [80] and Mitchell *et al.* [81]. From these investigations it has been found that the breakdown location can oscillate with an amplitude of as much as $20\%c_r$ [8]. In the results of Payne *et al.* [41], it was found that these oscillations had an amplitude of approximately $2\%c_r$ and occurred in an

antisymmetric manner over the left and right hand side of a full span wing.

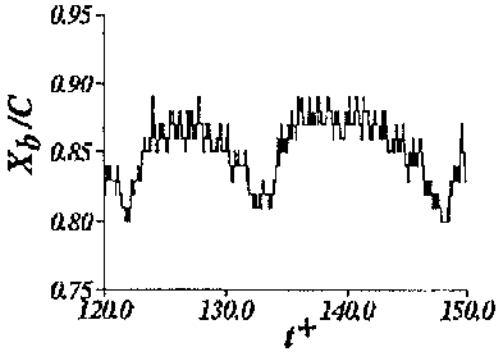

Figure 1.11: Streamwise fluctuations of vortex breakdown location at $\alpha = 32^o$ (from Ref. [10])

In the experiments carried out by Mitchell *et al.* [81] on a 70^o delta wing, this behaviour was also considered and the frequencies associated with this phenomenon were determined. The tests were carried out in a wind tunnel for a range of angles of incidence at Reynolds numbers of 9.75×10^5, 1.56×10^6 and 2.6×10^6. Laser sheet flow field visualisation techniques were used to determine the breakdown location and a time history of the behaviour was obtained for both leading edge vortices. From this study the asymmetry of the breakdown location was also witnessed and an interaction between the vortices was assumed. For all flow conditions tested, the frequencies of the breakdown oscillations were found to be in the range $St = 0.0443 - 0.0697$. The amplitude of the oscillations was found to be as much as $20\%c_r$ depending on the incidence and freestream velocity. The amplitude of the oscillation appeared to increase with increasing Reynolds number and decrease with increasing incidence.

Further work to consider the sensitivity of this phenomenon to Reynolds number was reported by Lambert and Gursul [82]. In this study wind tunnel tests were carried out at a Reynolds number of 1.6×10^6 on a 80^o delta wing at $\alpha = 50^o$. The unsteady behaviour of the flow was measured using surface pressure transducers downstream of the location of breakdown and the dominant frequencies were determined from the resulting analysis. The vortex breakdown oscillation was determined to correspond to a peak frequency of $St = 0.15$ and two further frequencies at $St \approx 1.5$ and $St = 2$ were attributed to the helical mode instability. Comparison with the results of other similar investigations carried out at relatively low Reynolds numbers [83, 84, 85] showed that the behaviour of the breakdown was insensitive to Reynolds number.

In the investigation carried out by Gursul and Yang [86] on a 70^o delta wing an attempt was made to determine the cause of these fluctuations and whether the helical mode instability could have an effect on the behaviour. From consideration of the frequency domain data gathered from LDV analysis of the flow downstream of breakdown it was determined that the non-dimensional frequency of the helical mode instability was dependent on the incidence and ranged between approximately $St = 1.72$ and 3.5. Similarly, the dominant peaks associated with the oscillation of breakdown location was defined to occur in the range $St = 0.07 - 0.12$. It is clear that the non-dimensional frequency response of the breakdown fluctuations is an order of magnitude lower than the response associated with the spiral breakdown. Due to this, it was determined that the helical mode instability was not directly responsible for the breakdown fluctuations. It was stated that, by this argument, the Kelvin-Helmholtz instability of the shear layer was also not responsible for the fluctuations of vortex breakdown position as its dominant frequency is known to be an order of magnitude higher than that found for the helical mode instability.

Further investigation into the behaviour and origins of the breakdown oscillation was carried out by Menke *et al.* [15] for a series of delta wings with varying sweep angle and for a range of angles of incidence, $\alpha = 25^o - 42^o$ using flow visualisation and LDV techniques. Again, this study found that the specific dominant frequency and amplitude associated with the fluctuation of the breakdown location was dependent on the angle of incidence. However, all dominant frequencies occurred in the range $St = 0.04 - 0.12$. A dependence on the sweep angle of the wing was also determined. Evidence of the asymmetry of the breakdown oscillations was found from consideration of the full wing. It was shown that the oscillations occur at the same frequency, however they are out of phase by approximately 180^o. It was determined that this asymmetry was due to an interaction between the vortices, caused by a streamwise instability of the two breakdown regions and is non-linear in behaviour. However, with the inclusion of a splitter plate, it was found that the oscillation of breakdown was still present although with a significant reduction in amplitude and RMS behaviour.

Jumper *et al.* [64] suggested a simple criterion for vortex breakdown based on a critical value of the circulation of the vortex. From consideration of their model, it was suggested that the oscillation of breakdown was due to a fluctuation of the circulation within the vortex core upstream of breakdown. As the circulation changed, the point of breakdown would move, either upstream or downstream, to a stable location in response to this change in upstream flow conditions. This was concluded from consideration of the rotational direction of the spiral breakdown in relation to the rotation of the vortex core and to the resulting induced velocity, which is in the opposite direction to the axial flow of the vortex upstream.

A consequence of vortex breakdown asymmetry and fluctuation is vortex interaction at high angles of incidence, where the vortices move inboard and become much closer. In an experimental investigation by Menke and Gursul [87], the overall unsteady nature of the leading edge vortices over a 75^o sharp leading-edge delta wing was considered. The experiment was carried out in a water tunnel at a Reynolds number of 4.1×10^4. It was found from LDV measurements and consideration of probability data that large amplitude velocity fluctuations occurred in the core of leading edge vortices upstream of breakdown position and even in cases where breakdown was not present. Frequency spectra were considered of the velocity time histories from three span-wise locations at $x/c_r = 0.6$. Each of the three positions gave noise-like, broad-band responses, with no discernible peaks. As the frequency range under consideration covered a number of unsteady phenomenon, such as the fluctuation of breakdown location, helical mode instability and the Kelvin-Helmholtz instability, these could be ruled out as the cause of the fluctuations. Another factor considered was vortex interaction, which was also discounted. It was consequently suggested that these velocity fluctuations were caused by a random "wandering" of the vortex core. Suggestions were also made as to the cause of the vortex wandering, such as the upstream influence of the turbulent unsteady flow in the wake and the effect of three-dimensional instabilities in the shear layer, however no conclusions were reached. In another investigation by Gursul and Xie [88], a link between this wandering behaviour and the presence of the Kelvin-Helmholtz instability in the separated shear layer was determined. It was suggested that this interaction between the shear layer instability and vortex wandering was due to the small scale vortices being convected around the primary vortex, therefore displacing the vortex core through the process of Biot-Savart induction.

This vortex interaction and unsteadiness can, at high angles of incidence beyond the stall angle of the wing, result in vortex shedding from the wing. This was found for a 76^o delta wing in the investigations by Rediniotis *et al.* [89, 90]. In the investigation the wing was tested at angles of incidence between 35^o and 90^o at Reynolds numbers ranging between 3.9×10^4 and 9.02×10^5. At angles of incidence greater than approximately 36^o periodic shedding was found to dominate the wake region of the wing. The behaviour of the periodic shedding was not found to be influenced by Reynolds number, however the angle of onset was sensitive. For higher Reynolds numbers the angle of onset was found to be slightly lower than for low Reynolds number. For lower angles of incidence, in-phase shedding was witnessed on the wing, with vortices being shed at the same time from both leading edges, however with a further increase in incidence above 70^o a second shedding mode was discovered. This mode was found to be an alternate shedding of vortices which occurs with the in-phase shedding. It was also found that the non-dimensional frequency (Strouhal number) of the periodic vortex shedding decreased with increasing incidence and occurred in the range $St = 0.05 - 0.4$. It was proposed that this shedding was due to the shear layer separating and no longer being able to create the swirling flow with a significant axial motion. This would result in vortical structures being shed to the freestream.

In the experiments carried out by Gursul and Xie [11, 91], the transition from the helical mode instability of breakdown to vortex shedding was investigated. The experiments were carried out in a water channel, using LDV and flow visualisation techniques on a 75^o sharp leading edged delta wing. LDV data was obtained from a plane perpendicular to the wing surface, situated at the trailing edge. From this data, at different angles of incidence between 31^o and 70^o, the changing behaviour of the flow was observed. This is shown in Figure 1.12. It is clear from this figure that with increasing incidence, the dominant frequency of the helical mode instability is found to decrease, whereas the frequency of the vortex breakdown oscillation and interaction is virtually constant. However, a change in the behaviour was found at an incidence of approximately 60^o, where the characteristic swirling flow disappears at the trailing edge and a separated shear layer region appears. These results were compared to the results from Rediniotis *et al.* [89] and Gursul [79] described above. The RMS velocities are also considered, which show the highest velocity fluctuations occurring initially within the vortex core region, and then with increasing incidence, in the shear layer itself. Spectral analyses of these velocity fluctuations were carried out for all angles of incidence. It was found that for the swirling flow, that two frequencies were dominant, which were virtually constant over the wing, corresponding to non-dimensional values of $St \approx 0.07$ and ≈ 1.0. The lower frequency is consistent with fluctuations of vortex breakdown location as discussed above whereas the larger frequency was attributed to the helical mode instability which is still present over the wing. These two peaks are found to occur in the flow up until the critical incidence of approximately 60^o mentioned before. Above $\alpha = 60^o$ where the swirling

flow disappears, the frequency response changes and there is only one dominant peak. The non-dimensional frequency of this dominant peak is found to be $St \approx 0.3$ which corresponds to the frequencies determined for vortex shedding in previous measurements of a delta wing wake [79]. As the change in dominant frequency of the flow is relatively sudden it is concluded that the transition in flow behaviour to vortex shedding is also abrupt.

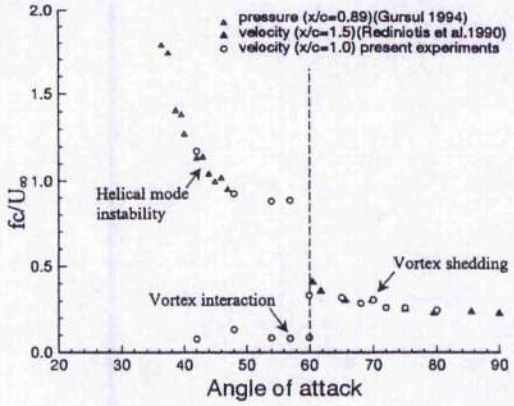

Figure 1.12: Variation of non-dimensional frequency for unsteady phenomena as a function of angle of incidence (from Ref. [11])

1.3.2 Shear Layer Instabilities

As mentioned previously, a shear layer is formed as the fluid flows over the leading edge of the delta wing, which rolls up and creates the leading edge vortices. However, the shear layer is subject to a number of instability phenomena. These instabilities have been seen to cause the occurrence of vortical sub-structures within the shear layer, which can be divided into three main forms [14]:

1. An unsteady form where the discrete vortical sub-structures move with time through the shear layer.
2. A steady laminar form, where the sub-structures are spatially fixed.
3. A mean stationary form observed in time averaged solutions of transitional/turbulent shear layers.

The first of these, an unsteady, time-varying instability, was first found by Gad-El-Hak and Blackwelder [38, 40] for both 60^o and 45^o delta wings through flow visualisation techniques. It was found that within the shear layer, discrete vortical sub-structures occurred which pair up and rotate around each other, as shown in Figure 1.13. These sub-structures could not be seen with the naked eye and only through the flow visualisation. They were found to exist all along and parallel to the leading edge and occurred at a frequency which was dependent on the freestream velocity. This type of behaviour is well documented for the development of two-dimensional shear layers between two streams of differing freestream velocity [92] and is known as the Kelvin-Helmholtz instability. Therefore, it was proposed that the behaviour was caused by a similar Kelvin-Helmholtz instability arising on the shear layer.

Figure 1.13: Kelvin-Helmholtz shear layer instabilities (from Ref. [6])

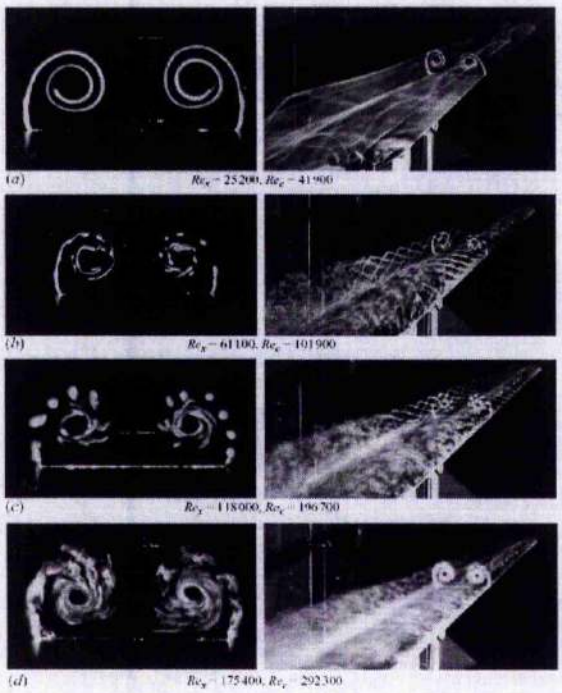

Figure 1.14: Shear layer instabilities and the effect of Reynolds number (from Ref. [12])

Further evidence of these unsteady structures was found in the time-accurate computational study carried out by Gordnier and Visbal [93]. In this investigation a 76^o delta wing was used at an incidence of 20.5^o. The flow conditions applied were a Mach number of 0.2 and Reynolds numbers of 0.5×10^5 and 9×10^5. The higher Reynolds number case was used in a previous study where the results were found to be unsteady [94]. This unsteadiness was attributed to the Kelvin-Helmholtz instability in the shear layer. A time step study was carried out, resulting in a time step of $\Delta\tau = 1.25 \times 10^{-4}$. For improved agreement with the experiments of Gad-El-Hak and Blackwelder [38] the lower Reynolds number was used for the majority of the calculations. Using instantaneous plots of the flow, the unsteady structures were shown to occur in the shear layer region and the roll up of the sub-structures were clearly seen. Time-histories of the pressure at different streamwise positions were measured and the dominant frequencies were considered. It was determined that the dominant frequency was almost linearly dependent on the streamwise position, with the Strouhal number decreasing with increasing chordwise position. In the experimental findings of both Gad-El-Hak and Blackwelder [38] and Lowson [39] the shedding frequencies of these structures are found to be uniform, only dependent on Reynolds number. However, the frequencies which occurred at the trailing edge were found to be consistent with the experimental values found. The effect of these structures on the surface pressure coefficient distributions was shown to be small for this Reynolds number however, it was stated that for the higher Reynolds number used the temporal effect was greater.

In the study by Riley and Lowson [12], the development of the shear layer was investigated using flow visualisation and LDA techniques. An 85^o delta wing was used, set at an incidence of 12.5^o. In this investigation both steady and unsteady instabilities were found to occur and it was determined that this occurrence was dependent on Reynolds number. For Reynolds numbers less than approximately 3×10^4 the shear layer appeared to be fully laminar with no clear structures being witnessed. However, with increasing Reynolds number streamwise structures first appear then become more distinct. An example of this effect and the shear layer structure is shown in Figure 1.14. This also clearly shows the occurrence of turbulent disturbances in the flow at the trailing edge which move upstream with increasing Reynolds number.

This dependence on Reynolds number was also found in the investigation carried out by Lowson [39]. After consideration of the onset of the unsteady instabilities, it was suggested that their appearance was dependent on tunnel velocity and therefore, the unsteady structures witnessed were a result of external instabilities in the tunnel and not a generic part of the flow. However, as mentioned before, in the original investigation by Gad-El-Hak and Blackwelder [38], it was noted that frequencies of the unsteady instabilities were dependent on the freestream velocities. This would, therefore, suggest that the instability would develop at the most unstable frequency in the flow, which may coincide with external disturbances [95]. This Kelvin-Helmholtz instability has also been witnessed in many

numerical calculations [14, 96, 97] which do not contain any external disturbances. Therefore, it must be assumed that this type of instability is an inherent part of the shear layer behaviour and not a result of external influences.

LDA measurements were taken at a number of positions within the flow, and from the results, laminar steady sub-structures were observed. These correspond to the second type of instability mentioned above which were also found from the flow visualisation results to be visible to the naked eye and very sensitive to external disturbances. In considering the behaviour of these stationary structures, it was found that their path was helical around the main vortex. It was also discovered that the velocity profiles were wake like when near to the leading edge but as the structures moved away, the velocity deficit with respect to the freestream disappeared. Their strength also increased with distance from the leading edge due to the diffusion of vorticity to the flow. The origin of these sub-structures at the leading edge was also investigated and it was determined that the presence of the secondary vortex was important. In a discussion of the cause of these sub-vortices being due to a cross-flow instability as suggested by Washburn and Visser [97], described below, it was stated that the secondary vortex may be the cause of the necessary spanwise gradient. In conclusion it was stated that the theory of a cross-flow instability was in essence, identical to that of the three-dimensional Kelvin-Helmholtz instability, therefore these co-rotating vortices must be due to a local Kelvin-Helmholtz mechanism occurring in the streamwise vortex feeding sheet. This process was also observed in the DNS calculation by Shan *et al.* [98] on the same 85° delta wing. The results obtained from the calculation were very similar to the experiment, however the laminar steady structures were not witnessed. Unfortunately, no further experimental or computational investigations have been reported which have also observed these laminar, steady structures for highly swept wings.

Gordnier and Visbal [96] carried out an investigation into the origin of the unsteady shear layer phenomenon, which was inspired by the findings of Riley and Lowson [12], detailed above, concerning the effect of external disturbances. Calculations were performed for three different wings with sweep angles of 70°, 75° and 85°, at a range of angles of incidence from 10° to 25° with two Reynolds numbers being considered: 1×10^4 and 5×10^4. The grid used was based on one detailed for a previous investigation [93]. A post-processing technique was utilised which allowed a simulated laser light sheet to be created in order to compare the results with experimental flow visualisations. Validation was carried out for a 70° delta wing and very good agreement was found for the flow visualisation, with similar sub-structures observed in the computational results. Further study was carried out to attempt to explain the mechanism which causes these unsteady structures and to determine if this could be same mechanism which occurs in experiments. It was determined from a grid refinement study that the axial grid resolution effects the shedding frequency of the sub-structures, however, no noticeable change in the overall behaviour of the flow was found. From consideration of all the results it was suggested that the shear layer unsteadiness was due to a boundary layer eruptive behaviour caused by the interaction of the primary vortex with the surface of the wing. The disappearance of these structures for low Reynolds number was also witnessed and was explained through the elimination of the eruptive behaviour. The effect of the incidence and sweep angles detailed before, was attributed to the increased strength of the primary vortex, thus amplifying the behaviour and causing more unsteadiness in the flow. It was also determined that the shedding frequency behaviour with chordwise position becomes increasingly linear with greater unsteadiness.

The third type of structure was found in the investigation by Washburn and Visser [97]. In this study, three delta wings with sweep angles of 70°, 76° and 80° were used to investigate the behaviour of steady sub-vortices. A five-hole probe was used to obtain velocity and pressure data to allow the measurement of the conditions for the sub-structures to occur and for their helical paths to be defined. The experiments were carried out for a range of angles of incidence between 10° and 25° and Reynolds numbers between 0.5×10^6 and 2×10^6 for each of the wings and sub-structures were found for almost all cases. Due to the limitations of the five-hole probe data, temporal instabilities could not be measured. Therefore, the structures observed were mean and steady in nature.

It was determined from the study that the size and rate of production of these vortices was dependent on the incidence and sweep angle. An increase in the incidence or a decrease in the sweep angle resulted in an increase in frequency and a decrease in the size of the sub-vortices. An increase in strength of the shear layer was attributed to the rise in frequency. It was also noted that with the same change in parameters that the structures formed closer to the leading edge. The paths of the sub-structures were shown to be helical, as initially assumed, however no evidence was found to support the theory that they are entrained into the vortex core downstream. From consideration of the vorticity behaviour, it was determined that these vortices were co-rotating with the primary vortex core and based on this, a theory to their cause was suggested. It was believed that the structures were due to an inviscid instability in the shear layer which was based on a cross-flow instability, similar to that found in three-dimensional boundary layers, where the resulting vortices are also found to be co-rotating. These steady state, mean structures were also found in the experimental investigations carried out by Payne [42], Mitchell *et al.*

[99, 100] and Honkan and Andreopoulos [101]. Figure 1.15 shows the helical paths of these structures from the results of Mitchell *et al.* [99, 100] captured using LDV techniques on a 70^o delta wing.

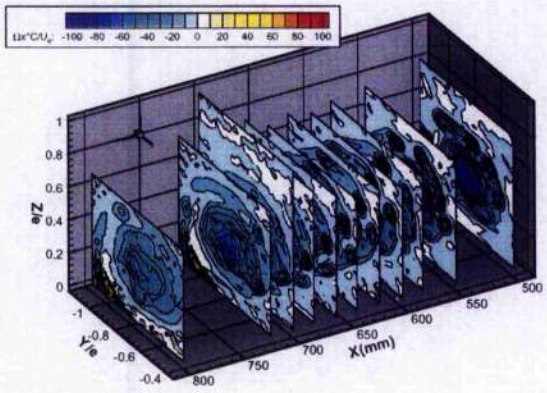

Figure 1.15: Stationary shear layer sub-structures shown using contours of x vorticity in planes perpendicular to the wing surface (from Ref. [13])

In a DNS investigation by Visbal and Gordnier [14], a 75^o semi-infinite delta wing is considered to determine the behaviour of the shear layer without any external influences such as the presence of vortex breakdown or trailing edge effects. The flow conditions used correspond to an incidence of 25^o and a Mach number of 0.1. The Reynolds numbers considered are dependent on the length of the region of interest and range between 6×10^3 and 5×10^4. The effect of Reynolds number was considered, in order to determine the effect without the presence of external forcing such as those witnessed in experiments. The behaviour computed was similar to that of the experiments with the present of a steady laminar vortical system at low Reynolds numbers and the increase in unsteadiness of the shear layer as the Reynolds number is increased. It was noted that the unsteady behaviour began toward the trailing edge of the wing and moved toward the apex with increasing Reynolds number as also found in the results of Riley and Lowson [12]. It is also determined that within a small range of Reynolds number, the complexity of the flow increases dramatically. A greater appreciation of the three-dimensional complexity of the flow and the differences caused by change in Reynolds number can be gained from Figure 1.16.

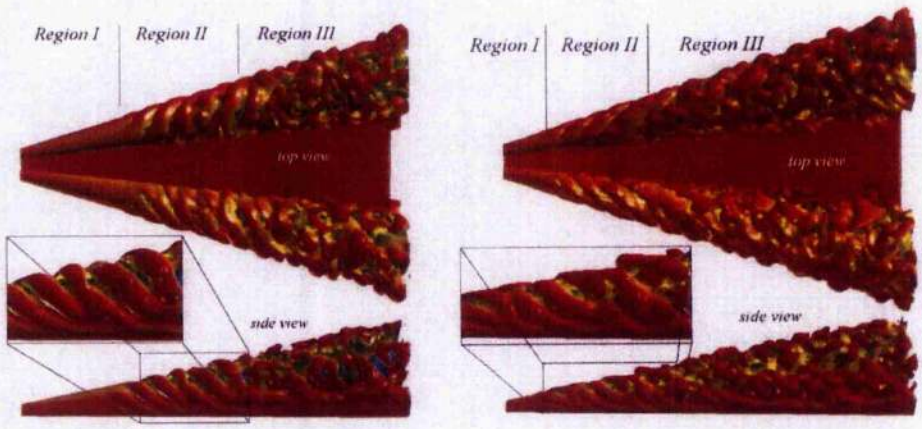

(a) $Re = 2.5 \times 10^4$ (b) $Re = 5 \times 10^4$

Figure 1.16: Instantaneous shear layer structure shown by iso-surface of axial vorticity for two Reynolds numbers (From Ref. [14])

It is clear from these diagrams that the flow is easily split into three streamwise regions, as suggested by the authors. Region I corresponds to a region where no sub-structures occur and the flow is found to be essentially steady. Region II refers to a region where the shear layer structures are evident, and appear to be well organised with a helical path around the vortex which, as they start close to the wing, are parallel to the leading edge then become further inclined toward the apex. In animations, it is stated that these structures are clearly seen to rotate around

the vortex. Further downstream, in Region III, the shear layer appears to be affected by further instabilities and therefore the flow becomes more complex. This further complexity may be caused by the sub-structures breaking down into further discrete concentrations of vorticity which continue in the helical path around the vortex. It is suggested that this is due to a secondary instability of the Kelvin-Helmholtz instability. Again, as in their previous investigation [96], it is suggested that the instabilities in the shear layer occur due to the interaction between the upper surface laminar boundary layer flow and the primary vortex. These results rule out the occurrence of unsteady separation from the trailing edge as a cause for the unsteadiness within the shear layer.

Consideration was given to the time-averaged or mean representation of the flow, which would allow closer validation with the experimental results gained by Washburn and Visser [97] and Mitchell *et al.* [99, 100]. Figure 1.17 shows the resulting plots. These plots show the shear layer, characterised by stationary helical sub-structures, which are co-rotating with the primary vortex as found in the experiments. From further consideration it is found that there are regions of high RMS velocity fluctuations within the shear layer, which appear to correspond to the positions of the helical sub-structures.

It is noted that the time-averaged structures only appear on the aft section of the wing (corresponding to Region III from before) with the rest of the time averaged shear layer appearing smooth. It is suggested that this behaviour is explained by the secondary instability occurring in Region III mentioned in the discussion of the instantaneous results. If this secondary instability occurs with a sufficient periodicity and wavelength, then it is suggested that it would be viewed in the time-averaged results. Therefore, the conclusion is made that the "stationary" and "unsteady" shear layer structures are not necessarily two separate phenomena but may in fact be different views of the same physical behaviour. It is noted that the laminar steady structures as shown in the investigation by Riley and Lowson [12] for a highly slender delta wing, have not been witnessed in this investigation.

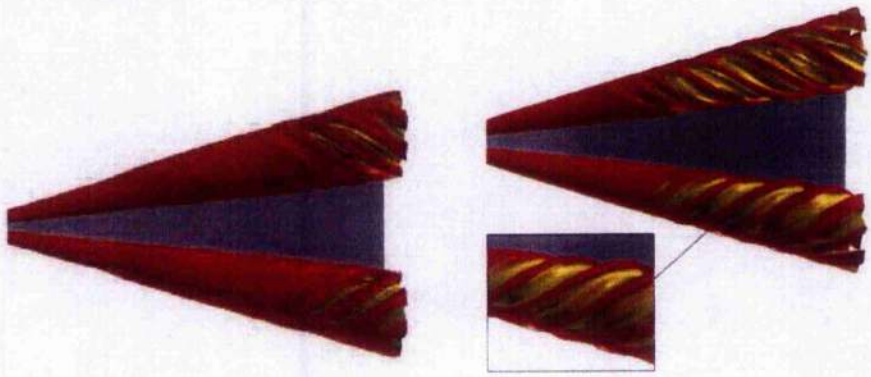

(a) $Re = 2.5 \times 10^4$ (b) $Re = 5 \times 10^4$

Figure 1.17: Time-averaged shear layer structure shown by iso-surface of axial vorticity for two Reynolds numbers (from Ref. [14])

1.3.3 Unsteady Flow Topology

From consideration of the literature summarised in the previous sections, an overall picture of the unsteady behaviour of delta wing vortical flows can be obtained. It is clear that there are many unsteady phenomena which exist in the flow, these include (in no particular order):

- Helical mode instability
- Shear layer instabilities
- Vortex Shedding - both from the trailing edge and at high angles of incidence
- Vortex core rotation
- Shear layer reattachment
- Vortex breakdown oscillation
- Turbulence downstream of breakdown

It has been found that characteristic frequencies exist in the flow which can be associated with each of these phenomena. From the literature review it is clear that there have been many investigations which consider the unsteady behaviour of vortical flows. Table 1.2 summarises these investigations, and details the frequencies assigned to each phenomenon. The column marked "*Other*" contains the frequencies which appeared in the investigations but were not assigned to any phenomenon. Some of the computational results detailed will be considered with respect to the numerical methods used in a later section.

This table allows a general appreciation of the frequency content to be obtained and patterns emerge relating to the order and size of the dominant frequencies. For example it would appear that the majority of the frequencies assigned to the helical mode instability fall between $St = 1-2$ and similarly for the oscillation of vortex breakdown location the majority of the investigations show this to occur with a Strouhal number between $St = 0.04-0.2$. Menke *et al.* [15] performed a similar analysis of the flow behaviour from work carried out by Gursul [79], Gursul and Yang [86], Gad-el-Hak and Blackwelder [38] and Gordnier and Visbal [93]. From this, a schematic of the frequency spectrum was created in an attempt to classify the unsteady frequencies. This is shown in Figure 1.18. Further consideration of the unsteady behaviour of the flow over delta wings can be obtained from the reviews by Gursul [95, 102].

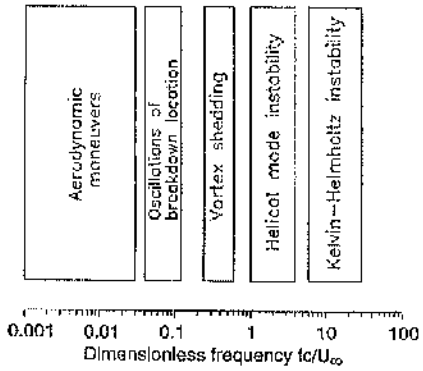

Figure 1.18: Spectrum of unsteady flow phenomena as a function of Strouhal number (from Ref. [15])

1.4 Transonic Effects on Vortical Flows

As the freestream Mach number is increased to transonic levels, $M > 0.7$, the vortical flow changes and behaves differently to that for the subsonic regime. In the experiments carried out by Erickson *et al.* [117, 118], it was found that increasing the Mach number from 0.4 to 0.95, changed the shape of the leading edge vortex. The vortex was found to become flat and elliptical in appearance and sat progressively closer to the surface of the wing. It was also found that with the increase in Mach number through the transonic regime, that the suction induced on the surface of the wing by the leading edge vortices was decreased due to a fall in the upwash created by the leading edges. From the experimental study by Elsenaar and Hoeijmakers [18] on a 65^o cropped delta wing it was also found that with increasing Mach number, the magnitude of the primary suction peak decreases, broadens and moves inboard for a given chordwise station. The secondary peak was also found to move inboard.

As the Mach number increases, it is found that the flow becomes locally supersonic and as a result shockwaves will appear in the flow, further altering the behaviour of the leading edge vortices. Stanbrook and Squire [119] determined that the change in behaviour of the leading edge separated flow could be correlated by considering the Mach number and incidence normal to the leading edge, defined respectively by

$$M_N = M_\infty \sqrt{1 - sin^2\Lambda cos^2\alpha} \quad \text{and} \quad \alpha_N = tan^{-1}\left(\frac{tan\alpha}{cos\Lambda}\right) \tag{1.1}$$

Using these flow parameters, the flow behaviour could be split into two main types of flow, separated and attached. These flow behaviours were separated by what is known as the Stanbrook-Squire boundary. Miller and Wood [16] gave further consideration to the types of flow over delta wings for transonic and supersonic regimes from experimental results on a number of delta wings with varying sweep angles for a range of Mach numbers and angles of incidence. From the analysis of the results, they classified the flow into six types of behaviour, including classical vortex, vortex with shock and shock-induced separation. These flow behaviours were also defined by

Experimental Results

	Conditions			*Phenomenon - Strouhal Numbers*				
Investigation	Λ	α	*Re*	*Helical Mode Instability*	*Shear Layer*	*Vortex Shedding*	*VBD Location*	*Other*
Ayoub and McLachlan [83]	76^o	25^o - 90^o	2.25×10^3	-	-	-	0.10 - 0.17	-
Furman and Breitsamter [103]	65^o	18^o, 23^o, 28^o	$1-2 \times 10^6$	1.65 - 2.1	-	-	-	-
Gad-El-Hak and Blackwelder [38]	45^o, 60^o	10^o - 15^o	1.3 - 3.5×10^5	-	$1625/\sqrt{Re}$, $\sim 3-15$	-	-	-
Gursul [79]	60^o,65^o 70^o, 75^o	15^o - 50^o	2.5×10^4 - 1×10^5	0.5 - 2	-	-	-	-
Gursul and Xie [11, 79, 88, 91]	75^o	31^o - 70^o	4.1×10^4	~ 1	-	0.3	0.04 - 0.12, 0.07	-
Gursul and Yang [86]	70^o	26^o, 30^o, 37^o	5×10^4	1.72 - 3.5	-	-	0.06 - 0.12	-
Helin and Watry [85]			1.16×10^4	-	-	-	0.10	-
Klute *et al.* [55, 6]	75^o	40^o	4.5×10^4	1.72	-	-	-	0.441, 2.78
Lambert and Gursul [82]	80^o	50^o	1.6×10^6	$\sim 1.5, 2$	-	-	0.15	-
Lee and Gursul [104]	85^o	20^o - 35^o	3.5×10^5	2	-	-	-	-
Lowson [105]	70^o	20^o	6.04×10^3 - 1.66×10^4	-	$2577/\sqrt{Re}$ ~ 20 - 32	-	-	-
Menke *et al.* [15]	65^o, 70^o, 75^o	25^o - 42^o	4.1 - 5.4×10^4	-	-	-	0.04 - 0.12	-
Mitchell [13]	70^o	27^o	1.56×10^6	-	-	-	0.015, 0.035	0.079, 0.59, 0.79, 4.15
Mitchell [81]	70^o	27^o	9.75×10^5 - 2.6×10^6	-	-	-	0.0443 - 0.0697	-
Portnoy [84]			3.8×10^3 - 4.96×10^4	-	-	-	0.04 - 0.10	-
Rediniotis [90]	75^o	35^o - 90^o	5.1 - 9.02×10^5	-	-	0.2	-	0.6 - 0.94
Renac *et al.* [106]	60^o	5^o - 35^o	1.2 - 3.5×10^6	~ 2	-	-	-	-
Taylor and Gursul [107]	50^o			-	1.2	-	0.6	-
Woppowa and Groshe [108]	25^o, 68^o	32^o	10^3 - 10^6	-	-	0.25, 0.5	-	-
Yaniktepe and Rockwell [109]	38.7^o	7^o - 17^o	10^4	0.51 - 3.29	3.39 - 4.73	-	-	-
Yavuz *et al.* [110]	38.7^o	10^o	10^4	1.65, 3.29	-	-	-	-

Table 1.2: Non-dimensional frequencies corresponding to important unsteady features of vortical flows from literature

Computational Results

	Conditions			*Phenomenon - Strouhal Numbers*				
Investigation	Λ	α	*Re*	*Helical Mode Instability*	*Shear Layer*	*Vortex Shedding*	*VBD Location*	*Other*
Cummings *et al.* [111, 112]	70^o	35^o	4.07×10^4	0.221, 1.35	6, 8.5	-	-	-
Gordnier and Visbal [14]	50^o	25^o	$2.5 - 5 \times 10^4$	-	42.5, 64, 11.5	-	-	-
Gordnier and Visbal [113, 114]	50^o	5^o - 15^o	2.6×10^4	-	10.7	-	0.63	2, 4, 8
Gordnier and Visbal [93]	76^o	20.5^o	5×10^4	-	10 - 30	-	-	-
Gordnier and Visbal [115]	75^o	10^o - 25^o	$1 - 5 \times 10^4$	-	5 - 25	-	-	-
Gortz [23]	70^o	27^o - 35^o		1.65, 1.75, 1.96	10.2	-	0.017, 0.04 - 0.6	0.34, 0.655, 0.7 1.295, 2.32, 2.5
Morton [30, 116, 24]	70^o	27^o	1.56×10^6	-	-	8	-	$\sim$ 5.3, 6, 9, 10, 20
Shan *et al.* [98]	85^o	12.5^o	1.96^5	-	1.086	-	-	-
Soemarwoto and Boelens [31]	70^o	27^o	1.56×10^6	-	-	-	-	9, 11, 18
Visbal [10]	75^o	17^o - 34^o	9×10^3	3.2 - 4	-	-	0.075	1.3, 2

Table 1.2: Non-dimensional frequencies corresponding to important unsteady features of vortical flows from literature (continued)

the normal Mach number and incidence used by Stanbrook and Squire and thus the classification diagram was redefined. This is shown in Figure 1.19.

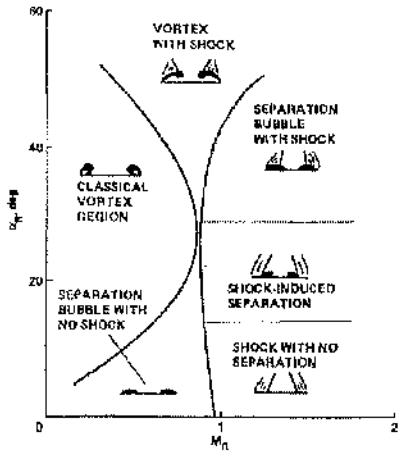

Figure 1.19: Classification of flow behaviour over delta wings by Miller and Wood [16]

In the detailed review by Narayan and Seshadri [120] on the transonic and supersonic behaviour of delta wings, further classification of the flow behaviour is considered. This takes into account the individual behaviour of the shocks in the flow and their location relative to the leading edge vortices. This provides a further three types of behaviour. However, all these behaviours can be considered as sub-types to the classification as defined by the Stanbrook-Squire boundary - leading edge attached flow and leading edge separated flows. Transonic flow over delta wings generally falls into the leading edge separated category with leading edge vortices being formed. However, depending on the Mach number, shocks are found to be present.

A large number of investigations, both experimental and numerical have been carried out, which have looked at the occurrence and behaviour of shockwaves in vortical flows for varying transonic conditions [17, 18, 117, 121, 122, 123, 124, 125]. From these investigations, a number of shockwave systems have been observed and detailed in the literature. In the investigation of the transonic behaviour of delta wing flows carried out by Elsenaar and Hoeijmakers [18], the presence of two main shockwave systems on the upper surface of the wing is discussed based on conjecture and experimental data. These are:

1. Underneath the primary vortex, at an approximately constant spanwise position, just outboard of the primary suction peak;

2. On the aft section of the wing, close to the trailing edge perpendicular to the plane of symmetry.

These shocks are termed cross-flow and rear/terminating shocks respectively. Using theoretical reasoning, it is stated that the cross-flow shock causes the secondary separation under the primary vortex. As the incidence is increased for a particular Mach number, the shock forms under the vortex creating a large adverse pressure gradient, which results in the separation of the boundary layer. This shock is the reason for the inboard movement of the secondary separation, mentioned above. It was determined that for a Mach number of 0.85 at the chordwise position $x/c_r = 0.6$, that the switch from pressure gradient separation to shock-induced separation occurs at an incidence of 14.5^o for this configuration. These cross-flow shocks may be apparent from the surface isobar plots as tight contours of pressure coefficient, however in the spanwise pressure coefficient distributions the position of these cross-flow shocks are not clear.

The occurrence of the rear shock is found from consideration of the chordwise pressure coefficient distribution at the plane of symmetry. At low angles of incidence and at low Mach numbers the distribution along the plane of symmetry gradually decreases toward the trailing edge as the flow conditions return toward freestream conditions, however at moderate angles of incidence with increasing Mach number there is a sharp change in distribution near to the trailing edge. This sharp change characterises the occurrence of a shock-wave in this region. It was found in this investigation that for an incidence of 15^o that the flow becomes supersonic over the wing at a Mach number between 0.8 and 0.85 and there is clear evidence of a rear shock-wave for these conditions. This rear shock was found to move downstream with increasing Mach number.

The occurrence of the two main shock systems was also determined from the experiments of Erickson *et al.* [117, 118], mentioned above, using surface pressure measurements and from surface reflective visualisation techniques used by Donohoe and Bannink [17, 122]. The surface reflective technique is a type of Schlieren visualisation which allows three-dimensional aspects of a flow to be captured and observed clearly. The experiments were carried out on a 65^o delta wing at $M = 0.8$ and from the results, schematic diagrams were produced showing the proposed behaviour and shape of the shocks in the flow. These are shown in Figure 1.20.

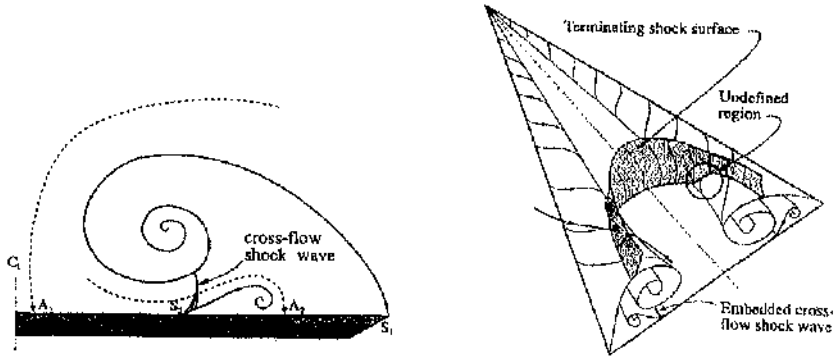

(a) Embedded cross-flow shock (b) Rear/terminating shock surface

Figure 1.20: Schematic diagrams showing proposed positions and shapes of shock systems over transonic delta wings [17]

It is clear that Figure 1.20(b) shows the rear shock as being perpendicular to the symmetry plane at the centreline of the wing, but then arcing downstream toward the primary vortices and appearing to intersect the vortex region. From the side view visualisations, it was also noted that at the symmetry plane the shock extends initially perpendicular from the wing surface, then curves upward toward the apex before returning to a perpendicular direction until it disappears. This shock was witnessed at an incidence of 15^o where breakdown did not occur and it was noted that it did not appear to disrupt the vortical flow. Due to this, it was proposed by the authors that the shock moves above the vortices as it curves downstream. These cross-flow and rear/trailing edge shocks have also been found in many computational investigations [121, 123, 124, 125, 126].

In the computational investigation carried out by Visbal and Gordnier [125], the effects of compressibility were considered for a 75^o delta wing for a range of Mach numbers at a constant Reynolds number. From the results of the calculations a number of shocks were witnessed in the flow for each Mach number. As well as the cross-flow shock underneath the primary vortex and the rear/terminating shocks described above, a two further shocks were witnessed on the wing. These were an upper cross flow shock, which sat above the primary vortex and a centreline shock, which sits parallel to the wing surface above the symmetry plane. The upper cross-flow shock has also been found experimentally for transonic delta wings [117, 118, 127].

The occurrence of these shockwave systems in the flow introduces the complex behaviour of shock/vortex and shock/boundary layer interactions [49, 128]. This is particularly important when considering the behaviour of vortex breakdown for transonic flows as the breakdown behaviour is quite different to that witnessed for subsonic vortical flows where the onset of breakdown is relatively gradual with increasing incidence [72]. The behaviour of vortex breakdown was also detailed in the investigation by Elsenaar and Hoeijmakers [18] mentioned before. The differences in the flow behaviour pre- and post-breakdown are shown using surface isobars and chordwise distributions of pressure coefficient at the symmetry plane. The pre-breakdown flow is shown at an incidence of 22^o and post-breakdown, at an incidence of 24^o. It is highlighted that within this relatively small incidence increment the position of breakdown is noted to jump from $x/c_r = 0.8$ to $x/c_r = 0.5$. The presence of the shock systems detailed above are apparent from the results, with the cross-flow and rear shock being clear for the pre-breakdown case. At moderate incidences, the location of this shock moves downstream toward the trailing edge with an increase in Mach number and incidence suggesting that its strength increases with an increase in these parameters. For the post-breakdown case, the cross-flow shock is still witnessed upstream of the breakdown position, however, there are now two rear shocks on the wing. The position of these shocks is clearly seen from consideration of the chordwise pressure coefficient distributions, which are shown in Figure 1.21.

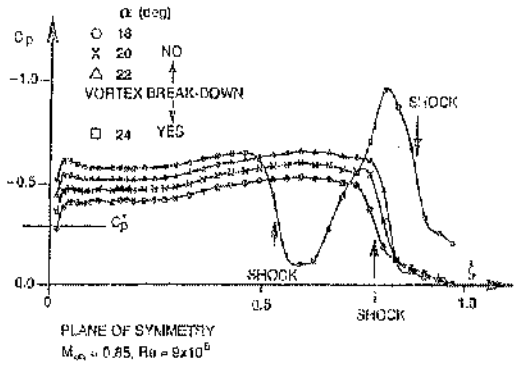

Figure 1.21: Chordwise pressure coefficient distribution at the symmetry plane for a range of angles of incidence pre- and post-breakdown [18]

Considering these results, it was found that the first rear shock is situated approximately at the point of breakdown on the wing with the second shock appearing at roughly $x/c_r = 0.9$. It is proposed that the first rear shock mentioned is actually the terminating shock from the pre-breakdown flow shifted upstream, however it is uncertain as to whether this upstream shift causes or was caused by vortex breakdown. It is conjectured, based on transonic flow over an airfoil, that the rear shock is weak and thus a small change in conditions downstream, caused by vortex breakdown, could force the shockwave to jump upstream to a new equilibrium position within the flow. The presence of the second shock is explained by the flow reaching supersonic conditions downstream of breakdown and thus returning to subsonic conditions before reaching the trailing edge.

In the investigation by Donohoe and Bannink [17], the presence and cause of vortex breakdown is also considered, and similar visualisations to that mentioned earlier, were carried out at higher angles of incidence. At an incidence of 18^o, asymmetric breakdown was witnessed over the wing. This phenomenon was found to occur on either the port or starboard side of the wing, for the same conditions with the breakdown position rapidly fluctuating as much as $0.4c_r$ on either side. It was found that on the side on which breakdown occurs the terminating shock also moves with the position of breakdown and is thus also highly unsteady. Therefore, it is noted that this shock must interact with the breakdown in some way. Similarly, at 20^o incidence, symmetrical breakdown is witnessed over the wing and the initial terminating vortex is seen to move upstream with the breakdown position, but retain its bowed appearance. This confirms the observations made by Elsenaar and Hoeijmakers [18] detailed previously. It was also found, for the $M = 0.8$ case, that a double terminating shock system appeared, with a second similar rear shock appearing at the trailing edge. Donohoe and Bannink suggest that this second shock may be caused by the acceleration of the flow in the centre region of the wing due to the symmetrical breakdown causing an effective nozzle about the wing centreline [17]. The position of breakdown is also noted to oscillate with time for this case but the magnitude of these fluctuations is much less than that for the asymmetric case. However, the frequency appears to be higher.

An experimental and numerical investigation was carried out by Houtman and Bannink [129], on a 65^o sharp edged delta wing at high subsonic and transonic speeds. In the experiment, at a Mach number of 0.85 and an incidence of 20^o, it was found that vortex breakdown occurred over the wing and that the flow exhibited an "irregular" behaviour which was not found for lower Mach numbers. This irregularity was observed in the spanwise pressure distribution at $x/c_r = 0.7$, where the suction peak was seen to collapse for these flow conditions. This collapse was attributed to vortex breakdown occurring over the wing and was shown in surface flow visualisation pictures occurring at approximately $x/c_r = 0.65$. Therefore, it is clear that the onset of transonic breakdown causes a sudden and complete loss of suction on the wing, characterised by the collapse of the surface pressure distribution suction peak. Again, as before, two shocks were noted above the wing surface normal to the wing surface and the symmetry plane. These were located between $x/c_r = 0.5$ and 0.6 and at approximately $x/c_r = 0.825$ from the chordwise pressure distribution at the root chord and from Schlieren pictures. It was proposed that the downstream shock was created by the vortex breakdown phenomena as the upstream shock was witnessed prior to breakdown occurring, although the position of this shock is not stated. Consideration was given to the effect of varying the Mach number for a fixed incidence and it was found that for slightly lower Mach numbers of 0.75 and 0.8 there was a similar pattern within the pressure coefficient distributions. However, no evidence was found of locally supersonic flow or rear shocks at these speeds. Due to this, the conclusion was made that the shockwaves occurring in the flow at high subsonic freestream Mach numbers do not have a large influence on the location of vortex breakdown.

From the flow visualisations of Donohoe and Bannink [17, 122] it was determined that the rear/terminating shock could exist for low to moderate angles of incidence and that vortex breakdown did not occur. It was proposed, due to this, that the shock sat above the vortex region and did not interact with the vortex core. However, what happens at this point is not well understood, and whether interaction occurs for lower angles of incidence is not known conclusively. From the study of the interaction between longitudinal vortices and normal shocks in supersonic flow [28, 130, 131] it has been found that it is possible for a vortex to pass through a normal shock without being weakened sufficiently to cause breakdown. However, the flow over slender delta wings is more complex as the shock does not appear to be normal to the freestream in the vortex core region. Therefore, it may be concluded that it is possible for a terminating shock system to exist without the breakdown of the vortical system, particularly at lower angles of incidence. The presence of the embedded cross-flow shock was also witnessed in Donohoe and Bannink's experiments [17, 122] and was found to occur almost to the trailing edge. This suggests that for this incidence the vortex is strong and thus, undisturbed by the presence of the trailing edge or indeed the rear shock.

The behaviour of shock/vortex interaction and transonic vortex breakdown was considered in the computational investigation of Kandil *et al.* [123, 124] using inviscid and laminar methods. In this study a 65^o delta wing was considered at Mach numbers of $M = 0.85$ and 0.90, Reynolds number, $Re = 3.23 \times 10^6$ and angles of incidence of $\alpha = 20^o$ and 24^o. From the results of the calculations, the cross-flow and rear/terminating shocks were determined, with the cross-flow shock causing the separation of the boundary layer to form the secondary vortex. Upstream of the rear/terminating shock, strong leading edge vortices were noted to occur, but immediately downstream of the shock location, the bubble form of vortex breakdown was found. With the increase in incidence, the rear/terminating shock and the breakdown location move upstream by $20\%c_r$. It was also found that this shock location moved downstream with increasing Mach number, in agreement with the observations of Elsenaar and Hoeijmakers [18]. Unsteady calculations were also carried out which showed that downstream of the rear/terminating shock the flow is highly unsteady with periodic fluctuations being present. An oscillation of the shock location and therefore breakdown location is also witnessed. The flow upsteam of the shock was found to be steady in nature.

The unsteady nature of the shock and breakdown location was considered by Kameda *et al.* [19] using PSP techniques on a 65^o flat plate delta wing. The wing was tested at a Mach number of $M = 0.90$ and incidence of $\alpha = 20^o$. Vortex breakdown was found to occur on the wing for this incidence and was noted to be caused by an interaction with the rear/terminating shock. The presence of the rear/terminating shock was noted from a significant increase in surface pressure detected by the PSP method and is clearly shown in Figure 1.22. The suction created by the leading edge vortices is clear close to the apex of the wing, and it is evident that this suction disappears at the same chordwise location as the region of high pressure. The sequence of PSP results indicates the unsteady nature of the shock and breakdown location.

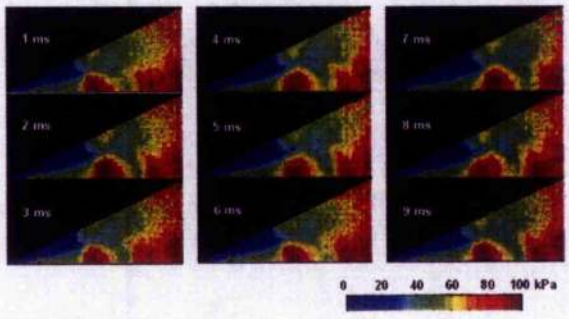

Figure 1.22: Snapshots of pressure distribution on the surface of the wing using PSP techniques (from Ref. [19])

An inviscid numerical investigation to consider the behaviour of breakdown location with increasing incidence was undertaken by Longo [121]. Three delta wings with varying sweep angles were used and the effect of increasing Mach number on the forces and moments of each wing was considered. From the calculations it was found that as the sweep angle is decreased the effect of Mach number increases. This was particularly evident for the 60^o wing where a sudden drop in lift coefficient occurs at the point at which vortex breakdown crosses the trailing edge followed by a flat recovery. This sharp change was also seen in the moment coefficient and has been attributed to a fast upstream shift in the vortex bursting location causing a large loss in vortex lift. However, this sudden behaviour in the force and moment curves did not appear for the higher swept wings. Further investigation into the movement of breakdown position with increasing incidence for the 60^o wing shows that the point of breakdown

moves from the trailing edge to a position of approximately $x/c_r = 0.35$ in 5^o.

The behaviour at $M = 0.8$ was also detailed considering the presence of vortex breakdown on the flow. For the 60^o wing, it is found that breakdown occurs downstream of the trailing edge at 14^o incidence. At this incidence, the flow under the vortex was found to be fully supersonic and a small region of sonic flow appeared at approximately $x/c_r = 0.4$ near the symmetry plane. A cross-flow shock was predicted close to the trailing edge but no rear shock was found above the wing. With increasing incidence, the cross-flow shock was found to move upstream with the position of vortex breakdown and a terminating shock appeared at the trailing edge due to the flow downstream of breakdown becoming supersonic. However, the location of this shock was not found to move with increasing incidence as described by Elsenaar and Hoeijmakers [18]. For the 70^o delta wing, the cross-flow shock behaved more like the experiments detailed previously and was situated under the vortex, upstream of breakdown, for all angles of incidence. However, it was noted that the shock was relatively weak for this case. There was no terminating shock predicted for any incidence over the 70^o wing, which is in agreement with the results of Houtman and Bannink [129]. It was proposed from the results, that the flow between the vortex axis and the surface of the wing may be considered as a convergent-divergent duct, where the flow is channelled and accelerates to supersonic speeds. This nozzle effect causes the cross-flow shocks to appear for relatively low freestream Mach numbers. It was concluded from the analysis that the decrease in suction peak with increasing Mach number could be attributed to the flow in this region becoming supersonic and that the increased rate of upstream progression of the vortex breakdown position could be attributed to supersonic core velocities within the vortex upstream.

Further consideration of the sudden change in flow behaviour due to vortex breakdown can be obtained by from detailed analysis of the results from the experimental database of Chu and Luckring [20, 132, 133, 134]. A large series of experiments were carried out in the National Transonic Facility (NTF) at NASA Langely for various Mach numbers and Reynolds numbers for a large range of angles of incidence. These results also form the basis for the papers by Luckring, which consider Reynolds number effects [135, 136] and compressibility effects [137, 138] for both sharp and rounded leading edged wings. The experiments were carried out using a 65^o delta wing with various leading edge profiles, which was instrumented with a series of 183 static-pressure ports on the starboard side of the wing. These ports were placed at spanwise intervals along five streamwise locations, $x/c_r = 0.2$, 0.4, 0.6, 0.8 and 0.95, with most of the ports being concentrated on the outboard section of the wing. Pressure ports were also placed on both (port and starboard) leading edges at the same streamwise locations to consider the symmetry of the flow behaviour. A sample of these results for the sharp leading edge wing under transonic conditions, $M = 0.85$, Reynolds number 6×10^6 and angles of incidence in the range, $\alpha = 18.6^o - 26.7^o$ is shown in Figure 1.23. This case was chosen for analysis as it corresponds to a test case used for the 2nd International Vortex Flow Experiment (VFE-2), which uses this configuration. Further details of the VFE-2 are given in Chapter 3.

Within the apex region, upstream of $x/c_r = 0.4$, it is evident that with increasing incidence, the suction peak generally increases in magnitude, broadens and moves inboard. This inboard movement is more pronounced between $\alpha = 19.6^o$ and 20.6^o, where the suction peak also reduces slightly. Above an angle of incidence of about 20.6^o, the secondary peaks, which are almost as strong as the primary peaks, also increase in size. However, they do not move inboard. Below $\alpha = 20.6^o$, strong secondary peaks are not obvious near the apex. At the $x/c_r = 0.6$ position, there is a clear difference in the flow structure with increasing incidence. For the incidence range of $\alpha = 18.6^o$ to 23.6^o there is still clear evidence of the primary and secondary vortices, which for the higher angles of incidence have maintained their suction from the previous chordwise station. There is also evidence of a cross-flow shock system with a sudden jump in pressure coefficient being observed just outboard of the primary suction peak. It is also believed that this cross-flow shock will also occur upstream of this location, however the pressure jumps are less obvious for the streamwise locations close to the apex. It is likely that this is due to the use of the non-dimensional scale on the spanwise axis which was used for clarity between the results at each incidence. This proposed cross-flow shock behaviour is much clearer for the downstream streamwise locations. For angles of incidence of 24.6^o and above, there appears to be a collapse in the primary vortex suction peak. It is also found that the secondary peak and cross-flow shock disappear altogether. This is similar to the behaviour noted by Houtman and Bannink [129] mentioned in Section 1.4, for the case when breakdown was found over the wing. Indeed, from considering the pressure coefficient plots at $x/c_r = 0.8$ and 0.95 for angles of incidence above 24.6^o, it is clear that breakdown has occurred due to the relatively flat distributions. Based on the these results and observations of Houtman and Bannink [129], it can be suggested that the location of breakdown is just upstream of the $x/c_r = 0.6$ position with the drop in suction peak being a direct consequence of this.

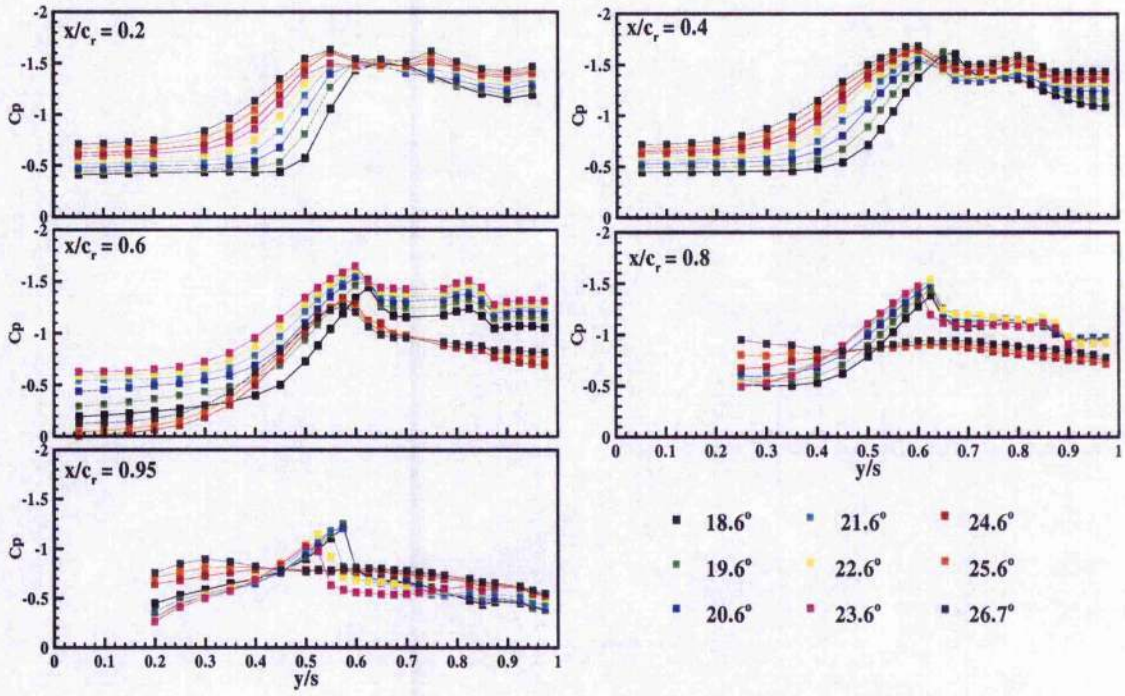

Figure 1.23: Experimental results from NASA NTF wind tunnel tests for conditions: $M = 0.85$ and $Re = 6 \times 10^6$, for the sharp leading edge, at a range of angles of incidence 18.5^o - 26.7^o. (data taken from Ref. [20])

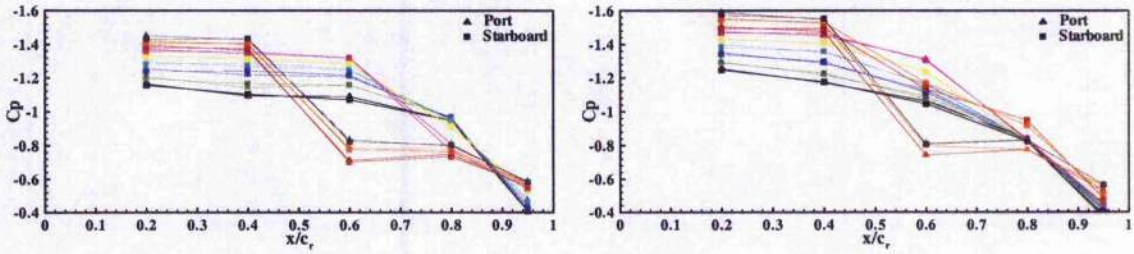

(a) $M = 0.851$, $Re = 6 \times 10^6$

(b) $M = 0.799$, $Re = 6 \times 10^6$

Figure 1.24: Experimental results from NASA NTF wind tunnel tests a range of angles of incidence 18.5^o - 26.7^o. Legend as shown for Figure 1.23 (data taken from Ref. [20])

Downstream at $x/c_r = 0.8$, for the lower angles of incidence there is still clear evidence of the primary and secondary vortices. The magnitude of the primary suction peak has also not decreased significantly. However, the cross-flow shock appears to have increased in strength, suggested by the greater magnitude and gradient of the jump in pressure coefficient. At the higher angles of incidence, the pressure coefficient profile is flat and uniform over the whole span with only a very slight change in magnitude with increasing incidence. Finally, at the trailing edge, it is found for the lower angles of incidence that the primary peak is still evident with the cross-flow shock, however the secondary separation appears to have disappeared. At this position it is apparent that the position of the vortex has moved inboard with increasing incidence and also that the magnitude of the peak has reduced. For the post-breakdown angles of incidence, the pressure coefficient distribution is similar to that for the $x/c_r = 0.8$ position, with a relatively flat profile. It should also be noted that on the lower surface for all chordwise stations that with increasing incidence, the average pressure coefficient values increase.

From these results, it is clear that by increasing the incidence from 18.6^o, the vortex moves inboard and becomes stronger until at a certain point vortex breakdown suddenly occurs quite far upstream on the wing, close the $x/c_r = 0.6$ chordwise position. This is in agreement with all the results discussed previously. Further consideration of the vortex breakdown behaviour can be obtained by considering the pressure coefficient distributions along the leading edges of the wing as shown in Figure 1.24. It is clear from Figure 1.24(a) for $M = 0.85$ that the pressure

coefficient distributions along both port and starboard leading edges are in good agreement and that they confirm the sudden upstream motion of vortex breakdown at $\alpha = 24.6^o$, which is shown by the increase in pressure coefficient. Interestingly, this shows that there is a change in distribution for the 23^o incidence, with an increase in pressure coefficient at $x/c_r = 0.8$, however breakdown is not present. Looking at the spanwise distributions at this station shows this reduction but also shows the presence of the primary and secondary suction peaks. Further flow field data would be needed in order to be able to comment on the cause of this increase.

Looking at the same distributions for $M = 0.8$, it is clear that a similar pattern emerges, however at $\alpha = 24.6^o$ it appears that the pressure distribution on the port side exhibits signs of vortex breakdown occurring suddenly on the wing, but that the starboard side does not. This is also the case at 25.6^o. However, the behaviour of both port and starboard is the same at $\alpha = 26.6^o$. From this data, it is evident that vortex breakdown occurs asymmetrically for this Mach number at a critical angle of 24.6^o before occurring symmetrically at 26.6^o as suggested by the spanwise distributions. Thus, from these results it is clear that asymmetric vortex breakdown occurs for a lower Mach number case but not for $M = 0.85$. From consideration of other datasets within the NASA results for the same Reynolds number but differing Mach numbers, it is found that this behaviour does not form a trend based on Mach number as asymmetric breakdown is also witnessed for $M = 0.9$, but not for $M = 0.831$ or 0.872. Thus, this behaviour must be caused by other factors. It is worth noting that the wing was only instrumented (with pressure taps) on the port side and it is on this side where breakdown appears first. This may suggest a sensitivity to surface disturbances.

The asymmetry of transonic vortex breakdown was also witnessed by Schrader *et al.* [139] for a 63^o sharp edged delta wing at angles of incidence at which breakdown first occurred on the wing. However, with a further increase in incidence, the asymmetry was found to disappear and symmetric breakdown was found. Further evidence of this asymmetrical flow behaviour was found from experiments carried out by Konrath *et al.* [140, 141, 142] within the framework of the VFE-2 mentioned above. These tests involved PSI pressure transducers, Pressure Sensitive Paint (PSP) and Particle Image Velocimetry (PIV) to further study the flow behaviour. These results were obtained for the 65^o configuration used in the Chu and Luckring experiments detailed above at a Mach number of $M = 0.80$, Reynolds number $Re = 3 \times 10^6$ and at a range of angles of incidence, $\alpha = 18.4^o - 25.9^o$. The PSP data from the experimental tests are shown in Figure 1.25, showing surface pressure coefficient for all angles of incidence tested.

From this data the change in vortex flow with increasing incidence is apparent. It is clear that as the incidence increases, the magnitude of the suction peaks increases, as witnessed for the transducer data discussed previously. The inboard motion of the vortical system is also evident. However, the most striking feature of these plots is the sudden asymmetric breakdown at 25.6^o, where vortex breakdown suddenly appears on the right hand side of the wing close to the $x/c_r = 0.6$ streamwise station. This asymmetry of breakdown is in agreement with the NASA data for a similar Mach number, however the critical onset angle is slightly higher. Unfortunately no data was obtained for higher angles of incidence, thus it is not possible to say if this behaviour changes to a symmetric breakdown with a further increase in incidence. It was found from the experimental tests that this behaviour was exhibited for all transonic conditions and that the asymmetry was consistently appearing on the same side of the wing - which coincided with the instrumentation as before [21]. Thus, this may be further indication of the sensitivity of transonic vortex breakdown to surface disturbances within experimental tests. It is also clear from these surface pressure plots, that none of the shock systems expected to occur on the wing are apparent. This is due to the time averaged nature of the PSP technique, which, due to the highly unsteady nature of the flow, causes the locations of shockwaves to become smeared [140]. It was also found that the PSP suction peak heights were underestimated due to temperature effects. However, in their analysis of the flow, Konrath *et al.* [140] witnessed two terminating shocks, one close to the sting tip curving downstream and a second located over the sting between the $x/c_r = 0.8$ and 0.9 streamwise locations. A curving of the vortex core trajectory was witnessed in the vicinity of the sting shock from these tests.

Consideration of the cross-flow behaviour upstream and downstream of breakdown can be obtained from the PIV results. Figure 1.26 shows the results for the post-breakdown case, $\alpha = 25.9^o$ at six chordwise stations. From these planes, the elongated shape of the leading edge vortex upstream of breakdown is clear and it is found that the axial velocity at the vortex core has a magnitude of approximately $1.9U_\infty$. A secondary vortex is also clear under the vortex, close to the leading edge. Breakdown appears to occur between $x/c_r = 0.6$ and 0.7 and the behaviour of the flow changes to a large region of reversed flow, which expands downstream and is relatively circular in nature. Inboard of this breakdown region, it is clear that the flow is still supersonic and appears to be accelerating. This may explain the occurrence of the second rear shock witnessed by Elsenaar and Hoeijmakers [18] mentioned above, as the flow accelerates between the breakdown regions on the wing.

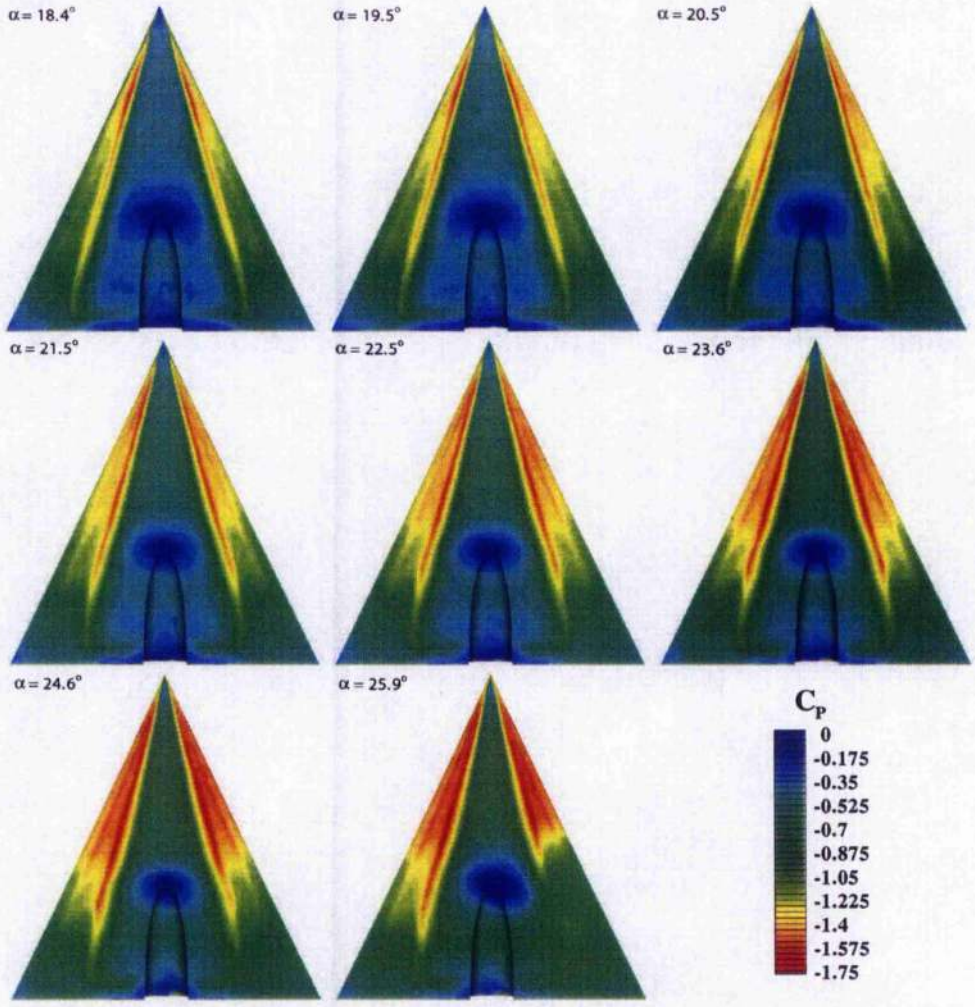

Figure 1.25: PSP surface pressure coefficient contours for $M = 0.8$, $Re = 2 \times 10^6$, $\alpha = 18.4^o - 25.9^o$ [21].

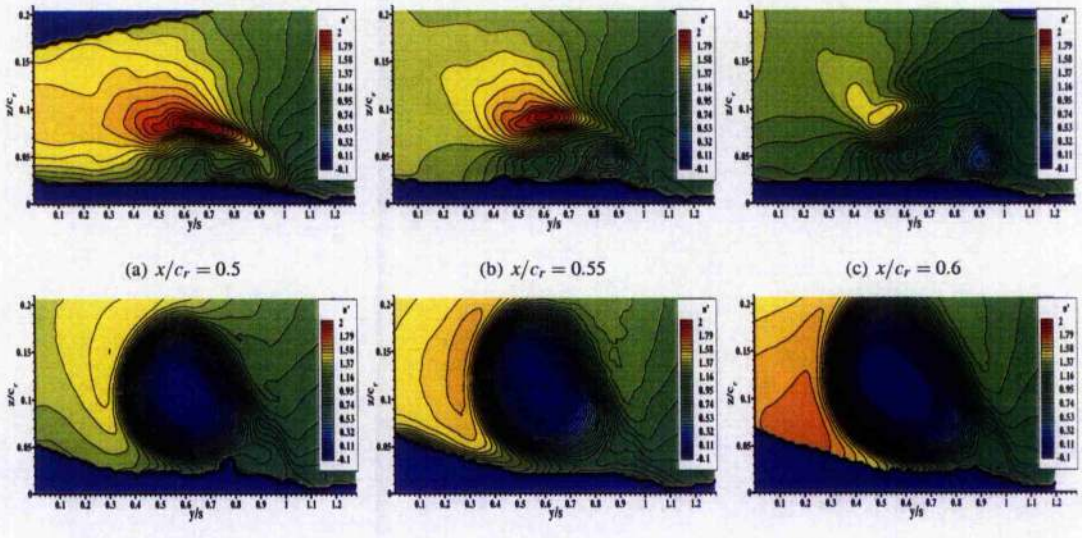

(a) $x/c_r = 0.5$ (b) $x/c_r = 0.55$ (c) $x/c_r = 0.6$

(d) $x/c_r = 0.7$ (e) $x/c_r = 0.75$ (f) $x/c_r = 0.8$

Figure 1.26: PIV results showing contours of non-dimensional u velocity for $\alpha = 25.9^o$ at $M = 0.80$ (data from Ref. [21])

1.5 Application of CFD to Delta Wing Vortical Flows

One of the most important issues in the use of CFD, for delta wings and in general, is the choice of turbulence model used [143]. There are a number of different approaches and methods to turbulence modelling, which range in complexity, accuracy and computational expense. These techniques, in order of complexity, are inviscid, laminar, RANS, DES, LES and DNS methods. The choice of turbulence model is normally a trade-off between computational expense and solution realism. Each turbulence treatment however, can be applied and used for the prediction of delta wing vortical flows, with varying degrees of realism. This section will discuss the available literature of each method applied to delta wing flows and consider the advantages and disadvantages of each method.

1.5.1 Inviscid Methods

Inviscid methods have been extensively used for the solution of the flow over delta wings. This is mainly due to their low computational cost when compared to Navier-Stokes calculations. However, as discussed above, this reduction in computational cost also means a reduction in the realism of the solutions. Nonetheless, the Euler equations can give reasonable approximations. By their nature, inviscid solutions do not predict boundary layers and therefore cannot predict separation. However, for sharp leading edge delta wings this is not a problem as the separation is fixed at the leading edge. Once the separation occurs, it has been found that the Euler equations can accurately predict the transport of vorticity and entropy within the leading edge separation and vortices [144]. Vortex breakdown can also be predicted by this model although it is evident from some calculations that the strength of the leading edge vortices is highly dependent on the grid used [145]. This will have a considerable effect on the vortex breakdown location and behaviour.

In a review of their earlier work, Murmann and Rizzi [146], state that they found that the most important features of the primary vortex and the vortex-wing interaction were modelled well by the Euler equations and that the results compared reasonably with experimental data such as surface pressure and flow visualisation. The calculations performed used sharp-edged wings, where the leading edge separation point is fixed and not dependent on viscosity. It was noted from their work that the Euler equations could not resolve the secondary separations of the flow. This has been found to be a limitation of the use of Euler equations for delta wings, but provided this is taken into account, the results may be assumed to be valid. It was also found for the inviscid computations, that the level of total pressure losses predicted in the vortex cores are realistic. This suggests that the mechanism for vortex breakdown may be driven by an inviscid phenomenon and that the fundamental structure of the primary vortices is insensitive to the level of viscosity, as long as it is present.

The inability of inviscid solutions to accurately predict the behaviour over rounded leading edged delta wings was considered in an investigation by Rizzi and Müller [147]. In this investigation the differences in solution between Euler and Navier-Stokes computations on a 65^o rounded leading edge wing at $M = 0.85$ and $\alpha = 10^o$ were considered. It was found for the Euler computations that the position of the formation of the leading edge vortices was delayed to approximately 25% chord of the wing. Whereas for the Navier-Stokes computations the vortices were formed from the apex region as for sharp leading edges. It was suggested that this difference is due to the mechanisms for the primary separations being different for the two computations, i.e. physical and computational viscosity. The surface pressure comparison with experiment shows good agreement for the Navier-Stokes calculations but not for the inviscid solutions. A secondary separation was found to occur close to the trailing edge for the inviscid solution, however it was determined that this was caused by the presence of a cross-flow shock under the primary vortex and did not result in the formation of a secondary vortex. It was found that the position of the primary vortex and the corresponding surface pressures did not agree with the experiment and, as mentioned before, were modelled more accurately using the Navier-Stokes equations. It was concluded from this study that the Navier-Stokes equations were needed to determine a realistic simulation of the flow over a rounded leading edge wing, due to the dependence of the separation points on viscosity. The same wing geometry was used by Tsai *et al.* [148], who came to the same conclusions in their study.

In a numerical investigation into vortex breakdown by Agrawal *et al.* [22, 149], both the Euler and Navier-Stokes equations are used to simulate the flow behaviour. The purpose of the study was to determine the effects of viscosity on the pre- and post-breakdown regions. The geometry used was the 70^o wing used in the experimental investigations by Kegelman *et al.* [44, 150, 151] and the results gained from these experiments are used for validation purposes in the study. The calculations were performed for a Mach number of $M = 0.3$ at various angles of incidence. The Reynolds number for the viscous calculations was $Re = 1 \times 10^6$. It was found from the investigation that the Euler equations predict the position of the vortex cores outboard of the viscous solutions and experimental results. As mentioned before, this is expected due to the secondary vortices not being resolved

by the Euler computations and therefore their effect on the primary vortex is ignored. From consideration of the surface pressure distributions compared to the experimental results, it was determined that the Euler results predicted the magnitude of the suction peak more accurately that the viscous models. It was also found that the Euler solution consistently predicted breakdown downstream of the experimental and viscous results. This is shown for the surface pressure contours at $\alpha = 30^o$ shown in Figure 1.27 for each solution. These differences in the flow solutions may have been due to the grid refinement in the near wing region not being sufficient to capture the boundary layer properties for the two viscous cases. This is not an issue for the Euler solutions, which do not model the boundary layer. The experimental breakdown location under the same conditions was found to be approximately $50\%c_r$.

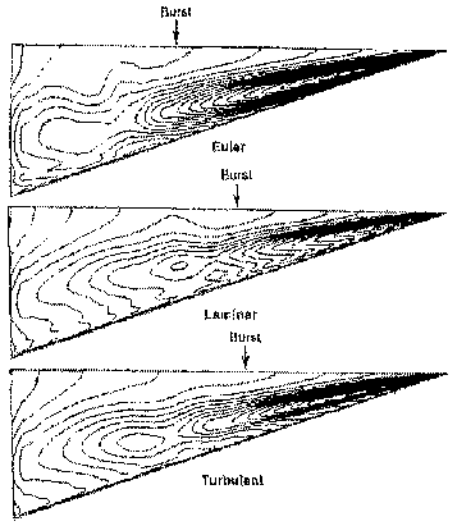

Figure 1.27: Surface pressure contours for Euler, laminar and turbulent computations, for $M = 0.3, \alpha = 30^o$ and $Re = 1 \times 10^6$ [22]

The structure of vortex breakdown using the Euler equations was investigated for a 70^o delta wing by Kumar [152, 153, 154] using an embedded conical grid. The wing has an incidence of $\alpha - 30^o$ and a freestream Mach number of $M = 0.3$. Three grids were used in the investigation and the effect of grid refinement on the solutions was considered. From this, it was found that with an increase in grid refinement the resolution of the subcore of the vortex improved, with an increase in axial and swirl velocities. Thus, this also confirms the dependence of the vortex strength on the grid refinement as mentioned above. From consideration of the breakdown region, it was found that the inviscid calculations predicted the spiral form of breakdown with a clear stagnation region and widening of the core at the breakdown location. Despite the simulations not being time accurate, an oscillation of the vortex breakdown location was witnessed and attributed a non-dimensional frequency of $St = 1.6$. However, this result should be considered with care, particularly as it is much higher than the frequencies found for this phenomenon in experiments - it is closer to the frequencies attributed to the helical mode instability discussed in a previous section.

A similar investigation was carried out by Strohmeyer *et al.* [155] on a 65^o cropped delta wing, to determine the ability of the Euler equations to describe the behaviour of breakdown over the wing. The investigation was carried out at two angles of incidence $\alpha = 10^o$ and 20^o at a Mach number of $M = 0.2$. As in the investigation by Kumar [152] described above, the calculations performed were steady state. However, it was also determined that the flow was unsteady downstream of breakdown with a periodic oscillation of the aerodynamic forces occurring. From analysis of the results the breakdown behaviour was also found to exhibit a spiral structure, which gave good agreement with the experimental data. Therefore, it was concluded that the Euler equations were sufficient to qualitatively resolve the salient features of the flow.

To consider the ability of the Euler equations to predict the unsteady behaviour of the vortical flow, an inviscid investigation was carried out by Görtz [23] using the 70^o full span wing used in Mitchell's experiments at ONERA. Time accurate calculations were carried out at three angles of incidence, 27^o, 30^o and 35^o for a Mach number of $M = 0.2$. The time steps used for this investigation were dependent on the angle of incidence and ranged from $3.37 - 3.406 \times 10^{-6}$ seconds, which corresponds to non-dimensional time steps of $\Delta\tau = 2.41 - 2.44 \times 10^{-4}$. The results were considered using flow visualisation methods, such as streaklines and isosurfaces of entropy. From the flow visualisation, the spiral form of breakdown was witnessed for all three angles of incidence, and behaved as

described in Figure 1.6. One rotation of the breakdown region at $\alpha = 30^o$ was found to have a period of $T = 0.008s$, which corresponds to a dimensional frequency of $f = 125Hz$ and a Strouhal number of $St = 1.75$. The bubble form of breakdown was also witnessed on the wing at intermittent intervals. The unsteady behaviour of the flow was also analysed from consideration of the unsteady aerodynamic load time histories. Figure 1.28 shows normal force coefficient time histories and power spectral density (PSD) analyses for each of the three angles of incidence used in the investigation. The PSD analysis provides details of the dominant frequencies and power of the fluctuations within the unsteady time histories.

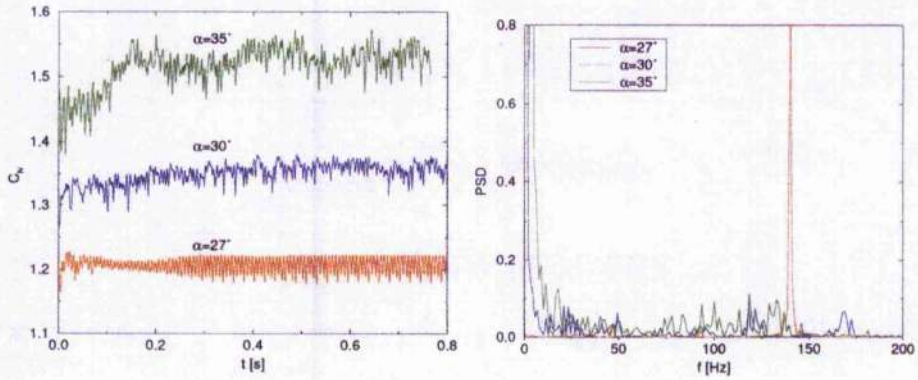

(a) Time history

(b) PSD vs. frequency

Figure 1.28: Sample of time histories and PSD analysis of normal force coefficient from Görtz's unsteady inviscid calculations [23]

From the C_N time history for $\alpha = 27^o$, it was determined that the behaviour was periodic in nature with harmonic oscillations occurring in the signal. As the incidence was increased to $\alpha = 30^o$, the fluctuations were found to become irregular, with an increase in magnitude. This was also the case for the $\alpha = 35^o$ incidence, however, a low frequency oscillation is clear from Figure 1.28. The harmonic behaviour was not found to occur for the larger angles of incidence. Considering the PSD results, the frequency content of each signal is clear. At $\alpha = 27^o$, it is clear from Figure 1.28 that there are three clear individual peaks, which occur at frequencies of approximately 47, 93 and $140Hz$, corresponding to Strouhal numbers of 0.6546, 1.2954 and 1.95. The dominant peak occurs at $St = 1.95$ and is assigned to the helical mode instability. It was noted that this is the third harmonic of the lowest frequency in the spectrum. The harmonic behaviour was attributed to an asymmetry of the location of vortex breakdown on the wing.

At $\alpha = 30^o$, it is clear that more frequencies exist and the dominant peak occurs at $1.18Hz$ ($St = 0.017$). Other peaks exist in the flow at 24, 50, 118 and $166Hz$ which correspond to non-dimensional frequencies of $St = 0.34$, 0.70, 1.65 and 2.32. The dominant peak is assigned to the oscillation of breakdown location as it is of the order of the results found in previous experiments [13]. The higher frequencies are all attributed to the helical mode instability, particularly the peak at $118Hz$ ($St = 1.65$) which is in agreement with the frequency of the rotation described from the flow visualisation. At the largest incidence, the frequency content has again increased, with peaks being visible at 2.87 and $18Hz$ ($St = 0.04$ and 0.25). A similar higher frequency content, 74 - $130Hz$ ($St = 1.03$ - 1.82) is also found, attributed to the upstream movement of the breakdown location with increase of incidence. It was noted that the frequency of the helical mode instability phenomenon was found to decrease with increasing incidence, which is in agreement with the results of Gursul [79] described in Section 1.3.1.

From these studies it is clear that despite its limitations in predicting separation and therefore the secondary vortex, the solutions of vortical flow over slender delta wings are reasonable. This suggests that for sharp leading edged delta wings, inviscid methods are sufficient to qualitatively evaluate the behaviour of the leading edge vortices and vortex breakdown at a much reduced computational cost compared to viscous methods.

1.5.2 Laminar Methods

The next level of modelling is to consider the flow as fully laminar, where the calculations are viscous but turbulence is not considered. As discussed in Section 1.2.1, a laminar boundary layer is particularly sensitive to an adverse pressure gradient and, thus, the separations predicted by this method are larger than for turbulent flow. This results in an over-prediction of the secondary vortex and as a result moves the location of the vortex core

inboard and away from the wing surface [22]. Fully laminar calculations are generally only considered when the Reynolds number is sufficiently low.

Gordnier [156] considered the unsteady laminar behaviour of delta wing vortices for a 65^o delta wing at an incidence of $\alpha = 30^o$. The flow conditions corresponded to a Mach number of $M = 0.2$ and Reynolds number of 3.2×10^4. Two structured grids were used in the investigation, which had a C-O topology and approximately 3.3×10^6 and 4.2×10^6 grid points. A short grid study was carried out and the effect of time step on the flow solution was also considered. For the time step study, three time steps were used, $\Delta\tau = 0.001, 0.0005$ and 0.00025. It was found from this study that with a reduction in time step size the solution improves, with less distortion of higher frequencies and a less diffused solution found for the smaller time steps. It was concluded from this study that a time step of $\Delta\tau = 0.0005$ was sufficient to resolve the main flow features. The results were compared to experimental data and were found to exhibit good agreement for the location of breakdown, which occurs at approximately $x/c_r = 0.288$ for the finer grid and at $x/c_r = 0.287$ in the experiments.

With the wing set to a -4^o roll angle, the unsteady behaviour of breakdown was considered, with the spiral form of breakdown being clearly seen in the results. This breakdown location was found to be unsteady, however the length of the calculation was not sufficient to determine its frequency. The spiral breakdown was also observed to rotate, but again no frequency was determined. It was concluded that the behaviour of breakdown was in agreement with experiments. Further consideration was given to the laminar behaviour of vortex breakdown over delta wings by Visbal [10], which was discussed in detail in Sections 1.2.2 and 1.3.1. The investigation by Gordnier and Visbal [96], which considers the cause of shear layer instabilities, discussed in Section 1.3.2 was also carried out using a laminar flow solver and again shows the ability of this method to accurately predict low Reynolds number flows.

The unsteady behaviour of laminar predictions may be further considered from the investigation by Cummings *et al.* [111, 112]. In this investigation, the flow over a semi-span 70^o delta wing is considered at an incidence of $\alpha = 35^o$, Mach number of $M = 0.1$ and Reynolds number of $Re = 4.07 \times 10^4$, to consider the effects of periodic suction and blowing to control the breakdown of the leading edge vortices. The calculations were carried out on two unstructured grids with approximately 5×10^5 and 1.24×10^6 cell volumes. Consideration was given to the optimal size of the time step for each grid by considering the frequency content of the normal force coefficient time histories, from this it was determined that for the fine grid the time step should be $\Delta t = 0.00005s$ which corresponds to a non-dimensional time step of approximately $\Delta\tau = 0.0025$. Two dominant frequencies were found within the fine grid solutions for the various time steps, which for the optimum time step corresponded to $St = 1.3$ and 6.0.

The unsteady flow behaviour, without the flow control, was considered by applying pressure taps within the computational flow field at the primary and secondary vortex cores. From these taps, the time histories of the pressure was obtained which were analysed using a PSD to consider the frequency content. In the primary vortex, prior to breakdown, the dominant frequency of the flow was found to be $St = 8.5$, however downstream of the breakdown location, this dominant frequency reduced significantly to approximately $St = 1.35$. These frequencies were witnessed from flow visualisations to correspond to the shedding of the shear layer from the leading edge and the helical mode instability, respectively. The shedding frequency was also found to be dominant in the pressure signals from the secondary vortex core region and was found to be within the range of frequencies predicted by Gad-El-Hak and Blackwelder [38]. From consideration of the breakdown behaviour of the flow, it was found that the secondary vortex broke down upstream of the primary vortex and was effecting the breakdown of the primary vortex. Further investigation determined that this behaviour was a result of the interaction between the secondary vortex flow and the shear layer instability mentioned. It was concluded that the three phenomenon occurring on the wing (primary and secondary vortex breakdown and the shear layer instability) must be directly linked.

Therefore, it is clear that for low Reynolds number flows, laminar flow solutions are reliable, without the need of large computational expense. However, as the Reynolds number is increased, transition to turbulent flow will occur on the wing and the validity of these solution would reduce.

1.5.3 Reynolds Averaged Navier-Stokes (RANS) Methods

To obtain further realism in the computational solutions of delta wing flows, the turbulent behaviour of the flow needs to be considered and modelled. One of the most common methods of treating the turbulence is to use Reynolds averaging. This method effectively simplifies the instantaneous Navier-Stokes equations into mean flow equations and deals with the contribution of the turbulence and the resulting extra term, known as the Reynolds stress tensor, through separate numerical models, known as turbulence models. There are a number of different

ways in which the Reynolds stress tensor can be modelled, using linear, non-linear and algebraic formulations. The methodology and formulation of Reynolds averaging, along with a number of turbulence models, are explained in more detail in Chapter 2.

A large number of turbulence models exist, which are generally classified by the number of additional equations needed to solve the complete turbulent flow behaviour. These include, Zero equation models, such as the Mixing Length model, one equation models such as the Spalart-Allmaras model and two equation models, for example the $k-\omega$ model. A further set of models can be thought of as Reynolds Stress models or Algebraic Stress models. However, not all turbulence models are directly suitable for use in considering delta wings and vortical flows. Therefore, a great deal of research has been done into determining what models are suitable and modifying models to give the most accurate results when compared to experimental data.

In the investigations by Gordnier [157], the linear two equation $k-\varepsilon$ turbulence model is used to calculate the turbulent flow over a 65^o delta wing at a Mach number of $M = 0.37$ and Reynolds number of $Re = 3.67 \times 10^6$. Two angles of incidence are used, $\alpha = 15^o$ and 30^o, to consider the flow with and without vortex breakdown in order to examine the suitability of this model in predicting the breakdown behaviour. A structured grid was used for this investigation which had a C-O topology and approximately 1.1×10^6 grid points. Results using the Baldwin-Lomax model with Degani-Schiff correction for vortical flows were also considered and compared to the results from the $k-\varepsilon$ model.

From the results of the investigation for $\alpha = 15^o$, it was found that the standard $k-\varepsilon$ model was unable to accurately predict the behaviour of the flow due to unphysical and excessive amounts of eddy viscosity, which had adverse effects on the vortex, were predicted. Therefore, modifications of the $k-\varepsilon$ model were proposed in order to reduce the build-up of eddy viscosity around the primary vortex core where the eddy viscosity should be negligible. This is a common problem for linear Boussinesq based turbulence models in predicting vortical flows and is a result of inaccurate prediction of the normal stresses in regions of high rotation, such as the vortex core. These modifications are based on limiting the production of the turbulence within the vortex core regions by taking the rotation of the vortex into account. The results using these corrections applied to the standard $k-\varepsilon$ model, showed a great deal of improvement in the resolution of the turbulence within the flow. The levels of eddy viscosity predicted were reduced, the vortices became stronger and the results obtained became more comparable with the experimental results. It was concluded from analysis of the pre-breakdown results, that the $k-\varepsilon$ model with a vorticity based correction provided the best solution and thus, only this model was used for the post-breakdown computations.

At $\alpha = 30^o$, this model predicted a bubble form of breakdown, which was not in agreement with the experimental results. In the experiment a spiral form was noted. The breakdown location was also further downstream in the computations than for the experimental results. The discrepancy of the form of breakdown was explained by considering the RANS formulation, which calculates the mean-flow equations with the turbulence model considering the turbulent fluctuations and considering the notion that the bubble form of breakdown is the time average of the spiral type, as discussed previously. Thus, it was proposed that the solution was exhibiting only the mean-flow, which would result in a bubble form of breakdown being predicted. In conclusion, Gordnier proposed that the RANS formulation could only predict mean-flow characteristics, even if an unsteady calculation was performed.

A similar investigation was carried out by Brandsma *et al.* [158], which considered the effects of two similar rotation corrections for the Wilcox $k-\omega$ linear turbulence model. The calculations were performed on a 65^o cropped delta wing at an incidence of $\alpha = 10^o$ at $M = 0.85$ and with a Reynolds number of $Re = 9 \times 10^6$. Again, a structured grid was used with a C-O topology and approximately 1.8×10^6 grid points. The rotation corrections applied to the standard $k-\omega$ model were similar to those used by Gordnier [157]. One limited the production of the turbulent kinetic energy, P_k, and the other enhanced the production of the dissipation rate, P_ω, in order to reduce the eddy viscosity in regions of high rotation. The conclusions of this investigation were very similar to those from Gordnier's work, where it was found that the standard model over-predicted the turbulence within the vortex core, which resulted in a weak vortex being predicted. With the modifications applied to the model, the results improved significantly with improved agreement with experimental data. However, the model which limited P_k was found to be more diffusive than the P_ω enhancing modification and did not adequately reduce the turbulence in the core. Therefore, it was concluded that the modification which utilised the enhancement of P_ω gave the best agreement with the experimental data and thus was best suited to the prediction of vortical flows.

Further consideration was given to the use of turbulence models for vortical flows over delta wings in the investigation by Dol *et al.* [159]. In this study the ability of a non-linear eddy viscosity model to predict the flow

behaviour is considered, in comparison with experiment and with the results of a standard linear two equation model with and without rotation correction. The standard model is the $k-\omega$ model. The non-linear model is an extension of this model, formulated from an explicit algebraic Reynolds stress model, which incorporates an extra anisotropic Reynolds stress term into the Boussinesq approximation resulting in an increased dependence of the model behaviour on the mean rotation tensor. The rotation correction used is the P_ω enhanced modification proposed by Brandsma *et al.* [158]. Further details of the application and formulation of both of these models is given in Chapter 2. The test case used for this investigation is the cropped 65^o delta wing used by Brandsma *et al.* [158], described above, with the same flow conditions for angles of incidence of $\alpha = 10^o$, 15^o and 20^o. The structured grid used is similar to that described above, with a C-O topology and approximately 1.8×10^6 grid points.

It was found from the results of the investigation that both the $k-\omega$ model with rotation correction and the non-linear version of the model provided a significant improvement on the results of the standard model. Both models reduced the predicted eddy viscosity levels in the vortex core by different means, which resulted in stronger vortices being formed over the wing surface. At $\alpha = 15^o$, it was found that the results from the rotation correction model were over-predicting the suction peak on the surface of the wing, however the non-linear model was showing very good agreement with the experimental results. This was also the case at $\alpha = 20^o$, where breakdown was also found to occur over the wing for the model with rotation correction depending on the initial conditions of the calculations. From these results, it was concluded that the non-linear model performed better in capturing the vortex flow than the linear model with the rotation correction. A similar conclusion was reached by Bartels and Gatski [160] for a delta wing at Mach numbers of $M = 0.6$ and $M = 0.9$. The linear Spalart-Allmaras and SST models were used and compared to results obtained using a non-linear explicit algebraic stress model. It was found from this study that the non-linear model gave much improved results compared to the linear turbulence models used.

In an investigation by Morton *et al.* [24, 161], the effect of turbulence modelling on the unsteady behaviour of the flow is shown. A 70^o semi-span delta wing is considered at a Mach number of $M = 0.069$, incidence of 27^o and a Reynolds number of 1.56×10^6, which corresponds to the experimental results by Mitchell [13]. Five turbulence models are used in this study, three RANS models, the one equation Spalart-Allmaras (SA) model, the Spalart-Allmaras model with a rotation correction (SARC), Menter's Shear Stress Transport model (SST) and two versions of a hybrid RANS/LES approach, DES, which will be discussed in more detail in the next section, are used. The DES models are based on the Spalart-Allmaras (SADES) and Menter's Shear Stress Transport (SSTDES) models. All calculations were run on an unstructured grid with 2.7×10^6 cells and used a non-dimensional time step of $\Delta\tau = 0.005$. Figure 1.29 shows a comparison of the PSD analysis of the normal force coefficient signals for each model used.

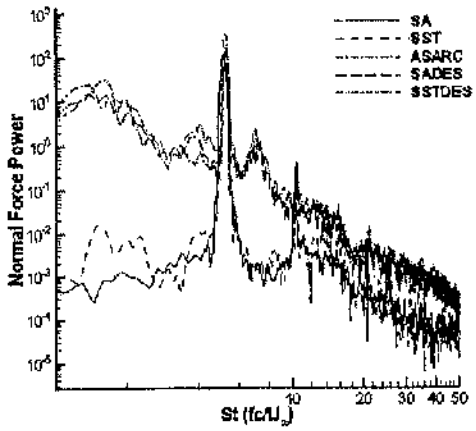

Figure 1.29: PSD comparisons of normal force coefficient for five turbulence models [24]

From consideration of the frequency content of the unsteady results for each of the RANS turbulence models it was found that the S-A and SST models are unable to resolve the majority of the frequencies in the spectrum. However, the SARC model had an improved spectrum, which was attributed to the correction eliminating turbulence dissipation within the vortex core. However, this model was still found to struggle with some mid to high frequencies associated with the post-breakdown turbulence scales. When comparing the results to the experimental data of Mitchell *et al.* [162], it was found that all the turbulence models except the SST model produced breakdown positions which were comparable to the experimental data. The SST breakdown position was approximately

10% upstream. Other results showed that although the general position of breakdown was predicted by the RANS models, they failed to resolve the basic characteristics of the breakdown region as shown in the experiments. It was determined from analysis of the flow behaviour and unsteady frequencies that the DES models, allowed a more accurate simulation of the vortex breakdown behaviour.

The unsteady behaviour of this test case was also considered by Soemarwoto and Boelens [31], with the same flow conditions using the P_ω modification of the $k-\omega$ turbulence model, proposed by Brandsma *et al.* [158]. As before, only the semi-span wing is considered and a structured multi-block grid with approximately 3.7×10^6 cells is used. After a brief time step study, a non-dimensional time step of $\Delta\tau = 0.0025$ was used for the time-accurate simulations. From the unsteady results, it was found that the instantaneous vortex breakdown oscillated in the range $x/c_r = 0.67 - 0.75$. However, the time-averaged solution showed breakdown to occur at approximately $x/c_r = 0.74$. This is downstream of the mean location found in the experiment which was found to be approximately $x/c_r = 0.65$. To consider the unsteady behaviour further, the frequency content of the normal force coefficient was analysed using PSD methods. From this analysis, it was found that a dominant frequency occurred in the signal at approximately $200Hz$, which corresponds to a Strouhal number of $St = 9$. Other peaks of significant power occurred at Strouhal numbers of approximately 11 and 20. The difference between the time-averaged and instantaneous flow structure was shown clearly using isosurfaces of total pressure loss. This showed that the spiral form of vortex breakdown is an unsteady phenomenon, which is instantaneous and not found in the time averaged flow.

It is quite clear that the ability of RANS methods to predict the behaviour, both steady and unsteady, of delta wing flows is highly dependent on the turbulence model chosen. It is evident that standard models predict unphysical levels of turbulence within the vortex core regions, resulting in poor predictions of the vortex behaviour. A number of rotation corrections for various models have been proposed, to sensitise the turbulence prediction to the highly rotational flow behaviour, with varying success. However, these are essentially "fixes" specific to vortex flows and are not based on general physical behaviour. A more general approach is the use of non-linear models, which by their nature are dependent on both rotation and strain-rate and so add more realism to the model. However, these models also have limitations, as the turbulent behaviour is still dictated by a numerical relationship between the eddy viscosity and the Reynolds stresses, which may not be physical for all flow regimes. However, for the majority of calculations RANS and URANS methods are relatively inexpensive and while being dependent on grid refinement for accuracy, do not require significantly large grids or small time steps to reach solutions which may be reasonable.

1.5.4 LES and DNS Methods

The most general methods of predicting turbulent flow are large eddy simulation (LES) and direct numerical simulation (DNS). DNS is a method which allows the full Navier-Stokes equations to be solved directly for all scales. The size of the grids required is highly dependent on the Reynolds number of the flow and thus DNS is only realistically used for low-Reynolds number flows. LES is a method which uses the size of the grid spacings as a filter to reduce the range of scales being fully resolved. The scales which are too small to be resolved on the grid are modelled using a sub-grid model. This allows much coarser grids to be used in comparison with the DNS method, meaning that higher Reynolds numbers can be used. However, the grid refinement required for LES calculations is still significantly larger than that needed for RANS calculations.

Despite the complexity of these methods and the grid refinement issues in the regions of interest, there have been a number of investigations which use these techniques to consider vortical flows. In the investigation by Mary [25], the use of large eddy simulation was considered for the resolution of vortex breakdown behaviour over a delta wing. The test case used was the 70^o delta wing from Mitchell [13] discussed previously, with an angle of incidence of $\alpha = 27^o$, Mach number of $M = 0.069$ and Reynolds number of 1.6×10^6. This Reynolds number is relatively high for a LES calculation, therefore the grid requirements are substantial. To reduce the computational expense of the calculations a localised structured mesh refinement method was used to refine the grid sufficiently in the regions of interest without creating an overall computational grid which was too large for reasonable calculation times. Three grids were created with varying refinement. However, it was accepted that the grid refinement would be relatively coarse and as such the reliability of the LES calculation for this type of flow was considered. The LES implementation used a laminar subgrid model and two different near-wall treatments to allow a further reduction in grid requirements. The first treatment applied a no-slip condition with a logarithmic law and the second simply applied a slip condition to the wall.

The results and resolution of the simulations appear to be dependent on the near-wall treatment. A Q-criterion

isosurface is used to highlight the flow behaviour, where the Q-criterion is defined as the second invariant of $\nabla \mathbf{u}$. The resulting plots are shown in Figure 1.30 for both near-wall treatments. With the slip condition applied the vortex appears to be smooth and well-organised in structure, until the point of breakdown, which fluctuates about a mean location of $x/c_r = 0.7$. However, with the no-slip condition applied, the flow exhibits shear layer structures upstream of the breakdown, which wind around the vortex core region. The breakdown location was found not to be influenced by the presence of these structures and occurs at the same location. Comparisons of the mean flow results to experimental data show that the results from the slip condition provide closer agreement with the experiment than the no-slip results. A fact which was surprising to the authors, however, neither solution was able to predict the behaviour accurately in the post-breakdown region. Despite the slip condition giving reasonable agreement with the experiment, by its nature no boundary layer was formed and therefore no secondary separations occurred, meaning that the solution was not physical. It was concluded that the wall functions used were not suitable for delta wing flow and that the grids used were insufficiently refined to capture the flow behaviour accurately.

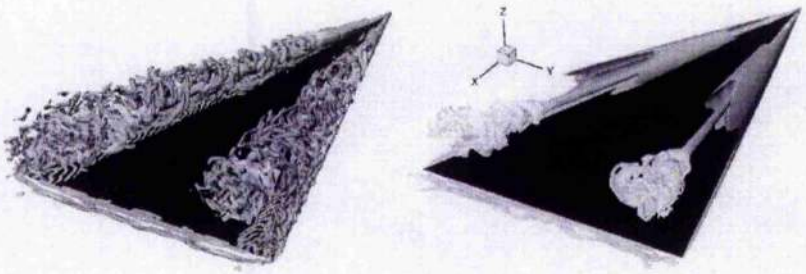

(a) No-Slip (b) Slip

Figure 1.30: Q-criterion isosurfaces of vortex behaviour for two different near-wall treatments (from Ref. [25])

A DNS calculation was carried out by Gordnier and Visbal [14], which was discussed in detail in Section 1.3.2 as it deals with the formation and behaviour of shear layer instabilities. This calculation was performed on a semi-infinite delta wing with a sweep angle of 75^o at Reynolds numbers between 6×10^3 and 5×10^4. These Reynolds numbers are very low in comparison with real configurations, however are similar to experiments carried out in water tunnels. Three levels of grid refinement are used, with sizes between 4.8×10^6 and 6.5×10^6 grid points. The calculations are carried out using a non-dimensional time step of $\Delta\tau = 1.25 \times 10^{-4}$, which for the highest Reynolds number provides a resolution of 125 time steps to a single period of the highest frequency observed. From these values it is clear that to scale this calculation up to Reynolds numbers, even of the order of 10^5 would mean extremely expensive calculations. However, the results obtained have a high level of accuracy and resolution, as shown in Figure 1.16.

DNS was also used by Shan *et al.* [98] to consider the behaviour of vortex shedding from the sharp leading edge of a delta wing and the formation of shear layer structures. The investigation was carried out for a relatively high Reynolds number of 1.96×10^5 at a Mach number of $M = 0.1$. The wing had a sweep angle of 85^o and incidence of $\alpha = 12.5^o$. For this study, the grid used had approximately 1.9×10^6 grid points. However, this appears to be very coarse in comparison with the grids used by Gordnier and Visbal [14], discussed above, however the grid topology is C-H, which may allow improved refinement over the wing. No mention of the size of time step used is made in the paper. The results show vortex shedding from the leading edge of the wing, caused by an interaction between the secondary vortex and the primary shear layer. This appears to be similar to the phenomenon described by Gordnier and Visbal [96] using a laminar flow solver at a lower Reynolds number, mentioned in Section 1.3.2. The unsteady nature of this vortex shedding was considered and a shedding frequency of approximately $St = 1.086$ was determined. Unfortunately, no direct comparisons with experimental results are made.

The same technique has also been applied to non-slender delta wings by Gordnier and Visbal [113, 114]. A 50^o delta wing was considered for a range of angles of incidence, $5^o \leq \alpha \leq 15^o$ at low Reynolds numbers and Mach numbers and the results were compared to experiments carried out under the same conditions. The grid used for this calculation had approximately 4.5×10^6 grid points and a time step of $\Delta\tau = 0.0005$ was used. These were shown to be sufficient for the temporal and spatial scales resolved at such low Reynolds numbers. As before, the agreement with the experimental results was shown to be very good, however for the highest incidence, the location of breakdown was predicted to be slightly further downstream than in the experimental results. No reasons for this discrepancy were given. The unsteady behaviour of vortex breakdown was also considered and dominant frequencies were found to occur from time histories of pressure coefficient. Upstream of breakdown these were

found to be $St = 0.63$ and 10.7, with further peaks at $St = 2$ and $St = 8$ found from the PSD analysis. The higher frequency was attributed to the shear layer structures while the lower frequency was assigned to a fluctuation of the vortex breakdown location. Downstream of breakdown, the frequency response was found to be more broadband in nature, between $St = 0$ and $St = 5$. It was also noted that the spiral form of breakdown was not found for these cases, however this is likely to be a feature of the sweep angle and not due to the computational solution.

From these studies, it is evident that the spatial and temporal resolution needed to fully resolve delta wing flows is prohibitive to the solution of flow at full scale Reynolds numbers. Particularly, for industrial application. However, as computational power rapidly increases, it may be possible that techniques like these may be used more extensively for vortical flows to validate and improve the accuracy of turbulence models and treatments in the future.

1.5.5 Detached Eddy Simulation (DES)

In order to reduce the spatial and temporal requirements of LES, particularly in the boundary layer region, hybrid URANS/LES methods have been proposed. These methods allow the advantages of each method to be utilised by applying the URANS turbulence models to the boundary layer regions and LES to the remainder of the flow domain. This has the advantage of considerably reducing the computational requirements of LES as the boundary layer region is not required to be as well refined. Due to the application of LES, the solutions are still heavily dependent on the spatial and temporal resolution and will therefore require substantially more computational resources than RANS methods. However, by using LES in the majority of the flow domain, the resolution of the overall flow behaviour will be much improved compared to standard RANS methods. Generally, these hybrid methods are known as Detached Eddy Simulation (DES). Further discussion and details of the formulation of such methods will be given in Chapter 2.

In the investigation by Morton *et al.* [24, 161], mentioned in Section 1.5.3, the RANS results for the flow over a 70^o wing was compared with that of two DES formulations. The DES formulations used were based on the RANS SA and SST models and as such were referred to as SADES and SSTDES. In order to run the DES calculations and due to their inherent sensitivity to time step size and grid resolution, both a time accuracy study and a grid dependence study were carried out. From a PSD analysis of the time history of C_N for various time steps, it was found that with decreasing time step size the dominant frequency of the signal tended toward an asymptote. Based on the final value of this asymptote, the optimum time step for the calculation was chosen as $\tau = 0.005$. Similarly, a detailed grid resolution study was carried out, which is detailed in [163]. The results of this study showed that both the medium, baseline and fine grids could capture the dominant frequencies. Thus, the baseline grid, with 2.45×10^6 cells was chosen to perform the comparison with the RANS models. As stated previously, it was found from the comparison shown in Figure 1.29, that the DES methods were able to capture the full range of frequencies which occur in the flows over delta wings. From analysis of the vortex breakdown behaviour, it was also found that the breakdown was more clearly resolved in the DES solutions. Overall it was concluded that the DES methods more accurately predicted the behaviour of the flow.

In a parallel study conducted by Mitchell *et al.* [29, 164], the presence of vortical substructures was investigated using DES based on the Spalart-Allmaras turbulence model for the same test case. As before time step and grid resolution studies were carried out. However, for this investigation a method known as "Adaptive Mesh Refinement" (AMR) was used to refine the grid in the regions of interest, namely the vortex core region. Five grids were compared, which were all unstructured and consisted of $1.2 \times 10^6, 2.7 \times 10^6, 6.7 \times 10^6, 10.7 \times 10^6$ grid points and an AMR grid of 3.2×10^6 grid points. The results agreed well with the experiments, with small spatially stationary sub-vortices observed in the shear layer of the very fine grid and the adapted grid. However, it was found that the structures observed in the adapted grid solution were closer to the experimental results than the very fine grid. Based on this it was suggested that the occurrence of the structures was extremely grid dependent. With the degradation of the results on the very fine grid being due to an increased refinement of the trailing edge vortices which seem to have an upstream effect on the shear layer. It was concluded from this study that further work was needed on a time-accurate simulation of these structures to determine their cause. The use of DES was recommended due to the accuracy of the solutions, however, it was noted that care must be taken over the creation of the grid as the results are heavily dependent on the resolution of the grid in the vortex region.

DES investigations have also been carried out by Görtz [5, 32, 165] using the same 70^o wing geometry at $\alpha = 27^o$ and with a Reynolds number of $Re = 1.56 \times 10^6$. This study differs from the previous investigations as it considers a full span wing and uses a slightly higher Mach number of $M = 0.2$. A structured grid was also used, with a H-C-H topology and approximately 4.23×10^6 cells. As before, a time step study was conducted. This study was

carried out on a semi-span wing in order to reduce length of the calculations. The time steps used and the resulting dominant frequencies from the PSD analysis of the C_N signals are summarised in Table 1.3.

$\Delta t, s$	$\Delta\tau$	*Dominant St of C_N Time History*
0.0005	0.0446	1.95
0.00025	0.0223	2.59
0.000125	0.0112	2.73
0.0000625	0.0056	2.72

Table 1.3: Time steps used in DES time accuracy study [32]

It was evident that with decreasing time step, that the dominant frequency increased. However, as in the investigation of Morton *et al.* [24], this value approached an asymptote. Therefore, a time step value of $\Delta t = 0.000065s$ was chosen as it appeared to provide reasonable temporal accuracy. Due to the expense of the calculation, the DES simulation was stopped after 89 non-dimensional time units, which corresponds to a total time of 0.0056 seconds. Due to this short time duration, the results gained may be susceptible to transients within the solution and as a result, were treated with caution. From the PSD analysis of the unsteady C_N signal two dominant frequencies were found, at 182 and $727Hz$, which correspond to Strouhal numbers of $St = 2.5$ and $St = 10.2$. The lower frequency was attributed to the helical mode instability and the higher frequency was determined to be related to frequencies found for the Kelvin-Helmholtz instability, and was assumed to be characteristic of vortical substructures in the flow. It should be noted that a Strouhal number of approximately 10 was also found in the investigation by Mitchell *et al.* [29, 164] detailed above for vortical substructures. However, from analysis of the flow solution, no vortical substructures were observed. It was proposed that this was due to the relative coarseness of the grid in the vortical region. The signal was not sufficiently long to detect any frequencies associated with vortex breakdown oscillation, however this behaviour was witnessed from the flow visualisations and the location and amplitude of the oscillation was found to agree well with experimental observations. Further analyses of the flow were considered and compared to experimental data and it was found, overall that the agreement was good. In conclusion, it was stated that DES is capable of predicting the unsteady behaviour of the vortex breakdown location accurately, however, that further work was needed to determine grid refinement issues.

The URANS investigation of this test case by Soemarwoto and Boelens [31] discussed in Section 1.5.3, was extended by de Cock *et al.* [166] using an alternative hybrid RANS/LES turbulence treatment called extra large eddy simulation (X-LES). This model uses the $k-\omega$ turbulence model within the boundary layer and LES for the remainder of the flow domain. The same grid and time step are used as in Ref. [31]. From consideration of the PSD analysis of the normal force coefficient signal, in comparison to the URANS solution detailed previously, it was found that the peak at $St \approx 9$ was not as dominant in the X-LES solution. However, more power was found in the higher frequencies, which indicates that this method is capturing more scales than the URANS calculation. Further examination of the flow structure showed that vortex breakdown was predicted further upstream at $x/c_r = 0.71$ which was in slightly better agreement with the experiment. It was concluded from this study that in comparison with the URANS results, the X-LES solutions exhibited a clear qualitative improvement due to an increase in resolution of the details of the flow.

From these investigations, it appears that DES can provide an increase in accuracy in comparison with URANS methods. However, as stated, this accuracy is highly dependent on temporal and spatial resolution, which results in large computational resources being required. However, these resources are not as considerable as those needed for LES or DNS as stated previously.

1.6 Objectives

From the literature review, it is clear that the flow over slender delta wings is complex, with the presence of breakdown and many other instabilities existing in the flow and the possibility of interactions with shockwaves occurring at transonic velocities. It is also clear that although much progress has been made in understanding this flow behaviour, there are still many aspects which are not well understood. One of these aspects is the nature of breakdown in transonic flow and the possible interactions which occur between the vortices and shocks. The sudden appearance of breakdown in transonic flow can have significant effects on the aerodynamic performance of an aircraft. The ability of CFD to predict this type of behaviour has also been considered and it is clear that this tool could provide more insight into the mechanisms which drive the abrupt nature of breakdown. Due to this, one of the aims of this project was to consider the transonic flow over a slender delta wing, with a view to considering the ability

of RANS methods to predict the flow behaviour and to examine the causes and behaviour of vortex breakdown within such a regime. This section of the project was carried out within the framework of a NATO AVT Task group.

The second aim of this work was to consider the unsteady behaviour of vortex flows at moderate angles of incidence where breakdown occurs on the wing. It is clear that the unsteady nature of the flow can have a significant effect on the overall flow behaviour and can interact with the surface of the wing or with other aircraft structures as buffet. It is evident from the literature review that much work has been carried out to consider this type of flow, particularly using CFD techniques and a number of high fidelity turbulence treatments have been proposed which allow further accuracy in the numerical solutions of such flows. It is clear that the use of DES allows a greater resolution of the unsteady flow behaviour, however this improvement in resolution come with a significant increase in computational expense over statistical methods such as URANS. It is interesting to consider the ability of DES and URANS methods to capture the main unsteady features. To assess the capabilities of the DES solution, comparison was made with experimental data and with existing DES calculations. The ability of URANS to predict the flow behaviour is then compared with the validated DES results.

1.7 Thesis Outline

Chapter 2 considers the numerical methods, turbulence models and other computational techniques used in the investigations. Chapter 3 considers the behaviour of vortical flows and vortex breakdown under transonic conditions. Chapter 4 considers the ability of the DES turbulence treatment to predict the unsteady behaviour of a subsonic delta wing vortex, including breakdown. Chapter 5 then considers the same test case, using URANS to consider whether this approach may be used to predict the main unsteady features of the flow compared to the DES solutions of the previous chapter. Finally, overall conclusions are drawn and extensions to the work will be considered.

Chapter 2

Methodology of CFD Investigations

2.1 Introduction: The Navier-Stokes Equations

Computational Fluid Dynamics (CFD) uses numerical methods to solve the conservation equations of fluid flow, known as the Navier-Stokes equations. These are a set of Partial Differential Equations (PDEs) which describe the conservation laws for mass, momentum and energy, given by,

- Mass - the continuity equation,

$$\frac{\partial \rho}{\partial t} + \frac{\partial (\rho u_i)}{\partial x_i} = 0 \tag{2.1}$$

- Momentum

$$\frac{\partial \rho u_i}{\partial t} - \frac{\partial (\rho u_i u_j)}{\partial x_j} = -\frac{\partial p}{\partial x_i} + \frac{\partial \tau_{ij}}{\partial x_j} \tag{2.2}$$

where τ_{ij} is the viscous stress tensor, which for a Newtonian fluid is proportional to the strain-rate tensor,

$$\tau_{ij} = 2\mu S_{ij} \tag{2.3}$$

where the viscous strain-rate tensor is,

$$S_{ij} = \frac{1}{2}\left(\frac{\partial u_i}{\partial x_j} + \frac{\partial u_j}{\partial x_i}\right) \tag{2.4}$$

and the laminar viscosity is defined by Sutherland's law,

$$\frac{\mu}{\mu_o} = \left(\frac{T}{T_o}\right)^{\frac{3}{2}} \frac{T_o + 110}{T + 110} \tag{2.5}$$

where μ_o is the reference viscosity at the reference temperature, T_o, where $\mu_o = 1.7894 \times 10^{-5} kg/ms$ and $T_o = 288.16K$.

- Energy

$$\frac{\partial (\rho E)}{\partial t} + \frac{\partial (\rho u_i E)}{\partial x_j} = -\frac{\partial (p u_i)}{\partial x_i} + \frac{\partial}{\partial x_j}(\tau_{ij} u_i - q_i) \tag{2.6}$$

where E is the total energy of the fluid, defined as

$$E = \rho\left(e + \frac{1}{2} u_i u_i\right) \tag{2.7}$$

The heat flux vector, q_i is given by Fourier's Law and is defined as,

$$q_i = -k_t \frac{\partial T}{\partial x_i} \quad \text{where} \quad k_t = \frac{1}{(\gamma - 1) M_\infty^2} \frac{\mu}{Pr} \tag{2.8}$$

These equations, along with the equations of state for a perfect gas

$$H = E + \frac{p}{\rho}, \qquad p = (\gamma - 1)\rho e, \qquad \frac{p}{\rho} = \frac{T}{\gamma M_\infty^2} = RT \tag{2.9}$$

provide a complete description of the flow and heat transfer of the three-dimensional, Newtonian fluid flows considered in this thesis.

2.2 Turbulence

At low Reynolds numbers, the Navier-Stokes equations predict behaviour known as Laminar flow. Viscous stresses and the viscous diffusion of vorticity and momentum damp out any small scale instabilities. However, as the Reynolds number is increased, inertial effects become increasingly important and the viscosity of the flow is no longer able to maintain the smooth behaviour. With the growth of instabilities, the flow becomes highly irregular and three-dimensional and the flow transitions from a laminar state to a turbulent one. Turbulence can be defined as an irregular flow where the physical properties fluctuate rapidly in time and space. These fluctuations occur over a large range of scales and are associated with structures in the flow, known as turbulent eddies. The size of these eddies can be described by their characteristic length ℓ. Associated with this length are characteristic velocity and time scales, $u(\ell)$ and $\tau(\ell)$ respectively.

The behaviour of the turbulent eddies in the flow is highly non-linear with interactions occurring between fluctuations with a wide range of wavelengths. The physical process, which allows these interactions, is known as vortex stretching. Vortex stretching is an inherently three-dimensional property of the flow which means that turbulence, by its nature is three-dimensional. The turbulence gains energy from the vortex elements in the flow, if they are aligned in such a way that the velocity gradients can stretch them. This process is known as the production of turbulence. As a result, the largest turbulent eddies within the flow carry most of the energy. However, the larger eddies also act on the smaller eddies, in turn stretching their associated vortex elements and transferring energy to them. This transfer of energy is then continued to even smaller eddies until the viscous forces become dominant and the energy is dissipated. This is known as the energy cascade. As well as transferring energy to the smaller eddies, the larger eddies also migrate across the flow carrying the smaller eddies with them. This movement of the turbulent structures results in an increase in the mixing and therefore, diffusion of mass, momentum and energy contained in the fluid. This is known as turbulent mixing.

The energy which is associated with turbulence and the cascade process is known as the turbulent kinetic energy, k and the rate at which this energy is transfered is termed the rate of dissipation, defined as,

$$\varepsilon = -\frac{dk}{dt} \tag{2.10}$$

The rate of dissipation is set by the largest eddies within the flow and the smallest eddies adjust to this value. The range of the scales in a turbulent flow, from the smallest to the largest eddies, is dependent on and increases in extent with Reynolds number as,

$$\frac{\eta}{\ell_o} \sim Re_T^{-3/4} \tag{2.11}$$

with η and ℓ_o being the characteristic lengths of the smallest and largest eddies respectively and Re_T being the Reynolds number based on the turbulent characteristics of the flow. In a similar manner, the ratio between the largest and smallest velocity and time scales can also be defined as,

$$\frac{u_\eta}{u_o} \sim Re_T^{-1/4}, \qquad \frac{\tau_\eta}{\tau_o} \sim Re_T^{-1/2} \tag{2.12}$$

From these equations, it is clear that the smallest scales of the flow can be many orders of magnitude smaller than the largest turbulent scales. It is also evident that as the Reynolds number increases the range of scales increases. As turbulence is a continuum phenomenon, the smallest scales are far larger than any molecular length scale. The size of the smallest scales was determined by Kolmogorov based on dimensional analysis and are dependent on the rate of dissipation and the kinematic viscosity, given by,

$$\eta = \left(\nu^3/\varepsilon\right)^{1/4}, \qquad u_\eta = (\varepsilon\nu)^{1/4}, \qquad \tau_\eta = (\nu/\varepsilon)^{1/2} \tag{2.13}$$

These are known as the Kolmogorov scales, where

$$Re = \eta u_\eta/\nu = 1 \tag{2.14}$$

In comparison, the largest scales in the flow can have the same order of magnitude the width of the flow, such as the boundary layer thickness, for example. During his study of turbulent scales, Kolmogorov made a number of hypotheses based on his observations. These included that at sufficiently high Reynolds numbers, the small scale turbulent motions were universal in that they were independent of the flow geometry and statistically isotropic. Anisotropic turbulent scales exist only for the largest length scales of the flow. According to Pope [167] this corresponds to the largest 16% of the eddies. As stated before, the largest eddies contain most of the energy of the flow

and therefore have the largest influence on the mean flow. As a result the anisotropic turbulence is known as the "energy containing range". In the isotropic turbulence range, which extends to the smallest turbulent scales, the energy cascade continues until at the smallest eddies, the molecular viscosity is sufficient to dissipate the energy to heat. This range of turbulent eddies is known as the "dissipative range" or "viscous range". The region in between the energy containing eddies and the dissipative range is known as the "inertial sub-range", where the behaviour of the energy cascade is dominated by inertial effects. The behaviour of this region can be uniquely described by a relation based on the rate of dissipation, ε.

The time and length scales of a flow are generally represented by frequencies and wavelengths (or wavenumbers, κ) which are obtained from the use of Fourier analyses of the temporal and spatial histories of the flow, respectively. Fourier analyses and statistical methods are discussed in more detail in Appendix B. It is more usual to consider turbulence as a range of wavenumbers, which are associated with the length scales of the turbulent eddies. Using this convention, the turbulent kinetic energy for a range of wavenumbers can be defined as

$$k = \int_0^\infty E(\kappa) d\kappa \tag{2.15}$$

where $E(\kappa)$ is the energy spectral density related to the Fourier analysis of k. From this relation, it is evident that the energy within a turbulent flow may be described from the energy spectrum, $E(\kappa)$ vs. κ. Figure 2.1 shows a representation of this spectrum on a log-log scale showing each of the ranges discussed above. This plot shows that the inertial sub-range is described by a straight line, which has a gradient of -5/3 and is only dependent on the rate of dissipation as described above. This slope was defined by Kolmogorov, as a result of his hypotheses and dimensional analysis and is known as the Kolmogorov -5/3 Slope (or Spectrum), given by,

$$E(\kappa) = C_K \varepsilon^{2/3} \kappa^{-5/3} \tag{2.16}$$

where C_K is the Kolmogorov constant.

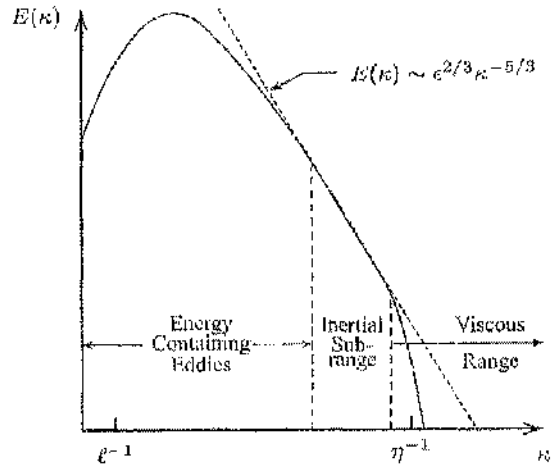

Figure 2.1: Energy Spectrum for a turbulent flow - log-log scales (From Ref. [26])

2.3 Turbulence Modelling

As mentioned before, the Navier-Stokes equations completely describe the behaviour of all the fluid flows considered in this thesis. For turbulent flows there are a large number of temporal and spatial turbulent scales, which need to be resolved. When the Navier-Stokes equations are solved to resolve all scales this is called Direct Numerical Simulation (DNS). However, this requires hugely refined grids to capture all the length scales of the flow and makes this method unrealistic for all but the most simple, low Reynolds number flows. Therefore, to reduce the computational expense in resolving all the scales of turbulence, mathematical modelling is introduced to account for a proportion of the small scale turbulent fluctuations. These mathematical techniques are known as Turbulence modelling. In this investigation two approaches to the simplification of the Navier-Stokes equations and the treatment of turbulence are used. These are the Reynolds averaging approach and Large Eddy Simulation.

2.3.1 Reynolds Averaging Approach

One method used to simplify the Navier-Stokes equations and to reduce the range of turbulent scales is Reynolds averaging. This involves decomposing the instantaneous flow into a mean flow and turbulent fluctuations, which is known as the Reynolds decomposition. It should be clarified at this point that "mean flow" is taken to mean the slowly varying flow behaviour, and is not necessarily constant with time. This decomposition is then substituted into the Navier-Stokes equations, before an averaging process is applied. There are three main methods for averaging the flow: time averaging, spatial averaging and ensemble averaging. The most common method within engineering flows, however, is time averaging, which will be detailed in this section. Details of other methods are given in Wilcox [26].

The velocity component, u_i, will be used to explain Reynolds averaging. This is applied to other flow variables in a similar way. Generally, the Reynold's decomposition takes the form,

$$u_i = U_i + u_i' \tag{2.17}$$

where U_i is the mean flow velocity and u_i' is the fluctuating velocity due to turbulence.
For statistically stationary turbulence, that is a turbulent flow where the mean flow does not vary with time, the time average is calculated from the instantaneous variable by using,

$$\bar{u}_i = \lim_{T\to\infty} \frac{1}{T} \int_t^{t+T} u_i dt \tag{2.18}$$

In practice, the term, $T \to \infty$, means that the integration time T should be of a sufficient length in comparison to the maximum period of the fluctuations. The time average of the instantaneous velocity decomposes to the time average of the mean flow, which due to its stationary nature is equivalent to the mean, $\bar{U}_i = \langle U_i \rangle$, and the time average of the turbulent fluctuations, which are zero, $\bar{u}_i' = 0$.

However, it has been discussed in Chapter 1 that delta wing vortical flows have an inherently unsteady behaviour, where the mean flow will vary with time. Therefore, any turbulence which occurs in the flow will fluctuate about an unsteady mean flow. This is known as non-stationary turbulence. For this case, the Reynolds decomposition as given in Equation 2.17 is still applicable, however, the mean flow velocity may be further decomposed into a stationary mean, $\langle U_i \rangle$, and unsteady component, u_i''.

$$U_i = \langle U_i \rangle + u_i'' \tag{2.19}$$

Thus, the instantaneous velocity can be decomposed into the form,

$$u_i = \langle U_i \rangle + u_i'' + u_i' \tag{2.20}$$

The application of the time average is also slightly different and takes the form,

$$\bar{u}_i = \frac{1}{T} \int_t^{t+T} u_i dt \tag{2.21}$$

where the sample time, T, should be chosen to be much larger that the small scale fluctuations of the turbulence, but also much smaller than the scales of the mean flow oscillations. This is due to the time averaging only being appropriate if the period of the oscillations of the mean flow are large in comparison to the time scales of the turbulent motion. This is an inherent complication of turbulence as it is not always possible to assume that the turbulent fluctuations will be small. However, from consideration of the discussion given in Section 1.3.3 which shows that the majority of characteristic flow features occur at very low non-dimensional frequencies of less than $St = 10$, it may be assumed for vortical flows that this is the case. However, care should be taken when analysing the results. Therefore, applying Equation 2.21 yields, as before, the time average of the mean flow, $\bar{U}_i$ and the time average of the turbulent fluctuations, which again will be zero, $\bar{u}_i' = 0$. However, this time, the time average of the mean flow does not equal the mean, $\langle U_i \rangle$

To form the Reynolds Averaged Navier Stokes (RANS) and Unsteady RANS (URANS) equations, the Reynolds decomposition, Equation 2.17, for each flow variable, is substituted into the Navier-Stokes equations. The time averaging process described above is then performed. Many of the new terms created from the Reynolds decomposition disappear due to the time averaging of the turbulent fluctuations, $\bar{u}_i' = 0$ and the momentum equations become,

$$\rho \frac{\partial \bar{U}_i}{\partial t} + \rho \frac{\partial \left(\overline{U_i U_j} + \overline{u_i' u_j'} \right)}{\partial x_j} = -\frac{\partial \bar{P}}{\partial x_i} - \frac{\partial (\tau_{ij})}{\partial x_j} \tag{2.22}$$

However, two new non-linear terms arise from the convective term as the time average of the product, $\overline{u_i u_j}$, yields,

$$\overline{u_i u_j} = \overline{(U_i + u_i')(U_j + u_j')} = \overline{U_i U_j} + \overline{u_i' u_j'} \tag{2.23}$$

For stationary turbulence, it was stated before that the time average of the mean flow is equal to the mean of the flow, therefore the term $\overline{U_i U_j}$ simplifies to $\langle U_i \rangle \langle U_j \rangle$. The second term, $\overline{u_i' u_j'}$, cannot be approximated and is consistent for both stationary and non-stationary turbulence. This creates a set of six new unknowns, $-\rho\overline{u_i' u_j'}$, which are known as Reynolds stresses and denoted by τ_{ij}^R, the Reynolds stress tensor. This term is usually included with the viscous stress tensor and the (U)RANS equations, for incompressible flow, become,

$$\rho \frac{\partial \bar{U}_i}{\partial t} + \rho \frac{\partial \bar{U}_i \bar{U}_j}{\partial x_j} = -\frac{\partial \bar{P}}{\partial x_i} + \frac{\partial}{\partial x_j}\left(\bar{\tau}_{ij} + \tau_{ij}^R\right) + \rho f_i \tag{2.24}$$

A similar process is carried out for the energy equation, which becomes,

$$\rho \frac{\partial (\bar{E})}{\partial t} + \rho \frac{\partial (\rho \bar{U}_i \bar{E})}{\partial x_j} = -\frac{\partial (\bar{P}\bar{U}_i)}{\partial x_i} + \frac{\partial}{\partial x_j}\left(\left(\bar{\tau}_{ij} + \tau_{ij}^R\right)\bar{U}_i - \left(q_i + q_i^R\right)\right) \tag{2.25}$$

where q_i^R is the turbulent contribution of the heat flux vector as defined in Equation 2.8, using the turbulent eddy viscosity and turbulent Prandtl number Pr_T. The presence of these unknowns creates a closure problem, which requires a new set of equations to calculate the Reynolds stresses from the known mean quantities. One common approach is based on Boussinesq's approximation.

The Boussinesq approximation is based on an analogy which likens the influence of the Reynolds stresses to the viscous stresses as defined in Equation 2.3. In this, way the anisotropic Reynolds stresses, $(a_{ij} = \overline{u_i' u_j'} - \frac{2}{3}k\delta_{ij})$, are assumed proportional to the mean strain rate and can be expressed as,

$$a_{ij} = -2\mu_T \bar{S}_{ij} \tag{2.26}$$

This introduces a viscosity parameter, known as the turbulent eddy viscosity, μ_T. As the Reynolds stresses also include an isotropic part, Boussinesq's eddy viscosity hypothesis becomes,

$$\tau_{ij}^R = -\rho\overline{u_i' u_j'} = 2\mu_T \bar{S}_{ij} - \frac{2}{3}\rho k \delta_{ij} \tag{2.27}$$

where k is the specific turbulent kinetic energy of the turbulent fluctuations, given by:

$$k = \frac{u_i' u_i'}{2} \tag{2.28}$$

which can also be thought of as half the trace of the Reynolds stress tensor. In reality, there are two assumptions being made in this approximation, 1. that the anisotropic Reynolds stresses can be defined at each point in space and time by the mean velocity gradients and 2. that the turbulent eddy viscosity is a scalar property of the flow meaning that the relationship between the anisotropy and the velocity gradients is linear. However, this method has the advantage that the Reynolds averaged equations have the same form as the Navier-Stokes equations as shown above and that the number of unknowns in the system of equations is reduced to one, greatly simplifying the closure problem. The turbulent eddy viscosity may be defined as the product of a velocity scale and a length scale. It is in the direct or indirect calculation of the eddy viscosity where the majority of (U)RANS turbulence models are applied and it is in the specification of these scales where the majority of models differ.

2.3.2 Favre-Averaging for Compressible Flows

In addition to fluctuations of velocity and pressure, the density and temperature will also fluctuate for compressible flows. This means that density is also now included in the partial differentials of the convection terms of the Navier-Stokes equations. If the Reynolds averaging procedure outlined in the previous section is applied to the resulting Navier-Stokes equations, with the density also defined as the sum of its mean and fluctuating parts, the complexity of the equations increases considerably. This is due to the introduction of correlations containing the fluctuating density, ρ'. This will also increase the required complexity of turbulence closure models.

This problem can be overcome by using the density-weighted averaging procedure proposed by Favre [168] (this procedure is also known as Favre-averaging). In this method, the mass average is introduced, in a similar way to the time average given in Equation 2.18, again using the velocity components, u_i as an example,

$$\tilde{u}_i = \frac{1}{\bar{\rho}} \lim_{T\to\infty} \frac{1}{T} \int_t^{t+T} \rho u_i dt \tag{2.29}$$

where $\bar{\rho}$ is the time averaged density. This method is similar to Reynolds averaging in that the instantaneous flow variables can be decomposed into mass averaged, $\tilde{u}_i$ and fluctuating parts, u_i'''.

$$u_i = \tilde{u}_i + u_i''' \tag{2.30}$$

The velocity decomposition is then multiplied by the density and time averaged to form the Favre average decomposition.

$$\overline{\rho u_i} = \bar{\rho}\tilde{u}_i + \overline{\rho u_i'''} \tag{2.31}$$

However, the Favre average of a fluctuating variable is equal to zero, therefore, the time average of the density correlation is equal to the time averaged density multiplied by the mass average of the variable,

$$\overline{\rho u_i} = \bar{\rho}\tilde{u}_i \tag{2.32}$$

or alternatively the mass average of the variables may be defined as,

$$\tilde{u}_i = \frac{\overline{\rho u_i}}{\bar{\rho}} \tag{2.33}$$

It is important to note that Favre averaging is only a mathematical simplification which eliminates the density fluctuations from the averaged equations. It does not, however, eliminate the effects of the density fluctuations on the turbulence in the flow.
Using the Favre averaging technique, the Navier-Stokes equations take the form,

$$\frac{\partial \bar{\rho}\tilde{u}_i}{\partial t} + \frac{\partial \bar{\rho}\tilde{u}_i\tilde{u}_j}{\partial x_j} = -\frac{\partial \bar{P}}{\partial x_i} + \frac{\partial}{\partial x_j}\left(\bar{\tau}_{ij} + \tau_{ij}^R\right) \tag{2.34}$$

$$\frac{\partial (\bar{\rho}\tilde{E})}{\partial t} + \frac{\partial (\rho \bar{u}_i \tilde{E})}{\partial x_j} = -\frac{\partial (\bar{P}\bar{u}_i)}{\partial x_i} + \frac{\partial}{\partial x_j}\left(\left(\bar{\tau}_{ij} + \tau_{ij}^R\right)\tilde{u}_i - q_i\right) \tag{2.35}$$

It is clear that these equations are analogous to the incompressible RANS equations given in Equations 2.24 and 2.25. However, in this case the Reynolds stress tensor is given by,

$$\tau_{ij}^R = \overline{-\rho u_i''' u_j'''} \tag{2.36}$$

As a result the Boussinesq approximation is slightly altered such that the strain-rate tensor used for the calculation of the anisotropic part of the tensor becomes,

$$S_{ij}^* = S_{ij} - \frac{1}{3}\frac{\partial u_k}{\partial x_k}\delta_{ij} \tag{2.37}$$

Due to the similar form of the Favre-averaged equations to the RANS equations, the details of the turbulent closure and applicable turbulence model are the same. Therefore for ease of presentation, all turbulence models are written in incompressible form.

2.3.3 Large Eddy Simulation

An alternative approach to simplifying the Navier-Stokes equations, is Large Eddy Simulation (LES). LES was initially proposed as a means to reduce the required computational expense of DNS. It does this by essentially applying DNS to much coarser grids and therefore only resolves the larger turbulent eddies in the flow. However, due to interactions between all scales in a turbulent flow the smaller scales are important to determine a complete and accurate turbulent solution. Thus, the influence of the scales smaller than the grid cell dimensions, known as Subgrid Scales (SGS), are modelled using what is known as "Subgrid Scale modelling". In resolving only the larger scales, much coarser grids and time steps can be used, compared to DNS, as the smallest resolvable scales of the flow are now much larger. This also has the consequence that LES is feasible at significantly higher Reynolds numbers.

To apply LES, the flow variables are again split into two parts: the resolvable (or filtered) component and the subgrid (or residual) component. As before, a velocity component will be used to illustrate. The decomposition is analogous to the Reynolds decomposition discussed above and takes the form

$$u_i = \widehat{u}_i + u_i^{SGS} \tag{2.38}$$

However, in this case the resolved scales may exhibit unsteady behaviour and the filtered residual does not become zero. These components of the instantaneous velocity can be further decomposed, to show what is being captured. Using similar terminology as for the URANS decompositions above, the filtered variables may be considered as the sum of the mean velocity, unsteady mean flow fluctuations and a proportion of the turbulent fluctuations resolved on the grid, defined by ϕ.

$$\widehat{u_i} = \langle U_i \rangle + u_i'' + \phi u_i' \tag{2.39}$$

The subgrid component constitutes the remaining turbulent fluctuations which are too small to be resolved,

$$u_i^{SGS} = (1 - \phi) u_i' \tag{2.40}$$

In the LES method, the two components of the decomposition, the resolvable and subgrid scales, are separated by applying filtering techniques. These techniques are applied in such a way that the maximum cell dimensions of the grid, given by Equation 2.41, are used as the filter width,

$$\Delta = max(\Delta_x, \Delta_y, \Delta_z) \tag{2.41}$$

The filter usually takes the form of a convolution integral,

$$\bar{u}_i(x) = \int G(x - x') u(x') dx' \tag{2.42}$$

where G is the filter function, which for a box filter, such as a computational grid, takes the form,

$$G(x) = \begin{cases} 1/\Delta, & |x| \leq \Delta/2 \\ 0, & otherwise \end{cases} \tag{2.43}$$

Using these techniques, the Navier-Stokes equations can be obtained for the filtered component of the flow. These equations take the form,

$$\frac{\partial \widehat{\rho} \widehat{u_i}}{\partial t} + \frac{\partial \widehat{\rho} \widehat{u_i u_j}}{\partial x_j} = -\frac{\partial \widehat{p}}{\partial x_i} + \frac{\partial \tau_{ij}}{\partial x_j} \tag{2.44}$$

As with the RANS method, this introduces a non-linear convective term into the equations. In this case, in a similar way to Reynolds averaging, the filtered product is not equal to the product of two filtered variables with the difference being the Sub Grid Scale (SGS) or residual stress tensor, τ_{ij}^{SGS}

$$\widehat{u_i u_j} = \widehat{u_i} \widehat{u_j} + \tau_{ij}^{SGS} \tag{2.45}$$

The sub grid scale stress tensor is the sum of a number of viscous stresses created from the filtering process due to the inequality $\widehat{\hat{u}_i} \neq \hat{u}_i$. These stresses are known as the Leonard Stresses, cross-stresses and SGS stresses which describe interactions between the resolved turbulence and the small scale turbulence. More detail of these stresses and their significance can be found in Pope [167] and in the lecture notes of Ferziger [169]. It can also be decomposed into anisotropic and isotropic parts.

$$\tau_{ij}^{SGS} = a_{ij}^{SGS} + \frac{2}{3} k_r \delta_{ij} \tag{2.46}$$

where k_r is the residual kinetic energy given by,

$$k_r = \frac{1}{2} \tau_{ii}^{SGS} \tag{2.47}$$

The filtered Navier-Stokes equations, now take the form,

$$\frac{\partial \widehat{\rho} \widehat{u_i}}{\partial t} + \frac{\partial \widehat{\rho} \widehat{u_i} \widehat{u_j}}{\partial x_j} = -\frac{\partial \widehat{p}}{\partial x_i} + \frac{\partial}{\partial x_j} \left(\tau_{ij} + \tau_{ij}^{SGS} \right) \tag{2.48}$$

Comparing Equations 2.24 and 2.27 with 2.44 and 2.46 it is clear that the filtered equations and subsequent stresses are analogous to the Reynolds averaged equations. Thus, the additional stress tensor can be treated in a similar way to the Reynolds stress tensor in the (U)RANS formulations. This is the basis for the simplest and most widely used approach for the subgrid scale modelling, proposed by Smagorinsky. In this model, the anisotropic stress tensor is assumed to be proportional to the filtered strain rate tensor in a similar manner to the Boussinesq approximation. As before, an eddy viscosity is associated with this relationship, known as the Smagorinsky eddy viscosity, μ_{SGS}.

$$a_{ij}^{SGS} = -2 \mu_{SGS} \widehat{S_{ij}} \tag{2.49}$$

The Smagorinsky eddy viscosity is taken to be a scalar quantity defined as,

$$\mu_{SGS} = \widehat{\rho}\,(C_s\Delta)^2\sqrt{\widehat{S_{ij}}\widehat{S_{ij}}} \tag{2.50}$$

where C_s is the Smagorinsky constant taken as 0.18. As for the Boussinesq approximation, this provides a linear relation for the sub-grid scale stress tensor

$$\tau_{ij}^{SGS} = 2\mu_{SGS}\widehat{S_{ij}} - \frac{2}{3}\widehat{\rho}k_r\delta_{ij} \tag{2.51}$$

It is important to note at this stage that although the sub grid scale stress tensor is analogous to the RANS Reynolds stress tensor and the role it plays is similar, the physics which is being modelled are quite different. Due to the formulation of LES discussed, the energy contained in the sub grid scales is a much smaller proportion of the total flow energy than the RANS turbulent energy. This suggests that only the smallest, isotropic scales need to be modelled and therefore the model accuracy may be less crucial for sub grid scale modelling than for (U)RANS computations, which need to consider the anisotropic scales. For a more detailed explanation of LES please refer to Pope [167].

2.4 Application of Turbulence models to Delta Wing Vortical Flows

To understand how turbulence models predict the behaviour of delta wing flows it is important to understand the behaviour of the velocity gradients and the production of turbulence in a turbulent flow and the mathematics which is used to describe these phenomenon.

The velocity gradients of the flow are the components of a second-order tensor and as such can be decomposed into isotropic, symmetric-deviatoric and anti-symmetric parts. A useful and detailed explanation of the properties of second-order tensors can be found in Appendix B of Pope [167]. The decomposition is shown in Equation 2.52 where the symmetric-deviatoric part corresponds to the strain rate tensor and the anti-symmetric-deviatoric part is the rotation tensor,

$$\frac{\partial u_i}{\partial x_j} = \frac{1}{3}\frac{\partial u_k}{\partial x_k}\delta_{ij} + S_{ij} + \Omega_{ij} \tag{2.52}$$

The strain-rate tensor was defined in Equation 2.4 and the rotation tensor is defined as,

$$\Omega_{ij} = \frac{1}{2}\left(\frac{\partial u_i}{\partial x_j} - \frac{\partial u_j}{\partial x_i}\right) \tag{2.53}$$

The rotation tensor is related to the vorticity of the flow,

$$\omega_i = -\varepsilon_{ijk}\Omega_{jk} \tag{2.54}$$

where ε_{ijk} is the alternating symbol defined as,

$$\varepsilon_{ijk} = \begin{cases} 1, & \text{if (i, j, k) are cyclic i.e 123, 231 or 312} \\ -1, & \text{if (i, j, k) are anticyclic i.e 321, 132 or 213} \\ 0, & \text{otherwise} \end{cases} \tag{2.55}$$

Generally, within shear layers it is found that the velocity gradients are dominated by the normal gradients, therefore, the strain-rate and rotational tensors will be roughly equal. However, as the vortex core is approached the flow tends to a purely rotational state and the rotational tensor will be larger.

The production of turbulent kinetic energy is defined as the product of the Reynolds stress tensor and the velocity gradient,

$$P_k = \tau_{ij}^R\frac{\partial \bar{U}_i}{\partial x_j} \tag{2.56}$$

This equation mathematically defines the transfer of energy from the mean flow to the fluctuating velocity field. This is caused by the mean velocity gradients interacting with the Reynolds stresses due to the process of vortex stretching discussed previously. An important feature of this behaviour is that only the symmetric part of the velocity gradient, the strain-rate tensor, and the anisotropic part of the Reynolds stress tensor contribute to the production of the turbulent kinetic energy, such that Equation 2.56 can be written

$$P_k = a_{ij}\bar{S}_{ij} \tag{2.57}$$

From this relationship, it is clear that the production of the kinetic energy is proportional to the strain-rate tensor. Considering the behaviour of delta wing vortical flows, Equation 2.57 implies that the production of turbulence will mostly occur within the shear layer and surrounding flow and not within the vortex core where the flow is highly rotational. Therefore, it would be expected that the turbulence within this region would be low and the core may be thought of as approaching a laminar state. A successful turbulence model for this type of flow should be able to predict this behaviour.

2.4.1 Wilcox $k-\omega$ Model

The $k-\omega$ model is a two equation Boussinesq based turbulence model proposed by Wilcox [34]. This model uses the flow parameters, k, specific turbulent kinetic energy and, ω, the specific dissipation rate per unit turbulent kinetic energy to calculate the eddy viscosity and to close the Reynolds averaged Navier-Stokes equations. The kinematic eddy viscosity for this model is given by,

$$\mu_T = \rho \frac{k}{\omega} \tag{2.58}$$

To calculate the turbulent kinetic energy and dissipation rate, two transport equations are added to the Navier-Stokes equations in the solution of the flow. The transport equation for the turbulent kinetic energy is given as,

$$\underbrace{\rho \frac{\partial k}{\partial t} + \rho \frac{\partial k U_j}{\partial x_j}}_{Convection} = \underbrace{\frac{\partial}{\partial x_j}\left[(\mu + \sigma^* \mu_T)\frac{\partial k}{\partial x_j}\right]}_{Diffusion} + \underbrace{P_k}_{Production} - \underbrace{\beta^* \rho k \omega}_{Dissipation} \tag{2.59}$$

This equation is similar in form to the momentum equations given in by Equation 2.2 and includes convection, diffusion, production and destruction terms as indicated. The transport equation for the dissipation, ω, takes a similar form and is given, along with all the definitions of the coefficients used in this model in Appendix A. To understand how this model applies to delta wing vortical flows, it is necessary to consider the production terms. The production of the turbulent kinetic energy was defined in Equation 2.56 and the corresponding term for the dissipation rate is given as,

$$P_\omega = \alpha \frac{\omega}{k} P_k \tag{2.60}$$

As mentioned, this model uses the Boussinesq approximation to calculate the Reynolds stresses and, thus, the production term is expanded to become

$$P_k = 2\mu_T \bar{S}_{ij} \bar{S}_{ij} \tag{2.61}$$

It is clear from these definitions that the production of k and ω within this model, are only dependent on the mean strain-rate of the flow and does not take the rotation rate into account. This is an over-simplification and results in a large over-production of turbulence within the vortex core as the regions of high vorticity are not accounted for by the model. This over-production of turbulence causes the model to predict exaggerated levels of vorticity diffusion and, thus, results in the prediction of a weak vortex which cannot be sustained and quickly diffuses.

2.4.2 $k-\omega$ with P_ω Enhancer

To rectify the inability of the "standard" Wilcox $k-\omega$ to accurately predict the turbulent structure of the vortex core, two different methods of rotation correction were proposed by Brandsma *et al.* [158]. These models were suggested to control the production of turbulent kinetic energy and hence the levels of turbulent eddy viscosity in the core region. The first method directly limits the production of k by using the dissipation term as a limiter. Whereas the second method, and the one used in this investigation, increases the production of the dissipation rate (ω) within regions of highly rotational flow. In order to apply this rotation correction to the appropriate regions within the flow, a suitable sensor was defined to distinguish between shear layers and vortex cores. This sensor considers the ratio of the magnitude of the zero-trace mean strain-rate tensor to the magnitude of the mean rotation tensor defined below as,

$$r = \frac{S}{\Omega} = \frac{\left(2\bar{S}_{ij}\bar{S}_{ij}\right)^{1/2}}{\left(2\bar{\Omega}_{ij}\bar{\Omega}_{ij}\right)^{1/2}} \tag{2.62}$$

As mentioned before, in shear layers, the strain-rate and rotational tensors are roughly equal, such that $r \approx 1$, whereas in the core of the vortex the flow approaches a rotational state, which implies $r \ll 1$. The correction for the dissipation production term is defined as,

$$P_{\omega_{new}} = \alpha \frac{\omega}{k} max\left\{\Omega^2, S^2\right\} \tag{2.63}$$

which is equivalent to dividing the production term of ω by $min\left(r^2,1\right)$, thus,

$$P_{\omega_{new}} = \frac{P_\omega}{min\left(r^2,1\right)} \tag{2.64}$$

Using this correction, the model now enhances the production of the dissipation and, thus, increases the dissipation of k, which, in turn, decreases the turbulent eddy viscosity and turbulent production within the core regions.

2.4.3 Non-Linear Eddy Viscosity Model

The non-linear eddy viscosity model (NLEVM) is based on the Wilcox $k-\omega$ model and uses the formulation of an explicit algebraic Reynolds stress model proposed by Wallin and Johansson [170] to model the Reynolds stresses. Essentially, this model introduces an extra term to the calculation of the anisotropic Reynolds stresses as defined by the Boussinesq approximation, such that,

$$a_{ij} = 2\mu_T \bar{S}_{ij} + a_{ij}^{(ex)} \tag{2.65}$$

The addition of this extra term, $a_{ij}^{(ex)}$ creates a non-linear relationship for the Reynolds stresses due to its dependence on both the mean strain-rate and rotational tensors. The equation for the Reynolds stresses then becomes,

$$\overline{u_i' u_j'} = k\left(\frac{2}{3}\delta_{ij} - 2\mu_T \bar{S}_{ij} + a_{ij}^{(ex)}\right) \tag{2.66}$$

In this model, the mean strain-rate and rotation tensors are normalised by the turbulent time scale, τ, i.e. $\mathbf{S} = \tau\bar{S}_{ij}$ and $\mathbf{\Omega} = \tau\bar{\Omega}_{ij}$, where

$$\tau = max\left\{\frac{1}{\beta^* \omega}, C_\tau\sqrt{\frac{\mu}{\beta^* k\omega}}\right\} \tag{2.67}$$

The extra anisotropy term is a reduction of the general form of a_{ij} used in explicit Reynolds stress models, which contains ten tensorially independent terms and is defined in Equation A.6. The reduced form, with tensor subscripts omitted, is,

$$\mathbf{a}^{(ex)} = \beta_3\left(\mathbf{\Omega}^2 - \frac{1}{3}II_\Omega\,\mathbf{1}\right) + \beta_6\left(\mathbf{S\Omega}^2 + \mathbf{\Omega}^2\mathbf{S} - II_\Omega\mathbf{S} - \frac{2}{3}IV\mathbf{1}\right) + \beta_9\left(\mathbf{\Omega S\Omega}^2 - \mathbf{\Omega}^2\mathbf{S\Omega}\right) \tag{2.68}$$

where $\mathbf{I}$ is the identity matrix, equivalent to δ_{ij} and II_Ω and IV are two of the independent invariants of $\mathbf{S}$ and $\mathbf{\Omega}$. The β_n coefficients are defined by these invariants and their definitions and other model constants are detailed in Appendix A.

In addition to introducing this new anisotropic term, the calculation of the turbulent eddy viscosity is also modified from the $k-\omega$ model and takes the form,

$$\mu_T = C_\mu^{\text{eff}}\rho k\tau \tag{2.69}$$

where

$$C_\mu^{\text{eff}} = -\frac{1}{2}\left(\beta_1 + II_\Omega\beta_6\right) \tag{2.70}$$

In this definition of the turbulent eddy viscosity it is clear that the behaviour of the rotation tensor is also taken into account.

To consider the behaviour of this model in the prediction of vortical flows, again the production of turbulence should be considered. This will also now have an additional term and takes the form,

$$P_k = \left(2\mu_T\bar{S}_{ij} - a_{ij}^{(ex)}\right)\bar{S}_{ij} \tag{2.71}$$

From this relationship, it is clear that the extra term acts to reduce the turbulent production from the original model. The relationship between the strain-rate and rotation rate tensors and the extra anisotropy are difficult to quantify due to the complexity of the model. However, it is evident from the formulation of the model that the rotational tensor and its invariants appear frequently. Therefore, it may be supposed that as the flow tends to a purely rotational state, the value of the extra anisotropy will increase and therefore reduce the turbulence within the vortex core region. The levels of turbulent eddy viscosity will also reduce in this region, further reducing the levels of turbulence in the flow.

2.4.4 Spalart Allmaras Model

The one-equation Spalart-Allmaras model [35] is another Boussinesq based model, which solves a single equation for a working variable $\tilde{\nu}$, which is related to the turbulent eddy viscosity of the flow such that,

$$\mu_T = \rho \tilde{\nu} f_{v1} \tag{2.72}$$

The single differential equation which defines this model was proposed for application in aerodynamic flows, such as transonic flow over airfoils, and was derived empirically using arguments based on dimensional analysis, invariance and molecular viscosity. The origin of each term is described in detail in Ref. [35]. The transport equation for the undamped eddy viscosity, $\tilde{\nu}$ is given as,

$$\underbrace{\frac{\partial \tilde{\nu}}{\partial t} + \frac{\partial (\tilde{\nu} u_j)}{\partial x_j}}_{Convection} = \underbrace{c_{b1} \tilde{\nu} \tilde{S}}_{Production} \underbrace{- c_{w1} f_w \left(\frac{\tilde{\nu}}{d}\right)^2}_{Destruction} + \underbrace{\frac{1}{\sigma} \frac{\partial}{\partial x_k} \left[(\nu + \tilde{\nu}) \frac{\partial \tilde{\nu}}{\partial x_k} \right] + \frac{c_{b2}}{\sigma} \frac{\partial \tilde{\nu}}{\partial x_k} \frac{\partial \tilde{\nu}}{\partial x_k}}_{Diffusion} \tag{2.73}$$

As before, the general form of the equation is similar to the momentum equations given in by Equation 2.2 and includes convection, diffusion, production and destruction terms as indicated. The wall destruction term is derived to reduce the turbulent viscosity in the laminar sublayer. All model coefficients and definitions are detailed in Appendix A. In the production term, it is important to note that $\tilde{S}$ denotes the modified magnitude of vorticity, defined in Equation A.22 and is not related to the strain-rate tensor.

After calculating the turbulent eddy viscosity using the transport equation, the Boussinesq approximation is used to determine the Reynolds stresses and close the Navier-Stokes equations. As a Boussinesq based model, the Spalart Allmaras model suffers from the same problems as the Wilcox $k-\omega$ model discussed previously. Due to the use of the strain-rate tensor in the calculation of the Reynolds stresses, the model may predict unrealistic contributions of the Reynolds stresses in regions of high rotational flow, such as the vortex core.

2.4.5 Detached Eddy Simulation (DES)

As detailed in the previous section, LES was proposed as a means to reduce the computational costs of DNS. However, limitations still exist on its use and in practice the method only increases the applicable Reynolds numbers by about a factor of 10 compared with DNS. These limitations are due to the application of LES on grids within the wall region of a domain. As the wall is approached, the turbulent length scales decrease in size and become of the order of the boundary layer thickness. Therefore, to accurately simulate the flow behaviour close to the wall, the grid refinement needed approaches DNS levels. This is a significant problem for the application of LES to practical engineering flows, such as full aircraft, as the problem of computational expense returns.

To overcome these issues, without compromising the solution accuracy anymore than is necessary, a new approach was proposed by Spalart *et al.* [171]. This approach utilises both LES and RANS within the solution domain, to take advantage of the benefits of each method and to gain an accurate solution, at moderate computational expense. This hybrid method is known as Detached Eddy Simulation (DES) and works by applying a RANS model within the boundary layer region to utilise its near-wall modelling approach to avoid computational cost and applying LES to the remainder of the flow domain, where larger turbulent eddies dominate. The model used in this investigation uses the Spalart-Allmaras model as the URANS model in the implementation as initially proposed by Spalart *et al.* [171].

The use of the Spalart-Allmaras model within the DES formulation is based on the connection between the production and destruction terms of the partial differential equation defined in Equation 2.73. Balancing these two terms gives the relationship,

$$\tilde{\nu} \propto \tilde{S} d^2 \tag{2.74}$$

From consideration of the Smagorinsky SGS model in Section 2.3.3 and in particular the expression for the Smagorinsky eddy viscosity given by Equation 2.50, it is clear that a similar proportionality exists, with the term Δ, based on the grid spacing, (see Equation 2.41) replacing the distance d, such that

$$\nu_{SGS} \propto \hat{S} \Delta^2 \tag{2.75}$$

Based on this similarity, it was suggested that if d is replaced with Δ in the wall destruction term, the Spalart-Allmaras model will act as a Smagorinsky LES model. Therefore, in order for the Spalart-Allmaras model to exhibit both URANS and LES behaviour, d in the Spalart-Allmaras model is replaced by,

$$\tilde{d} \equiv min\{d, C_{DES}\Delta\} \tag{2.76}$$

where C_{DES} is a constant, which has been set to 0.65 as suggested by Shur *et al.* [172] for homogeneous turbulence. From this formulation, the model acts as a RANS model for $d \ll \Delta$ and as a subgrid scale model for $d \gg \Delta$. Thus, this method restricts the use of the URANS model to near wall regions and allows LES to be used elsewhere based on these parameters. This is shown schematically by Figure 2.2.

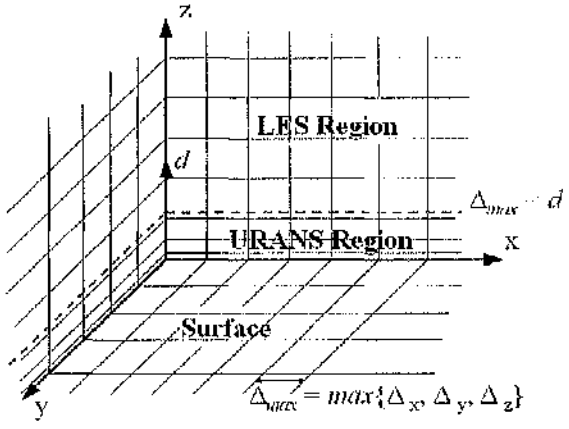

Figure 2.2: Schematic of DES formulation on a structured grid

Using DES, allows the application of LES to the vortical region above the wing. In using LES, the Boussinesq approximation is not applied and thus all large scale rotations, stresses and strains are resolved fully on the grid. This will result in a more accurate prediction of the production of turbulence and the overall behaviour of the leading edge vortex system. Generally, the subgrid contribution to the turbulence will be small, therefore keeping the turbulence levels within the vortex core region low and more realistic than for the Boussinesq based models. However, to keep this contribution small, the grid should be adequately refined such that the majority of the flow scales are resolved on the grid. Thus, the computational expense of such calculations is much larger than for more traditional turbulence models as described previously.

2.4.6 Computational Cost of Turbulent Calculations

In a review by Spalart [33], the relative computational costs of DNS, LES, DES and URANS were compared in a similar manner for a target flow of a full aircraft or a car. The numerical background of each method was considered and the suggested grid size and number of time steps needed to advance a sample calculation by roughly six "spans of travel", meaning the time taken for an air particle to travel six times the length of the model. This may only result in a calculation total time of a fraction of a second in real time. The results of this analysis of each method is shown in Table 2.1.

Type	*Empiricism*	*Grid Size*	*Time Steps*	*Ready?*
3D URANS	Strong	10^7	$10^{3.5}$	1995
DES	Strong	10^8	10^4	2000
LES	Weak	$10^{11.5}$	$10^{6.7}$	2045
DNS	None	10^{16}	$10^{7.7}$	2080

Table 2.1: Summary of computational costs of various turbulence methods according to Spalart (adapted from Ref. [33])

Using the proposed computational cost of the methods, Spalart also attempted to define a readiness date for each method, based on that method becoming a "Grand Challenge" to general CFD practitioners as opposed to everyday industrial use. These dates are also included in Table 2.1. This data provides a measure of the computational costs described above and the prospect of widespread use in the future. However, it remains to be seen whether these predicted values are accurate or if complex geometries and modelling strategies will increase these requirements.

2.5 PMB solver

All computations were performed using the Parallel Multi-Block (PMB) flow solver developed at the University of Glasgow, which has been continually revised and updated over a number of years. The solver has been successfully

applied to a variety of problems including cavity flows, hypersonic film cooling, spiked bodies, flutter and delta wing flows amongst others. The PMB code is a multi-block structured solver which solves the unsteady RANS equations in a global 3D Cartesian frame of reference [173]. The conservation laws described in Section 2.1 can be converted into vector form to simplify their use in the computational method, the Navier-Stokes equations now take the form,

$$\frac{\partial \mathbf{W}}{\partial t} + \frac{\partial \left(\mathbf{F}^i + \mathbf{F}^v\right)}{\partial x} + \frac{\partial \left(\mathbf{G}^i + \mathbf{G}^v\right)}{\partial y} + \frac{\partial \left(\mathbf{H}^i + \mathbf{H}^v\right)}{\partial z} = 0 \tag{2.77}$$

where $\mathbf{W}$ is the vector of conserved variables, defined by

$$\mathbf{W} = (\rho, \rho u, \rho v, \rho w, E)^T. \tag{2.78}$$

The superscripts i and v in Equation 2.77 denote the inviscid and viscous components of the flux vectors, $\mathbf{F}$, $\mathbf{G}$ and $\mathbf{H}$, respectively. The inviscid flux components are given by

$$\begin{aligned}
\mathbf{F}^i &= \left(\rho u, \rho u^2 + p, \rho uv, \rho uw, u(\rho E + p)\right)^T, \\
\mathbf{G}^i &= \left(\rho v, \rho uv, \rho v^2 + p, \rho vw, v(\rho E + p)\right)^T, \\
\mathbf{H}^i &= \left(\rho w, \rho uw, \rho vw, \rho w^2 + p, w(\rho E + p)\right)^T.
\end{aligned} \tag{2.79}$$

The viscous flux vectors contain terms for the heat flux and viscous forces exerted on the body are

$$\begin{aligned}
\mathbf{F}^v &= \frac{1}{\mathrm{Re}} \left(0, \tau_{xx}, \tau_{xy}, \tau_{xz}, u\tau_{xx} + v\tau_{xy} + w\tau_{xz} + q_x\right)^T, \\
\mathbf{G}^v &= \frac{1}{\mathrm{Re}} \left(0, \tau_{xy}, \tau_{yy}, \tau_{yz}, u\tau_{xy} + v\tau_{yy} + w\tau_{yz} + q_y\right)^T, \\
\mathbf{H}^v &= \frac{1}{\mathrm{Re}} \left(0, \tau_{xz}, \tau_{yz}, \tau_{zz}, u\tau_{xz} + v\tau_{yz} + w\tau_{zz} + q_z\right)^T.
\end{aligned} \tag{2.80}$$

The terms τ_{ij} in Equation 2.80 represent the viscous stress tensor components while q_i denotes the heat flux vector. These equations can be transformed into the averaged equations simply by substituting $\left(\tau_{ij} + \tau_{ij}^R\right)$ for τ_{ij} and $\left(q_i + q_i^R\right)$ for q_i and taking the flow variables as averaged quantities as defined in Section 2.3. All quantities are non-dimensionalised using the relations,

$$\begin{aligned}
x &= \frac{x^*}{L^*}, \quad y = \frac{y^*}{L^*}, \quad z = \frac{z^*}{L^*}, \quad t = \frac{t^*}{L^*/U_\infty^*}, \\
\rho &= \frac{\rho^*}{\rho_\infty^*}, \quad u = \frac{u^*}{U_\infty^*}, \quad v = \frac{v^*}{U_\infty^*}, \quad w = \frac{w^*}{U_\infty^*}, \\
p &= \frac{p^*}{\rho_\infty^* U_\infty^{*2}}, \quad T = \frac{T^*}{T_\infty^*}, \quad e = \frac{e^*}{U_\infty^{*2}} \quad \mu = \frac{\mu^*}{\mu_\infty^*}
\end{aligned} \tag{2.81}$$

where the superscript * denotes the dimensional variables. For this investigation, the non-dimensional characteristic length, L^*, is taken to be the root chord length of the delta wing, c_r.

2.5.1 Steady State Solver

The PMB flow solver uses a cell-centred finite volume approach to discretise the governing equations described above. According to this method, the spatial discretisation of the RANS equations for each cell results in the equation,

$$\frac{d}{dt}\left(\mathbf{W}_{i,j,k} \mathscr{V}_{i,j,k}\right) + \mathbf{R}_{i,j,k} = 0. \tag{2.82}$$

where $\mathscr{V}_{i,j,k}$ denotes the cell volume, which due to using a fixed grid is constant for the current work, and where $\mathbf{R}_{i,j,k}$ represents the flux residual. The convective fluxes are discretised using Osher's upwind scheme [174], however Roe's flux-splitting scheme [175] is also available. The MUSCL variable extrapolation method is employed to provide second-order accuracy with the van Albada limiter being applied to remove any spurious oscillations across shock waves. The central differencing spatial discretisation method is approximate to solve the viscous terms.

The system of equations defined in Equation 2.82 are integrated in time to reach a steady state solution using an implicit time-marching scheme, defined by

$$\frac{\mathbf{W}_{i,j,k}^{n+1} - \mathbf{W}_{i,j,k}^{n}}{\Delta t} = \frac{1}{\mathscr{V}_{i,j,k}} \mathbf{R}_{i,j,k}^{n+1} \tag{2.83}$$

where the flux residual $\mathbf{R}^{n+1}_{i,j,k}$ is linearised in time as,

$$\mathbf{R}^{n+1}_{i,j,k} \approx \mathbf{R}^{n}_{i,j,k} + \frac{\partial \mathbf{R}^{n}_{i,j,k}}{\partial \mathbf{W}^{n}_{i,j,k}} \left(\mathbf{W}^{n+1}_{i,j,k} - \mathbf{W}^{n}_{i,j,k} \right) \tag{2.84}$$

By substituting Equation 2.84 into Equation 2.83, the non-linear system of equations can be approximated as

$$\left(\frac{1}{\Delta t} + \frac{\partial \mathbf{R}^{n}}{\partial \mathbf{W}} \right) \Delta \mathbf{W} = -\frac{1}{\mathscr{V}_{i,j,k}} \mathbf{R}^{n} \tag{2.85}$$

where the subscripts i, j, k have been dropped for clarity and $\Delta W = \left(\mathbf{W}^{n+1}_{i,j,k} - \mathbf{W}^{n}_{i,j,k} \right)$.

To solve this linear system of equations using a direct method is prohibitive as the number of equations becomes large. Therefore, an iterative Generalised Conjugate Gradient method is used as it is capable of solving sparse equations efficiently in terms of time and memory requirements. This is used in conjunction with a Block Incomplete Lower-Upper (BILU) factorisation method used as a pre-conditioner to solve the system of equations.

Implicit schemes require particular treatment during the early stages of the iterations. Generally, the traditional approach is to initially use a low CFL number and increase this as the solution progresses. However, it has been found that smoothing out the initial flow by using an explicit method for a number of initial iterations before switching to the implicit method was just as efficient. Therefore, in all calculations performed, a number of explicit iterations are specified before the implicit scheme is then used.

Due to the fact that the formulation of most turbulence models can also be represented in vector form, similar to Equation 2.77, the steady state solver for the turbulence model equations are formulated and solved in a similar manner to the mean flow as described, with the vector $\mathbf{W}$ replaced by the equivalent turbulent vector $\mathbf{Q}$ and an equivalent substitution for the flux residual. For the turbulence model equations the flux residual also contains the dissipation source term, however the production term is solved explicitly. The eddy viscosity is calculated from the turbulent quantities as specified by the model and is used to advance the mean flow solution. This new mean flow solution is then used to update the turbulence solution, freezing the mean flow values.

2.5.2 Unsteady Solver

The implicit dual-time method proposed by Jameson [176] is used for time-accurate calculations. The residual is redefined to obtain a steady-state equation which can be solved using acceleration techniques. Using a three-level discretisation of the time derivative, the updated flow solution is calculated by solving

$$\mathbf{R}^{*}_{i,j,k} = \frac{3\mathbf{W}^{n+1}_{i,j,k} - 4\mathbf{W}^{n}_{i,j,k} + \mathbf{W}^{n-1}_{i,j,k}}{2\Delta t} + \frac{1}{\mathscr{V}_{i,j,k}} \mathbf{R}_{i,j,k} \left(w^{k_m}_{i,j,k}, q^{k_t}_{i,j,k} \right) = 0 \tag{2.86}$$

where $\mathbf{R}_{i,j,k} \left(w^{k_m}_{i,j,k}, q^{k_t}_{i,j,k} \right)$ is the spatial discretisation as described above, with $w_{i,j,k}$ and $q_{i,j,k}$ being the vector form of the values of $\mathbf{W}$ and $\mathbf{Q}$, the turbulent residual, in the surrounding cells. Similarly for the turbulence model,

$$\mathbf{Q}^{*}_{i,j,k} = \frac{3\mathbf{Q}^{n+1}_{i,j,k} - 4\mathbf{Q}^{n}_{i,j,k} + \mathbf{Q}^{n-1}_{i,j,k}}{2\Delta t} + \frac{1}{\mathscr{V}_{i,j,k}} \mathbf{Q}_{i,j,k} \left(w^{k_m}_{i,j,k}, q^{k_t}_{i,j,k} \right) = 0 \tag{2.87}$$

These equations represent a coupled non-linear system of equations. The superscripts, k_m, k_t, l_m and l_t determine the time levels of the variables used in the spatial discretisation and determine the behaviour of the coupling between the systems of equations. If $k_m = k_t = l_m = l_t = n+1$ then the mean and turbulent quantities are advanced in real time in a fully coupled and implicit manner. However, if $k_m = l_m = l_t = n+1$ and $k_t = n$ then the equations are advanced in sequence in real time i.e. the mean flow is updated using frozen turbulence values and then the turbulent values are updated using a frozen mean flow solution. This has the advantage that the only modification, when compared to the laminar case, to the discretisation of the mean flow equations is the addition of the eddy viscosity from the previous time step. The turbulence model only influences the mean flow solution through the eddy viscosity therefore any two equation model can be used without modifying the mean flow solver. Hence the implementation is simplified by using a sequenced solution in real time. However, the uncoupling could adversely affect the stability and accuracy of the real time stepping, with the likely consequence of limiting the size of the time step that can be used.

This non-linear system of equations can be solved by introducing an iteration through pseudo time, $\hat{t}$, to the steady state. This is given by,

$$\frac{\mathbf{W}_{i,j,k}^{n+1,k+1} - \mathbf{W}_{i,j,k}^{n+1,k}}{\Delta \hat{t}} + \frac{1}{\mathcal{V}_{i,j,k}} \mathbf{R}_{i,j,k}^{*} = 0 \tag{2.88}$$

with an equivalent form for the turbulent system of equations. It is clear that this takes the form of the steady state solver formulation as given in Equation 2.83 such that if $\mathbf{R}_{i,j,k}^{*}$ is replaced with $\mathbf{R}_{i,j,k}$ a non-time varying flow will be solved. Using this formulation the system of equations can again be linearised and iterated to a steady state solution in pseudo time before being advanced in real time.

The flow solver can be used in serial or in parallel mode. In order to obtain an efficient parallel method based on domain decomposition, different methods are applied to the flow solver. An approximate form of the flux Jacobians resulting from the linearisation in pseudo-time is used which reduces the overall size of the linear system by reducing the number of non-zero entries. Between the domains of the computational grid, the BILU factorisation is also decoupled thereby reducing the communication between processes. Each processor is also allocated a vector that contains all the halo cells for all the blocks in the grid. Message Parallel Interface (MPI) is used for the communication between the processors in parallel. All computations undertaken have been performed on the Beowulf Pentium 4 120-processor workstation cluster of the CFD Laboratory at the University of Glasgow.

2.6 Unsteady Time Step Calculation

One of the most important factors in the execution of an unsteady calculation is the choice of time step. If a time step is too large then the high frequency detail of the flow can be missed, however with a very small time step the computational resources and time taken for the calculation increases. Therefore, care must be taken to select a time step which is small enough to adequately resolve the unsteady fluctuations of the flow, but large enough not to make the required computational resources too great. This generally requires a prior knowledge of the approximate scale of the important frequencies in the flow. For numerical calculations, the non-dimensional time step is usually used and so the the non-dimensional frequency (or Strouhal number) should be considered. For delta wing flows, the non-dimensional time and Strouhal number are related to the dimensional time and frequency using,

$$St = \frac{f c_r}{U_\infty} \quad \text{and} \quad \tau = \frac{U_\infty t}{c_r}. \tag{2.89}$$

The unsteady behaviour of delta wing flows was considered and discussed in the previous chapter and the major frequencies of the flow were highlighted for various investigations in Table 1.2. From this discussion, it is evident that the majority of the frequencies associated with the dominant flow features are less than approximately $St = 10$. A time step of $\Delta\tau = 0.01$ is the lowest time step which can be used to capture this frequency.

To show how this value for the time step was reached it is clearer to start with the sample rate at which the unsteady behaviour is to be sampled. To adequately capture an unsteady oscillation it may be assumed that a minimum of five time steps are needed per cycle. Therefore, the period of the maximum frequency captured will be $5\Delta\tau = 0.05$. A frequency can then be obtained from the inverse of this value, which gives $St = 20$. In signal processing and data sampling theory, it is important to avoid aliasing, where higher frequencies are superimposed onto lower frequencies, which can distort the resulting sampled signal. In order to do this the Nyquist criterion is used which determines the maximum frequency which can be detected for a given sample rate $\Delta\tau$,

$$St_N = \frac{1}{2\Delta\tau} \tag{2.90}$$

This essentially reduces the maximum captured frequency for a given time step by a factor of two, therefore the maximum frequency which can be obtained from a sample rate of $\Delta\tau = 0.01$ is $St = 10$. From this analysis, it is clear that in halving the time step, the maximum frequency is doubled.

This is generally adequate for URANS calculations as the choice of time step is independent of other calculation parameters. However, for DES calculations the size of the time step is directly related to the size of the cells within the computational grid and there is an optimum time step for a given grid size. Therefore, as the grid is refined the time step is also refined. This was briefly discussed in the previous section dealing with the computational cost of DES calculations. In a guide to creating DES grids and running calculations, Spalart [177] recommended

calculating the required time step necessary for a given grid, based on the the minimum target grid spacing within the region of interest and the maximum velocity in the flow (as a multiple of the freestream velocity), such that,

$$\Delta\tau = \frac{\Delta_{max}}{U_{max}} \tag{2.91}$$

However, this relationship is only a guide and as such the effect of temporal refinement should be considered when using the DES formulation.

2.7 Post-processing Techniques

Before presenting the results of the investigations, it is important to explain some of the techniques used to process the solutions obtained from the CFD calculations. As both steady and unsteady calculations are performed within this investigation it is important to consider the relevant output files and the way in which they are processed. For an unsteady calculation, there are three main types of solution file. These are:

- Domain solution data
- Integrated loads
- Point probe data

The domain solution data file is created at the end of every specified time step calculation and provides data on instantaneous flow variables for every point within the grid file used for the calculation. The integrated loads file is updated for each time step and, therefore, provides the time histories of the loadings and similarly, the probe data files provide time histories of flow variables at points within the flow domain specified at the start of the calculation. For a steady state calculation, only two files are created at the end of the calculation once the solution has converged, the steady state domain solution and the integrated loads. Each of the files described are processed in a different way and some details of these processes are given in this section.

2.7.1 Domain Solution data

As stated, the three-dimensional domain files contain flow variables at each grid point within the flow domain. These variables are ρ, u, v, w, p and the turbulent quantities k, ω and Re_T for the $k-\omega$ based models and μ_T and Re_T for the Spalart-Allmaras based models. The flow variables in the domain files are non-dimensionalised by the freestream properties of the flow as described in Equation 2.81. The turbulent quantities are, therefore, also non-dimensional. In this work, the all flow properties are non-dimensional, unless otherwise stated.

To analyse the domain files, the visualisation package *Tecplot* is used, which allows both single and multiple files to be viewed and manipulated. Due to the large grid sizes used in these investigations, using the complete flow domain for analysis was restrictive due to memory requirements and so a number of macros were written to extract the relevant flow details for analysis. These extracted data files allow both two and three-dimensional visualisation techniques to be employed for either single or multiple files. The extracted details include, 1-D and 2-D slices of the solution and 3-D isosurfaces of variables, such as velocity.

The use of macros in *Tecplot*, also allows the same views of each time step to be created and captured for comparison and provides the means to create short movies of the unsteady behaviour. From these movies, it is possible to pick out and track some of the unsteady features of the flow. With the knowledge of the time step size between each frame it may be possible to resolve the frequencies of particular features and relate these back to the data obtained from the unsteady probe and integrated loads files.

The variables provided by PMB in the output file are not always sufficient to capture specific flow features adequately and other flow parameters are required. A number of flow parameters were calculated within this investigation using *CFD Analyzer*, which is an add-on package for *Tecplot*, these include the components of vorticity, ω_i, the Mach number, M, entropy, s, and pressure coefficient, C_p. The relationships used to derived these variables are given in Equations 2.92 to 2.95, respectively.

$$\omega_i = \frac{\partial u_i}{\partial x_j} - \frac{\partial u_j}{\partial x_i} \tag{2.92}$$

$$M = \frac{|u|}{a} \quad \text{where} \quad a = \sqrt{\frac{\gamma P}{\rho}} \tag{2.93}$$

$$s = c_v ln\left(\frac{P}{P_\infty}\right) + c_p ln\left(\frac{\rho_\infty}{\rho}\right) \tag{2.94}$$

$$C_p = 2\left(P - \frac{1}{\gamma M_\infty^2}\right) \tag{2.95}$$

2.7.1.1 Shock Detection and Analysis

When considering transonic flows it was also necessary to consider means to identify the locations and strengths of shockwaves which occur in the flow. In order to facilitate the identification of the shocks, a shock detection algorithm was used, which was provided in the *CFD Analyzer* add-on. The algorithm is based on the work of Lovely and Haimes [27] and calculates the locations of shocks by using the pressure gradient to calculate the Mach number normal to a shock surface. Where the normal Mach number is greater than or equal to one, a shock is identified. The pressure gradient of the flow is always normal to a shock surface and so the algorithm calculates the pressure gradients in the flow in order to determine the orientation of the shock. The local Mach vector at each point normal to this surface is then calculated. This is shown schematically in Figure 2.3.

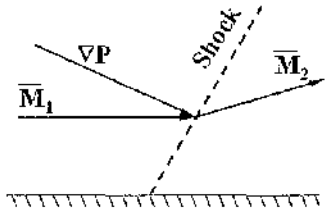

Figure 2.3: Shock detection test quantity (Adapted from Ref. [27])

The normal Mach number or shock test value at each point in the flow is then created by using the dot product of these pressure gradients and local Mach vectors,

$$M_N = M_1 \cdot \nabla P \tag{2.96}$$

In the *CFD analyzer* version of this algorithm, the pressure gradient vector is normalised by its magnitude. Due to the negligible thickness of shockwaves, the algorithm calculates shock surfaces which surround the region where a shock is calculated to form and this creates a new flow variable within the domain solution. When this variable is greater than one it is proposed that a shock may occur. To initially visualise the suggested locations of the shocks within the flow isosurfaces of this shock variable were plotted. However, it became clear that there were regions of spurious shock surfaces, where it was not expected that shocks would occur. Therefore, to allow validation of this algorithm and confirm the locations of the shocks in the flow, the solutions were also analysed manually using the variables: Mach number, entropy and pressure gradients (both magnitude and in all directions). Contours of these variables were compared to the shock feature contours produced by the algorithm described above. Thus, considering the distributions of all of these variables and reasoning based on previous investigations, the locations of shocks in the flow were established.

2.7.2 Integrated Loads and Probe Analysis

The analysis of the time series of flow properties provided by the integrated loads and point probe files are carried out using *Probe Analyser*. This is a custom-made program created in *Matlab*, which allows the manipulation and plotting of the data, using statistical analysis and signal processing techniques. *Probe Analyser* is based on the initial program by Lawrie [178], and further developed by Nayyar [179], for cavity flows and has been further extended in the course of this investigation, specifically for unsteady delta wing flows. Details of the program, its current capabilities and an explanation of the techniques used in this investigation are given in Appendix B.

Before either file is analysed, a number of pre-processing techniques are necessary. Generally for the integrated loads file this only involves deleting the initial transients of the signals created from the start of the unsteady calculation. However, for the probe files this is slightly more involved. The data written to the probe files from PMB, is not directly usable and a number of different manipulations are needed before the results can be viewed. For this

purpose, a number of utility programs have been written to concatenate and convert the probe data from the block probe files into the format used by *Probe Analyser*. The initial transients are also removed from these files.

As stated before, the unsteady integrated loads files contain the time histories of the loadings on the wing surface, these include the normal force coefficient, C_N, lift coefficient, C_L, drag coefficient, C_D, and moment coefficient, C_M. The analysis of the time histories of these variables can tell much about the overall unsteady nature of the flow and through calculation of such quantities as the power spectral density, an overview of the dominant unsteady forces on the wing and their frequencies can be obtained. Generally, the quantity which is of particular interest is the normal force coefficient, however similar analysis can be carried out on the lift, drag or moment coefficients also. Useful quantities which are calculated for these variables include the mean and RMS values along with the PSD as mentioned above.

The analysis of the probe data is a little different to the integrated loads file purely due to the volume of information which can be contained in the files. The probe files contain all the unsteady flow variable data for each specified point in the flow. Therefore, the time histories of ρ, u, v, w and p are available for multiple points through the flow domain. *Probe Analyser* allows for each probe to be considered separately or for a range or selection of probes to be considered and cross-plotted together for comparison, it also allows multiple probe files from different calculations to be analysed and compared at the same time. The same analysis techniques can be applied to each flow variable as described for the integrated loads, but there are also many more functions that can be performed on the probe file data. These include, time averaging of a signal and the calculation of turbulent quantities and correlations such as the Reynolds stresses or turbulent kinetic energy based on either a stationary or non-stationary mean.

Chapter 3

Transonic Vortical Flow on a Slender Delta Wing

3.1 Introduction

As detailed in the literature review in Chapter 1, much is known about vortical flow over slender, sharp edged delta wings and there are many reviews which detail the volume of data available on the subject, both experimental and computational [49, 58, 102, 126, 180]. For the most part, this data concerns subsonic freestream flow and vortex breakdown. However, an area of delta wing vortical flow which is not so well understood is the behaviour of the flow under transonic conditions.

From the literature, it is evident that the behaviour of the flow is somewhat different to vortical flow in the subsonic regime. With an increase in Mach number, the size and shape of the vortex system changes [118] and the primary vortex is found to sit progressively closer to the wing surface. Despite this increased proximity to the wing, the vortex system creates a much reduced suction peak on the wing compared to subsonic flow. The shock waves which appear are caused by localised supersonic flow regions. A number of investigations, both experimental and numerical have been carried out, which have looked at the occurrence and behaviour of shockwaves in vortical flows for varying transonic conditions [17, 18, 117, 121, 122, 123, 124, 125]. From these investigations, a number of shockwave systems have been observed and described in the literature. From the work of Elsenaar and Hoeijmakers [18], a plot was created, which detailed the onset of various flow behaviours with Mach number and incidence, which is shown in Figure 3.1. From this diagram, it is clear, that for transonic flow both rear/terminating and cross-flow shocks appear for increasingly lower angles of incidence. The critical incidence for breakdown is also shown and indicates that the incidence at which vortex breakdown occurs decreases with increasing Mach number. Further detail on the nature and behaviour of the shockwaves was given in Section 1.4.

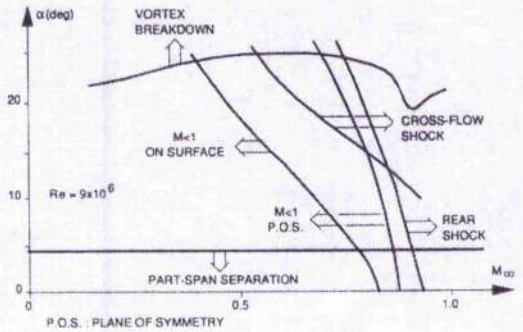

Figure 3.1: A summary of the flow features for various Mach numbers and angles of incidence (from Ref. [18])

The occurrence of these shockwave systems in the flow introduces complex shock/vortex interactions particularly at moderate to high angles of incidence. These interactions have a significant effect on vortex breakdown and the breakdown behaviour is quite different to that witnessed for subsonic vortical flows where the onset of breakdown is relatively gradual with increasing incidence [72]. An interaction between the rear/terminating shock, described in Section 1.4, and the primary vortex has been found, in some cases, to cause breakdown [17, 123] and with

increasing incidence this shock can jump upstream quite abruptly. The upstream shift of the shock is likely to occur in reaction to changes in the flow behaviour [17], such as adverse pressure gradient, caused by an increase in incidence. If the conditions are sufficient that the shock/vortex interaction causes breakdown, the sudden upstream movement of the shock will also cause the breakdown location to move upstream. This can cause the location of breakdown to shift upstream by as much as 30% of the chord in a single 1^o incidence interval [18, 121].

From the literature it has also been noted that it is possible for a terminating shock system to exist without the breakdown of the vortical system [17] particularly at lower angles of incidence. Whether an interaction occurs in this case is not well understood. From the study of the interaction between longitudinal vortices and normal shocks in supersonic flow [130] it has been found that it is possible for a vortex to pass through a normal shock without being weakened sufficiently to cause breakdown. However, the flow over slender delta wings is more complex as the shock does not appear to be normal to the freestream in the vortex core region [17]. Therefore, further investigation is needed to consider the behaviour and onset of vortex breakdown, particularly with respect to shock/vortex interactions.

It is clear from consideration of the literature that the change in flow behaviour with increasing Mach number is quite considerable, with the occurrence and movement of shocks in the flow and the possibility of abrupt shock-induced breakdown. This has obvious detrimental effects on the aerodynamic performance of the wing. Aerodynamic characteristics such as lift coefficient distribution, stall and pitch may all be badly affected by such flow behaviour. Therefore, understanding this behaviour is important, particularly for fighter configurations, such as Eurofighter and JSF, which will perform manoeuvres at transonic Mach numbers.

Therefore, to consider this behaviour, the flow over a sharp leading edged, slender delta wing was considered under subsonic and transonic conditions. This investigation was undertaken as part of the 2nd International Vortex Flow Experiment (VFE-2), a facet of the NATO RTO AVT-113 Task Group, which was set up to consider the flow behaviour both experimentally and computationally over a specified 65^o delta wing geometry. The work of the VFE-2 continues on from the first International Vortex Flow Experiment (VFE-1) [181] carried out in the late eighties, which was used to validate the inviscid CFD codes of the time. Much progress has been made in both experimental and computational aerodynamics, particularly in turbulence models since the conclusion of the VFE-1. Therefore, it was proposed by Hummel and Redecker [182] that a second experiment should be undertaken to provide a new, comprehensive database of results for various test conditions and flow behaviours, to further the understanding of vortical flows. The test conditions considered under the VFE-2 framework include both subsonic and transonic Mach numbers for low, medium and high angles of incidence at a range of Reynolds numbers [183].

For this investigation two test conditions were analysed from the cases specified by the VFE-2, at a single Reynolds number, $Re = 6 \times 10^6$. Both subsonic, $M = 0.4$, and transonic flow conditions, $M = 0.85$ will be considered, with emphasis on the behaviour of the transonic vortical flow. Two angles of incidence are used for consideration, which correspond to pre- and post-breakdown flow behaviour, $\alpha = 18.5^o$ and 23^o. Further details of the test case, geometry and calculation set up will be given in the following section, before analysis of the subsonic and transonic calculations are detailed. For the transonic conditions, from consideration of the literature, it is found that both these cases fall within the regions where it is highly likely that cross-flow and rear shocks will occur in the flow. Therefore, the occurrence of these shocks are analysed. Comparisons between each of the calculations and with available experimental data are made and consideration of the sensitivity of the flow behaviour to a number of computational factors, such as grid refinement detailed. A comparison to other numerical investigations from the VFE-2 will also detailed, before consideration of shock/vortex interaction and the occurrence of vortex breakdown over the wing is undertaken. Finally the results are discussed and conclusions made with respect to the discussion given above.

3.2 Summary of Test Case

The geometry used for the VFE-2 is originally from experiments carried out by Chu and Luckring [20, 132, 133, 134] in the National Transonic Facility (NTF) at NASA Langley. These experiments considered a 65^o delta wing with four leading edge profiles (one sharp and three rounded with small, medium and large radii) for a wide range of conditions both subsonic and transonic and for both test and flight Reynolds numbers. This data has been compiled into a comprehensive experimental database and forms the basis for the investigations of the VFE-2. The geometry is analytically defined for all leading edge profiles. Both the medium radius and sharp leading edge profiles are considered within VFE-2, however, for this investigation, only the sharp leading edge profile is considered. Figure 3.2 shows the wing situated in the NTF wind tunnel and a brief overview of the analytical dimensions of the wing.

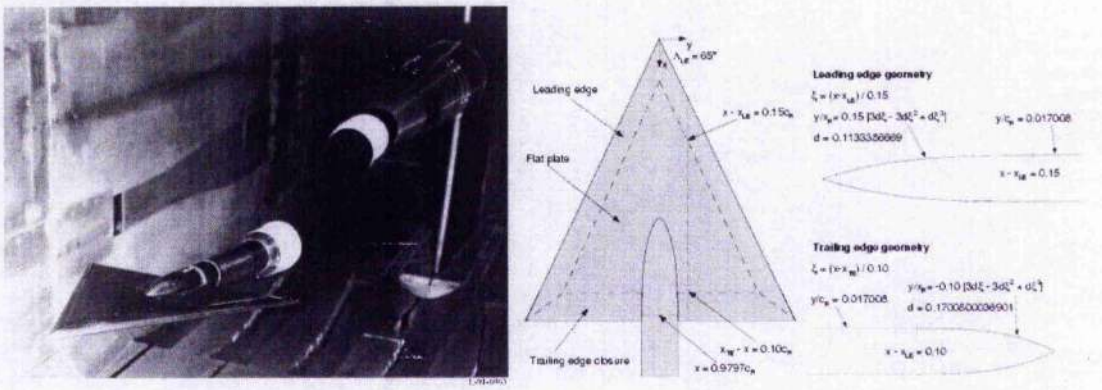

(a) Wing in NTF facility at NASA Langley [20]

(b) Analytical definition of wing data [184]

Figure 3.2: VFE-2 65^o delta wing geometry used in investigation

All calculations performed were steady state and used the $k-\omega$ turbulence model with P_ω Enhancer [158]. This model is detailed and discussed with reference to its use for vortical flow in Chapter 2. It has been well validated against experiment for similar sub- and transonic steady vortical flow calculations [144, 158, 159].

3.2.1 Grid Generation

One of the most important issues for computational flow calculations is grid generation and establishing the dependence of the solution on the grid. There have been many investigations considering various aspects of grid generation particularly for delta wing flows [153, 154, 156, 185, 186, 187]. From these investigations the importance of having a grid which is suitably refined in the regions of interest, in order to accurately capture the most important and influential flow features over the wing, is apparent. These areas include, for a delta wing, the boundary layer, the shear layer region and the leading edge vortex core. Other factors which have been highlighted are: grid topology, cell skewness, wall spacing and overall grid refinement and distribution.

The structured multi-block grids used in this investigation were manually created using the ICEMCFD mesh generation package, *Hexa*. The computational model consists of the semi-span wing, reproduced from the analytical definition. The sting was also reproduced to approximately one chord length downstream of the trailing edge, based on the recommendations of Allan *et al.* [71], who found that the effect of a sting or support apparatus was negligible beyond this location. Downstream, an approximation to the experimental sting was defined to the far field, which was defined as $20c_r$ in each direction from the wing apex to minimise the effect of the boundaries on the results.

An H-H topology was chosen with a collapsed edge at the apex of the wing. In order to allow for a smooth grid point distribution and refinement of the grid, a structured Ogrid was used around the sting. An example of this and the surface blocking topology is shown in Figure 3.3. Overall, the blocking structure was optimised for reduced skewness, particularly in the sting tip region and as a result a total of 353 blocks was used. Based on this block topology, two grids were created for this investigation with varying refinement. These are classed as coarse and fine with the important details of each grid summarised in Table 3.1. The nominal y^+ value is based on the first wall spacing and the Reynolds number of the flow and may vary slightly over the surface of the wing. A comparison of the relative refinement of the grid on a plane upstream of the sting blocking at $x/c_r = 0.5$ is shown in Figure 3.4. Each grid distribution allowed for an efficient load balance of grid points across the optimum number of processors used for the calculations.

			Nominal	*Number of Points on Wing Surface*		
Type	***Grid Size***	***Wall Spacing***	y^+	***Streamwise @ LE***	***Spanwise @ TE***	***Normal***
Coarse	2,451,314	$\sim 2 \times 10^{-5} c_r$	~ 4.4	117	171	49
Fine	6,993,522	$1 \times 10^{-5} c_r$	2.2	170	228	81

Table 3.1: Summary of main features of grids used for VFE-2 investigation

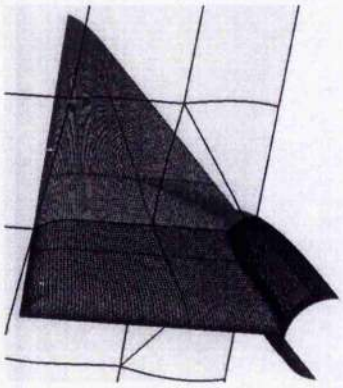

Figure 3.3: Surface mesh and ogrid topology around sting region for 65^o VFE-2 delta wing

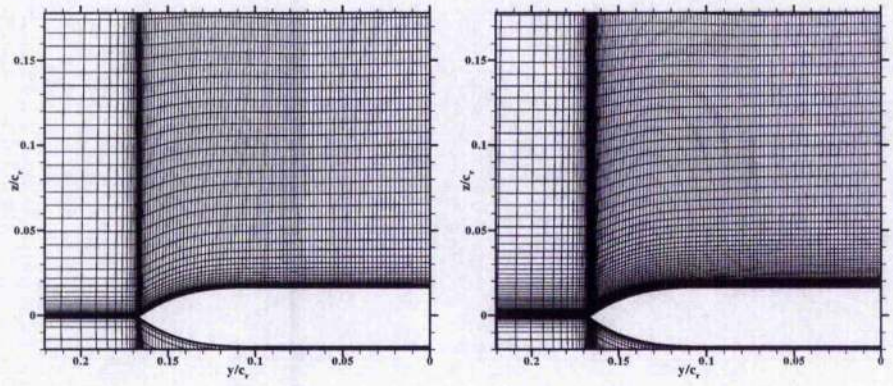

(a) Coarse Grid (b) Fine Grid

Figure 3.4: Comparison of grid refinement at $x/c_r = 0.5$

3.2.2 Transition Treatment

Convergence issues associated with the apex singularity of the H-H grid, mentioned above, are dealt with by fixing a transition from laminar to turbulent flow downstream of the apex in the computational domain. Transition was applied at various constant streamwise locations $x = 0.1 - 0.4$ to consider the effect on the flow behaviour for both the subsonic and transonic conditions. From this analysis, it was found that the subsonic results were highly sensitive to transition location, with the optimum solution being obtained for $x = 0.1$ ($x/c_r = 0.10154$ on the wing surface). However, the transonic results were not found to be sensitive and thus, the transition was set to $x = 0.4$, which corresponds to $x/c_r = 0.406125$ on the wing upper surface.

3.3 Subsonic Vortical Flow: Results

As stated in the introduction to this chapter, both subsonic and transonic cases were considered within the VFE-2 framework for the sharp leading edge wing. Although the main purpose of this study is to consider the transonic behaviour of vortical flow and vortex breakdown on the wing, it is also important to consider the behaviour under subsonic conditions. This will allow for further validation of the CFD solutions and therefore greater confidence in the the predicted flow behaviour for the more complex transonic flow. Two angles of incidence were considered - 18.5^o and 23^o at a Mach number of $M = 0.4$ and Reynolds number of 6 million. As mentioned previously, these conditions correspond to pre- and post-breakdown flow behaviour for this geometry. All results were obtained on the fine grid as detailed in Table 3.1.

To allow validation of all computational results, comparisons were made with the NASA NTF experimental pressure coefficient distributions at five streamwise locations on the wing surface, $x/c_r = 0.2$, 0.4, 0.6, 0.8 and 0.95, shown in Figure 3.5. It is clear that the agreement between the computational solutions and the experiments are

very good. For most streamwise locations, the position and magnitude of the suction peaks are well predicted for both angles of incidence. Surface contours of pressure coefficient are also shown, which clearly show the extent of the primary peak and also the existence of secondary vortices close to the leading edge. From the spanwise distributions, the suction peak due to the secondary vortices is much clearer than shown for the experimental results. The comparable strength of this region is evident from slight differences in primary peak location for $\alpha = 18.5^o$. This shows the computational suction peak located slightly inboard compared to the experimental data, suggesting that the secondary vortices are larger for the computational results. However, this does not appear to be the case for $\alpha = 23^o$.

At $\alpha = 23^o$, breakdown occurs on the wing. However, agreement with the experiments is still good in the post-breakdown region, with only a slight under-prediction of the suction peak magnitudes. This suggests that breakdown may be slightly more severe in the computational results than in the experiment. An interaction between the breakdown region and the surface of the wing is apparent from the surface contours of pressure coefficient shown in Figure 3.5, where a small low pressure region is found downstream of the breakdown location.

Figure 3.6 shows contours of x vorticity and u velocity at streamwise slices over the wing, which allows the structure of the flow to be seen clearly. In each of the plots the vortex core trajectory is defined. Considering the 18.5^o case first, it is clear that breakdown does not occur and that the primary vortex core is strong and relatively straight over the wing. The contours of x vorticity also show the presence of the strong secondary vortex system, described previously. From analysis of the axial velocity of the vortex core, it was found that the axial flow accelerates up to a maximum of $1.95U_\infty$ at $x/c_r = 0.9$ after which it appears to decelerate. This deceleration of the vortex core may be caused by the highly curved nature of the trailing edge geometry. Also clear is an area of stagnant flow and the apparent breakdown of the secondary vortex. It is possible that this unusual behaviour is caused by the rounded nature of the trailing edge and the intersection between the leading edge and trailing edge curvature.

Comparing the contour plots for the pre-breakdown flow to those for $\alpha = 23^o$, shows that the size and strength of the vortices increase with increasing incidence. It is also found that the distance between the vortex core and wing surface increases. The spiral behaviour of the vortex breakdown is obvious from the vortex core trajectory with the expansion of the vortex core and the flow reversal shown clearly by the contours of u velocity. Upstream of breakdown the maximum axial velocity within the vortex core was found to be approximately $2.2U_\infty$, which is almost a 12% increase on the pre-breakdown case. The location of vortex breakdown, taken as the location on the vortex core where the axial flow stagnates, $U_{axial} = 0$, is approximately $x/c_r = 0.775$. For the higher incidence, the secondary vortex is also clear from the flow structure. A third vortex core trajectory is also evident, which appears to intersect regions of higher vorticity in the shear layer.

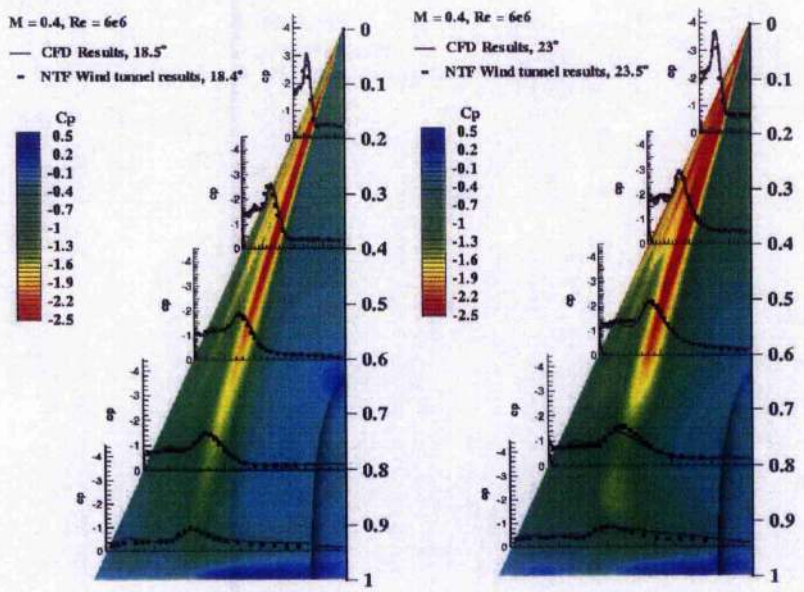

(a) 18.5^o (b) 23^o

Figure 3.5: Computational results compared to experimental data, $M = 0.4$, $Re = 6 \times 10^6$

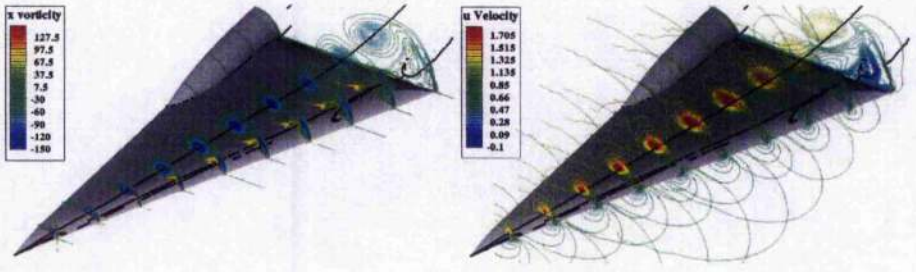

(a) 18.5^o

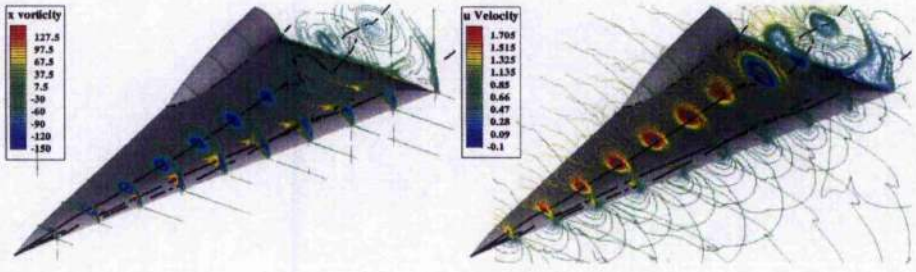

(b) 23^o

Figure 3.6: Contours of x vorticity and u velocity on slices through the vortex core for $\alpha = 18.5^o$ and 23^o - $M = 0.4$ and $Re = 6 \times 10^6$

To allow further validation of the results, the subsonic solutions from this investigation were also compared to results generated by other institutions as part of the VFE-2. Figure 3.7 shows comparisons of the surface pressure coefficient distributions with results obtained by NLR and EADS-MAS. Details of the grids, turbulence models and flow solvers used for these results are given in Ref. [188] and summarised in Section 3.6. It is clear from these plots that there is close agreement between the computational results, with only slight differences in the size of the primary and secondary suction peaks. Further details and comparisons between the current work and the results from these institutions will be given in a later section detailing the transonic flow behaviour.

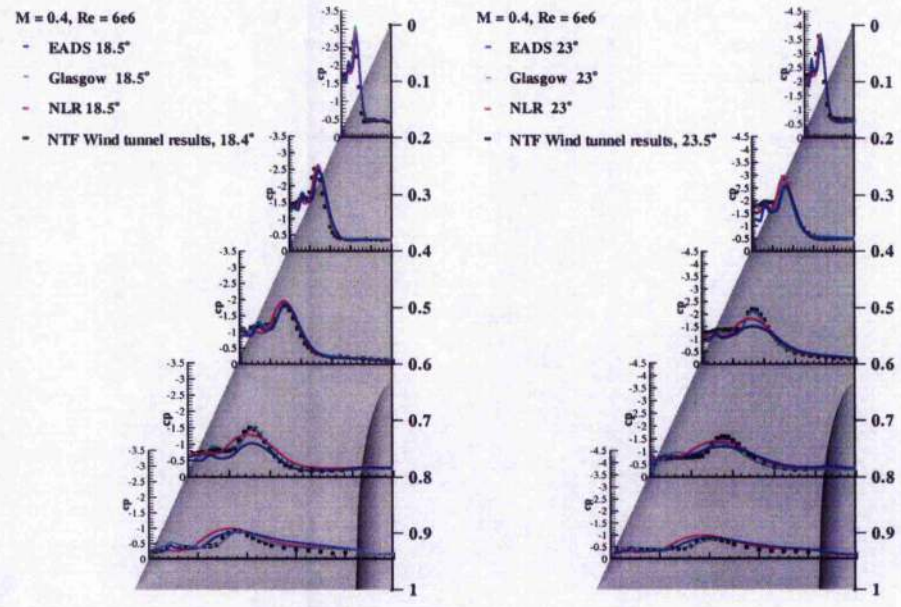

(a) 18.5^o

(b) 23^o

Figure 3.7: Comparison of computational results and experimental data, $M = 0.4$ and $Re = 6 \times 10^6$

3.4 Transonic Vortical Flow: Results

The calculations performed to consider the transonic regime correspond to conditions, $M = 0.85$, a Reynolds number of $Re = 6 \times 10^6$ at the same angles of incidence, $\alpha = 18.5^o$ and 23^o. As before, all results were obtained on the fine grid. However, the effect of grid refinement will be considered and is detailed in a subsequent section. As the main purpose of this investigation is to consider the behaviour of transonic vortical flow, the results will be considered in more detail than the subsonic results. The results at each incidence will, initially, be considered separately under the headings pre- and post-breakdown flow.

3.4.1 Pre-Breakdown Flow - $M = 0.85$, $\alpha = 18.5^o$

The computational results and corresponding NASA NTF experimental data [20] for $\alpha = 18.5^o$, are shown in Figure 3.8. At this incidence, it is clear that, overall, the agreement between the results is good. For most streamwise locations, the magnitudes and positions of the suction peaks are well predicted. Although, as with the subsonic results, there does seem to be a consistent over-prediction of the secondary vortex peak, which appears to lessen with increased distance from the apex. This is not related to the location of forced transition as it was found from investigation, that the overall flow behaviour was insensitive to transition location and the strength of the secondary vortex was relatively unchanged.

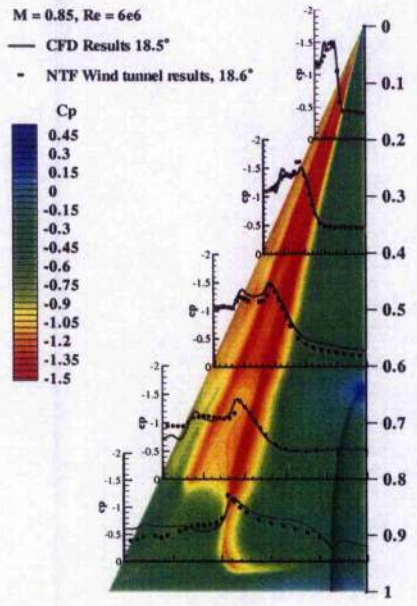

Figure 3.8: Computational results compared to experimental data, $\alpha = 18.5^o$, $M = 0.85$ and $Re = 6 \times 10^6$

Contours of surface pressure coefficient, are also shown in Figure 3.8. These clearly show the primary and secondary suction peaks and their behaviour. Downstream of $x/c_r = 0.8$, it appears that the secondary vortex disappears and the primary vortex curves inboard toward the sting region at the trailing edge. This is also clear from consideration of the pressure coefficient distributions, which show a flat distribution outboard of the primary vortex for $x/c_r = 0.95$. The axial velocity through the vortex cores was analysed and it was found that the secondary vortex breaks down in this region as it approaches the trailing edge, as shown in Figure 3.9. From this plot, it is evident that the secondary vortex breaks down at approximately $x/c_r = 0.85$, however, the primary vortex does not. This behaviour is very similar to that observed for the subsonic case and, thus, may also be due to the geometry in this region. From Figure 3.9 it is clear that the maximum axial velocity of the primary vortex is approximately $1.7U_\infty$ which corresponds to a maximum local Mach number of 1.8 and indeed the axial flow in the secondary vortex is also supersonic upstream of breakdown. Thus, it may also be suggested that this location coincides with the presence of a shock in the flow and that a type of shock/vortex interaction is occurring. However, if this is the case, the primary vortex is largely unaffected by the interaction. Further consideration of this region and analysis of the flow solutions is needed to determine the causes of this behaviour. Analysis and discussion of the presence of shocks and shock/vortex interactions will be given in a later section.

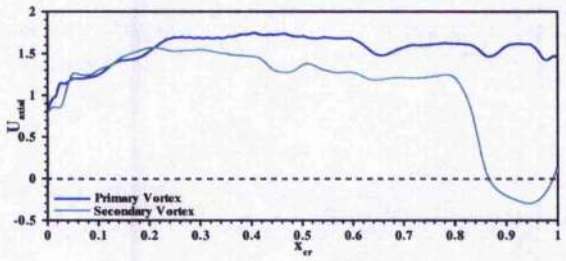

Figure 3.9: Axial velocity through primary and secondary vortex cores, $\alpha = 18.5^o$, $M = 0.85$ and $Re = 6 \times 10^6$

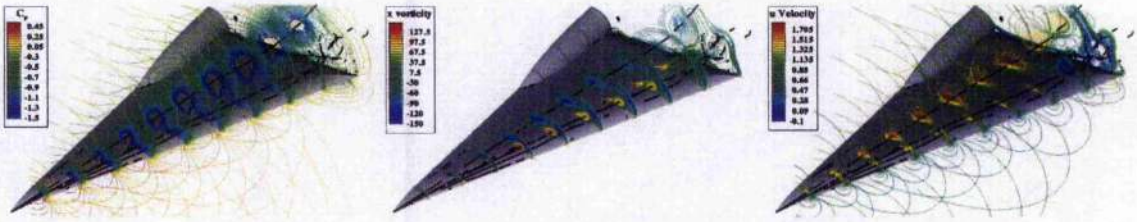

(a) Pressure coefficient (b) x vorticity (c) u velocity

Figure 3.10: Contours of x vorticity and u velocity on slices through the vortex core for 18.5^o, $M = 0.85$ and $Re = 6 \times 10^6$

The flow structure of the leading edge vortices was considered from the plots shown in Figure 3.10 with contours of pressure coefficient, x vorticity and u velocity used to aid in the understanding of the behaviour of the three dimensional flow. From consideration of the contours of pressure coefficient, it is clear that the vortex cores have a quite uneven shape, particularly in comparison to the subsonic vortices which are quite round and uniform in the pre-breakdown flow. The vortices are also closer to the wing surface. From examination of the x vorticity contours, it is found that the vortex system is relatively flat and elongated over the wing surface. Closer to the apex of the wing, a tertiary vortex is found under the secondary vortex. Analysis of the contours of u velocity and the vortex core trajectories, also confirms the occurrence of the secondary vortex breakdown between the streamwise positions of $x/c_r = 0.8$ and 0.9 with a large region of reversed flow occurring outboard of the primary vortex. A fourth vortical region, with the same sign as the the primary vortex is found outboard of the primary vortex within the shear layer. Its location is virtually constant at each streamwise positions, until the secondary vortex breaks down, where it moves upward, away from the leading edge region.

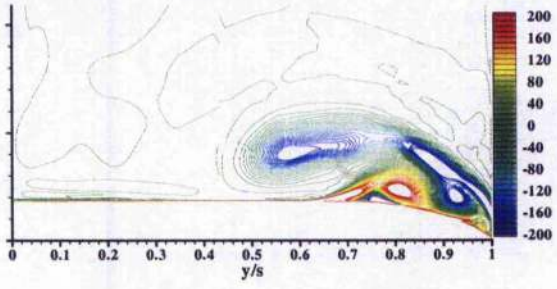

Figure 3.11: Contours of x vorticity at a position $x/c_r = 0.4$ for $\alpha = 18.5^o$, $M = 0.85$ and $Re = 6 \times 10^6$

The vortex core structure can be further considered by examining a single slice through the vortex core. Figure 3.11 shows contours of x vorticity on a slice of the domain at the streamwise location, $x/c_r = 0.4$. At this location, both secondary and tertiary separation regions are found and the large size and strength of the secondary vortex is evident. Outboard of the secondary vortex, the fourth vortical region mentioned above is clear. Initially it was thought that this small region of vorticity may be evidence of a shear layer instability. However, its behaviour is not the same as the shear layer structures described in Chapter 1 due to the steady nature of the solution. Further analysis suggests that the structure is caused by an interaction of the secondary vortex and the shear layer. This will be caused by the close proximity of the primary vortex to the surface of the wing and the over-predicted strength

of the secondary vortex, which would cause high velocities in this region. Outboard of the vortex, on the wing surface, a much smaller region of vorticity is found, which suggests that the boundary layer separates again under the influence of this region.

3.4.2 Post-Breakdown Flow - $M = 0.85$, $\alpha = 23^o$

As before, the pressure coefficient distributions are compared in Figure 3.12. From these comparisons, it is clear that close to the apex of the wing i.e. $x/c_r = 0.2$ and 0.4, the agreement is good, with the magnitude and location of the primary and secondary peaks being predicted well. However, downstream of the $x/c_r = 0.4$ location, the computational results show large discrepancies with the $\alpha = 23.6^o$ experimental results. From consideration of the behaviour of transonic vortex breakdown described in Section 1.4 and the surface pressure coefficient contours, it is clear that these discrepancies are due to vortex breakdown occurring on the wing. Analysis of the NASA NTF experimental data has shown that vortex breakdown occurs at an incidence of 24.6^o, which is the next test point in the data set. These results are also included in Figure 3.12 and show a much improved agreement with the computational results. Therefore, it may be concluded that the vortex breakdown behaviour is predicted well. However, discrepancies exist in the prediction of the critical onset angle. Further consideration of this will be given in a later section.

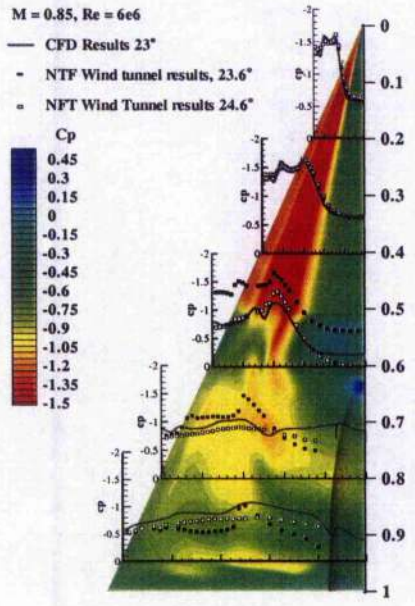

Figure 3.12: Computational results compared to experimental data, $\alpha = 23^o$, $M = 0.85$ and $Re = 6 \times 10^6$

From the surface pressure coefficient contours, the abrupt nature of vortex breakdown is evident. Upstream it is clear that the vortex system is coherent and strong, however, the vortices disappear quite suddenly. This is quite unlike the vortex breakdown found for the subsonic case. The axial velocity through the primary vortex core (Figure 3.13) also shows the almost immediate onset of breakdown, which occurs at approximately $x/c_r = 0.57$. Comparing the axial flow to the $\alpha = 18.5^o$ case shows that the maximum axial velocity has increased to approximately $1.8U_\infty$. Therefore, as expected, the vortices have increased in strength.

The three-dimensional behaviour of the flow can be seen in the plots of Figure 3.14, which are similar to those shown for the pre-breakdown case in Figure 3.10 . Compared to the results for 18.5^o it is clear that the size of the vortex core upstream of breakdown has increased in diameter, however, the vortices still have a very elongated shape. The region downstream of breakdown is also relatively flat against the surface of the wing, possibly caused by the high freestream velocity limiting the growth of such a structure into the flow. The fourth vortical structure found in the pre-breakdown flow, is also found for this case upstream of breakdown at a constant location outboard of the primary vortex. At the breakdown of the secondary vortex, which also occurs slightly upstream of the primary vortex for this case, this vortex is swept upward away from the leading edge and entrained into the post-breakdown flow.

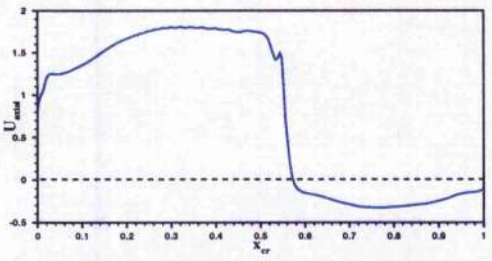

Figure 3.13: Axial velocity through vortex core for post-breakdown flow, $\alpha = 23^o$, $M = 0.85$ and $Re = 6 \times 10^6$

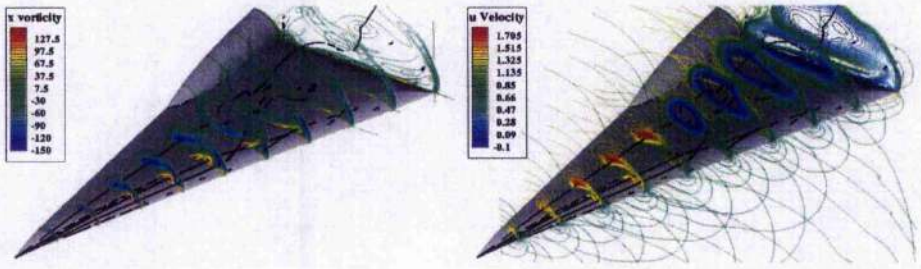

(a) x vorticity (b) u velocity

Figure 3.14: Flow structure for $\alpha = 23^o$, $M = 0.85$ and $Re = 6 \times 10^6$

3.5 Occurrence of Shocks in the Flow

As detailed in the literature review in Section 1.4, it is expected that a number of shock systems will be present for these conditions. Care was taken to analyse the flow solutions described in the previous section to determine the occurrence, location and behaviour of shockwaves in the flow. The method of analysis used was described in Chapter 2 and allowed the interpretation of both shocks occurring in the cross-flow and those normal to the flow direction and wing surface. Each of these shocks will be considered separately in this section.

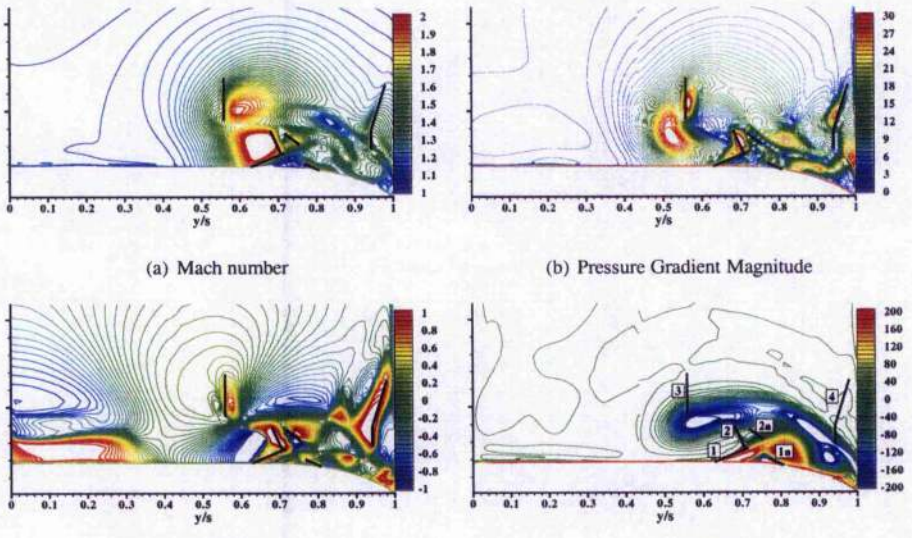

(a) Mach number (b) Pressure Gradient Magnitude

(c) Shock feature (d) x vorticity

Figure 3.15: Plots for $x/c_r = 0.4$ showing contours of flow variables to highlight locations of cross flow shocks for $\alpha = 18.5^o$, $M = 0.85$ and $Re = 6 \times 10^6$

3.5.1 Cross-Flow Shocks

Evidence of a complex cross-flow shock system for both angles of incidence, beneath and around the primary and secondary vortices was found from consideration of the flow structure in a spanwise cut using the methods described previously. An example of this flow behaviour at $x/c_r = 0.4$ and the plots used for determination of the shock locations for the pre-breakdown case is shown in Figure 3.15. Each of the identified shock locations are marked on the variable contour plots.

The determination of the first of these cross flow shocks, denoted by [1] in Figure 3.15(d), was aided by consideration of the pressure coefficient distributions and surface contours shown in Figures 3.8 and 3.12 in the previous sections. In these plots it was found that outboard of the primary vortex suction peak, sharp changes in pressure coefficient are found. These sharp changes in pressure coefficient may indicate the presence of a shock in the flow as described in Section 1.4 and shown in Figure 1.20(a). It is clear from the surface pressure coefficient contours and was also indicated from analysing multiple slices through the domain (not detailed here), that this shock occurs in the flow for a constant non-dimensional spanwise location, defining a conical ray from the apex of the wing. These locations are approximately $y/s = 0.64$ for the $\alpha = 18.5^o$ solution and $y/s = 0.62$ for the $\alpha = 23^o$ solution. With closer inspection, it was found that coinciding with the location of this shock close to the wing, the boundary layer thickens and separates to form a strong secondary vortex as shown in Figure 3.16.

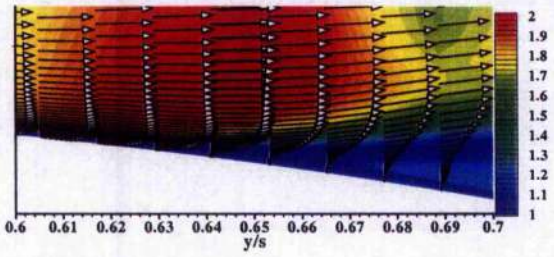

Figure 3.16: Velocity vectors and contours of Mach number at chordwise station $x/c_r = 0.2$ showing secondary separation for $\alpha = 18.5^o$, $M = 0.85$ and $Re = 6 \times 10^6$

A second sharp increase in pressure coefficient was also found outboard of the secondary vortex in the pressure coefficient surface contours as described before. Again, as before, a small shock can be found in the cross-flow planes corresponding to this location and denoted by [1a] in Figure 3.15(d). This shock is likely to be caused by a similar mechanism as shock [1], but occurs under the secondary vortex with the cross-flow travelling toward the centreline of the wing. Inboard of this location a small tertiary vortex system is found and it is supposed that the separation is again caused by the adverse pressure gradient associated with the shock. As with shock [1], the shock is conical and has a constant spanwise location of $y/s = 0.82$ for both $\alpha = 18.5^o$ and $\alpha = 23^o$ angles of incidence. It should be noted that while it is proposed in this work that regions [1] and [1a] correspond to the locations of shocks in the flow, it is difficult to confirm this conclusively. There remains a possibility that these shocks are in fact strong compression regions, which are causing the separation of the flow. Further work, both experimentally and computationally are needed to confirm this.

Between the secondary separation region and the primary vortex, the spanwise flow behaves in a similar manner to that in a convergent-divergent duct and accelerates to supersonic conditions. At some point, the flow can no longer maintain these high velocities and a shock appears to decelerate the flow. This is likely to be the cause of shocks [2] and [2a] in Figure 3.15(d). Shock [2a] appears to occur due to the flow accelerating again beyond shock [2]. It is not clear at this point whether shock [1] and shock [2] are connected or interact. However, it appears that they sit very close and it is possible that shock [2] is a stronger continuation of shock [1]. If this is indeed the case, the resulting shock curves upward from the surface to the primary vortex, as suggested by the diagram of Figure 1.20(a). From the literature, it is known that a shock sits in the region between the primary vortex and the surface of the wing [121, 122]. However, there is little existing data which confirms the shape of this shock.

Two other shocks were found to occur in the cross-flow. Shock [3] is found to sit above the primary vortex and is similar to that found in the computations of Gordnier and Visbal [125] and Shock [4] sits above the primary shear layer, close to the leading edge. Both these shocks are likely to be caused by the curvature of the shear layer causing the flow to accelerate up to conditions which cannot be sustained. All these shocks were also found to

occur for the $\alpha = 23^o$ case, although the majority of the shock locations are different due to the inboard movement and relative increase in size of the vortical system. This is shown in Figure 3.17.

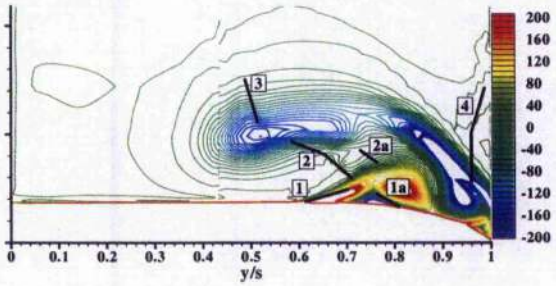

Figure 3.17: Contours of x vorticity on a $x/c_r = 0.4$ plane, highlighting locations of cross flow shocks for $\alpha = 23^o$, $M = 0.85$ and $Re = 6 \times 10^6$

3.5.2 Normal Shocks

Normal shocks are also found to occur in this flow, and are identified by plotting the pressure coefficient along the symmetry plane as shown in Figure 3.18 for both angles of incidence. For the 18.5^o case, it is clear that two normal shocks occur at the symmetry plane. The first occurs upstream of the sting tip at approximately $x/c_r = 0.6$, which is most likely to be caused by the sting geometry. Further downstream at approximately $x/c_r = 0.85$ a second shock is found. This second shock is likely to corresponds to the rear/terminating shock as described in the literature [17, 18, 129] for similar conditions. A third compression region is also found close to the trailing edge, and a third shock is found from the surface pressure contours at this location outboard of the symmetry plane on the wing surface. A shock occurring at this location is likely to be caused by the high curvature of the wing geometry and the necessity of the flow to return to freestream conditions at the trailing edge.

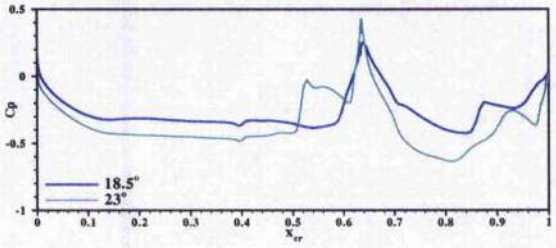

Figure 3.18: Pressure coefficient distribution at the symmetry plane on the wing for both angles of incidence

As the incidence is increased and vortex breakdown occurs on the wing, the behaviour at the symmetry plane, again, shows the shock at the sting tip at approximately $x/c_r = 0.6$. However, another shock is also found in the flow slightly upstream of this location at about $x/c_r = 0.52$. Downstream of the sting tip, it is evident that the rear/terminating shock described for the $\alpha = 18.5^o$ case is no longer present. From the behaviour described in the investigations of Elsenaar and Hoeijmakers [18] under similar conditions, it is possible that the new shock upstream of the sting tip is the rear/terminating shock having undergone an upstream shift with the increase of incidence. However, due to the presence of the sting and the shock caused by this geometry, it not possible to state this conclusively. As before, it is found that three normal shocks occur at the symmetry plane and close to the trailing edge, as also found in the experiments, a second normal shock is observed. This is likely to be the same trailing edge shock as found for $\alpha = 18.5^o$.

Considering the three-dimensional behaviour of the normal shocks, it is found that the shock occurring upstream of the sting tip curves downstream and intersects the rolled up shear layer of the vortex as shown in Figure 3.19 and highlighted by the dashed lines. This is also in agreement with the observations of Donohoe and Bannink [17] and the schematic shown in Figure 1.20(b) for the rear/terminating shock. However, it is likely that this curvature is caused by the sting presence for this configuration. Also highlighted are the locations of the other normal shocks described above. The rear/terminating shock in the 18.5^o solution is found to be normal to the freestream and wing surface and does not appear to curve downstream outboard of the symmetry plane. This lack of curvature may be due to the influence of the sting on the flow, as previous investigations have considered a flat wing without sting

support [17]. Also clear from this plot are the two cross-flow shocks which sit above the vortex described above (3 and 4 from Figures 3.15 and 3.17). It is possible, for both angles of incidence, that there is an interaction between these cross-flow shocks and the normal sting tip shock, which will further increase the complexity of the flow in this region. However, further experimental data is needed in this region to determine this behaviour.

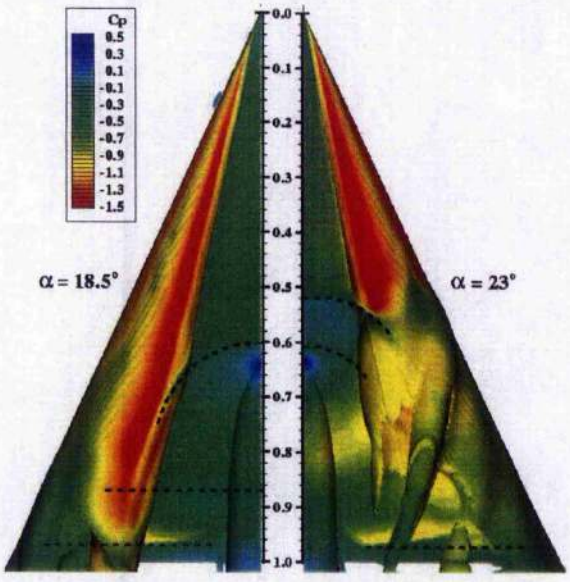

Figure 3.19: Isosurface of x vorticity coloured by pressure coefficient showing primary vortex shear layer and normal shock shape for both angles of incidence

3.6 CFD Sensitivity Study

As has been shown in the previous sections, the agreement with the experimental data is good for the pre- and post breakdown flow, however the critical incidence for vortex breakdown on the wing is not predicted well. Due to the presence of the shocks in the flow, it is quite likely that this flow will be more sensitive to computational factors than a subsonic flow and this must be checked in order to improve confidence in the solutions. In this section, a number of parameters will be considered. These include grid issues such as refinement and type, turbulence modelling, convergence and time accuracy issues. For all cases, with the exception of the effect of grid refinement, only the post-breakdown case, $\alpha = 23^o$, for conditions $M = 0.85$ and $Re = 6 \times 10^6$ will be considered.

To allow further analysis of various aspects of the flow behaviour, comparisons were made with calculations performed by other institutions as part of the VFE-2. These institutions are EADS Military Air Systems (EADS-MAS) and NLR using structured, multi-block grids and the United States Air Force Academy (USAFA) using an unstructured grid. Each institution uses its own well-validated 3D RANS flow solver; *FLOWer 116.17* at EADS-MAS [189], *ENSOLV* at NLR [190, 191, 192] and *Cobalt* at USAFA [193], respectively. Comparisons between the structured flow solvers and PMB at Glasgow University have been made in the past [194]. Detailed descriptions of each of these flow solvers, computational set-up and grids used in the structured grid comparisons can be found in Ref. [188] and are summarised along with the current investigation details in Table 3.2.

		Size	*No. of Grid Points on Wing*			
Institution	***Topology***	$\times 10^6$	***Spanwise***	***Streamwise***	***Normal***	***Turbulence Model***
EADS	C-O	~ 10.6	129	257	129	Wilcox k-ω and Reynolds Stress Model
NLR	C-O	~ 4	192	112	96	TNT k-ω with P_ω Enhancer
Current Investigation	H-H with O-grid	~ 7	170	228	81	Wilcox k-ω with P_ω Enhancer and NLEVM

Table 3.2: Summary of grids and turbulence models used for VFE-2 structured grid comparisons

The effect of time accuracy is considered by comparing the current solutions to calculations performed by USAFA using the Spalart-Allmaras DES turbulence treatment on a unstructured grid. The grid used had approximately 7.89×10^6 cells and an average first wall spacing of $y^+ = 0.68$, created specifically for a Reynolds number of 6×10^6. It was refined within the vortex core region to improve the grid for the application of DES. The grid structure at the symmetry plane is shown in Figure 3.20. The time step was defined as $\Delta t = 5 \times 10^{-6}$ seconds, which corresponds to a non-dimensional time step of $\Delta\tau \approx 0.0047$. The calculation was allowed to run for approximately 20600 time steps, which results in a total time of approximately 0.1 seconds. For these comparisons, both instantaneous and time averaged (mean) solutions were necessary and thus, a time averaged file was created over a total of 4000 time steps.

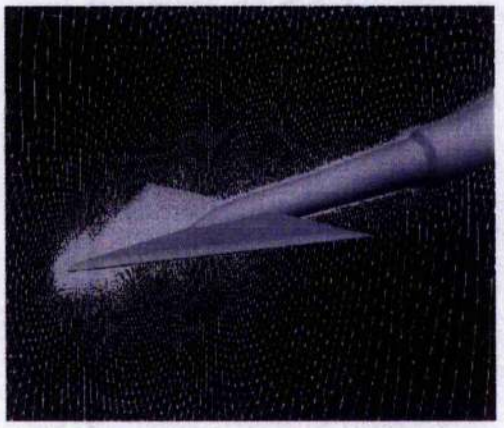

Figure 3.20: USAFA grid at symmetry plane

3.6.1 Effect of Grid Refinement

As stated, the effect of grid refinement was considered for both pre- and post-breakdown flow for the transonic conditions. In this study, the solutions detailed previously for the fine grid are compared to results obtained using the coarse grid described in Section 3.2.1. Comparisons of the surface pressure coefficient distributions for both angles of incidence with the relevant experimental data are shown in Figure 3.21.

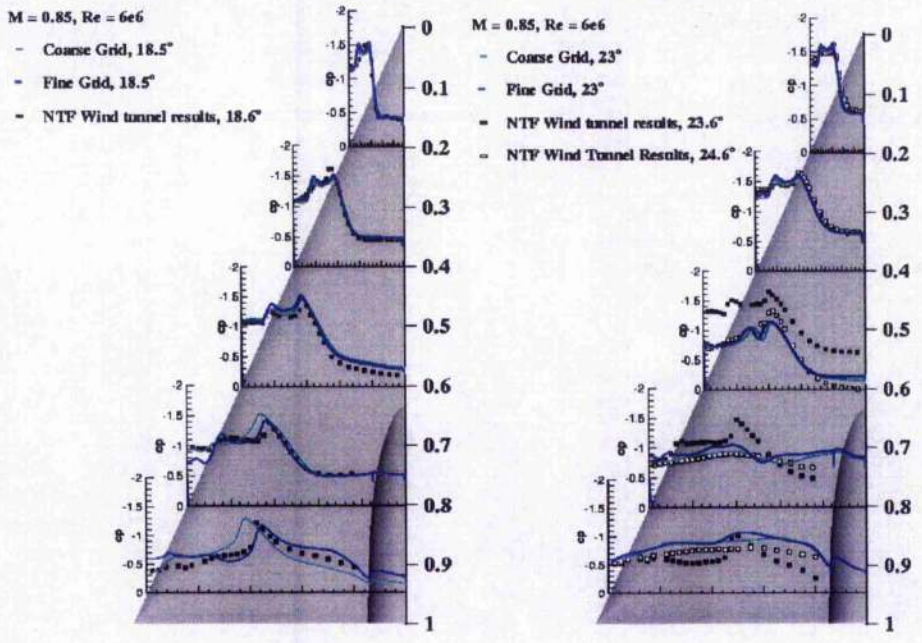

(a) 18.5^o (b) 23^o

Figure 3.21: Comparison between the H-H grids for transonic conditions at $\alpha = 18.5^o$ and 23^o

Considering both angles of incidence, it is clear that there are a number of differences between the solutions on the two grids, particularly in the trailing edge region. Close to the apex, agreement is good for both cases, with the fine grid giving slightly higher suction peaks than the coarse grid. In this region, both primary and secondary vortex suction peaks are clear and coincide for both grids, up to $x/c_r = 0.6$ for $\alpha = 18.5^o$ and $x/c_r = 0.4$ for $\alpha = 23^o$. Downstream of these locations, the differences in the distributions become more pronounced. For $\alpha = 18.5^o$, at $x/c_r = 0.8$, the pressure coefficient distribution shows that the fine grid gives better agreement with the experimental data. It is clear from the under-prediction of the pressure gradients that the coarse grid is not resolving the cross-flow shocks as well as the fine grid, as expected. Similar behaviour is shown at $x/c_r = 0.95$, where the cross-flow shock region is much further outboard and the suction peak is over-predicted. For $\alpha = 23^o$, downstream of breakdown, the agreement between the two grids is close, with a similar reduction in suction peak found at $x/c_r = 0.6$ and similar flat distributions obvious downstream of this location.

Further comparisons can be made from the pressure coefficient contours on the wing surface, shown in Figure 3.22. For the pre-breakdown case, these plots emphasise the smearing of the gradients on the coarse grid, with the primary vortex suction peak being much broader. Also evident is the behaviour of the secondary vortex which does not appear to have such an obvious breakdown location in contrast to the fine grid. Considering the post-breakdown case, the differences between the two solutions are, again, harder to determine. The behaviour of the vortex breakdown is almost identical, with the location of the normal shock upstream of the sting tip coinciding. It is likely that as with the pre-breakdown case, the shocks in the flow are more smeared for the coarse grid, however this does not appear to have a significant effect on the flow behaviour and the occurrence of vortex breakdown.

Figure 3.23 shows the axial velocity through the primary vortex cores for both cases. It is clear that with the increase in grid refinement, the axial velocity increases by approximately $30\%U_\infty$ for both cases. This increase in axial velocity is expected and is most likely to be due to the improved refinement of the vortex core region. For the post-breakdown case, the onset and behaviour of breakdown is evident from this plot. It is clear that the onset of breakdown occurs at roughly the same point over the wing ($x/c_r = 0.57$ for the fine grid and $x/c_r = 0.58$ for the coarse grid).

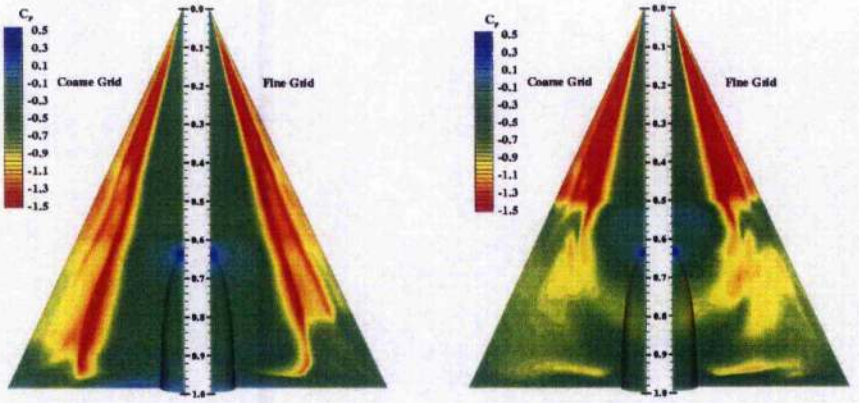

(a) 18.5^o (b) 23^o

Figure 3.22: Surface contours of pressure coefficient for comparison between the H-H grids

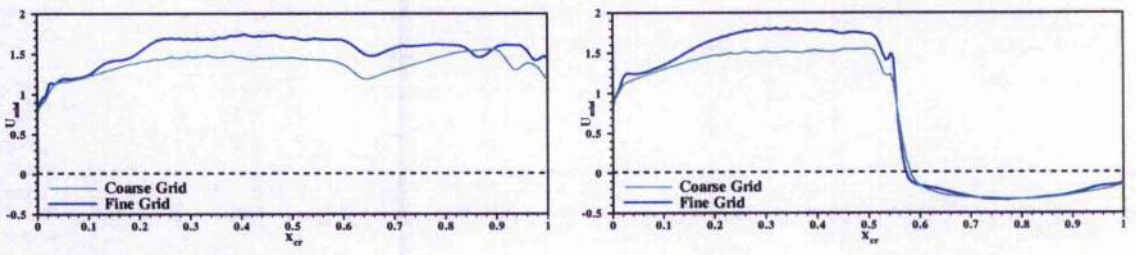

(a) 18.5^o (b) 23^o

Figure 3.23: Comparison of axial velocity through the vortex cores for coarse and fine grid solutions

The differences in vortex core resolution are also shown by analysing contours of x vorticity on a cross-flow plane. Figure 3.24 shows a cross-flow slice at $x/c_r = 0.4$, for both grids at $\alpha = 18.5^o$. It is clear from these plots that the fine grid predicts a much more compact vortical system than the coarse grid. Both the primary and secondary vortices are stronger for the fine grid solutions and as a result the outboard vortical region in the shear layer is not found on the coarse grid. Tertiary vortices are found for both cases and in general the location of each of the vortices is the same for both grids. Similar comparisons were also made for the post-breakdown case, but are not shown.

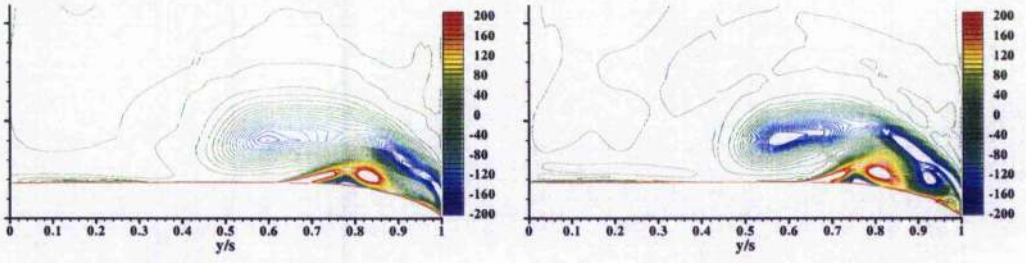

(a) Coarse grid

(b) Fine grid

Figure 3.24: Contours of x vorticity at chordwise station $x/c_r = 0.4$ at 18.5^o

This study has shown that the behaviour and location of vortex breakdown within transonic flow are not greatly affected by the grid refinement carried out. It is also evident that the critical angle for vortex breakdown onset is independent of grid refinement, as vortex breakdown is predicted to occur early for both grids.

3.6.2 Effect of Turbulence Model

The effect of turbulence model on the flow behaviour was considered by comparing the results detailed in the previous sections, calculated using the $k-\omega$ with P_ω Enhancer model to results obtained using the Non-Linear Eddy Viscosity model for the post-breakdown incidence, $\alpha = 23^o$. The Non-Linear Eddy Viscosity model calculation was performed using the same flow conditions as before and was started from the end of the $k-\omega$ with P_ω Enhancer calculation discussed in the previous sections. It was run for the same number of total iterations using the same calculation parameters. Further consideration of the effect of turbulence model will be obtained from a similar study carried out by EADS-MAS for the same case, comparing the standard Wilcox $k-\omega$ and a Reynolds Stress model (RSM).

Considering the current results first. The surface pressure coefficient distributions are compared for each turbulence model and to the relevant experimental data as shown in Figure 3.25(a). It is clear that close to the apex, at $x/c_r = 0.2$ and 0.4, the agreement between the distributions is very good. However, downstream at $x/c_r = 0.6$ there is a significant difference in the pressure coefficient distributions. The Non-Linear Eddy Viscosity model predicts behaviour which is still in good agreement with the experimental data for the 23.6^o data point, which suggests that at this location breakdown has not yet occurred. Whereas for the original results, it was found that breakdown occurred at $x/c_r = 0.57$, therefore this streamwise location is downstream of breakdown and the agreement with the 24.6^o experimental data is good, where breakdown also occurs on the wing. Further downstream, by $x/c_r = 0.8$, it is clear that vortex breakdown has occurred for the Non-Linear Eddy Viscosity solution, although inboard there is still some agreement with the experimental results for $\alpha = 23.6^o$. There is little agreement with the results for the $k-\omega$ with P_ω Enhancer model, which as described previously, shows a very flat distribution downstream of breakdown. This difference in solution behaviour continues downsteam.

Further evidence of the differences between the two solutions can be obtained from direct comparison of contours of the surface pressure coefficient for the whole wing. These are shown in Figure 3.26(a). It is evident from this plot that the location of breakdown is quite different for each solution. From analysis of the vortex core behaviour it was found that the location of vortex breakdown for the Non-Linear Eddy Viscosity model was $14\%c_r$ further downstream at $x/c_r = 0.71$. However, upstream of breakdown, it was found that the solution were in good agreement, with the same axial velocity being predicted and a similar vortex structure, as described for the original results in the previous section, for the Non-Linear Eddy Viscosity model results. The location of shocks within the flow was relatively similar for the Non-Linear Eddy Viscosity results, with cross-flow shocks appearing in the flow as previously described. A normal shock was found to occur slightly upstream of the sting tip, however a second shock upstream of this location was not found for this case. Downstream close to the trailing edge, a third

normal shock is also apparent, which is in agreement with the results predicted for the $k-\omega$ with P_ω Enhancer model solutions. Therefore, from these comparisons, it appears that the choice of turbulence model influences the location of breakdown, but the general behaviour of the flow is relatively unchanged, particularly upstream of breakdown.

A similar analysis was carried out on the results from the EADS investigation, which shows that there is little difference in the solutions predicted by the Wilcox $k-\omega$ and RSM turbulence models. From the surface pressure distributions in Figure 3.25(b), it is clear that the predicted behaviour is similar with the main differences occurring at $x/c_r = 0.6$, outboard in the secondary vortex location. Vortex breakdown occurs slightly downstream of this location for both cases, at approximately $x/c_r = 0.68$ for the Wilcox $k-\omega$ model and at approximately $x/c_r = 0.70$ for the RSM. This slight difference in location may explain the discrepancy in the secondary vortex prediction at $x/c_r = 0.6$, which is not found to be significant to the overall flow behaviour. Downstream of breakdown, differences in the pressure coefficient distributions are apparent, but the agreement with the 24.6^o experimental data point is relatively good for both models. Further evidence of the similarities between the flow solution is found from the contours of surface pressure coefficient shown in Figure 3.26(b). This highlights the slight change in location of the breakdown but confirms the overall agreement in the behaviour on the wing surface. It is clear that the agreement downstream of breakdown is much better for these results compared to the current results, however the change in breakdown location is not as significant.

Therefore, it may be concluded that main effect of the choice of turbulence model is in the predicted location of the breakdown. The differences found in the flow solution appear to originate with this change and not in differences of fundamental flow behaviour. Each model still predicts breakdown to occur on the wing at an incidence which is lower than that witnessed in the experiment, thus, it may also be concluded that the critical angle for breakdown to occur on the wing is unaffeced by turbulence model.

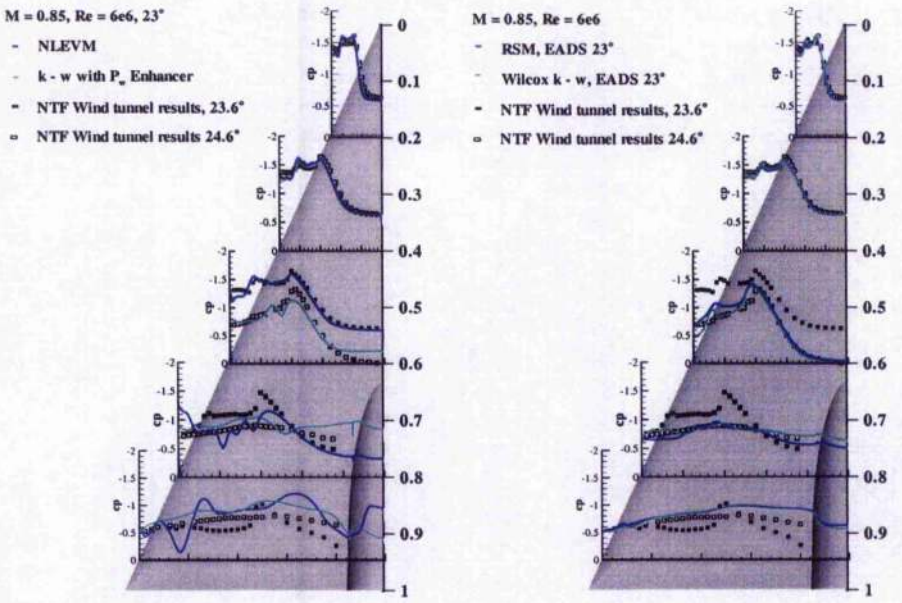

(a) Comparison between NLEVM and $k-\omega$ with P_ω Enhancer model (Current Results)

(b) Comparison between RSM and Wilcox $k-\omega$ model (EADS-MAS Results)

Figure 3.25: Effect of turbulence model on flow solution with comparison to experiment for $M = 0.85$, $Re = 6 \times 10^6$ and $\alpha = 23^o$

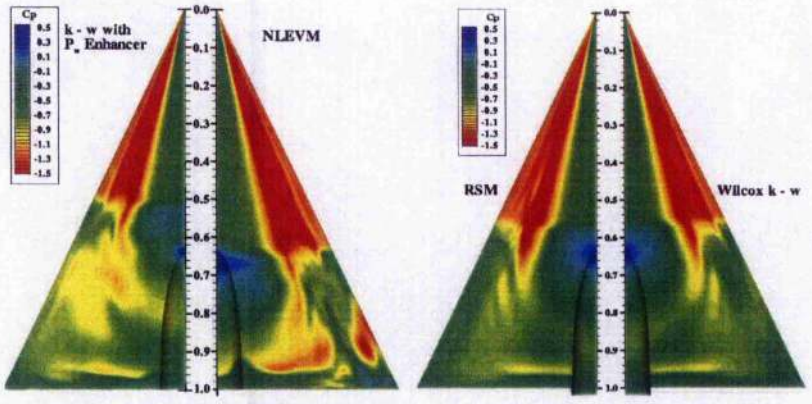

(a) Comparison between NLEVM and k-$\omega$with P_ω Enhancer model (Current Results)

(b) Comparison between RSM and Wilcox k-ω model (EADS-MAS Results)

Figure 3.26: Contours of surface pressure coefficient showing effect of turbulence model on flow solution with comparison to experiment for $\alpha = 23^o$, $M = 0.85$ and $Re = 6 \times 10^6$

3.6.3 Effect of Solution Convergence

As stated in the previous section, the Non-Linear Eddy Viscosity model was started from the end of the original $k - \omega$ with P_ω Enhancer model solution discussed in the previous sections. Due to this restart, it is important to consider the effect of convergence on the flow solutions, particularly in order to strengthen the conclusions made in the previous section and to determine if the restart would have an effect on the solution. To perform this investigation, the original calculation was again restarted, using the same turbulence model and run for an additional 4500 implicit time steps. Figure 3.27 shows the convergence history of the original and restarted calculations. The residual is the index of the error in the numerical computations, therefore by reducing the residual by one, the error reduces in size by an order of magnitude. The plot shows the residual for the mean flow computations (lower trace) and the turbulence model computations (upper trace). It is clear that for the original calculation, the residual reduces rapidly then begins oscillating in an irregular manner, which dies down, before reaching its final values of $10^{-2.75}$ and $10^{-3.7}$. With the restarted calculation, it is evident that the behaviour of the residuals becomes more periodic in nature, however the unsteadiness does not disappear. The residuals are found to oscillate about mean values of approximately $10^{-2.8}$ and $10^{-3.8}$, which are not significantly lower than the final values of the initial calculation.

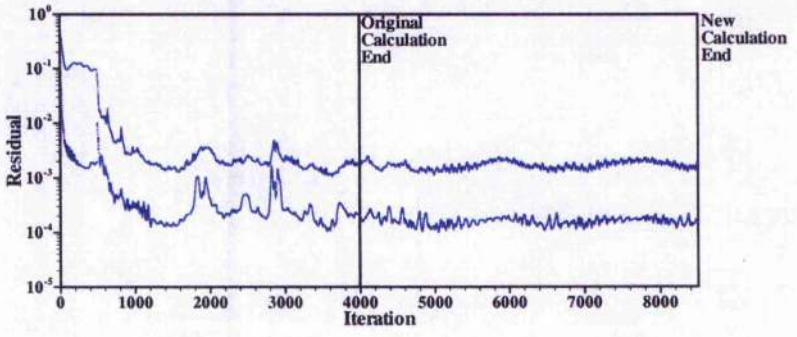

Figure 3.27: Convergence history of residuals for $k - \omega$ with P_ω Enhancer model; $\alpha = 23^o$, $M = 0.85$ and $Re = 6 \times 10^6$

Considering the results of the restarted calculation and the original results shown in the previous sections. Figure 3.28 shows the surface pressure coefficient distributions for both solutions at streamwise stations compared to the relevant experimental results. As with all other comparisons, it is clear that there is little effect on the flow close to the apex region at $x/c_r = 0.2$ and 0.4. Downstream at $x/c_r = 0.6$, the overall behaviour of the distribution is similar with a reduction in suction peak compared to the pre-breakdown experimental data point ($\alpha = 23.6^o$). However, the inboard distribution has a lower pressure coefficient distribution and the suction peak is higher for the restarted calculation results. These results give an improved agreement with the $\alpha = 24.6^o$ experimental data. In the original results, the breakdown location was found to be slightly upstream of this location, at $x/c_r = 0.57$ and it is clear that breakdown will be close to this region for the restarted results. Downstream, it is evident that the

overall flow behaviour has not changed significantly with increased convergence with a relatively flat distribution of surface pressure coefficient found for both solutions at $x/c_r = 0.8$ and 0.95.

From the contours of surface pressure coefficient for each solution, shown in Figure 3.29, it is clear that the breakdown location is further downstream for the restarted calculation solution. From analysis of the vortex core behaviour this location was found to correspond to approximately $x/c_r = 0.64$, which is a $7\%c_r$ downstream shift. As with the original calculation, the breakdown location is downstream of a normal shock, however only one shock occurs in this region. It is clear that downstream of the location of the normal shock that a suction peak continues for both solutions, however it appears to last longer for the restarted calculation solution. Upstream of breakdown the flow behaviour predicted is almost identical, with the same axial velocity found in the vortex core. The shockwaves described for the original results are also found for the restarted calculation, as expected, with the only exception being the second normal shock upstream of the sting tip, as mentioned. Therefore, it may be concluded that the most obvious effect of increasing the calculation run time and thus of the convergence of the solution, is to shift the breakdown location further downstream. This may also suggest that the large difference in breakdown location between the Non-Linear Eddy Viscosity model and the original results, detailed in the previous section, is partly due to the effect of turbulence model and partly due to the effect of the convergence behaviour at the end of the calculation.

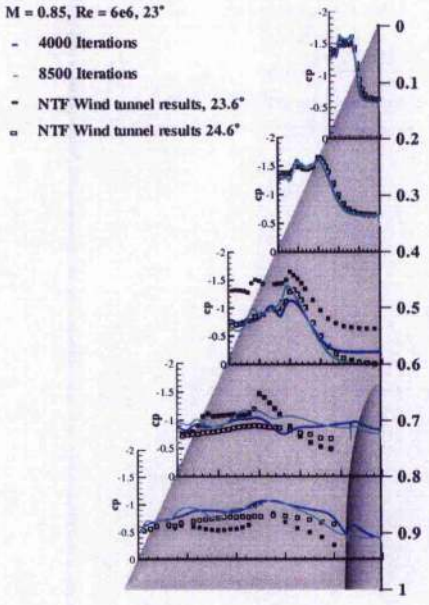

Figure 3.28: Effect of turbulence model on flow solution with comparison to experiment for $\alpha = 23^o$, $M = 0.85$ and $Re = 6 \times 10^6$

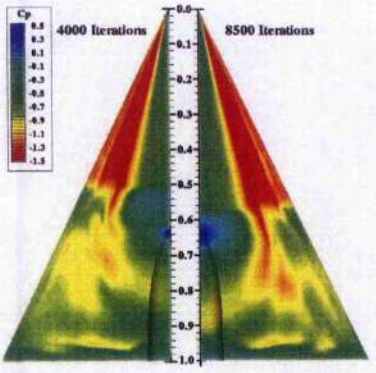

Figure 3.29: Contours of surface pressure coefficient showing effect of turbulence model on flow solution with comparison to experiment for $M = 0.85$, $Re = 6 \times 10^6$ and $\alpha = 23^o$;

From further analysis, it was found that despite the difference in breakdown location, the overall flow behaviour of the further converged solution was very similar to the original calculation results detailed in the previous sections. As this calculation has been shown to have an improved convergence behaviour, the new solution will be used for the comparisons and analysis in the following sections.

3.6.4 Comparison with Other Structured Grid Results

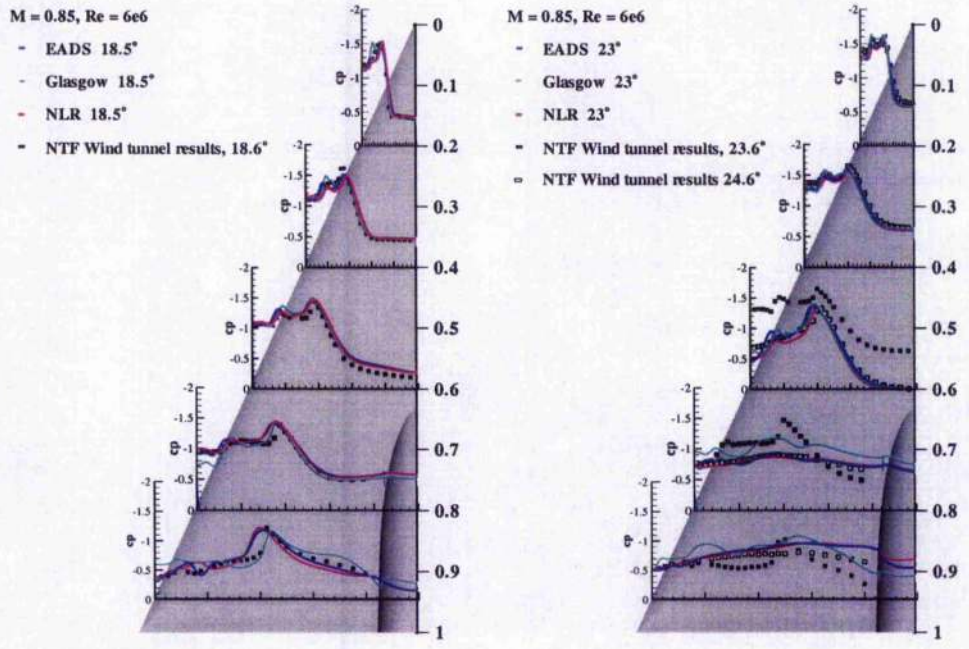

(a) Pre-breakdown case, $\alpha = 18.5^o$

(b) Post-breakdown case, $\alpha = 23^o$

Figure 3.30: Comparisons between computational results and experiment for all codes for $M = 0.85$, $Re = 6 \times 10^6$

Comparisons were made with the structured grid results of EADS-MAS and NLR as described previously, to further consider the validity of the solutions presented. Referring to the pre-breakdown case first in Figure 3.30(a), it is clear that the agreement between the computational results and the experimental data is good. As discussed in Section 3.4, the current results predict a secondary vortex which is slightly too strong compared to the experimental data. However, it is clear that the EADS-MAS and NLR solutions predict vortices which are much weaker and have suction peaks less than the experimental values. These discrepancies may be attributed to differences in transition treatment, with both EADS-MAS and NLR running fully turbulent calculations compared to the current results which has a forced transition from laminar to turbulent flow at $x = 0.4$. Downstream close to the trailing edge at $x/c_r = 0.95$, the agreement between each of the computational solutions lessens. Both the EADS-MAS and NLR solutions predict the suction peak and sudden increase in pressure further outboard than both the experiment and the current results. This is likely to be due to grid refinement and topology in this region as both the EADS-MAS and NLR grids use a conical C-O topology and Glasgow uses an H-H grid, which is more refined close to the trailing edge. This behaviour is also clear from the surface pressure coefficient distributions of Figure 3.31. For each solution, the location of the vortical system is the same with a well defined primary and secondary vortex. The secondary vortex breakdown as described before is evident for both the EADS-MAS and NLR solutions, however it occurs further downstream for both cases. This supports the suggestion that the secondary vortex breakdown may be caused by a shock/vortex interaction.

For $\alpha = 23^o$, it is clear from Figure 3.30(b) that close to the apex of the wing i.e. $x/c_r = 0.2$ and 0.4, the agreement between all the computational solutions and the experimental data is good, with the magnitude and location of the primary and secondary peaks being predicted well. As before, for the pre-breakdown case, the secondary vortex is slightly stronger for the current results compared to the EADS-MAS and NLR solutions. Downstream, vortex breakdown occurs for all solutions and the flow exhibits good agreement with the experimental post-breakdown flow. However, it is evident from the surface pressure coefficient contour plots that the location of vortex breakdown is different for each solution.

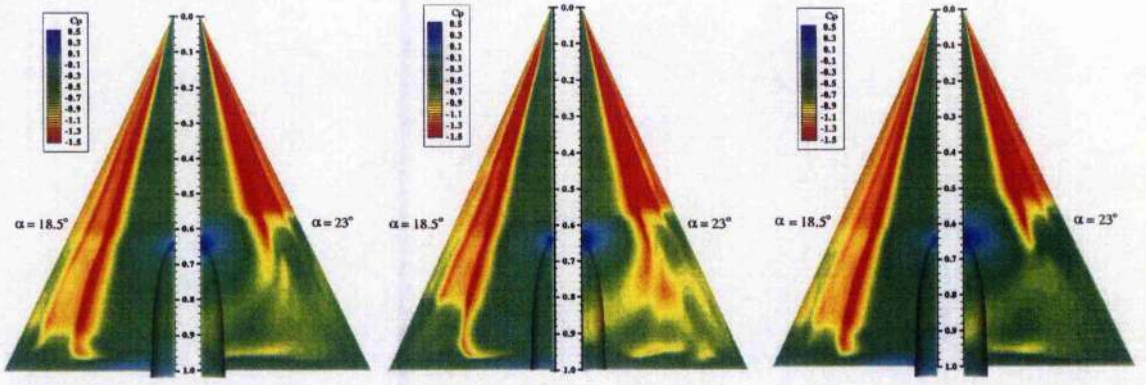

(a) EADS-MAS (b) Glasgow (c) NLR

Figure 3.31: Surface pressure coefficient contours for all codes, $M = 0.85$, $Re = 6 \times 10^6$

Figure 3.32 shows the behaviour of the axial velocity through the vortex core and the location of vortex breakdown is clear for each of the solutions. The locations for vortex breakdown for this case corresponds to approximately $x/c_r = 0.68$ for EADS-MAS, $x/c_r = 0.67$ for NLR and $x/c_r = 0.64$ for the current results. Upstream of the breakdown location, it is clear that there is some difference in the predicted maximum axial velocities, caused by differences in grid resolution or turbulence models used.

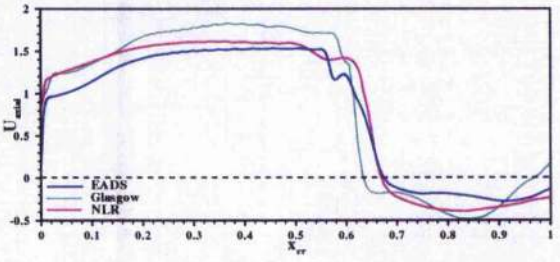

Figure 3.32: Axial velocity through primary vortex core for all codes $\alpha = 23^o$, $M = 0.85$, $Re = 6 \times 10^6$

As before, consideration was given to the flow on a slice through the vortex core at a constant streamwise location, $x/c_r = 0.4$, shown in Figure 3.33 for each solution. In each plot, the elongation of the primary vortex is clear and the position of the vortex cores is almost identical. Both secondary and tertiary separation regions occur in the flow at this location for all solutions. Outboard of the secondary vortex, the thickening of the shear layer region is found in all three solutions, however the strength of this region appears to be directly linked to the relative strength of the secondary vortex. With the strong secondary vortex for the current results producing a fourth vortical region, as discussed previously.

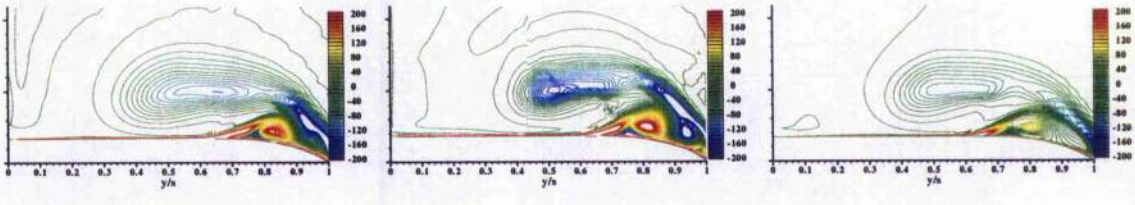

(a) EADS-MAS (b) Glasgow (c) NLR

Figure 3.33: Contours of x vorticity at $x/c_r = 0.4$ for all results, $\alpha = 23^o$, $M = 0.85$, $Re = 6 \times 10^6$

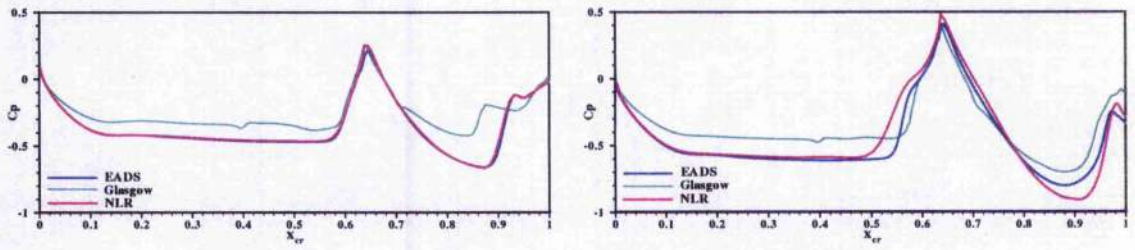

(a) 18.5^o (b) 23^o

Figure 3.34: Pressure coefficient distribution at the symmetry plane on the wing

The locations of the normal shocks in the flow solutions are also slightly different for each solution. The pressure coefficient at the symmetry plane is shown in Figure 3.18 for each set of results. For the pre-breakdown case, the sting tip shock is evident for all cases at approximately $x/c_r = 0.64$, however the location and strength of the rear/terminating shock downstream differs between results. This shock occurs at approximately $x/c_r = 0.9$ in the EADS-MAS and NLR results and earlier at $x/c_r = 0.85$ in the current results. The differences in strength and location of this shocks is likely to be due to the nature of the grids in this region. At an incidence of 23^o, the behaviour of the solutions at the symmetry plane, again, shows the shock at the sting tip at approximately $x/c_r = 0.6$, but this time it appears that a second shock occurs in the flow slightly upstream of this location. However, the compression of these two shocks appears to merge into one for all solutions. The difference in shock strength is likely to be caused by variations in grid refinement, particularly in the axial direction, which will cause varying shock resolutions. Despite the variation of shock strength, the locations of these shocks are very similar with the upstream shock occurring at about $x/c_r = 0.52$ for the NLR results, $x/c_r = 0.56$ for the EADS-MAS results and slightly downstream at $x/c_r = 0.58$ for the current results .

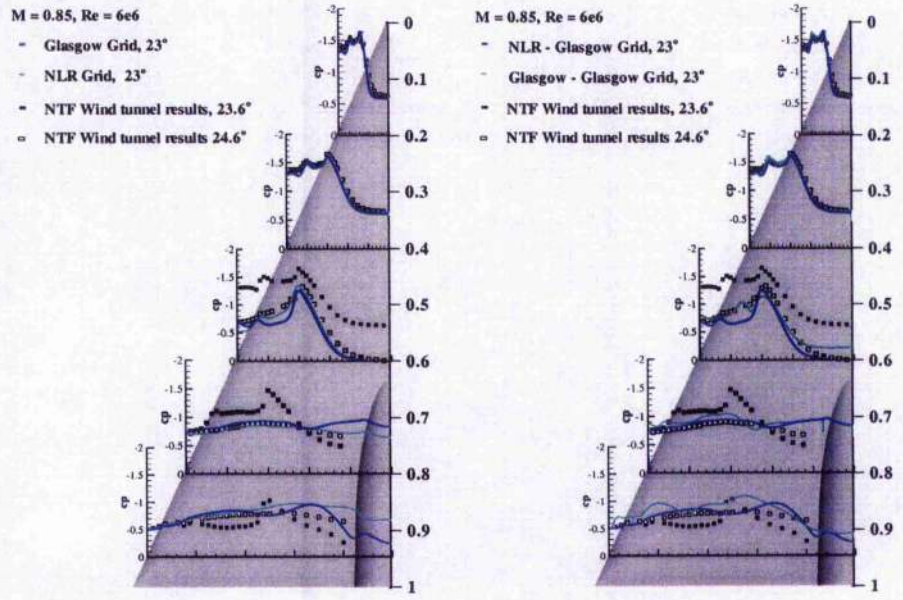

(a) Effect of grid topology (b) Effect of common grid

Figure 3.35: Effect of grid on flow solution with comparison to experiment for $\alpha = 23^o$, $M = 0.85$ and $Re = 6 \times 10^6$; a) Comparison between results from Glasgow and NLR grids (NLR Results); b) Comparison between Glasgow results and NLR results on common grid using similar turbulence model.

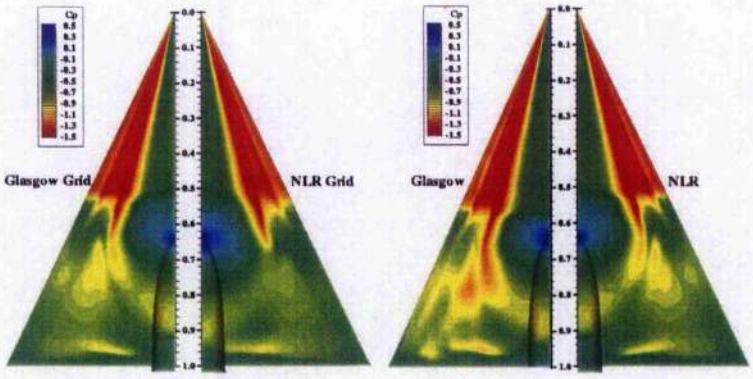

(a) Effect of grid topology (b) Effect of common grid

Figure 3.36: Contours of surface pressure coefficient showing effect of grid on flow solution with comparison to experiment for $M = 0.85$, $Re = 6 \times 10^6$ and $\alpha = 23^o$; a) Comparison between results from Glasgow and NLR grids (NLR Results); b) Comparison between Glasgow and NLR results on common grid using similar turbulence models.

To further aid in the comparisons between each of the computational solutions consideration was given to the effect of grid topology. This was considered by running the same solver and turbulence model on two of the grids with differing topologies. These were the fine H-H grid as described in Section 3.2.1 and NLR's C-O grid. It is clear from Tables 3.1 and 3.2 that the overall sizes of the grids are quite different. However, this is mostly due to the topology and chosen far-field definitions and it is found that the number of grid points over the wing surface is similar for both the normal and spanwise direction. The results of this comparison are shown in Figures 3.35 and 3.36. The pressure coefficient distributions show very little difference between the solutions, both upstream and downstream of breakdown. Considering the pressure coefficient contours, it is clear that the apparent strength of the normal shock and the suction peaks of the vortical system in the region of this shock are different. This is most likely to be due to differences in axial grid refinement rather than the topology of the grids.

A comparison between the solutions for the Glasgow and NLR CFD solvers on a common grid was also performed. The turbulence models used by these two institutions are similar, with the difference mainly in the specification of the turbulence model diffusion coefficients [195]. It is clear that the solutions are very similar. This is also true of the surface pressure coefficient contour plots for this case, although a slight difference in the predicted breakdown location is clear. This is likely to be due to the level of convergence of the solutions as a comparison of the NLR results with the original calculation described in Sections 3.4 and 3.5, shows no difference in breakdown location.

3.6.5 Influence of Time Accuracy

All the computations described so far have assumed that the flow is steady state. However, it is clear from the literature discussed in Chapter 1, particularly for the post-breakdown case, that the flow will be highly unsteady. Therefore, it is necessary to consider the effect of time accuracy on the solutions and the behaviour of the flow. In order to consider this, comparisons were made with an unsteady calculation, for the same transonic conditions, carried out by the United States Air Force Academy (USAFA) as part of the VFE-2.

Figure 3.37 shows the comparison of surface pressure coefficient distributions for the time averaged USAFA solutions and the steady state Glasgow solution. From this plot it is clear that close to the apex, at $x/c_r = 0.2$ and 0.4, the agreement between the time averaged and steady state solutions is good. However, downstream where the leading edge vortex has broken down, large differences between the flow solutions are found. At $x/c_r = 0.6$, the time averaged solution shows good agreement with the post-breakdown experimental data inboard close to the symmetry plane, but outboard of the primary suction peak large secondary suction peak is evident at this station, suggesting that the secondary vortex is still present. The steady state solution also displays a small peak in this region which suggests that a very weak secondary vortex may still occur at this location. Further downstream, the time accurate result behaves slightly different to the steady state solution and post-breakdown experimental results, and appears to be slightly closer to the experimental results for the 23.6^o experimental data point. Vortex breakdown can be confirmed to occur in the flow by considering the surface pressure coefficient contours shown in Figure 3.38.

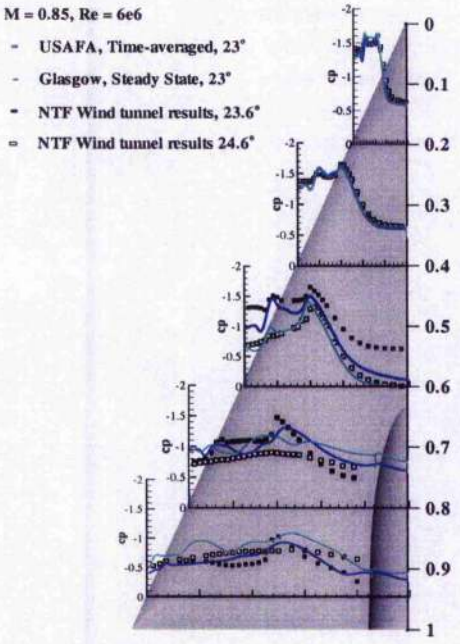

Figure 3.37: Comparisons between computational results and experiment for current results and USAFA time accurate solutions for $\alpha = 23^o$, $M = 0.85$, $Re = 6 \times 10^6$

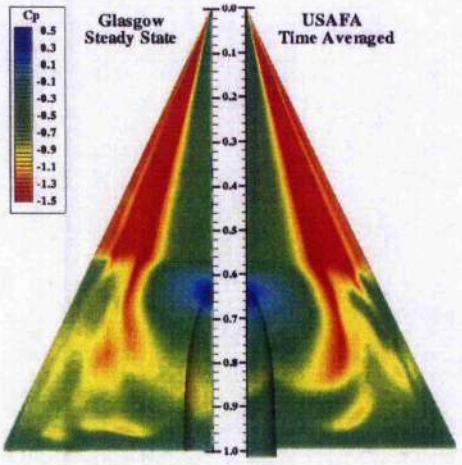

Figure 3.38: Surface pressure coefficient contours comparing USAFA time averaged results with steady state current results, $\alpha = 23^o$, $M = 0.85$, $Re = 6 \times 10^6$

From Figure 3.38, it is evident that the behaviour of the flow upstream of vortex breakdown is very similar. However, the steady state result predicts vortex breakdown slightly further upstream than the time averaged solution, $x/c_r = 0.64$ for the steady state solutions compared to $x/c_r = 0.68$ for the time averaged results. Downstream of breakdown the solutions are again similar, however the suction peak which is found downstream of breakdown exists for approximately $25\%c_r$ in the time accurate result and only about $15\%c_r$ for the steady state result. This behaviour is confirmed by considering the axial velocity through the vortex cores for each case, as shown in Figure 3.39. From this plot, it is again clear that the steady state solution predicts breakdown further upstream than the time accurate solution. However, the levels of axial velocity upstream of vortex breakdown are similar. Further consideration of this behaviour will be given in the following section.

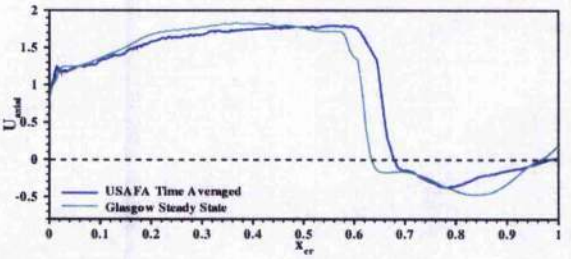

Figure 3.39: Comparisons between computational results and experiment for current steady state results and USAFA time accurate solutions for $\alpha = 23^o$, $M = 0.85$, $Re = 6 \times 10^6$

Considering the three-dimensional behaviour of the flow shown in Figure 3.40, it is clear that the difference in vortex breakdown location is clearly associated with the location of the normal shock at the symmetry plane. For the time averaged case, the shock at the sting tip appears to interact with the primary vortex shear layer in a similar manner to the shock in the steady state results. Thus, it may be stated that the mechanism for breakdown is likely to be the same, but that some difference between the solutions is changing the location of the impinging shock. Further consideration of this will be given in a later section. Also shown in Figure 3.40 is the presence of the cross-flow shocks (3 and 4) described in the analysis of Section 3.5, impinging on the shear layer.

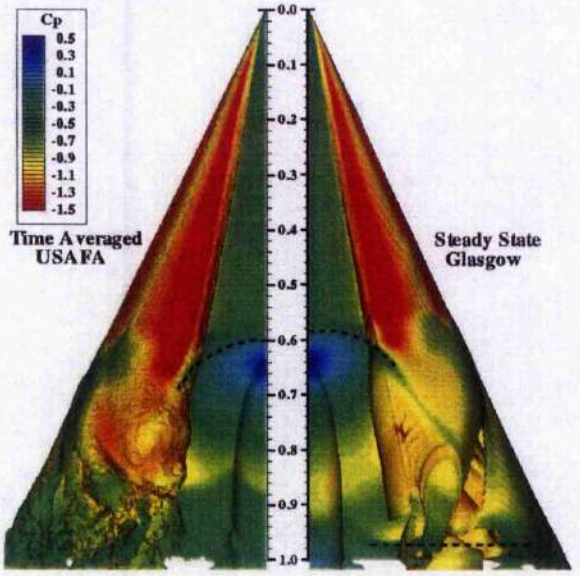

Figure 3.40: Isosurface of x vorticity coloured by pressure coefficient showing primary vortex shear layer and normal shock shape for current results and USAFA time accurate solutions; $M = 0.85$ and $Re = 6 \times 10^6$

Therefore, it is evident that the overall agreement between the steady state and time average solutions is reasonable, with vortex breakdown being predicted over the wing. It is found that the vortex breakdown locations are different, but despite these differences, the vortex core properties upstream are similar and the shape and relative locations of the shocks in the flow correspond well. It may be suggested that the effects of time accuracy on the prediction of transonic vortex breakdown are not significant for the purposes of predicting the main features of the flow. This further suggests that the steady state solution can be used as a useful approximation to the complex unsteady flow behaviour. However, the discrepancies in the location of breakdown should be kept in mind. This short study also eliminates the effects of time accuracy on the critical onset angle for vortex breakdown, as these solutions are also predicting breakdown to occur early on the wing.

3.7 Shock-Vortex Interaction and Vortex Breakdown

As mentioned in Section 3.5.2 and detailed in Figures 3.19 and 3.40, it is apparent that the sting tip shock intersects the vortex system. Therefore, it is suggested that some shock/vortex interaction takes place, particularly for higher angles of incidence. To consider this, the pressure in the freestream direction through the vortex cores for both

angles of incidence were analysed. This is shown in Figure 3.41, with the calculated pressure ratios for each proposed shock/vortex interaction location marked. For $\alpha = 18.5^o$, the interactions occur without vortex breakdown. It has been previously suggested that this is due to the shock sitting above the vortex core [17]. However, from consideration of the vortex core properties it is found that there are three regions of adverse pressure gradient which may suggest direct interactions. These coincide with the two normal shocks at the symmetry plane and the trailing edge shock, detailed previously, and are clear from the three dimensional view in Figure 3.19. The pressure ratios for all three are less than 1.5 and, as shown, the primary vortex recovers after passing through each. Therefore, it may be suggested that these are weak interactions.

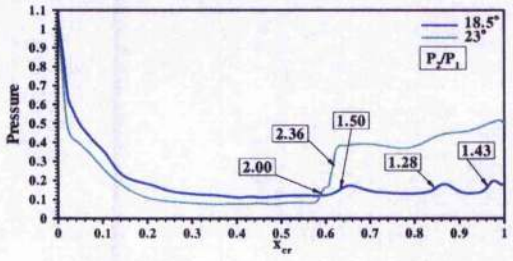

Figure 3.41: Pressure distribution through vortex cores for both angles of incidence; The numbers on the plot signify the magnitudes of the pressure ratios through the intersecting shocks

At $\alpha = 23^o$, where breakdown occurs on the wing, it is clear that there are two regions of high adverse pressure gradient at the vortex core. The first coincides with the location of the normal shock upstream of the sting tip as shown at the symmetry plane in Figure 3.18 and also with the onset of vortex breakdown. Very close to this, the second, higher pressure gradient coincides with the occurrence of complete vortex breakdown, which can be seen in Figure 3.32. These pressure gradients have ratios of 2.00 and 2.36 respectively. It is likely that the first pressure increase is due to the effect of the normal shock at the symmetry plane on the vortex core, in a similar manner to the interaction at the lower incidence. The second pressure gradient is much stronger and may indicate a direct interaction between the downstream section of the shock and the vortex core and indeed this location corresponds to the region where the shock intersects the vortex core as demonstrated in Figure 3.40. Further detail of this region is found in Figure 3.42, which shows contours of Mach number on a plane through the vortex core. The vortex core trajectory that the data of Figure 3.41 is obtained from is highlighted. This shows the presence of the shocks prior to and at vortex breakdown, where the Mach number drops significantly and suddenly.

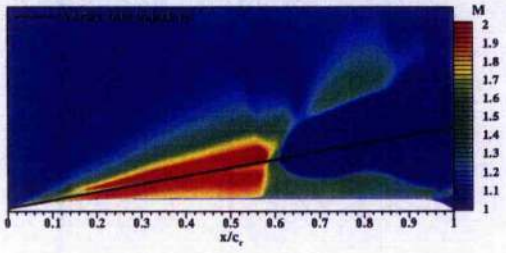

Figure 3.42: Contours of Mach number on slice through vortex core at a constant $y/s = 0.56$ for $\alpha = 23^o$, $M = 0.85$ and $Re = 6 \times 10^6$

From these results, it is evident that there are interactions between the shocks and vortex core for both angles of incidence, with weaker interaction occurring for the lower incidence. Thus, it may be suggested that there is a limiting behaviour below which the vortex can retard the effects of the shock and remain coherent. Above this limit, the interaction causes a considerable weakening of the vortex core, which results in vortex breakdown. In his comprehensive review, Deléry [49] demonstrated the importance of a number of parameters for vortex breakdown caused by shock/vortex interaction. These include the tangential or swirl velocity, U_θ, and the axial velocity of the vortex core, U_{axial}. He also proposed that the swirl ratio or the Rossby number may be used as a measure of the vortex intensity and, thus, the susceptibility of the vortex to shock induced breakdown. The Rossby number is a non-dimensional parameter, defined as the ratio of the axial and circumferential momentum in a vortex as defined by Equation 3.1. In this investigation, the maximum axial velocity at the vortex core and the maximum swirl velocity of the vortex are used. This relationship is the inverse of the axial swirl parameter described in Ref. [49], which is used as a breakdown criterion for a free-vortex.

$$Ro = \frac{U_{axial}}{r_c \Omega} = \frac{U_{axial}}{U_\theta} \tag{3.1}$$

As a vortex passes through a normal shock, the tangential velocity is found to stay relatively constant while the axial velocity decreases, therefore reducing the Rossby number [28]. With the reduction in the Rossby number comes an increase in vortex intensity and, as a result, the susceptibility of the vortex to breakdown increases. A criterion for breakdown using the Rossby number has also been investigated by Spall *et al.* [59] and by Robinson *et al.* [60], who applied it to computational results on slender delta wings and determined that the limiting Rossby number occurs between 0.9 and 1.4 for most cases, with a stable vortex core occurring for values above 1.4. To consider this criterion, the Rossby number was calculated for both pre- and post-breakdown angles of incidence and the resulting graph is shown in Figure 3.43 with respect to streamwise location on the wing. Also noted on the plot are the critical Rossby numbers for vortex breakdown.

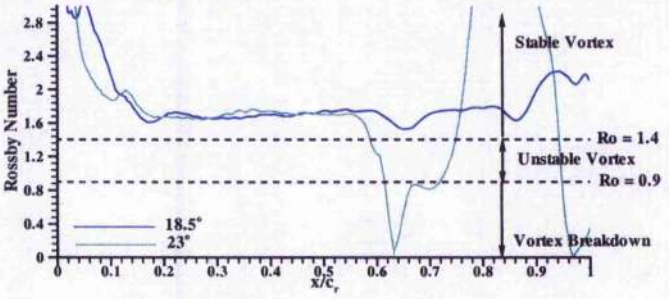

Figure 3.43: Rossby number distribution against root chord location for pre- and post-breakdown cases

These results also show the influence of the shocks on the vortex behaviour. At $\alpha = 18.5^o$, it is clear that weak interactions occur as the Rossby number decreases. However, this reduction is not significant which shows that the vortex is not sufficiently weakened by the shock. A recovery is witnessed downstream. At $\alpha = 23^o$, a similar behaviour is noted where at $x/c_r = 0.58$ the vortex is affected by the normal shock. However, the reduction in Rossby number is greater than for $\alpha = 18.5^o$ and the vortex becomes unstable. Complete vortex breakdown is then caused by a second shock at approximately $x/c_r = 0.62$ which has a greater effect on the already weakened vortex flow, and breakdown is almost immediate. It is interesting to note that upstream of vortex breakdown the value of the Rossby number is very similar for the two angles of incidence. This shows that for a given set of conditions, the Rossby number is independent of incidence. For this case, the mean Rossby number is approximately 1.7. This suggests that if the Rossby number of a vortex is constant for increasing incidence, another parameter is needed to define the limit which causes vortex breakdown to occur on the wing.

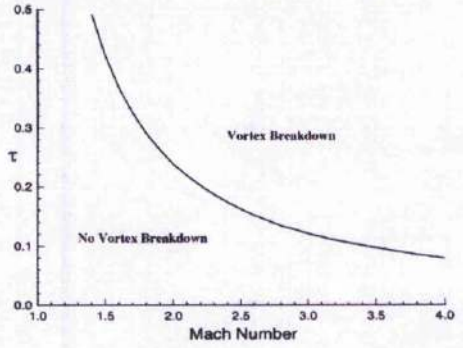

Figure 3.44: Theoretical limit curve for normal shock vortex interactions, where τ is the swirl ratio $= 1/Ro$ (adapted from Ref. [28])

It was also suggested by Deléry [49] that the susceptibility of a vortex to breakdown is linked to the strength of the impinging shock and, thus, on the upstream Mach number. In the study by Kalkhoran and Smart [28], a vortex breakdown limit for normal shock/vortex interaction based on upstream Mach number and swirl ratio is discussed for supersonic vortices with uniform Mach number profiles. The resulting limit is shown in Figure 3.44. This shows that for a given swirl ratio, a limiting Mach number exists above which vortex breakdown occurs. However, this curve may not be applied to transonic delta wings as the leading edge vortices have jet-like velocity profiles and the impinging shocks in the flow may not be normal to the vortex axis. This will change the behaviour of the interactions and, therefore, the limit for breakdown.

To investigate a limit for transonic delta wing vortices, the strength of the impinging shocks should be considered, pre- and post-breakdown. Unfortunately, little experimental data exists to allow the shock strength to be measured through the vortex core. However, the strength of the shocks incident on the surface of the wing may be considered to improve confidence in the computational solutions. For the NASA NTF experimental results, the pressure distributions on the surface of the wing at a constant spanwise location of $y/s = 0.3$ were considered for the 23.6^o and 24.6^o angles of incidence and are shown in Figure 3.45. Unfortunately, there are only five data points, however, the presence of an increase in pressure between $x/c_r = 0.6$ and 0.8 for the 23.6^o incidence and $x/c_r = 0.4$ and 0.6 for the 24.6^o incidence is still clear. As the sting tip is located at approximately $x/c_r = 0.64$, these pressure jumps are most likely to be located close to the $x/c_r = 0.6$ streamwise location. Using this as a guide, an approximation to the shock strength at this location can be determined. The approximate values calculated are given in Table 3.3.

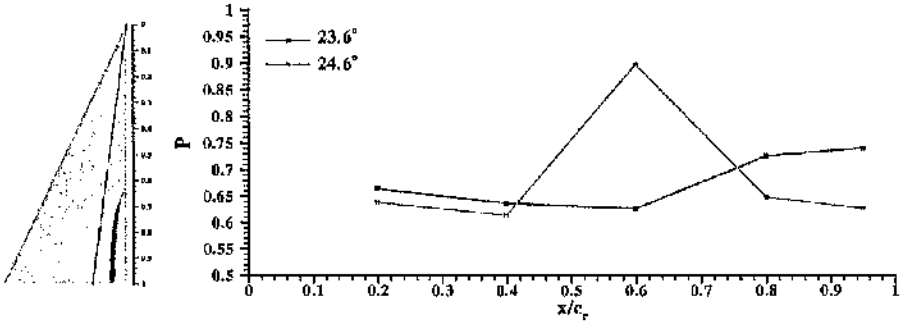

Figure 3.45: Experimental surface pressure data on conical ray at constant $y/s = 0.3$ to show experimental shock strength for $\alpha = 23.6^o$ and 24.6^o, $M = 0.85$, $Re = 6 \times 10^6$ from NASA NTF data

	$\frac{P_2}{P_1}$
NASA NTF Experiment - 23.6^o	1.16
NASA NTF Experiment - 24.6^o	1.4673
CFD - 18.5^o	1.2314
CFD - 23^o	1.4695

Table 3.3: Summary of shock strength on surface conical ray at constant $y/s = 0.3$ for all solutions at $M = 0.85$, $Re = 6 \times 10^6$ and $\alpha = 23^o$ compared to NASA NTF data.

Using the values in Table 3.3 as a guide, it is evident that there is a considerable difference in the calculated pressure changes at the sting tip location for the pre- and post-breakdown experimental results. The calculated pressure ratio for the post-breakdown case is roughly 25% larger than for the pre-breakdown case. Similar distributions were also obtained from the computational solutions for the pre- and post-breakdown cases and the shock strengths calculated are also stated in Table 3.3. From a comparison with the experimental data it is clear that the magnitude of the post-breakdown pressure ratio is very similar, however, the pre-breakdown ratio is larger. This means that overall the increase between the pre- and post-breakdown cases for the computational results is less. The larger pressure ratio of the computational results for the pre-breakdown case may have implications for the onset of breakdown. If the shock strength is over-predicted in the computational results, it is likely that breakdown would occur earlier on the wing compared to the experimental results for a given vortex strength.

To consider the incidence at which vortex breakdown first occurs on the wing and relative strength of the shocks in the flow, additional calculations were performed for intermediate angles of incidence between 18.5^o and 26^o for the same flow conditions as before ($M = 0.85$ and $Re = 6 \times 10^6$). A summary of the important flow details are shown in Table 3.4. These details include whether vortex breakdown occurred, the maximum vortex core axial velocity, Mach number and the strengths and locations of the first impinging shock at each incidence. The location of the shocks can be taken as analogous to the vortex breakdown location, where appropriate. From the analysis, it was found that the 23^o case was the only incidence to exhibit the double shock at vortex breakdown and so the combined shock strength is instead shown for comparison with the other results. As these calculations were performed to the same convergence level as the original calculation, the data from the original calculation has also been included. The further converged solution results are also shown for completeness. As discussed previously, it was found that the convergence level only affected the location of breakdown, therefore, this should not influence the critical angle for the onset of breakdown over the wing.

α	*VBD?*	*Max.* U_{axial}	*Max.* M_{axial}	$\frac{P_2}{P_1}$	*Shock* x/c_r
18.5^o	×	1.74	1.76	1.5	0.62
19^o	×	1.76	1.80	1.67	0.64
20^o	√	1.74	1.83	3.73	0.64
21^o	√	1.74	1.86	4.87	0.64
22^o	√	1.79	1.88	4.67	0.51
23^o	√	1.80	1.92	5.25	0.55
23^o †	√	1.83	2.00	4.75	0.62
24^o	√	1.84	2.05	5.93	0.49
25^o	√	1.84	2.10	5.64	0.47
26^o	√	1.84	2.20	5.48	0.40

Table 3.4: Summary of shock and vortex core data for all steady state calculations at $\alpha = 18.5^o - 26^o$, $M = 0.85$ and $Re = 6 \times 10^6$ † indicates further converged solution results.

Before considering the onset of breakdown, it is important to note the behaviour of the flow variables with increasing incidence. It is clear from Table 3.4, that the predicted shock strength increases with incidence, which is in agreement with the experimental data in Table 3.3. The axial velocity and Mach number are also found to increase, however, the Rossby number was found to be consistent at ≈ 1.7 for each incidence as described before. From the theory of supersonic flows, it is known that the strength of a shock is dependent on the upstream Mach number, thus for a higher axial flow, a stronger shock will occur. However, in this case the relationship does not appear to be linear. This is most likely to be due to changes in the shape of the shock in response to changes in the flow behaviour and the equilibrium conditions as the incidence is increased. This may also suggest that the behaviour of the vortex breakdown is also non-linear in nature.

Vortex breakdown first appears on the wing at $\alpha = 20^o$, which coincides with a significant increase in shock strength. At this point it may be assumed that the strength of the shock is high enough to cause a complete reorganisation of the flow behaviour. Thus, the shock strength limit for breakdown for these solutions may be given as 3.73. This appears to confirm the proposal made previously, that the normal shock strength is over-predicted, thus causing the breakdown to occur earlier over the wing for the vortex core behaviour predicted. To determine a link between the vortex flow conditions, as described by the Rossby number, and the shock strength for breakdown to occur on the wing, further data, both experimental and computational, is needed. By considering different flow conditions and configurations a trend similar to Figure 3.44 may be determined for transonic vortex breakdown.

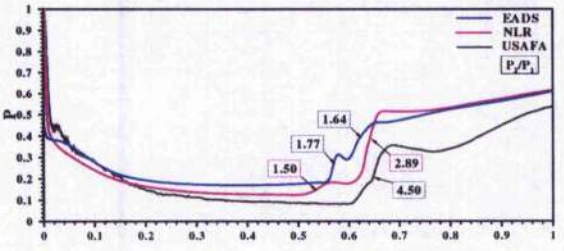

Figure 3.46: Pressure distribution through vortex cores for EADS and NLR solutions

To further consider the relation between the occurrence of breakdown, the vortex core behaviour and the predicted shock strength, the vortex core data for the EADS-MAS, NLR and time averaged USAFA results are considered in a similar manner. The pressure behaviour through the vortex core, with the pressure ratios marked, is shown in Figure 3.46. From this plot, it is clear that a similar behaviour occurs, with shocks intersecting the vortex core axis and vortex breakdown occurring. From the EADS-MAS and NLR solutions, the pressure ratios through the shocks are approximately 1.77 and 1.64, and 1.5 and 2.89, respectively. The USAFA time averaged solution has only one shock region with a ratio of 4.5. However, from analysis of the instantaneous solutions, it was found that two shocks also exist at breakdown, which for the solution at a time step of $\tau = 16600$ correspond to 2.25 and 2.71.

While the predicted strength of a shock can be dependent on such factors as grid refinement, turbulence model and solver treatment, it is also apparent that there are corresponding differences in predicted maximum axial velocity through the vortex core, as shown in Figures 3.32 and 3.39 and summarised in Table 3.5. The current solution has predicted a maximum axial velocity which is the same as the USAFA solutions and higher than for the EADS-MAS and NLR solutions. As a result of this increase in axial velocity the Mach number upstream of the shock

will increase, and the upstream pressure will reduce, resulting in a stronger shock to maintain equilibrium of the flow. However, it is evident that the Rossby number in each case is similar. This suggests that the shock strength predicted by the computational solutions is dependent on the vortex core behaviour predicted upstream. The axial flow behaviour is also dependent on the computational parameters mentioned above. However, despite the differences in flow solutions and computational set-up, the behaviour and effect of the shocks on the flow are the same.

				Vortex core Shocks			***Shock at*** $\mathbf{y/s = 0.3}$**:**	
	$\mathbf{U_{axial}}$	$\mathbf{M_{axial}}$	**Ro**	***1st:*** $\frac{P_2}{P_1}$	***2nd:*** $\frac{P_2}{P_1}$	***Total:*** $\frac{P_2}{P_1}$	$\frac{P_2}{P_1}$	***VBD*** $\mathbf{x/c_r}$
EADS	1.50	-	~ 1.67	1.77	1.64	2.55	1.4274	0.68
Glasgow	1.83	2.00	~ 1.7	2.00	2.36	4.75	1.4695	0.64
NLR	1.60	-	~ 1.74	1.50	2.89	4.33	1.5075	0.67
USAFA (time ave.)	1.80	2.03	~ 1.67	-	-	4.50	1.4409	0.68
USAFA (instant.)	-	-	-	2.51	2.71	4.75	-	0.66

Table 3.5: Summary of maximum axial velocity, shock strength and breakdown location for all solutions at $\alpha = 23^o$, $M = 0.85$ and $Re = 6 \times 10^6$

To consider the ability of the computational solutions to predict the axial flow upstream of breakdown, the PIV results obtained at DLR and described in Konrath *et al.* [21] were considered. These experiments were detailed in Section 1.4 and were carried out for a slightly different flow conditions, with a Mach number of $M = 0.80$ and Reynolds number of $Re = 3 \times 10^6$. To compare with these results, a new set of calculations were performed, using the $k - \omega$ with P_ω Enhancer turbulence model for $M = 0.80$ and $Re = 2 \times 10^6$ at angles of incidence of $\alpha = 18.5^o - 26^o$. Figure 3.47 shows a comparison of the cross-flow behaviour for a nominal incidence of $\alpha = 26^o$. The effect of the difference in Reynolds numbers will be negligible due to the sharp leading edge. In the experiment, it was found that vortex breakdown occurred between the $x/c_r = 0.6$ and 0.7 streamwise stations. However, the computations predict breakdown further upstream at $x/c_r = 0.4$. Therefore, to make a comparison of the pre-breakdown flow, the results were compared on planes which were a similar non-dimensional distance from the breakdown location, this corresponds to $x/c_r = 0.5$ for the experiment and $x/c_r = 0.3$ for the computational results assumming that the breakdown occurs close to the $x/c_r = 0.6$ location.

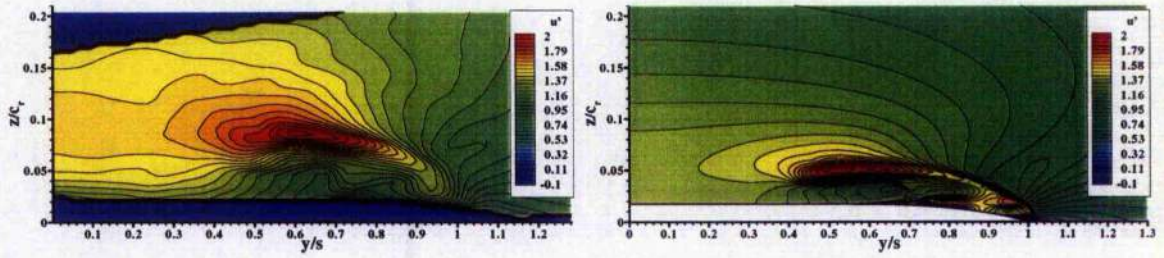

(a) PIV, $\alpha = 25.9^o$, $Re = 3 \times 10^6$

(b) CFD $\alpha = 26^o$, $Re = 2 \times 10^6$

Figure 3.47: Comparison between u velocity contours for experimental PIV and computational results for $M = 0.80$ on a slice at $x/c_r = 0.5$.

From the comparisons of the non-dimensional u velocity contours, a number of observations may be made. It is clear that the location of the vortex core is very different between the computational and experimental results, however this is likely to be due to the proximity of the computational slice to the apex of the wing as further downstream the vortex would lift further from the wing surface. However, the shape of the vortical system is the same, with a very elongated primary vortex clear for both sets of results. Considering the vortex core properties, from the experimental data at three pre-breakdown PIV planes, it was found that the u velocity corresponds to 1.962 at $x/c_r = 0.5$, 1.870 at $x/c_r = 0.55$ and 1.522 at $x/c_r = 0.6$. Although the maximum velocity found from the measurement planes is 1.962, it is likely that the actual maximum velocity will be larger. This is evident from Figure 3.48, which plots these three points along side the velocity behaviour of the computational results. The maximum u velocity for the computational results corresponds to $u = 1.88$, which is slightly lower than the maximum experimental value. Therefore, it is likely that the axial flow behaviour is under-predicted in the computational solutions.

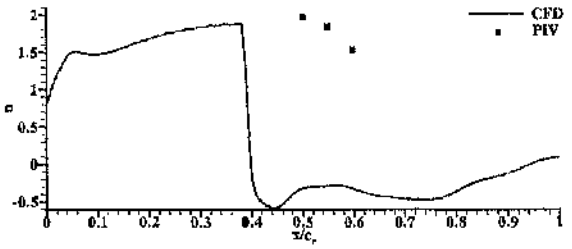

Figure 3.48: u velocity through vortex core for computational results compared to experimental PIV data for $M = 0.80$, $\alpha = 26^o$

Returning to the issue of the secondary vortex breakdown which occurs for the pre-breakdown case at $\alpha = 18.5^o$ and was initially mention in Section 3.4. The location of this breakdown, is clear from Figure 3.9 and corresponds to $x/c_r = 0.86$. It is evident from the location and interaction of the shocks in the flow with the primary vortex, shown in Figure 3.41, that this location coincides with a normal shock at the primary vortex core and with a normal shock that the symmetry plane. Due to this, it may be suggested that a phenomenon similar to that described above for the primary vortex breakdown is the cause of the unusual behaviour. From Figure 3.41 it is found that this shock has a strength of $P_2/P_1 = 1.28$, and although it has been found that this shock interacts with the primary vortex, it does not cause vortex breakdown. However, the secondary vortex does not have as high an axial velocity and therefore strength as the primary vortex. Therefore, if a shock/vortex interaction occurs, it is likely that the secondary vortex cannot recover downstream and vortex breakdown occurs.

3.8 Discussion

Having considered the mechanisms which cause vortex breakdown to occur on the wing, it is possible to return to the issue of the discrepancies between the CFD and experimental results. It was found from the experimental data used in this study that vortex breakdown jumps abruptly from a location downstream of the trailing edge to a location upstream on the wing for a small increases in incidence. Indeed from the results summarised in Table 3.4, it is clear that the flow seems to go from full vortical flow over the whole wing surface to breakdown occurring close to the $x/c_r = 0.6$ location in a one degree increase.

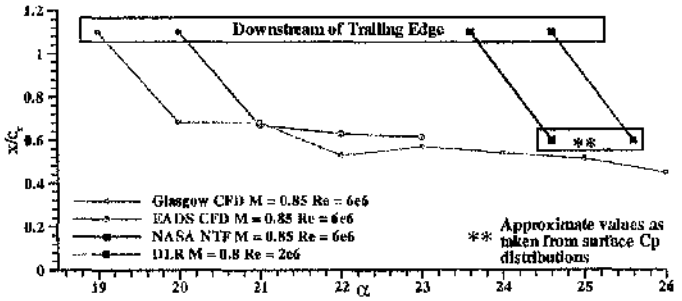

Figure 3.49: Vortex breakdown location for both computational and experimental results

The location of vortex breakdown with incidence is plotted in Figure 3.49 which also shows similar results for EADS-MAS solutions and comparisons to available experimental data. For the experimental data, the exact location of vortex breakdown is not known, however from the surface pressure coefficient distributions the approximate locations could be determined. From this plot it is clear that the behaviour of the onset of vortex breakdown is very similar for both the CFD and experiment, however the angle at which this occurs varies. With further consideration of the literature it was found that there is a large spread of values for this critical angle. These are detailed in Table 3.6 below. It is quite clear from all these results that the critical onset angles for vortex breakdown over the wings for current CFD solutions are consistently earlier than for the majority of the experimental results.

Source	*Type*	*Conditions*	α_{cr}
Elsenaar and Hoeijmakers [18]	exp.	$M = 0.85, Re = 9 \times 10^6$	23^o
Houtmann and Bannink [129]	exp.	$M = 0.85, Re = 3.6 \times 10^6$	20^o
Chu and Luckring [20]	exp.	$M = 0.799, Re = 6 \times 10^6$	26.6^o
"	exp.	$M = 0.831, Re = 6 \times 10^6$	24.6^o
"	exp.	$M = 0.851, Re = 6 \times 10^6$	24.6^o
"	exp.	$M = 0.871, Re = 6 \times 10^6$	24.7^o
"	exp.	$M = 0.9, Re = 6 \times 10^6$	22.6^o
"	exp.	$M = 0.849, Re = 11.6 \times 10^6$	24^o
Longo [121]	CFD	$M = 0.8$, Inviscid	25^o
Glasgow	CFD	$M = 0.85$ $Re = 6 \times 10^6$	20^o
EADS-MAS	CFD	$M = 0.85$ $Re = 6 \times 10^6$	21^o

Table 3.6: Critical incidence for transonic vortex breakdown to be found on 65^o delta wings

To explain this difference, further consideration is needed to the discussion given above considering a critical limit for breakdown to occur dependent on the vortex core strength and the strength and locations of the shockwaves in the flow. As shown, with an increase in incidence the strength of the shocks in the flow increases, most likely as a response to the increased acceleration of the flow over the wing surface. Similarly, the axial velocity in the vortex core increases and it has been shown that there is a critical relationship between these quantities which results in breakdown for a critical incidence. To change the angle at which vortex breakdown occurs, it will be necessary to have a change in either one of these parameters. For example, with an increase in vortex intensity and therefore a decrease in axial velocity or an increase in tangential velocity, the strength of the shock needed to cause breakdown will decrease and breakdown will occur earlier on the wing.

From the results detailed in the previous section, it may be suggested that two factors are causing the early prediction of breakdown on the wing. These are an under-prediction of the axial velocity, which results in a vortex more susceptible to breakdown and an over-prediction of the strength of the shocks within the flow. From consideration of the effects of a number of flow parameters, it appears that these predictions are not greatly effected by grid structure, turbulence model, convergence or time accuracy. The effect of grid refinement was also considered, which also concluded that the overall refinement of the grid had little effect on the solution. However, this study did not consider localised refinement, particularly in the vortex core region. Despite continuing improvement in CFD codes, turbulence models and practises, prediction of the vortex core behaviour and axial flow is still a challenge. There have been a number of collaborations and investigations which have considered the vortical flows over delta wings, which have also generally predicted the flow behaviour well, however the axial velocity is almost always much lower than that found from experiments. This is also true for this case and may be attributed to the abilities of turbulence modelling and restrictions in grid refinement for the core region. To fully resolve the vortex core behaviour it would be necessary to have similar refinement as is applied to boundary layer regions. It is unclear at this time whether an improvement in vortex core axial velocity would alter the predicted strength of the shocks in the flow, however, if the shock strength remained constant, with an increase in axial velocity, it may be suggested that the angle of incidence at which breakdown occurred would increase.

3.9 Conclusions

The behaviour of transonic delta wing flows and the ability of CFD to predict these flows was considered in this chapter. To consider this, two angles of incidence were used which corresponded to solutions which predicted pre- and post-breakdown flows. The initial analysis showed that the CFD solutions predicted the behaviour over the wing very well for the pre-breakdown flow, however the high incidence showed a discrepancy with the experimental results. Where the experiment was exhibiting a full vortex to the trailing edge, the CFD solution was predicting breakdown to occur. However, it was found that breakdown occurred on the wing for the next experimental data point and from comparison of the CFD results with this data, it was found that the CFD solutions gave good agreement. Therefore, it was concluded that the flow behaviour was predicted well but that the critical incidence for breakdown was not well predicted.

A number of transonic flow features were determined from analysis of the solutions, particularly the occurrence of a complex cross-flow shock system and the abrupt behaviour of vortex breakdown. However, more experimental data, particularly considering the off-surface flow behaviour, is needed to both confirm the existence of these

shocks and to further validate the flow solutions.

A thorough sensitivity study was carried out to determine the effect of a number of computational factors on the flow behaviour. These factors included turbulence model and time accuracy. However, it was found that although the flow was affected by these factors, the influence was small and there was no effect on the onset of breakdown on the wing.

The mechanisms which determine the behaviour of transonic vortex breakdown were shown to be highly complex and are dependent on the vortex core strength and the strength and location of the shocks in the flow. Through consideration of computational solutions, a means to analyse the influence of each of these parameters was established and it has been shown that a relationship must exist, which describes the critical limit for vortex breakdown to occur. Further research is needed, both experimental and computational, to confirm the behaviour of this relationship and to allow for further analysis of the critical limit of shock/vortex interactions for delta wing flows.

It was concluded from the discussion of the shock/vortex interaction and the presence of a limit for breakdown that further work is needed to consider the prediction of the vortex core axial velocity and shock strengths in order to accurately capture the onset of the breakdown behaviour in comparison to the experimental data. However, the predictions of the flow behaviour were found to be otherwise adequate.

Chapter 4

Application of DES to Delta Wing Vortical Flows

4.1 Introduction

The flow over a delta wing is dominated by the leading edge vortices. As the angle of incidence is increased the vortices become unstable and vortex breakdown can occur over the wing. This flow is found to be highly unsteady. For aeroelastic behaviour, such as buffet, of existing configurations, it is clear that understanding the behaviour of unsteady forcing is crucial to allow the alleviation of any structural response, which may exist. This is potentially important for complex fighter configurations such as the EuroFighter and is compounded by the emergence of new UAV and UCAV technologies, which are tending toward planforms where unsteady vortical flows play a large role. This means that the need for a more complete understanding of the unsteady behaviour of vortical flows is becoming increasingly important.

To date, there has already been a great deal of research, which has considered the unsteady behaviour of this flow and what is generally known was discussed in a summary of the literature given in Chapter 1. From this research, it is clear that the unsteady behaviour of the vortical flow is complex, with a large number of flow phenomenon existing and interacting, over and downstream of the wing. These flow phenomenon include the helical mode instability of vortex breakdown, vortex wandering, vortex breakdown oscillations and shear layer instabilities. From consideration of the literature available, the frequencies associated with these phenomenon were considered and summarised in Table 1.2. From this condensation of the available data, patterns emerge relating the order and size of the non-dimensional frequencies for these flow features. This is summarised further in Table 4.1.

Phenomenon	*Strouhal Number*
Helical Mode Instability	1 - 2
Shear Layer Instabilities	8 - 10 and higher frequencies
Vortex Shedding - T.E	~ 8
Vortex Shedding - high α	0.2 - 0.5
Vortex Breakdown Oscillation	0.01 - 0.08

Table 4.1: Frequencies corresponding to important unsteady features of vortical flows

It was found that other dominant frequencies also featured in the literature, which were not clearly attributed to specific phenomenon. These are, $St = 2.5$ - 4, $5 - 6$ and the higher frequencies ~ 20. It is possible that these frequencies also correspond to the phenomenon detailed above, however further investigation is needed. It is also important to note, that there may be more than one dominant frequency associated with a particular phenomenon, due to the complexity of the unsteady behaviour. For example, shear layer instabilities will have at least two associated frequencies, this is due to the rolling up of the shear layer into discrete subvortices, which will have a frequency of rotation and also due to the movement of these structures around the vortex core. It may be difficult to separate these frequencies within a single solution, however, it may help to explain the spread of data and dominant frequencies assigned to particular flow features.

To allow for further understanding, these phenomena can be split into two categories, those which occur upstream of breakdown and those occurring downstream. This is shown in Figure 4.1. Splitting the flow features in this way allows for an appreciation of which features will dominate, depending on where vortex breakdown occurs

on the wing. For breakdown close to the trailing edge, it is likely that the shear layer attachment and shear layer instabilities would dominant the flow, however as the breakdown moves upstream, it is likely that the helical mode instability may dominate the frequency content. This will be important when considering the frequency content of the results at specific regions in the flow and looking at the flow behaviour overall - particularly when considering the unsteady loading on the wing.

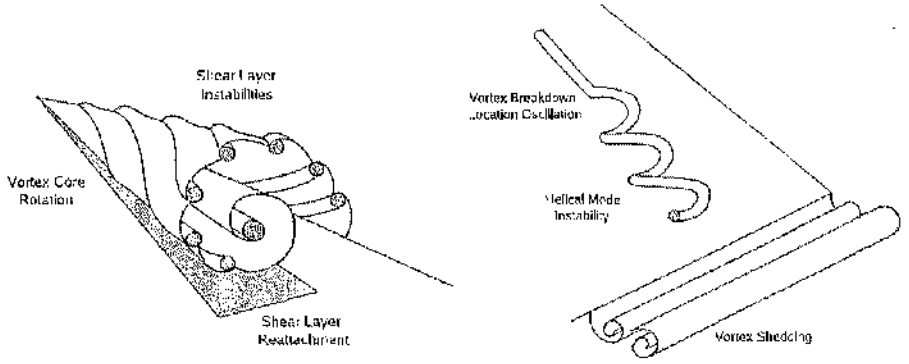

(a) Upstream (b) Downstream

Figure 4.1: Schematic diagrams showing flow topology upstream and downstream of vortex breakdown

Accurately predicting this complex flow is a challenge for numerical methods. In recent times the capabilities of CFD solvers have improved, with more complex turbulence modelling and treatments being utilised. One such method is DES, which is a hybrid URANS/LES turbulence treatment. This model was proposed initially by Spalart [171] to reduce the fine resolution of the grid in the boundary layer region needed for high Reynolds number LES calculations and is described in detail in Chapter 2. With this treatment many of the smaller turbulent scales can be captured, which has led to a greater ability to predict more and more complex flow behaviour accurately. This has been shown from existing DES calculations on delta wing geometries [30, 161, 164] using unstructured grids, mostly carried out by the United States Air Force Academy (USAFA). Therefore, the use of DES for this type of flow using structured grids will be considered.

This chapter considers the results of an investigation applying DES to the unsteady vortical flow over a slender delta wing. The test case will be outlined, with the computational set up and grid generation discussed. The effect of the temporal and spatial refinement on the DES results will be considered before the application of DES and the resolution of the LES region is analysed. The final results will then be compared to existing DES results and validated against experiment before the results are discussed and conclusions made.

4.2 Summary of Test Case

The test case chosen for this investigation is a 70^o delta wing at an incidence of $\alpha = 27^o$. Vortex breakdown occurs over the wing and there is an extensive database of experimental data, both time-averaged and unsteady for validation purposes. There is also a considerable database of computational results available for this configuration using both URANS and DES turbulence models [23, 24, 29, 30, 70, 71, 116, 144, 161, 165, 187, 196] from the NATO RTO Task group AVT-080 which considered *"Vortex Breakdown over Slender Wings"* [197]. The experimental data is taken from the PhD thesis by Mitchell [13] and associated papers [81, 99, 100, 162, 197]. The experiments were carried out in ONERA's F2 and S2Ch subsonic wind tunnels with a wide range of experimental techniques used to elucidate the flow features and create a large database of experimental results. These techniques include: 3D Laser Doppler Anemometry (LDV), Particle Image Velocimetry (PIV), Laser tomoscopy, Surface oil flow visualisation and data from both steady and unsteady pressure transducers (Kulites^{TM}).

The wing used in the experiments has a root chord length of $950mm$ and a sweep angle of 70^o. It has flat upper and lower surfaces with a 15^o bevel at the leading edge. The trailing edge is blunt with a thickness of $20mm$. These details are shown in Figure 4.2. The experimental test conditions used by Mitchell were: an incidence of $\alpha = 27^o$, $U_\infty = 24ms^{-1}$, which corresponds to a Mach number of $M = 0.069$ and a Reynolds number based on the root chord of $Re = 1.56 \times 10^6$. To help with the convergence of the compressible flow solver, the Mach number used for the investigation was raised to $M = 0.2$, which gives a free-stream velocity of $U_\infty = 68ms^{-1}$. As this Mach number is still relatively low, this should not have a significant effect on the solution as compressibility effects will be

negligible. All non-dimensional frequency data calculated for the computational results in this investigation will use this altered free-stream velocity, to allow fair comparison with the experimental data.

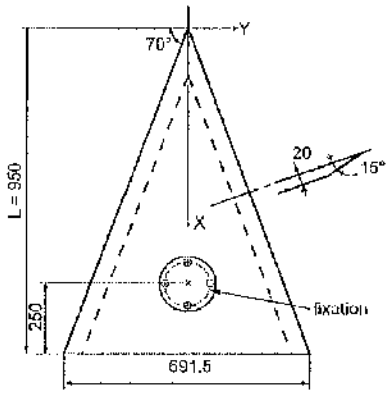

Figure 4.2: 70° ONERA geometry (all distances marked are in mm) [13]

This test case is also used for the investigation into the performance of URANS turbulence models for unsteady vortical flow prediction in the following chapter and as such the grids generated for the DES calculations were also used for this work. All grids used and the computational set up of the calculations for both investigations will be detailed in this chapter and will not be repeated in later sections.

4.2.1 Grid Generation

As stated in Chapter 3, there are a number of factors, which are important in the creation of grids for use in CFD calculations. When creating a grid for use in a DES simulation, these factors are compounded by the sensitivity of the solution to both the spatial and temporal resolution of the calculations. As stated previously, the solution of the DES model is highly dependent on the maximum cell dimension, $\Lambda_{max} = max(\Lambda_x, \Lambda_y, \Lambda_z)$, through its use within the LES region as a spatial filter. For a URANS calculation, the aim of grid refinement is numerical accuracy, however, for LES the refinement of the grid determines the level of the sub-grid scale model, which in turn determines the smallest resolved eddies in the flow. This means that for the LES region, the maximum cell size determines the range of scales which are subject to modelling rather than prediction by the conservation laws. This value also determines the size of the URANS region close to the wall. For an optimum DES calculation, the grid cells should be orthogonal, ideally cubic, particularly within the regions of interest and at the interface between the URANS and LES zones [177]. Attempting to create a sufficiently refined structured grid with uniform cubic cells in all regions of interest is impractical for delta wing geometries as the required size of the grid would be too computationally expensive to run. However, achieving orthogonality is not difficult for this type of grid and only requires a suitable grid topology to reduce the presence of cell skewness, and allow an even distribution of points within the regions of interest. As the physical accuracy of the DES model is dependent on small cell sizes, it would seem prudent to refine the grid as much as is practical.

With an increase in spatial refinement comes a need for temporal refinement. This further increases the computational expense, which can be prohibitive to allowing the computation of a fully optimised solution. Further discussion of temporal dependency will be given in a later section. Grid refinement in the spanwise direction at the leading edge is still important for the URANS zone to allow the accurate prediction of the flow separation and shear layer region within the boundary layer. As these grids are to be used for both DES and URANS calculations, it is important to consider the needs of each type of turbulence treatment in the creation of the grids.

To create the structured multi-block grid, the *ICEMCFD* mesh generation package, *Hexa* was used. The trailing edge wing geometry was altered to include a 15° bevel, similar to the leading edges. A semi-span H-H grid topology with no sting arrangement was used, which sets the incidence of the wing to 27° in the grid. The grid also uses a "collapsed apex" blocking strategy, where the edges of the blocks in the wing apex region have been collapsed to create a singular point. An example of the blocking topology is shown in Figure 4.3. Convergence problems associated with the singularity were again, dealt with by using laminar flow at the apex and fixing transition to turbulence at a constant streamwise location in the grid, which will be discussed in a later section. As for the VFE-2 grids, the far field was defined $20c_r$ in each direction from the wing apex to minimise the effect

of the boundaries on the flow. This grid topology has been used successfully in a number of investigations using RANS turbulence models by Allan [144, 198, 199].

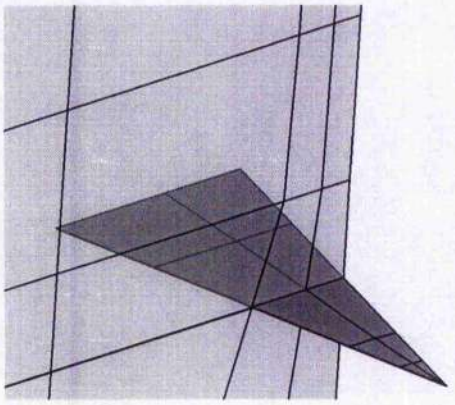

Figure 4.3: Grid topology of H-H grids used in investigation

Using one of the grids created by Allan as a starting point, two grids were created with differing levels of refinement, coarse and fine. Both grids have a first wall spacing of $1 \times 10^{-6} c_r$, which corresponds to a y^+ value of approximately 0.1 and a stretching ratio, within the boundary layer region, of 1.2. The y^+ value is sufficient for the Reynolds number used in this investigation and the stretching ratio is within the recommended range for adequate log-layer resolution suggested for RANS calculations by Spalart [177]. Examples of the grid refinement in a plane perpendicular to the wing surface and the freestream flow direction at a location $x/c_r = 0.63$ are shown in Figure 4.4. This shows the relative refinement, particularly close to the leading edge and in the boundary layer region. The fine grid has a higher concentration of points in these regions than the coarse grid and also has a much improved orthogonality over the whole area of interest close to the wing. This is demonstrated further by Figure 4.5 which shows the grid distribution on the symmetry plane.

A third grid was also created for the DES calculations, to consider the effect of refinement in the trailing edge region on the upstream vortical flow. This grid was based on the fine grid with the same distribution of points over the wing. However, in the region downstream of the trailing edge more grid points were added and the stretching ratio was decreased to improve the refinement in this region. Figure 4.6 shows the grid refinement at the trailing edge for the two grids. The effect of this refinement on the DES results will be discussed in a later section. A summary of the main features, including the number of grid points over the wing in each direction, for each grid is given in Table 4.2.

		No. of Grid Points on Wing		
Type	***Grid Size***	***Streamwise***	***Spanwise***	***Normal***
Coarse	3,969,310	102	80	89
Fine	7,767,081	167	112	107
Fine - Refined TE	8,768,970	167	112	107

Table 4.2: Summary of main features of grids used in DES and URANS investigations

As this study considers DES calculations, it is important to be able to consider the active LES and URANS areas within the grid structure. As part of the DES formulation two important grid parameters are calculated, the distance from the wall, d_{min} and the maximum cell length $C_{DES}\Delta_{max}$ at each cell location. The relationship between these variables in the DES implementation was used to create a flag parameter, which demonstrates the distribution of the two turbulence treatments. Where $d_{min} > C_{DES}\Delta_{max}$, the flag is set to 1.0 and LES is active in that region and similarly where $d_{min} < C_{DES}\Delta_{max}$, it is set to 0.0, and the URANS model is active. Based on the explanation of the DES model given in Section 2.4.5, it is expected that the RANS model is only active within the boundary layer region, close to the wing surface i.e. where the value of d_{min} is less than $C_{DES}\Delta_{max}$. Figure 4.7 shows contours of the flag parameter on a slice at $x/c_r = 0.63$ and through the vortex core region at a constant $y/s = 0.7$ for the fine grid. These show two contour regions denoted by red and green which signify the LES and URANS regions, respectively. It is clear from these plots that the region in which URANS is active is very small, close to the wing surface. Thus, LES is active for the majority of the region where vortical flow occurs.

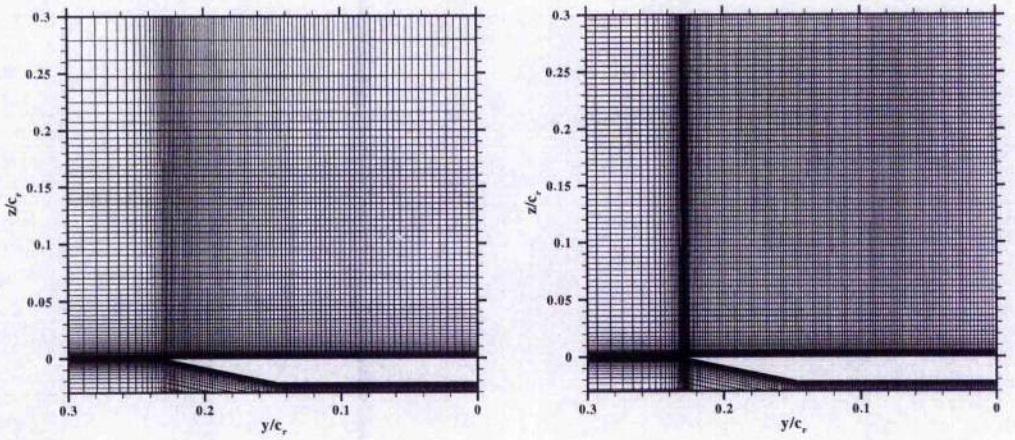

(a) Coarse grid (b) Fine grid

Figure 4.4: Comparison of grid refinement at $x/c_r = 0.63$ plane

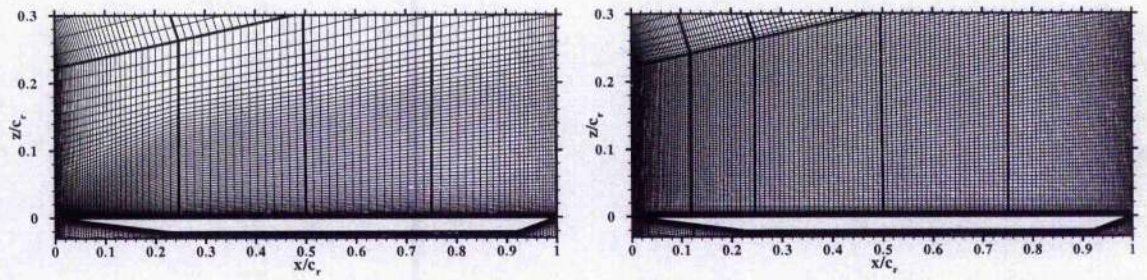

(a) Coarse grid (b) Fine grid

Figure 4.5: Comparison of overall grid refinement at symmetry plane for coarse and fine grids

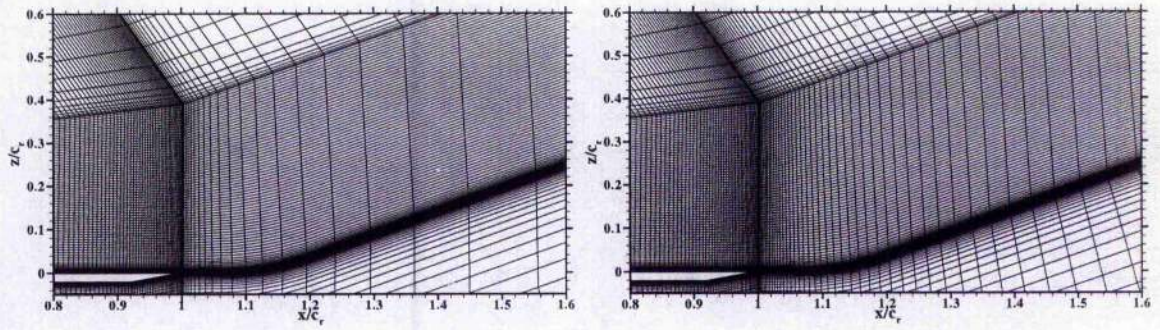

(a) Fine grid (b) Fine grid with refined trailing edge

Figure 4.6: Comparison of grid refinement in trailing edge region for fine grid and refined TE grids

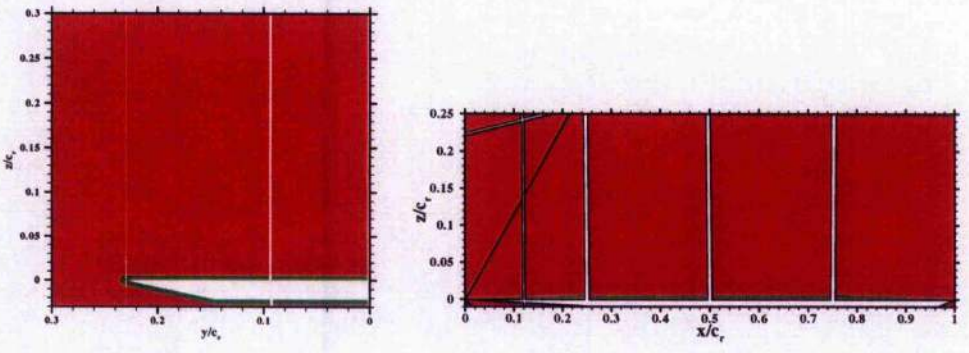

(a) $x/c_r = 0.63$ (b) $y/s = 0.7$

Figure 4.7: DES active area for fine grid; red denotes LES region and green shows URANS region.

4.2.2 Transition Treatment

The location of the transition between laminar and turbulent flow must be specified for these calculations. Ideally, this would be a location which would correspond to the natural transition line or to the line of a forced transition in the experiment. In the computational investigation carried out by Morton *et al.* [30], time-accurate calculations were performed for this test case using the SA-DES model. The flow conditions were as described above and the investigation was carried out on a series of unstructured meshes with varying refinement. A grid of approximately 2.4×10^6 grid points, locally refined in the region of the vortex core, was initially used and the flow was fully turbulent over the wing at the start of the investigation. Two transition locations were considered and compared to the experimental surface flow visualisations from Mitchell's investigation [13]. In the experiment, Mitchell noted that there was an inflection of the secondary separation line at approximately $x/c_r = 0.4$, which would suggest the transition from laminar to turbulent flow at this point. However, no details of transition inboard of this location were given. From Morton's study, it was determined that the location of transition had quite a significant effect on the flow behaviour. However, from comparison with the experimental results it was concluded that a constant transition line situated at $x/c_r = 0.4$ gave the most accurate results.

Based on this investigation and the experimental results, the location of a transition line was set to $x = 0.4$ for all calculations. This value of transition corresponds to a value of $x/c_r = 0.35914$ on the wing upper surface. It was felt that this slight upstream shift of transition compared to the DES results of Morton is not likely to affect the validity solutions significantly as the actual experimental transition is still largely unknown. No further investigation into transition will be given in this study.

4.2.3 Probe Application

In Mitchell's investigation a series of 17 Kulite^{TM} unsteady pressure transducers was used to consider the unsteady behaviour of the flow. These sensors were situated at the same chordwise stations as the time averaged data was obtained, at constant non-dimensional spanwise locations. Details of the locations of each probe, and its number, are given in Table 4.3. The unsteady data was obtained from 10^4 samples taken at a frequency of $5kHz$ over 2 seconds, which corresponds to a non-dimensional sample rate of $\Delta\tau = 0.0051$.

Probe	*Location*		*Probe*	*Location*		*Probe*	*Location*		*Probe*	*Location*	
	x/c_r	y/s		x/c_r	y/s		x/c_r	y/s		x/c_r	y/s
1.	0.84	0.7	5.	0.74	0.75	10.	0.63	0.7	14.	0.53	0.7
2.	0.84	0.65	6.	0.74	0.7	11.	0.63	0.65	15.	0.53	0.65
3.	0.84	0.6	7.	0.74	0.65	12.	0.63	0.6	16.	0.53	0.6
4.	0.84	0.5	8.	0.74	0.6	13.	0.63	0.5	17.	0.53	0.5
			9.	0.74	0.5						

Table 4.3: Experimental unsteady pressure probe locations

To compare with these locations and to consider the predicted unsteady behaviour, point probes were applied to the computational domain for these calculations. At the outset of the investigation, it was not known where the regions of interest lay for this case and so a large number of probes were applied, both upstream and downstream

of vortex breakdown. Probes were placed on constant chordwise locations: $x/c_r = 0.1, 0.2, 0.4, 0.53, 0.63, 0.74, 0.84$ and 1.0. Additional probes were also added, at a later stage, to consider the behaviour of the flow downstream of the trailing edge at $x/c_r = 1.1$, 1.2 and 1.3 In the spanwise direction, the probes were placed at y/s values of 0 - 1.1 at 0.1 intervals and normal to the wing the points were situated at $z/c_r = 0$, 0.001,0.005, 0.01, 0.02, 0.04, 0.08, 0.1, 0.15, 0.2 and 0.4. The spanwise and streamwise locations of the probes were chosen to coincide with the positions used in Mitchell's experiments [13] described above. In total, 1496 probes were placed for this investigation. Schematics showing the majority of the probe positions are given in Figure 4.8.

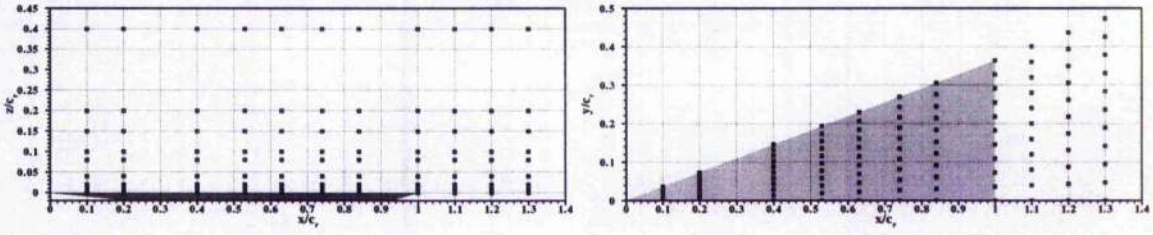

(a) Side view

(b) Plan view

Figure 4.8: Positions of probes for 70^o ONERA wing

The resulting signals from all the probes are collected in a series of files which are processed using a custom-made program, *Probe Analyser* created using Matlab. Details of this process were discussed in Chapter 2 and the theory behind the analyses are explained in Appendix B.

As discussed, there are two important numerical parameters in performing good DES calculations, the grid refinement and the time step size. Each will be considered separately before the validity and applicability of DES to delta wing vortical flows will be considered.

4.3 Effect of Time Step Refinement

The effect of temporal refinement is initially considered using the fine grid for three non-dimensional time steps with increasing refinement. These are $\Delta\tau = 0.01$, 0.005 and 0.0025. Each calculation was run for a similar total time, which meant that the number of time steps used for the calculation increased as the time step was decreased. From the calculations, a number of instantaneous domain files and the time histories of the probe files were obtained. These files will allow a comparison of the flow behaviour for each time step used as described in Section 2.7.

As mentioned in the previous section, a large number of probe locations were specified within the flow domain above the wing surface. To simplify and reduce the amount of data analysed, five probes were considered through the vortex core region. These probes sit at a constant height from the wing surface, $z/c_r = 0.1$, on the plane at a constant y/s station of 0.7. The five probe locations chosen occur at chordwise stations of $x/c_r = 0.53$, 0.63, 0.74, 0.84 and 1.00. Figure 4.9 shows these probes with instantaneous isosurfaces of x vorticity for the $\Delta\tau = 0.01$ solution as an example. This shows the behaviour of the vortex relative to the probe locations. The relative locations of the vortex and the probes are similar for the other two solutions.

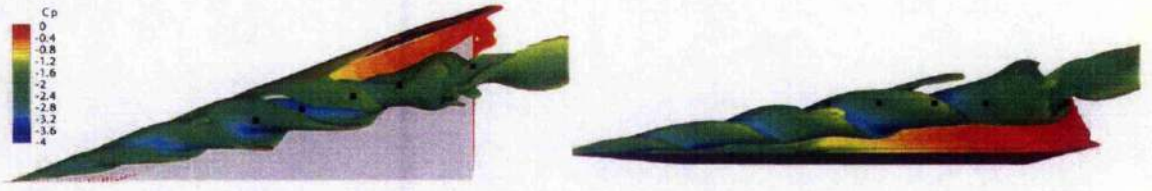

Figure 4.9: Isosurfaces of x vorticity coloured by pressure coefficient showing instantaneous vortex core behaviour at $\tau = 50$ with core probe locations marked for $\Delta\tau = 0.01$

Initially, the mean location of vortex breakdown was obtained for each solution by considering the flow domain output files at every full non-dimensional time period, $\tau = 1, 2\ldots$ etc. This effectively allowed a sample of the flow behaviour at every 100, 200 and 400 time steps for the $\Delta\tau = 0.01$, 0.005 and 0.0025 calculations, respectively. This provides a low sample rate, however for the purpose of calculating the mean location this was deemed sufficient.

From this analysis it was found that the mean breakdown location differed slightly for each case, occurring at $x/c_r = 0.88$ for $\Delta\tau = 0.01$, $x/c_r = 0.84$ for $\Delta\tau = 0.005$ and $x/c_r = 0.85$ for $\Delta\tau = 0.0025$. Initially, it was proposed that these differences may be due to the sample rate of the analysis as it was not expected that the time step should have a significant effect on the mean flow behaviour.

To consider this further, the mean and RMS velocity components were calculated for each of the probe locations. The results of this analysis are shown in Figure 4.10. It is evident from this figure that changing the time step does indeed have an effect on the predicted flow. However, with the exception of the w velocity, it is found that this mostly occurs in the region close to breakdown. For the u and v velocities, at $x/c_r = 0.53$ and 0.63 the predicted values are all in very good agreement and do not appear to be affected by temporal resolution. As the region of breakdown is approached, the difference between the coarse time step, $\Delta\tau = 0.01$ and the other solutions increases, however there is little difference between the finer time step solutions. The behaviour of the w velocity is different, with a larger difference between all the solutions being clear. For all locations there is a decrease in the velocity in the normal direction for the $\Delta\tau = 0.0025$ solution compared to the other time steps. This is particularly interesting as the agreement between the $\Delta\tau = 0.005$ and $\Delta\tau = 0.0025$ solutions is good for the other velocity components. However, this may be due to an inboard shift of the vortex core for this case, particularly as the RMS velocity values are similar. Closer to the breakdown region at $x/c_r = 0.84$, the differences in the mean flow increases for all velocity components.

Considering the mean u velocities with respect to the mean location of breakdown, mentioned above and it is clear that the breakdown location for the $\Delta\tau = 0.005$ and $\Delta\tau = 0.0025$ solutions may in fact be the same. However, the breakdown location for the coarse time step solution is clearly further downstream. Therefore, it is clear that the temporal refinement does have an effect on the location of the vortex breakdown in the flow. It is possible that this is due to the relative resolution and inter-dependency of the time step and grid refinement discussed previously. Particularly, as the RMS velocities in this region are very similar for each of the solutions. However, it is evident that the mean behaviour of the $\Delta\tau = 0.005$ and $\Delta\tau = 0.0025$ is very similar and therefore, it may be suggested that convergence of the time step has occurred.

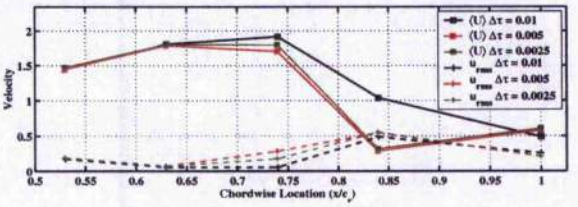

(a) u velocity

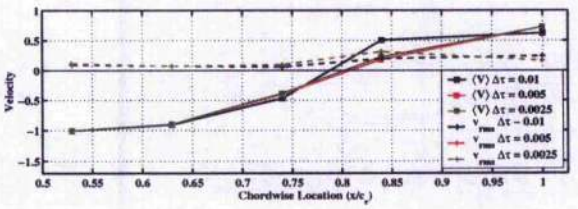

(b) v velocity

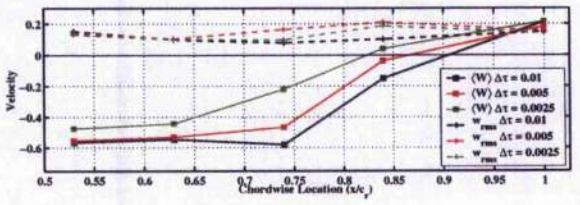

(c) w velocity

Figure 4.10: Mean and RMS behaviour of non-dimensional velocity components at five probe locations through vortex core region for each solution of the time step study

Figure 4.11 shows a slice through the vortex core region at $y/s = 0.7$ with instantaneous contours of y vorticity for each of the solutions. From these plots it is clear that despite some differences in the mean flow behaviour the

instantaneous behaviour is similar. The location of the vortex breakdown is close and the winding of the vortex core in the breakdown region is comparable. To compare the unsteady behaviour, a single probe above the trailing edge on the vortex core plane is considered for each solution. The time history of each velocity component was considered and a PSD analysis of the signal was performed. The results of this analysis are shown in Figure 4.12. At this location it is found from the time trace that the amplitude of the signals are very similar. However, it is clear that the signal behaviour is different, particularly the signal from the $\Delta\tau = 0.01$ solution which clearly exhibits a lower frequency oscillation that the other two signals. From the PSD analysis of these results, the dominant frequencies are determined and again the differences between the coarse time step and the other results is striking. Both the $\Delta\tau = 0.005$ and 0.0025 results show the dominant frequency to occur at approximately $St = 3.25$. However, for $\Delta\tau = 0.01$ this is lower at approximately $St = 2.25$. Similarly for the lower dominant frequency in the signals, the signal for $\Delta\tau = 0.01$ exhibits a frequency lower than the peak at $St = 0.07$ found for the other two results. The agreement between the $\Delta\tau = 0.005$ and 0.0025 unsteady behaviour is, again, very good, further suggesting that the time step has converged.

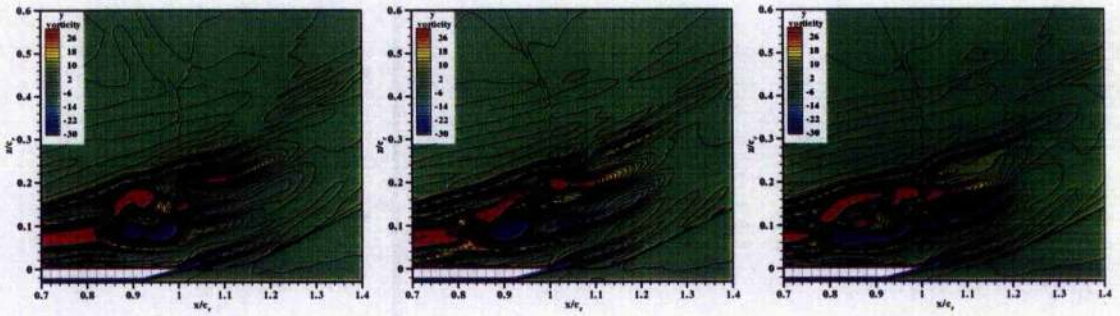

(a) $\Delta\tau = 0.01$ (b) $\Delta\tau = 0.005$ (c) $\Delta\tau = 0.0025$

Figure 4.11: Instantaneous contours of y vorticity on a slice through the vortex core region at $\tau = 50$

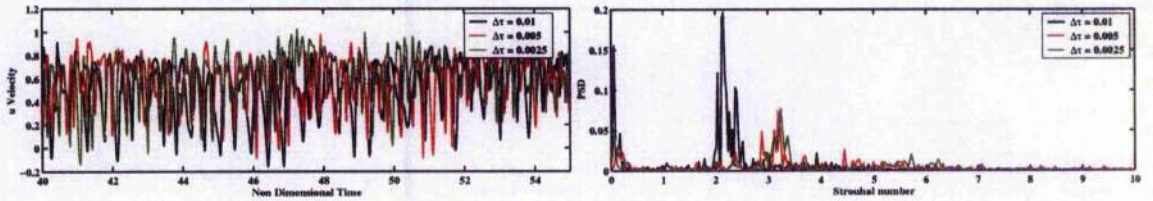

(a) u velocity

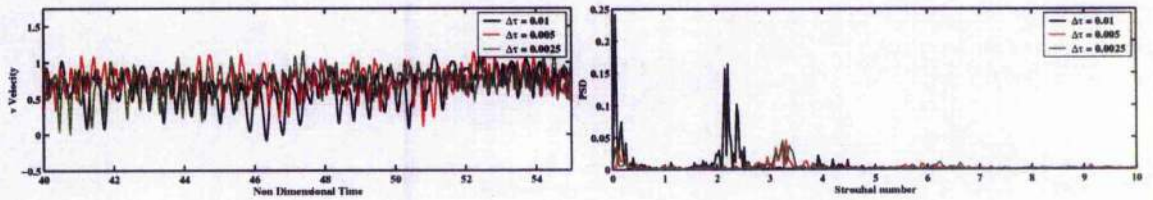

(b) v velocity

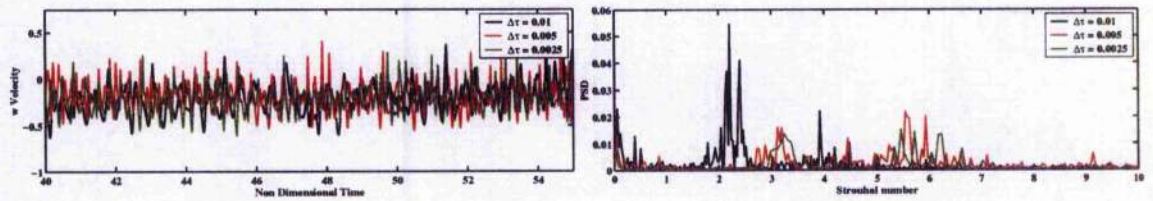

(c) w velocity

Figure 4.12: Unsteady behaviour of non-dimensional velocity components shown by time histories and PSD frequency plots for a probe at $x/c_r = 1.00$, $y/s = 0.7$ and $z/c_r = 0.1$; fine grid solutions for time steps of $\Delta\tau = 0.01$, 0.005 and 0.0025

To consider the appropriate time step for use in the DES calculations for this grid, the time step guide recommended by Spalart [177] was used. This uses the nominal grid size in the region of interest to define a guideline time step for a particular grid and was discussed in Section 2.6 and defined by Equation 2.91. From Figure 4.13, which shows the values of Δ_{max} on a plane at the trailing edge on the fine grid, it is clear that the nominal value in the region of interest is approximately 0.0055. Assuming that $U_{max} = 2.5$, the guideline time step can be calculated as $\Delta\tau = 0.0022$. Based on this analysis and the results of the comparisons of the unsteady behaviour detailed in this section it is concluded that the most suitable time step for use with this grid is $\Delta\tau = 0.0025$. From consideration of the time step calculations in Section 2.6, this should correspond to a maximum non-dimensional frequency of approximately $St = 40$.

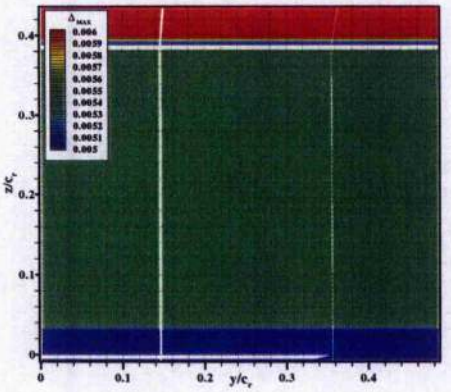

Figure 4.13: Δ_{max} of fine grid on slice at trailing edge, $x/c_r = 1.00$

4.4 Effect of Grid Refinement

From the fine grid results detailed for the time step study, it was noted that the flow behaviour and small scale flow structures appeared to dissipated too soon beyond the trailing edge. It was supposed that this was likely to be due to the large stretching ratio of the grid points in this region. To investigate this, a grid was created which had greater refinement in this region as shown in Figure 4.6 and described in Section 4.2.1. The grid was created from the fine grid and as such the maximum cell dimensions upstream of the trailing edge is the same for both grids as shown in Figure 4.14. However, for the new grid, this refined region was extended further downstream by improved grid refinement in the streamwise direction. This grid will be referred to as the "Refined TE Grid". A calculation was performed for this new grid using a non-dimensional time step of $\Delta\tau = 0.0025$ and the results were compared to the fine grid results, with the same time step, detailed in the previous section.

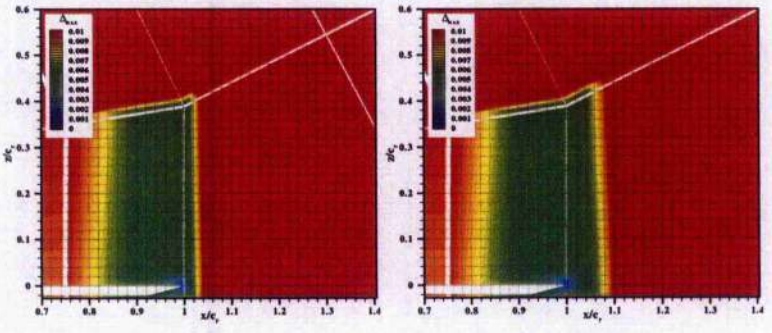

(a) Fine Grid (b) Fine Grid - Refined TE

Figure 4.14: Contours of Δ_{max} on a slice through the vortex core for both grids used in grid refinement study

A similar analysis to that conducted for the time step study was performed to consider the effect of the grid refinement at the trailing edge. However, a further three probes were considered downstream of the trailing edge to determine any changes in the flow at this location. These probes sit along the same plane as the probes described previously at streamwise stations of $x/c_r = 1.1$, 1.2 and 1.3 and were analysed in the same way. The location of the probes in the trailing edge region is shown in Figure 4.15, which shows instantaneous contours of y vorticity

for each grid through the vortex core region at the trailing edge. This figure highlights the relative behaviour of the wake region for each of the grids, with the vortex breakdown region being clear. It is apparent that the wake is swept in the direction of the freestream, which is upward from the wing surface. Thus, a fourth probe will also be considered which sits at a central location within the wake region at $x/c_r = 1.2$ and $z/c_r = 0.2$. This is also shown in Figure 4.15 and will be compared to the probe at the trailing edge, $z/c_r = 0.1$. From analysis of multiple instantaneous flow domain data files for each solution, it was found that the mean locations of vortex breakdown were very similar. This location is approximately $x/c_r = 0.86$ for the Refined TE grid solution.

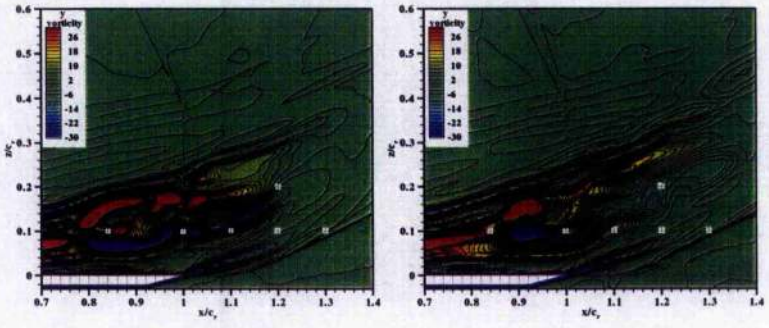

(a) Fine Grid (b) Refined TE Grid

Figure 4.15: Contours of instantaneous y vorticity on a slice through the vortex core for the fine and refined TE grid at $\tau = 50$

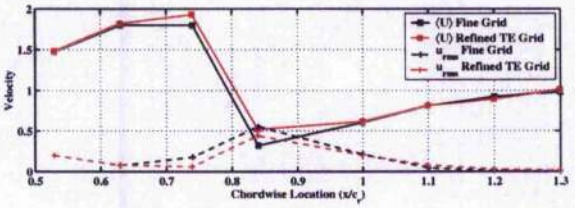

(a) u velocity

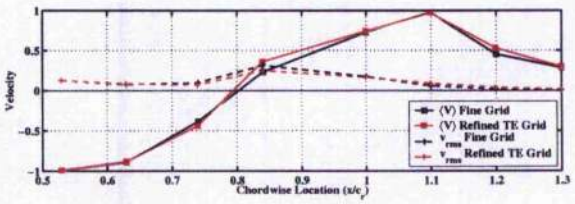

(b) v velocity

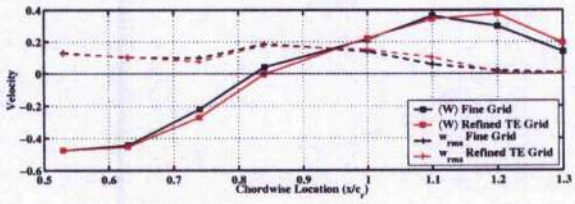

(c) w velocity

Figure 4.16: Mean and RMS behaviour of non-dimensional velocity components at eight probe locations through vortex core region for the fine and refined TE grids

The mean and RMS velocity components for the probes through the vortex core region are shown in Figure 4.16. From analysis of these plots, it is clear that the mean velocity behaviour at each of the probe locations both upstream and downstream of the trailing edge are very similar for the two grids. Due to the slight difference in the mean breakdown locations determined from the instantaneous domain files as described previously, there are some differences between the solutions close to the breakdown location. This is the case for all velocity components,

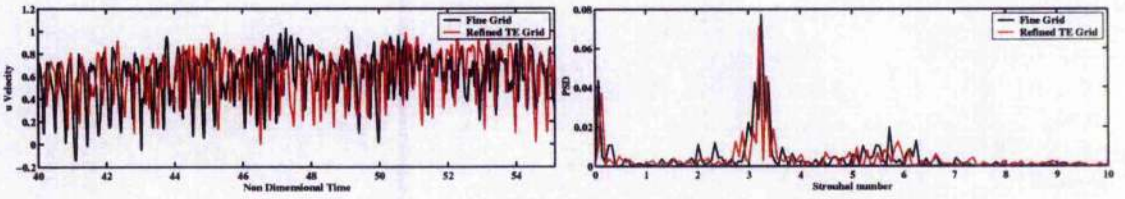

(a) u velocity

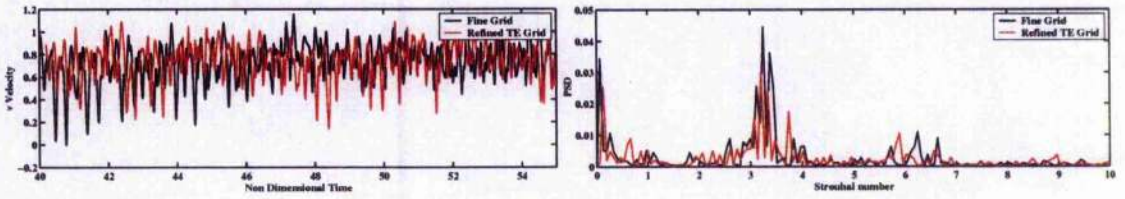

(b) v velocity

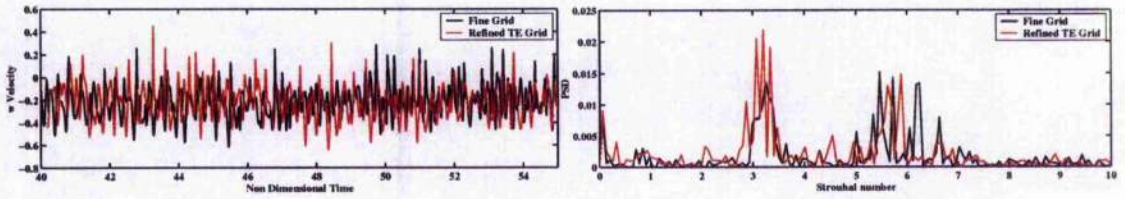

(c) w velocity

Figure 4.17: Unsteady behaviour of non-dimensional velocity components shown by time histories and PSD frequency plots for the probe at $x/c_r = 1.00$, $z/c_r = 0.1$ for the fine and refined TE grids

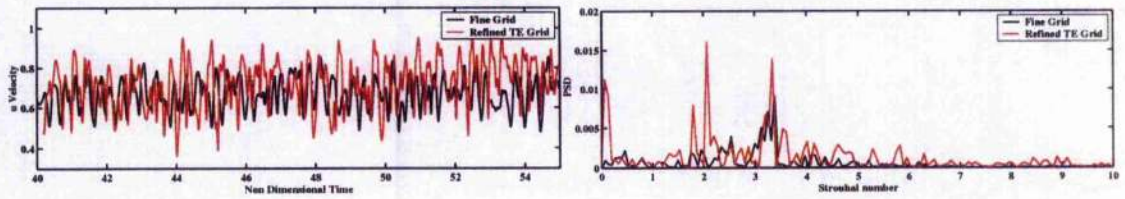

(a) u velocity

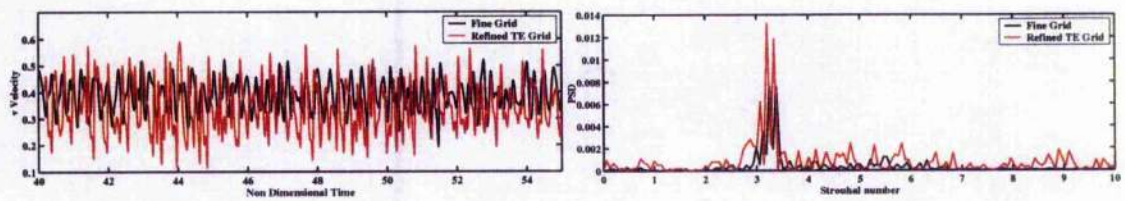

(b) v velocity

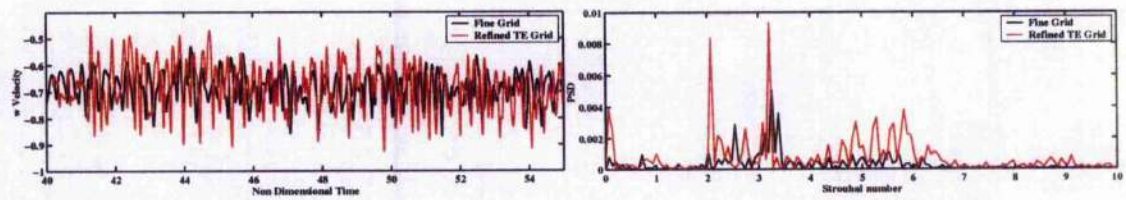

(c) w velocity

Figure 4.18: Unsteady behaviour of non-dimensional velocity components shown by time histories and PSD frequency plots for the probe at $x/c_r = 1.2$, $z/c_r = 0.2$ for the fine and refined TE grids

however, these differences are not significant. Downstream in the wake region, the agreement is very good and although there is a slight difference in mean w velocity at $x/c_r = 1.2$ overall the flow behaviour is very similar. These slight differences may be due to differences in the location of the probes in relation to the mean post-breakdown flow. The RMS velocities are also in very good agreement both upstream and downstream of breakdown. Downstream of the trailing edge, as the flow returns to freestream conditions beyond the wake, the RMS velocities tend to zero and the unsteady behaviour disappears.

Consideration of the unsteady behaviour on the two grids is obtained from analysis of the probe signals at the trailing edge and within the wake, as specified previously. The time histories and PSD analyses of the velocity components at the trailing edge probe are shown in Figure 4.17. From the time histories, it is evident that the mean and amplitude of the signals from the two solutions are very similar, which is in agreement with the mean and RMS plots discussed above. From consideration of the frequency content of the signals, evidence of the similarity of the two solutions is clear. All the dominant frequencies of the flow identified in the previous section, for this location on the fine grid, are captured in the Refined TE grid solution. The agreement is good for both frequency and magnitude. Therefore, it may be concluded that at this location and upstream, over the wing, the trailing edge refinement has little effect on both the mean and unsteady behaviour of the flow.

To consider the effect of the refinement on the unsteady behaviour further within the wake region, the time histories and PSD analyses for the probe at $x/c_r = 1.2$, $z/c_r = 0.2$ are shown in Figure 4.18. The time histories of each velocity component show that the refined TE grid predicts a larger amplitude than the fine grid, however the mean values appear to be similar. Also clear from the time histories for the refined TE grid is that there appears to be more fluctuations at higher frequencies. This is confirmed from the PSD analysis which shows more energy occurring at frequencies in the range $St = 8 - 10$ for all the velocity components. Also present in the u and w velocities for this solution, is a second dominant peak at $St \approx 2$, which has similar energy to the $St = 3.25$ peak. This frequency content is suggested by the fine grid results but is not well defined. Therefore, it is evident that the trailing edge refinement has an effect on the unsteady behaviour of the flow within the wake. However, this does not have an upstream effect on the flow over the wing and on the breakdown location. It is clear that the streamwise refinement of the grid does allow some higher frequency content to be predicted, however this is still lower than would be expected for turbulence and from Figure 4.15 it is clear that any small scale structures in the flow still dissipate quickly downstream of the trailing edge. This suggests that significantly more grid points are needed in the trailing edge region to capture the frequencies associated with turbulence. It may also be suggested that the overall refinement should be considered in this region and not just in the streamwise direction.

From this investigation, it is clear that the trailing edge refinement and resolution of the near trailing edge wake has little overall effect on the predicted unsteady behaviour of the flow upstream of the trailing edge, with only a slight downstream shift in mean breakdown location being found. However, the resolution of higher frequencies within the wake has been slightly improved. Therefore, as this will improve the DES solution overall, with more scales being resolved, it is concluded that the refined TE grid results will be used for the remainder of the DES investigation. However, throughout, it should be noted that the fine grid results are very similar.

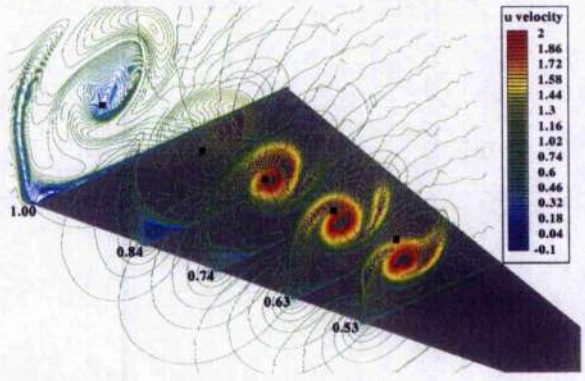

Figure 4.19: Location of probes though vortex core region compared to u velocity contours at each streamwise location

4.5 Evaluation of LES Region

As mentioned above, the best available solution from the DES calculations was that obtained using the Refined TE grid with a time step of $\Delta\tau = 0.0025$. Further analysis was performed on these results to consider the unsteady behaviour of the flow and the ability of DES to predict this behaviour.

4.5.1 Unsteady Behaviour of DES Solution

To consider the unsteady behaviour of the flow solution, the same five probes as used in Sections 4.3 and 4.4 are used. These are shown in Figure 4.19 relative to the vortex system at each streamwise location. From this Figure, it is clear that the probes at $x/c_r = 0.53$, 0.63 and 0.74 are upstream of vortex breakdown, with the probe at $x/c_r = 0.53$ sitting above the vortex core within the shear layer and probes at $x/c_r = 0.63$ and 0.74 close to the vortex core. The probe at $x/c_r = 0.84$ also sits within the vortex core and is found to be close to the mean vortex breakdown location, which was found to occur at $x/c_r = 0.86$. The probe at $x/c_r = 1.0$ is downstream of breakdown, below the vortex core winding. Keeping these locations in mind, the velocity components were analysed. This analysis was carried out by considering the mean and RMS values at each location and by evaluating the time histories and PSD frequency content of the signals. The results of these analyses are shown in Figures 4.20 and 4.21 respectively.

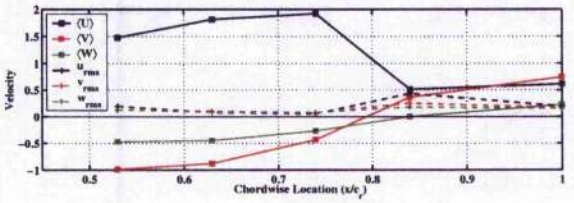

Figure 4.20: Mean and RMS behaviour of non-dimensional velocity components through vortex core

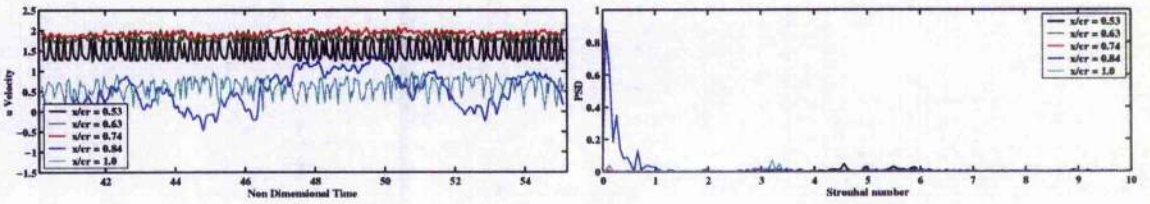

(a) u velocity

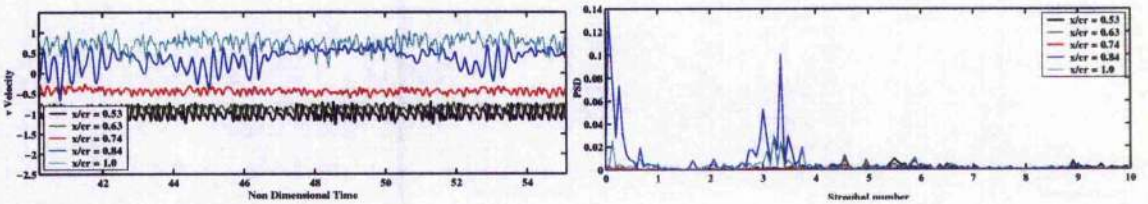

(b) v velocity

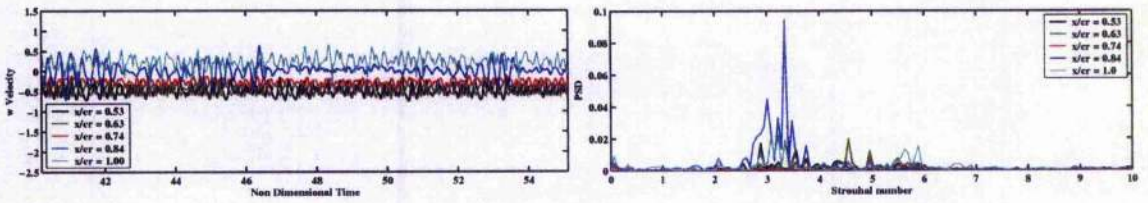

(c) w velocity

Figure 4.21: Unsteady behaviour of non-dimensional velocity components at probes through vortex core region shown by time histories and PSD frequency plots.

At $x/c_r = 0.53$, the time history of u exhibits a relatively large amplitude periodic oscillation with a high frequency. Closer to the vortex core at $x/c_r = 0.63$ and 0.74, the signal oscillation becomes more irregular and the amplitude decreases significantly. This reduction in amplitude is consistent with the reduction of the RMS values given in Figure 4.20 for these locations. At $x/c_r = 0.84$, the time history changes significantly from the upstream probes, with a high amplitude, low frequency oscillation being clear. This also coincides with a large increase in RMS velocity, however the mean velocity has decreased. The mean velocity at this location is positive. However, from the time history it is evident that the flow does reverse and that breakdown crosses the probe location. Downstream of the breakdown location the amplitude decreases and a more periodic waveform returns. The mean velocity at this point has only increased slightly compared to the $x/c_r = 0.84$ location, however the RMS value has decreased and the flow does not recirculate in this region (the u velocity does not become negative).

Considering the frequency content of the u velocity signals given by the PSD plots, a number of dominant frequencies at each of the probe locations is clear. The most dominant frequency found occurs for the probe at $x/c_r = 0.84$ at a non-dimensional frequency of approximately $St = 0.07$. Two other low frequencies are also apparent at $St \approx 0.27$ and 0.67 but there is little energy at higher frequencies at this location. As vortex breakdown is found to oscillate across this probe location, it may be suggested that this phenomenon produces this low frequency. Due to the energy in this low frequency being so large, the frequency content of the other probes is unclear using the scale of Figure 4.21. Therefore, Figure 4.22 shows the same PSD plot with the $x/c_r = 0.84$ signal removed. From this plot, it is clear that at $x/c_r = 0.53$, the high frequency content mentioned above corresponds to frequencies in the range $St = 4.5 - 6$, with frequency content also present at $St \approx 9$. Again, due to the location of this probe in the shear layer, it may be suggested that these frequencies are due to shear layer instabilities and structures, such as the Kelvin-Helmholtz instability. Downstream, close to the vortex core, it is apparent that there is little energy in the signal, however, with a further change in scale (not shown) it is found that at $x/c_r = 0.63$ there is a weak presence of the frequencies in the range $St = 4.5 - 6$ and at $x/c_r = 0.74$ the $St = 0.07$ frequency is weak but dominant similar to the downstream probe at $x/c_r = 0.84$. Finally, downstream of breakdown, a new range of dominant frequencies is found. These occur in the range $St = 3 - 3.5$, with a dominant peak at approximately $St = 3.25$. There are also frequencies present at approximately $St = 0.13$ and in the range $St = 5 - 6$. These frequencies are most likely to be connected to the upstream phenomena causing the frequencies discussed for the other probes.

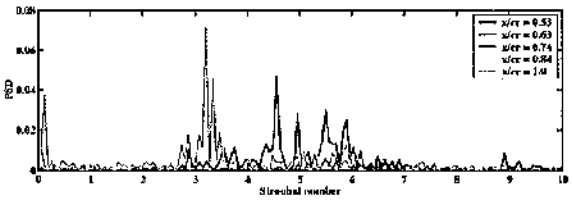

Figure 4.22: PSD of u velocity with $x/c_r = 0.84$ probe signal removed for clarity of frequency content of remaining probes

To consider the behaviour in the spanwise direction, the v component of velocity is considered. From Figure 4.19, it is evident that the probes upstream of breakdown do not sit exactly on the vortex core axis. This is confirmed from the mean velocity plot as the v velocity at each probe location does not have a zero mean. The probes at $x/c_r = 0.53$, 0.63 and 0.74 sit above the vortex axis and the probe at $x/c_r = 0.84$ sits below. The vortex core axis is crossed at approximately $x/c_r = 0.8$. As the vortex core axis is approached the RMS levels decrease, with an increase occurring close to vortex breakdown. Downstream of breakdown the RMS velocity decreases again. This is also apparent from the relative amplitudes of the time histories shown in Figure 4.21(b). As before the fluctuations at $x/c_r = 0.84$ are greater than for the other probe locations with an obvious low frequency content. This frequency corresponds to that found for the streamwise velocity, $St \approx 0.07$, and shows that the vortex breakdown location also oscillates in the spanwise direction. However, unlike for the streamwise velocity there is also a higher frequency range present in the signal at $St = 3 - 3.5$. Which corresponds to the frequency identified as being caused by the vortex core winding downstream of breakdown. Therefore, it may be suggested that the helical winding mode causes a spanwise motion of the vortex core close to breakdown. At $x/c_r = 0.53$, the amplitude of the signal is less than that found for the streamwise velocity, however the frequency content is similar with the dominant frequencies occurring at $St = 4.5 - 6$ and $St \approx 9$. The frequency content of the probes at $x/c_r = 0.63$ and 0.74 is also very similar to the streamwise velocity plots, however the power of the response at $St = 4.5 - 6$ increases at $x/c_r = 0.63$. Thus, the shear layer instabilities appear to have a greater effect on the vortex in the spanwise direction. Downstream of breakdown, the behaviour is again comparable to the streamwise velocity, although the strength of the signal is lower.

Finally, the normal w velocity is considered in the same way. Again, from the mean velocity plot it is evident that only the probe at $x/c_r = 0.84$ sits exactly on the vortex core axis due to its zero mean. Upstream of this location the probes sit inboard of the axis as the normal velocity is negative at these locations. The behaviour of the RMS velocity is very similar to the spanwise velocity as the trailing edge of the wing is approached. Considering the time histories, it is evident that the amplitudes of the signals are comparable to those for the spanwise velocity. However, the frequency content is, again, slightly different. For the probe at $x/c_r = 0.53$, it was found that dominant peaks occur at $St \approx 3$ and 3.5 with the frequency at $St = 4.5$ becoming more prominent compared to the other velocity components. There is also no peak found at $St = 9$ for this case, suggesting that the shear layer instabilities have no higher frequency normal component at this location. Overall it appears, that the frequencies in the w velocity signal are lower than for the other components. Downstream at $x/c_r = 0.63$, there is also energy at frequencies of $St = 4.5 - 5$. At $x/c_r = 0.84$, the most striking difference in the frequency content compared to the other velocity components is the disappearance of the low frequency peak at $St = 0.07$. This suggests that there is no vertical motion of the vortex breakdown location. However the dominant frequencies at $St = 3 - 3.5$ are still evident, caused by the rotation of the helical mode of breakdown just downstream of this location. At the trailing edge, this frequency is also found, with another dominant frequency occurring at $St = 5.5 - 6$.

From this analysis, it is clear that there are a number of identifiable features, both upstream and downstream of the breakdown location with relatively low frequencies. Upstream, the flow is dominated by a strong vortical system, containing both primary and secondary vortices. Close to the vortex core this flow exhibits only small fluctuations and the influence of other flow phenomena is apparent. Within the shear layer, evidence of shear layer roll up instabilities, such as the Kelvin-Helmholtz type instability have been found from the frequency data at $St = 4.5 - 6$ and ≈ 9. At breakdown, the flow is dominated by the motion of the breakdown location which oscillates in the streamwise and spanwise direction at a very low non-dimensional frequency of $St = 0.07$. Downstream of breakdown, the helical mode instability is present and the frequencies corresponding to its rotation and general behaviour have been isolated, $St = 3 - 3.5$, and specifically a dominant peak at $St = 3.25$. A summary of the frequencies determined for each flow feature is given in Table 4.4 in a similar manner to Table 4.1.

Phenomenon	*Strouhal Number*
Helical Mode Instability	$3 - 3.5, 3.25$
Shear Layer Instabilities	$4.5 - 6, \approx 9$
Vortex Breakdown Oscillation	0.07

Table 4.4: Frequencies corresponding to important unsteady features of vortical flows from unsteady DES results

It is in the post-breakdown flow where turbulent behaviour is expected to be found as the vortex breaks down and loses its structure. However, from these results it is clear that the helical mode winding exhibits coherent periodic behaviour, which suggests that it is not driven by turbulent phenomenon. In fact, all the phenomena described above have been found to occur for a range of configurations as detailed in Table 1.2, and none appear to be dependent on turbulence within the flow. Further evidence of this may be obtained from the results of a highly under resolved (both spatially and temporally) DES calculation which was performed on the coarse grid described in Section 4.2.1 using a time step of $\Delta\tau = 0.01$. Using such a coarse calculation, it is not likely that any small scale fluctuations will be captured and indeed from the time history and PSD plot for the same probe location shown in Figure 4.23 it is clear that none are found. It is clear from the PSD analysis that the frequency of the helical mode instability is identical for this case at $St = 3.25$ and although no small scale structures were captured this had no effect on the prediction of the vortex breakdown winding and its frequency.

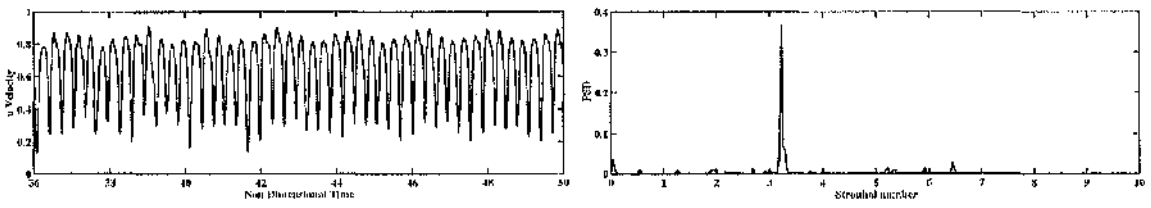

Figure 4.23: Non-dimensional u velocity time history and PSD for a probe on the vortex axis, downstream of vortex breakdown, from a highly under-resolved DES solution, coarse grid, $\Delta\tau = 0.01$

This conclusion is also confirmed from consideration of the literature. A number of numerical investigations have been performed using both inviscid [23] and laminar [111, 112] methods, which clearly show the helical mode instability behaviour. These investigations and their results were discussed in detail in the literature review of Section 1.5.

4.5.2 Decomposition of LES Solution

It seems possible that the majority of the frequencies captured by the DES calculation can be attributed to the large scale, coherent, low frequency flow phenomena discussed above. As these unsteady flow phenomena are dominant flow features and an inherent part of the unsteady flow behaviour, they may be considered as part of the mean flow and not part of the unsteadiness due to turbulence. Thus, in the post-breakdown flow, the turbulence should be treated as non-stationary. Considering the discussion of non-stationary turbulence and LES given in Chapter 2, the decomposition of the instantaneous velocity was described in Equations 2.38 - 2.40 and can be summarised as,

$$u_i = \underbrace{\langle U_i \rangle + u_i'' + \phi u_i'}_{\textit{Resolved on grid}} + \underbrace{(1-\phi)u_i'}_{\textit{modelled by SGS}} \tag{4.1}$$

The unsteady flow phenomena described above may be said to contribute to u_i'', the unsteady part of the mean flow. The DES signals shown in Figure 4.21 can then be thought of as being made up of the sum of the mean, unsteady mean flow component and a percentage of the turbulence resolved on the grid. To identify each of these components and their respective behaviour, the u velocity signal was time averaged in a similar manner to that used for the URANS method and given by Equation 2.21. By applying this method, the non-stationary mean may be separated from the turbulent fluctuations of the signal. However, the non-stationary mean is determined from the time averaging sample rate, T, and therefore care should be taken when choosing this parameter. For non-stationary turbulence, the sample rate should be large in comparison with the turbulence time scales but small in comparison with the mean flow fluctuation time scales. To investigate the optimum sample rate for the DES solutions, consideration was given to the u velocity signal from the probe at the trailing edge, $x/c_r = 1.0$, detailed in the previous section. Figure 4.24 shows the PSD of this signal against both the non-dimensional frequency, St, and the non-dimensional period of the oscillation, $1/St$. Considering the analysis given in the previous section, it is clear that there is a dominant frequency in the flow at approximately $St = 3.25$, which has been attributed to the motion of the helical mode instability. At this location higher frequencies are also present in the flow, around $St = 6$, but it is not clear if these are related to a coherent structure in the flow in this region. Therefore, it is taken that the highest mean flow frequency is $St = 3.25$, which corresponds to a non-dimensional period of 0.31.

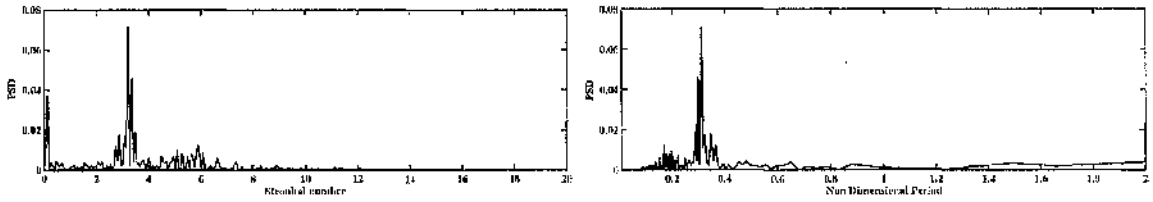

(a) PSD vs. St

(b) PSD vs. Non dimensional period

Figure 4.24: PSD against St and non-dimensional period for non-dimensional u velocity for a probe at $x/c_r = 1.0$ on the vortex core axis.

Using this period as a starting point, the time average of the signal was calculated with the resulting time histories and PSD analysis plots shown in Figure 4.25. In each plot, the calculated fluctuating mean and the original signal are shown, with the stationary mean shown in the time histories for comparison. As the initial sample rate is equal to the period of the expected mean flow it is clear that it is insufficient to capture all the mean flow fluctuations. Indeed the dominant frequency of the mean flow, at this sample rate, is equal to the vortex breakdown oscillation. Therefore, the sample rate was increased and the mean flow was recalculated for $T = 0.1$, 0.05 and 0.01 as shown in Figure 4.25. It is clear from this analysis, that as the sample rate was decreased, more of the flow features were captured within the mean flow. Until at $T = 0.01$ the mean signal and the original signal coincide.

As the two signals coincide at a sample rate of $T = 0.01$, which is four times the time step used for the calculation and an order of magnitude larger, it is evident that despite refining the time step, as detailed in Section 4.3, the level of temporal resolution has not increased. For a time step of $\Delta\tau = 0.0025$ it was expected that the maximum resolvable frequency would be approximately $St = 40$ (based on a minimum of 5 samples per fluctuation, see Section 2.6). However, it is clear that this level of resolution has not been obtained and the effective time step of the solution is approximately $\Delta\tau = 0.01$. This corresponds to a maximum frequency of $St = 10$ which is closer to the maximum frequencies found in the PSD analyses. As both the spatial and temporal refinement are equally important for DES calculations, it may be suggested that this under-resolution of the frequency content of the flow is due to the grid not being refined enough in the post-breakdown flow region, where the turbulence will begin to form.

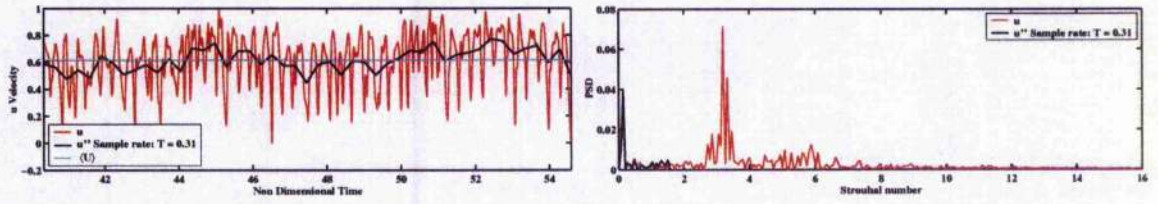

(a) $T = 0.31$

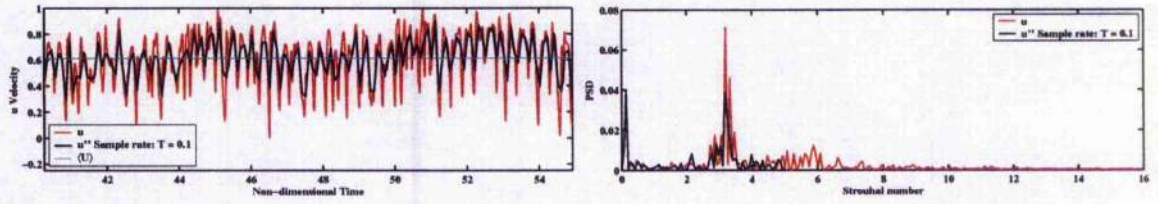

(b) $T = 0.1$

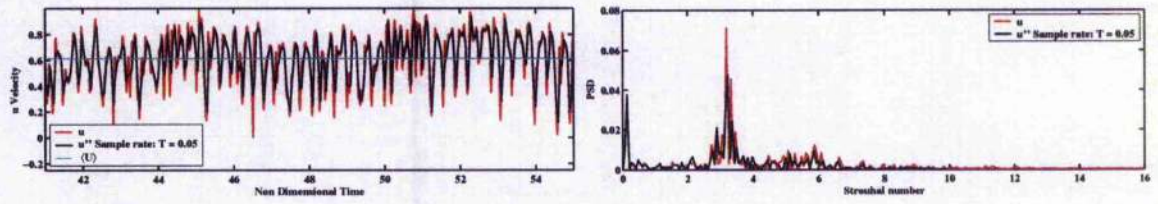

(c) $T = 0.05$

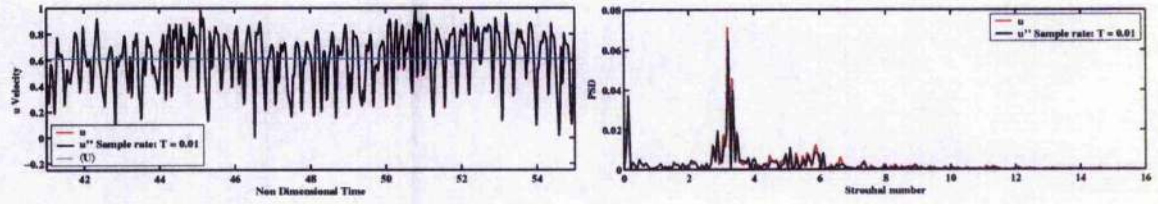

(d) $T = 0.01$

Figure 4.25: Non-dimensional u velocity time histories and PSD plots for a probe on the vortex axis, downstream of vortex breakdown showing both the stationary and non-stationary mean at different sample rates

4.5.3 Resolution of DES Solution

To consider this further it is necessary to examine the behaviour of the unsteady flow on the grid in this region. For an unsteady and turbulent flow it should be possible to see the fluctuations of flow parameters on the grid. As discussed previously, the grid is used as a spatial filter and, thus, the size of the cells are used as the spatial sample rate, in a similar manner to the use of the temporal sample rate, $\Delta\tau$. However, as also mentioned before, it is not practical to keep this sample rate uniform throughout the regions of interest for delta wing geometries. Figure 4.14(b) shows contours of Δ_{max} for the refined trailing edge grid in the vortex core region which shows the changes in grid size over the post-breakdown region. From this plot, it is clear that in the region of interest, close to the trailing edge the grid size is relatively constant at approximately $0.0055c_r$. Using this as the sample rate, the maximum wavenumber of the spatial resolution can be determined. In Spalart's guide to DES grid generation [177], it is suggested that the minimum wavelength of a structure captured by a grid will be equal to five times the maximum grid size i.e. $5\Delta_{max}$. Using this as a guide, it can be calculated that the minimum non-dimensional wavelength captured in this region will be $0.0275c_r$. This corresponds to a maximum non-dimensional wavenumber of approximately $\kappa = 18$ and a minimum eddy size of $0.055c_r$ due to the Nyquist criterion.

To confirm this analysis, a 1-D slice through the vortex core region ($y/s = 0.7$) was taken at a constant height above the wing surface ($z/c_r = 0.1$). Treating this slice in the same way as a time trace, with x/c_r being analogous to time, the data was analysed using the probe analyser program as before. Figure 4.26 shows the results of this

analysis. In a similar manner to a time history, a plot of u velocity against x/c_r is plotted for the flow downstream of breakdown. This shows that only large scale fluctuations appear to occur downstream of the breakdown location. Consideration of the PSD analysis of this signal confirms this, as the dominant peak occurs at a wavenumber of approximately $\kappa = 0.5$ (not shown). However, it was found that there is energy at higher wavenumbers up to approximately $\kappa = 18$, although very small. Most of the energy on the grid is found for wavenumbers less than 10, which is similar to the temporal analysis. This suggests that although smaller eddies are captured by the grid, they are very weak in comparison with the larger structures.

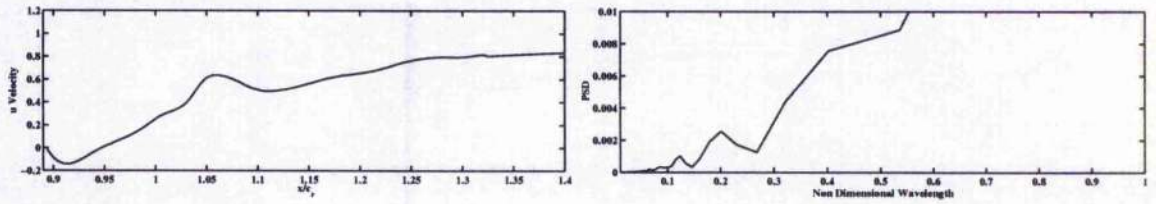

(a) Spatial history

(b) PSD vs. Wavelength

Figure 4.26: Analysis of u velocity behaviour from spatial slice through vortex core at $z/c_r = 0.1$ to determine resolution of grid

The physical size of these eddies can be considered from analysis of the non-dimensional wavelength of the signal, as shown in Figure 4.26(b). The wavelength is calculated as the inverse of the wavenumber. This plot is very interesting as it shows that the minimum wavelength captured on the grid is also close to $0.05c_r$. However, the lowest clear peak is 0.11. Confirmation of the size of the captured eddies may be taken from the contours of y vorticity shown in Figure 4.15(b), which clearly show structures with diameters of approximately 0.06. It is evident from this analysis that the minimum eddy size is still approximately 5% of the root chord, which is relatively large, particularly with respect to the expected size of any small scale turbulent eddies, which would be less than $1\%c_r$.

To consider how this spatial under-resolution would affect the temporal resolution of the solution, it is possible to relate the frequency of the eddies to their wavelength, and therefore wavenumber, using the local velocity magnitude. This relationship is defined as,

$$St = u_{local}\kappa \tag{4.2}$$

As the velocity at a given location will fluctuate in time, this relationship may only serve as a guide to the effect on the temporal resolution. However, in the post-breakdown flow, the instantaneous velocity is almost always less than the freestream velocity. Therefore, the maximum non-dimensional frequency resolved on the grid will be less than 18. The ability of the spatial and temporal sampling rate to capture the turbulence may be determined by considering a log-log plot of the PSD analysis. Figure 4.27 shows the results of this analysis. The spatial resolution can be compared to the Kolmogorov -5/3 slope, which describes the theoretical behaviour of the energy within the turbulence for the inertial subrange. It is clear that there is very good agreement with the theory, thus the grid is capturing the energy cascade well, despite the maximum resolved frequency being low in comparison to the turbulent scales. For a further refined grid, it would be expected that this gradient was maintained, however there would be more power at higher frequencies and more of the unsteady flow behaviour would be resolved.

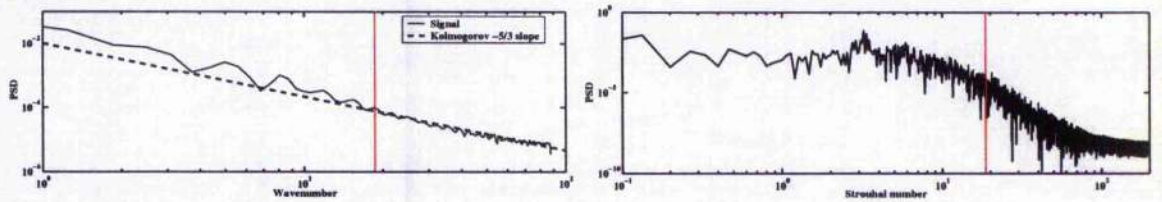

(a) Spatial - PSD vs. κ

(b) Temporal - PSD vs. St

Figure 4.27: Turbulent spectrum for both spatial and temporal scales to show accuracy of energy cascade within computational results

The temporal resolution plot is created from the non-dimensional u velocity at the post-breakdown probe location detailed previously and also shows the maximum resolvable frequency. It is clear that beyond this point the gradient of the plot increases and the energy within the scales reduces rapidly as the frequency content of the flow is

modelled by the subgrid scale and so is not present in the time trace of the velocity.

Therefore, from this analysis, it has been shown that in the post-breakdown region, the unsteady flow exhibits non-stationary mean flow and turbulent fluctuations. From the decomposition of the instantaneous velocity given in Equation 4.1, we can attribute the mean flow fluctuations to u_i'' based on a sample rate of $T = 0.01$ for the time average. However, this shows that there are few turbulent fluctuations captured in the DES signal and so ϕ, the level of turbulence captured by the grid, is close to zero. This means that the majority of the turbulence for this solution is modelled by the subgrid scale model. Further analysis on the grid shows that the maximum eddy size captured by the grid is approximately $5\%c_r$, which is large for turbulent scales. This confirms that the grid in the post-breakdown region is under-resolved and that the LES region is in fact acting in a similar way to a URANS model. However, despite the under-resolution of the results, it is clear that the characteristic behaviour of vortex breakdown is captured and so the question arises: What effect does the turbulence downstream of vortex breakdown have on the overall flow behaviour? It may be proposed that the turbulence downstream of breakdown and the trailing edge has a minimal effect on the mean flow behaviour, such as the helical mode instability and its characteristic frequency. Therefore, it may also be proposed that URANS may be able to adequately predict this behaviour at smaller computational expense. However, before testing this proposal, it is necessary to validate the DES solution with existing DES and experimental data.

4.6 Qualitative Comparison with Cobalt Results

It is helpful to compare the results with other DES calculations. One of the most prominent users of DES for delta wing vortical flows is the United States Air Force Academy (USAFA) [24, 29, 30, 116, 161, 163]. A great deal of work was carried out by the USAFA, using the unstructured flow solver, *Cobalt*, as part of the NATO RTO Task Group AVT-080 [197, 200]. This group considered the behaviour of the flow on the 70° ONERA test case used here. As there is a great deal of experience at the USAFA, it was felt that a qualitative comparison with their results would give an indication on how well the structured DES results were performing and, therefore, would allow a benchmark of the current results.

As the majority of the unsteady results obtained from the AVT-080 Task group involved only the behaviour of the normal force coefficient, further data was needed to consider the flow behaviour in the post-breakdown region. Thus, the unsteady results from the VFE-2 case, described in Chapter 3, will be used as well. Despite this case being transonic, the non-dimensional behaviour of the flow should generally be similar and thus a qualitative comparison may be made.

4.6.1 Comparison with 70° ONERA SA-DES Results

The USAFA geometry for the 70° wing differs slightly to that used in the current investigation as the trailing edge has not been bevelled and is blunt, similar to the experimental configuration. Another difference is that the USAFA solutions have been obtained with the experimental Mach number of $M = 0.069$. This discrepancy should not make a significant difference to the results, particularly if the non-dimensional behaviour is considered.

A time step study was carried out by Morton *et al.* and is detailed in Ref's [24] and [161]. Six different time steps of varying refinement were considered for a baseline grid with 2.7×10^6 cell volumes. The non-dimensional time steps were: $\Delta\tau = 0.00125, 0.0025, 0.005, 0.01, 0.02$ and 0.04. Using the PSD data of the resulting normal force coefficients, and plotting the PSD against the non-dimensional period $(1/St)$ it was found that with decreasing time step the dominant frequency of the flow approached an asymptotic period of approximately 0.1 ($St = 10$). From this investigation, a baseline time step of $\Delta\tau = 0.0025$ was deemed to be the optimum for accuracy and for reasonable computational expense for this grid size. This can be compared to the time step study detailed in Section 4.3, where it was also found that the non-dimensional period of the dominant frequency reduced with a reduction in time step size.

The effect of grid refinement has also been considered and is detailed in Ref's [29, 30, 116, 163]. In these investigations a number of grids of varying refinement were created and the solutions compared. Adaptive mesh refinement (AMR) was also used to determine the effect of localised refinement in the areas of interest. The baseline grid described above was initially used and a factor of $\sqrt{2}$ was then applied to scale the initial overall refinement and to create grids with 1.2×10^6, 6.7×10^6 and 10.6×10^6 cell volumes. The AMR grid was created from the baseline grid solution with isosurfaces of vorticity being used to define the region where the grid would be refined. This was performed twice, with the distribution of grid points being doubled each time. Overall, this resulted in a grid

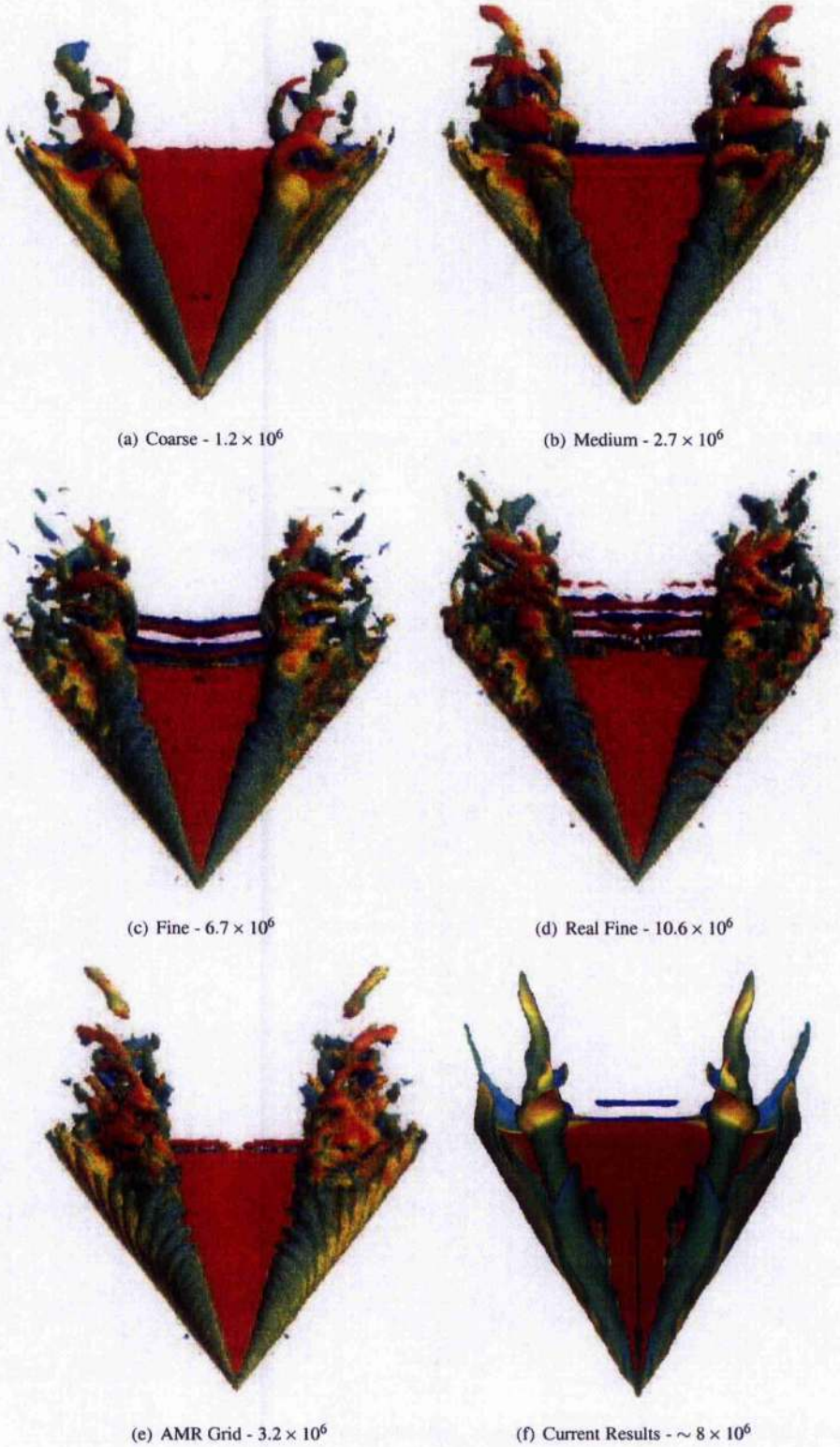

(a) Coarse - 1.2×10^6

(b) Medium - 2.7×10^6

(c) Fine - 6.7×10^6

(d) Real Fine - 10.6×10^6

(e) AMR Grid - 3.2×10^6

(f) Current Results - $\sim 8 \times 10^6$

Figure 4.28: Isosurfaces of vorticity for various USAFA unstructured grids compared to current results on refined trailing edge structured grid. The number of cell volumes for each grid are given for comparison. [29]

with 3.2×10^6 cells. The non-dimensional time steps used were also scaled to the size of the grid, with a time step of $\Delta\tau = 0.0025$ being used for the baseline grid and the factor of $\sqrt{2}$ being applied in a similar manner as before. Table 4.5 details the time step and grid size for the coarse, baseline and fine grids. The table also contains details of the cell size in the focus region as described in Ref. [177]. These features are also included for the refined TE grid used for the current results.

	Cells	Δ_{max}	$\Delta\tau$
USAFA Coarse	1.2×10^6	0.0065	0.00357
USAFA Medium (baseline)	2.7×10^6	0.0046	0.0025
USAFA Fine	6.7×10^6	0.0035	0.0018
Current Results	$\sim 8 \times 10^6$	0.0055	0.0025

Table 4.5: Details of grid features for USAFA grid study and comparison with current results

It is interesting to note that the maximum cell dimensions in the focus region for the baseline grid, Δ_{max}, is close to that used for the current results, however the overall size of the USAFA grid is much smaller. This is due to the refinement in the region of interest having to be carried out to the far field for the structured grid. This increases the grid size and the relative computational expense. Therefore, the structured grid is of comparable refinement to the baseline grid from the USAFA results. This is also clear from comparison of the flow solutions. Figure 4.28 shows instantaneous isosurfaces of vorticity magnitude for each of the grids, and highlights the increasing resolution of the flow structure with increasing grid refinement. From this, it is evident that the level of vortical structures captured by the current results is between the coarse and the baseline grid solutions. It is also interesting to note that the AMR grid is comparable in flow resolution to the fine grid with 6.7×10^6 cell volumes.

To consider the unsteady aspects of the flow, the time histories of normal force coefficient were used for analysis. Figure 4.29 shows the comparisons between a) the coarse, medium and fine grids; b) the very fine grid (G4), an AMR grid of 2.4×10^6 cells (G9A4) and a similar AMR grid with sting and wind tunnel walls included (G7A1) and c) the current results. From these plots it is clear that as the overall refinement of the grid increases, the unsteady behaviour captured also increases and there is more energy in the higher frequencies. This is in agreement with the findings of the grid study for the current results detailed in Section 4.4. It would be expected that the highest frequencies captured would be much higher for the finer grids, however considering the current results it appears that the relative level of energy in the higher frequencies is similar. It should be noted that the scale of the PSD for the current results differs to the USAFA results. It is possible that this may be due to the method chosen to calculate the PSD of the signal and may not be a reflection of the level of energy in the flow. What is important, in this comparison, is the relative energy of the signals, which appear to be very similar. It is also clear that the dominant frequency of the current results is lower than for the finer grids of the USAFA study, sitting at approximately $St = 5 - 6$ compared to $St = 8 - 10$ respectively.

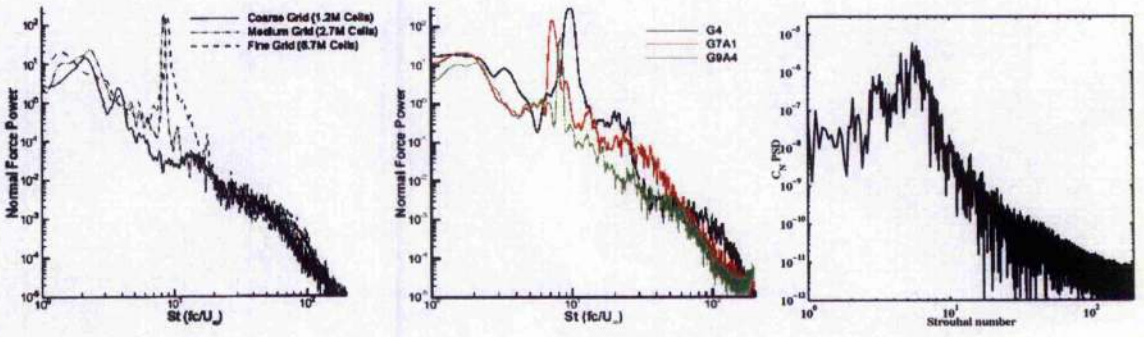

(a) USAFA Results [24] (b) USAFA Results [30] (c) Current Results

Figure 4.29: PSD plots of normal force coefficient for current results compared to USAFA results from literature

In Ref. [30], the resolution of turbulent kinetic energy in the vortex core was considered for the coarse, baseline, fine and very fine grids detailed above. This is shown in Figure 4.30, with a comparison of the current results. From the study it was found that as the grid resolution was increased, the value of the turbulent kinetic energy in the vortex core approached the experimental value of 0.5. Thus, the turbulent properties of the flow were concluded to be resolved well for the finer grids. However, as the time averaging analysis of vortical flow in Section 4.5.2

shows, these values are high as the mean flow fluctuations will be included in the calculation of the turbulent kinetic energy. The plot of the current results shows the mean non-dimensional turbulent kinetic energy calculated, both using the stationary mean (as in the experimental and USAFA results) and the non-stationary mean (calculated using a sample rate of $T = 0.1$), which is subtracted from the signal before the fluctuating velocities are used. It is clear that there is a significant difference between the results, particularly close to breakdown, where the mean flow fluctuates considerably. However, the results obtained from the stationary mean do give reasonably good agreement with the USAFA results, particularly if the location of vortex breakdown is considered. Which occurs for $x/c_r = 0.5$, 0.58, 0.62 and 0.62 for the coarse, baseline, fine and very fine grids respectively and at a mean location of $x/c_r = 0.86$ for the current results. Unfortunately, it is not possible to state the peak value for the current results, as this will occur downstream of breakdown and there are insufficient point probes in the vortex core region to determine this value.

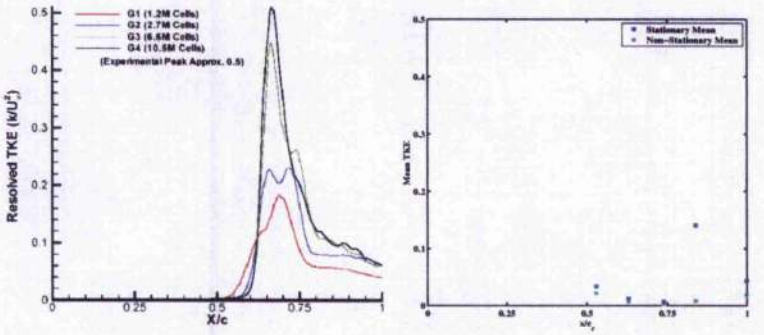

(a) USAFA Results (b) Current Results

Figure 4.30: Comparison of turbulent kinetic energy through vortex core between current results and USAFA results from literature

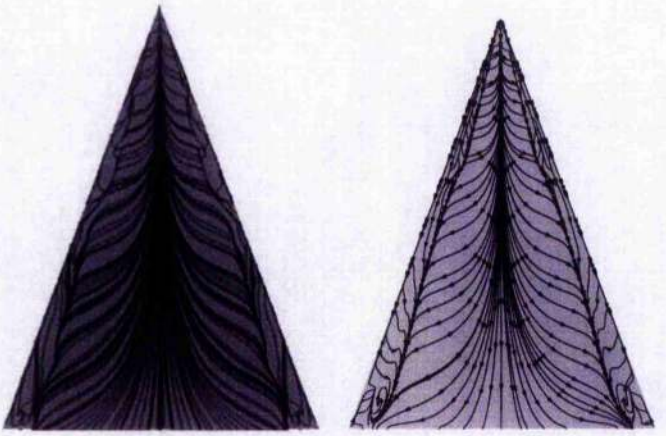

(a) USAFA Results [30] (b) Current Results

Figure 4.31: Comparison of surface streamlines between current results and USAFA results from literature

As stated in Section 4.2.2, a transition study was carried out by Morton [30] to consider the influence of a forced transition location on the computational results and therefore on the comparison with the experiment. The conclusions of this investigation stated that a forced transition line at constant $x/c_r = 0.4$ gave the most appropriate agreement with the experimental results. This investigation provided the basis for the choice of transition line applied in the current investigations which corresponds to a constant line at approximately $x/c_r = 0.36$. To consider the behaviour of the flow due to transition, the surface streamlines are compared in Figure 4.31. From these two plots, it is clear that the behaviour on the surface of the wing is very similar. As expected, the transition occurs slightly upstream for the current results. However, this does not appear to have a significant effect on the downstream flow. Both plots are taken from instantaneous results, however the current results do not exhibit any clear evidence of unsteadiness in the streamlines. In contrast, the secondary separation line for the USAFA results

shows undulations which may be associated with the unsteady nature of the flow. Interestingly, both solutions exhibit "whorl" patterns in the trailing edge region, close to the leading edge. Initially, for the current results, this was attributed to recirculation of the flow due to the bevelled trailing edge. However, the USAFA geometry was exactly reproduced from the experiment and had a blunt trailing edge. Further investigation of this region is needed to determine the cause of this phenomenon. This region is unclear from the experimental results.

4.6.2 Comparison with 65^o VFE-2 SA-DES Results

To allow further comparisons of the unsteady behaviour of the Cobalt DES solutions with the current results, the unsteady data from the VFE-2 solutions described in Chapter 3 were used. Details of the grid and time step, detailed previously, are summarised in Table 4.6. In a similar way to the current results, a number of point probes were situated in the flow as described previously. To make detailed comparisons, but to restrict the amount of data used, two probes from these calculations were chosen to compare qualitatively with the 70^o test case results. These probes were situated on the vortex core, which for this case sits at a constant $y/s = 0.6$, at a constant height, $z/c_r = 0.1$ from the surface of the wing for locations pre- and post-breakdown, $x/c_r = 0.7$ and 0.9 respectively. As discussed in Chapter 3, the mean location of breakdown for this case was found to be $x/c_r = 0.68$. These probes are to be compared to the signals from the probes on the vortex core at $x/c_r = 0.84$ and 1.0 detailed before for the current results. Although the locations of these probes are quite different, the non-dimensional distance from the mean vortex breakdown location are similar. $x/c_r = 0.02$ and $x/c_r = 0.04$ upstream and $x/c_r = 0.22$ and $x/c_r = 0.14$ downstream of breakdown for the USAFA and current results respectively. Therefore, a qualitative comparison of the flow behaviour may be made for these locations. Figure 4.32 shows the probe locations for the USAFA results, with isosurfaces of x vorticity shown to demonstrate the location with respect to the flow features. This can be compared to Figure 4.19 for the current results.

	Cells	*Grid Type*	$\Delta\tau$
USAFA	7.89×10^6	Unstructured	0.0047
Current Results	$\sim 8 \times 10^6$	Structured	0.0025

Table 4.6: Details of grid and time step for USAFA VFE-2 calculation and current results

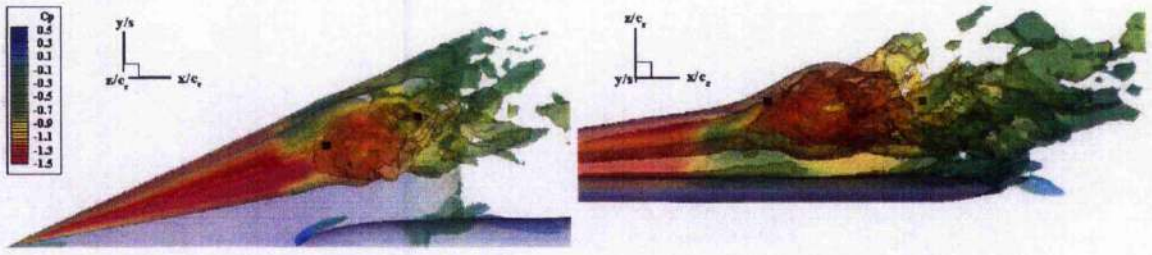

(a) Plan view

(b) Side view

Figure 4.32: Location of probes through vortex core with reference to isosurface of x vorticity for 65^o VFE-2 USAFA DES calculation

Figures 4.33 and 4.34 show the non-dimensional velocity component time histories and PSD frequency plots respectively for both cases in pre- and post-breakdown flow. In Figure 4.33 the time histories of each case are shown separately due to the differences in non-dimensional time and likewise, for clarity Figure 4.34 shows the PSD analysis of the pre-breakdown and post-breakdown results separately for comparison between cases. From the time histories, particularly for the u velocity, it is clear that there are many similarities between the two results. In both cases, the location of vortex breakdown periodically moves upstream of the pre-breakdown probe location. This is evident from the low frequency, high amplitude behaviour and the magnitude of the u velocity traces periodically reducing to less than zero, indicating reversed flow. The fluctuations of the location of breakdown seem to be more pronounced for the USAFA case, however this is likely to be due to the presence of shocks in the flow, which have been shown to move abruptly. It is also clear from consideration of all three velocity components that when the breakdown location is upstream of the probe, there is less unsteadiness in the flow. Again, this is more pronounced for the USAFA case, however the amplitude of the current results also noticeably decreases at this point. Considering the frequency content of the solutions at this location shows that the dominant frequency of the flow is in good agreement at approximately $St = 0.1$. However, the power of the USAFA signal at this frequency is

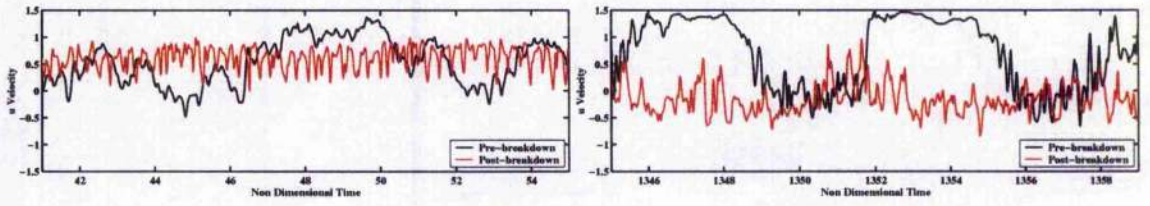

(a) u velocity

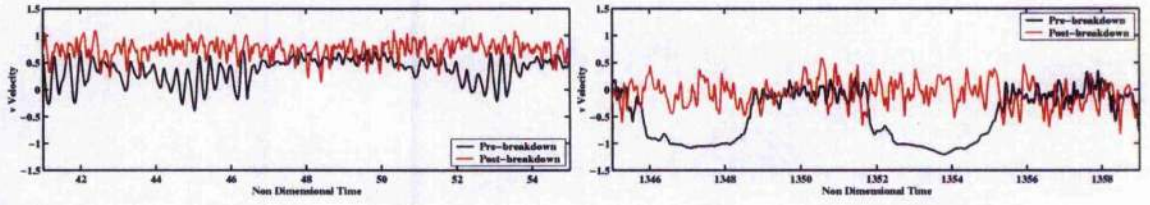

(b) v velocity

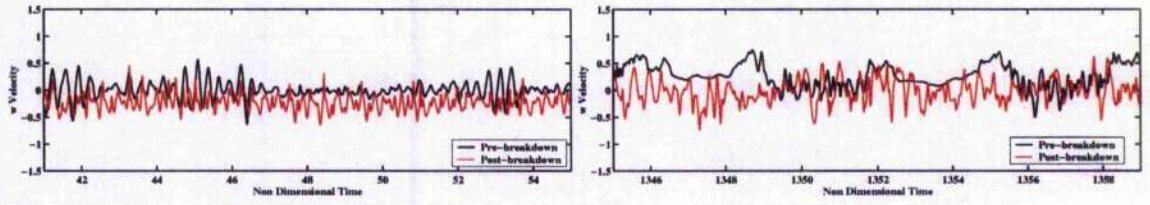

(c) w velocity

Figure 4.33: Comparison between time histories at similar probe locations on the vortex core in the pre- and post-breakdown flow. Current results on the left hand side and USAFA results on the right.

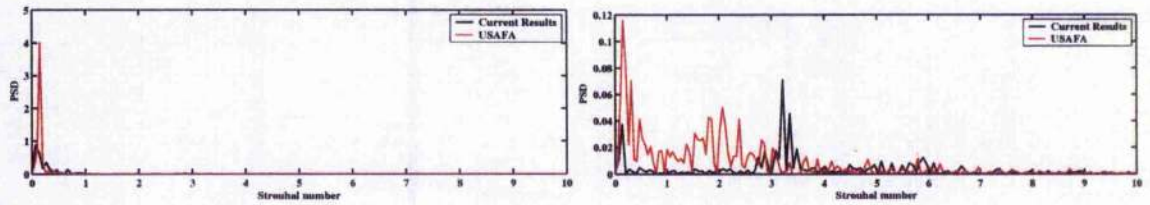

(a) u velocity

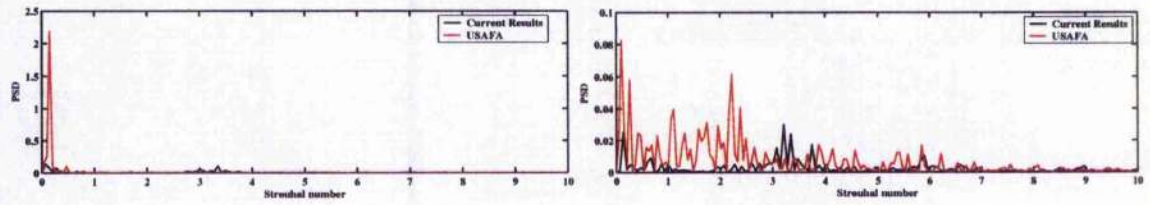

(b) v velocity

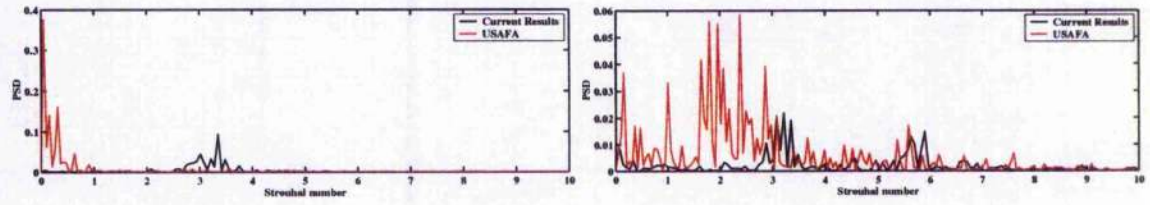

(c) w velocity

Figure 4.34: Comparison between PSD frequencies at similar probe locations on the vortex core in the pre- and post-breakdown flow. Pre-breakdown results on the left hand side and post-breakdown results on the right.

greater, again likely due to the occurrence of shocks in the flow. For the current results, higher frequencies between $St = 3$ and 4 are evident in the spanwise and normal velocity components, due to the influence of the helical mode winding, downstream of breakdown. This is not found in the USAFA solutions, but again this is likely to be caused by the presence of the shocks which will not allow any instabilities to propagate upstream.

Downstream of breakdown it is clear that the flow behaviour is again very similar. The amplitude of the time traces is in good agreement, particularly for the u and w velocities. However, mean values are different. For the u velocity this is likely to be due to differences in the severity of breakdown between the subsonic and transonic test cases, as described in Chapter 3. Whereas for the v and w velocities, this is likely to be caused by differences in the location of the probes with respect to the vortex breakdown structures, such as the helical mode instability. Considering the frequency content of the two signals for each velocity component, it is clear that there are more frequencies present for the USAFA results. However, the low frequency response of the vortex breakdown location is still found for both cases, as is a frequency which can be associated with the helical mode. This is close to $St = 2$ for the USAFA results and $St = 3 - 4$ for the current results, as stated previously. The occurrence of many more frequencies within the post-breakdown flow signal, may be attributed to the presence of more smaller structures occurring in the flow for the USAFA solution, as shown in Figure 4.32. However, it is interesting to note that there is still little frequency content for frequencies close to or above a Strouhal number of 10, which would be expected for small scale turbulent structures.

To consider this further, analysis of the turbulence on the grid was performed in a similar manner as shown in Section 4.5.3. A 1-D slice is taken through the vortex core region at $z/c_r = 0.1$ and a PSD analysis is performed to consider the spatial behaviour of turbulence. This analysis was then compared to the current results shown previously. Figure 4.35(a) shows the behaviour of the u velocity on the slices for both results, downstream of the breakdown location. As the location of breakdown is different for each solution, the relative distance from the breakdown location is used. It is clear from this plot that there are more fluctuations of the u velocity in the post-breakdown region for the USAFA results. Performing a PSD analysis on this data allows the wavenumber content to be considered and the resolved eddy sizes and wavelengths to be determined. The results of this analysis are also shown in Figure 4.35. Compared to the results for the current grid, it was found that the dominant peak in the PSD analysis also occurs at a wavenumber of $\kappa = 0.5$. It was also found that there is more energy in the larger wavenumbers for the USAFA results, however the maximum wavenumber resolved is still only approximately $\kappa = 20$. This translates to a minimum wavelength of approximately $x/c_r = 0.035$, which is found from Figure 4.35(b). This is not significantly higher than the minimum wavelength of the current grid. Despite this similarity of minimum scales, more energy appears in the flow for all wavenumbers. This may be a consequence of the resolution of smaller scales which capture the energy transfer more accurately, due to a smaller sample rate and therefore less turbulence modelled on the grid.

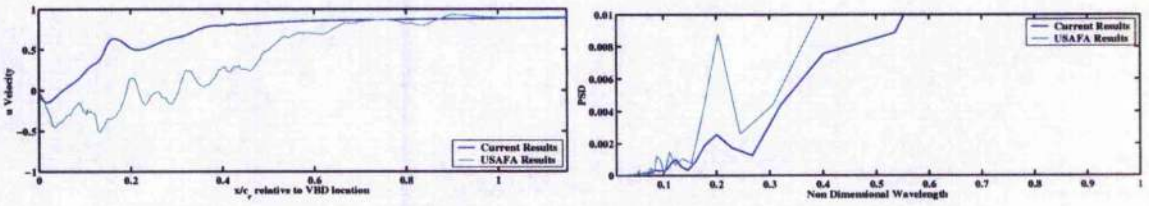

(a) Spatial history relative to vortex breakdown

(b) PSD vs. Wavelength

Figure 4.35: Analysis of u velocity behaviour from spatial slice through vortex core at $z/c_r = 0.1$ to determine resolution of grid for both current results and USAFA 65^o VFE-2 DES results

As before, further consideration of the level of turbulence captured in the flow solutions can be obtained by comparing the log of the PSD plot with the Kolmogorov -5/3 slope. Figure 4.36 shows this comparison along with the temporal comparison for the non-dimensional u velocity at the trailing edge. It is evident from both plots that the general frequency behaviour is very similar between the two sets of solutions. Although the USAFA grid exhibits slightly more energy at higher wavenumbers in the spatial comparison, the temporal comparison is nevertheless very similar, with the same gradient to higher frequencies being present. Therefore, despite the higher grid resolution of the USAFA solution demonstrated by the smaller scale structures found in the post-breakdown flow and the greater frequency content, it may be stated that a similar level of turbulence is captured by each solution.

From the comparisons with the USAFA results for the 70^o and 65^o test cases, it has been found that the overall flow behaviour is being captured well by the current DES solutions. However these results appear to be under resolving the smaller flow features due to lack of refinement in the post-breakdown region.

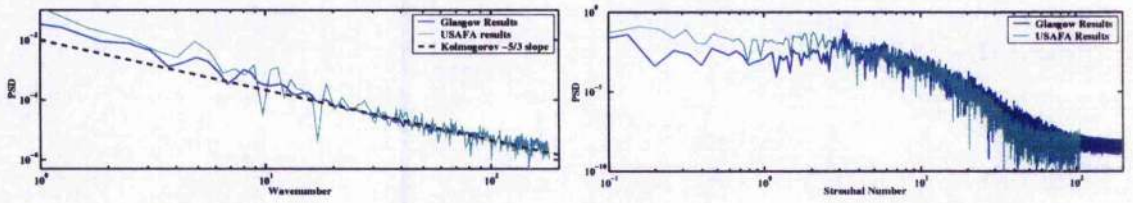

(a) Spatial - PSD vs. κ compared to Kolmogorov -5/3 slope

(b) Temporal - PSD vs. St for u velocity from probe in post-breakdown flow at $x/c_r = 1.00$

Figure 4.36: Spatial and temporal comparisons of current and USAFA DES results

4.7 Validation of DES Results

As shown in the previous section, the current results agree qualitatively with other DES results. However, it is also important to gauge the behaviour of the solutions against experimental results. The experimental test data gathered by Mitchell [13] will be used mostly for this task, however unsteady data from other experiments will also be considered qualitatively to further assess the validity of the results.

4.7.1 Comparison with Mitchell's Experiment

The set up of the experiments carried out by Mitchell was described in Section 4.2 and as such will not be discussed here. A large proportion of the data presented in Mitchell's work was time averaged. This time averaging process is akin to calculating the stationary mean of the flow and does not take the unsteady mean flow, as discussed in Section 4.5, into account. This makes comparisons between the computational and experimental results difficult, particularly as the turbulent quantities calculated will be considerably larger than those which may have existed. This was also considered when considering the levels of turbulent kinetic energy compared to the USAFA results in Section 4.6.

Instantaneous full domain flow solutions could not be used to compare with the time-averaged experimental data. Therefore, a stationary mean was calculated from 100 time steps, over a total time of $\tau = 1$, which gives a sample rate of $T = 0.01$. This provides a relatively small period over which to average, but the amount of data needed to perform a full mean calculation over the all the calculation time steps was prohibitive. Due to this, the comparisons should be treated with caution, but should be sufficient for the purposes of validation of the basic flow behaviour.

Figure 4.37 show contours of the non-dimensional velocity components for each of the chordwise stations for both the experiment and the mean computational flow. From the contours of u velocity it is clear that for the experimental data breakdown occurs upstream of the $x/c_r = 0.74$ position, as at this location reversed flow is found. Indeed, from the investigation it was found that the mean position of breakdown occurred at approximately $x/c_r = 0.65$. Considering the current results, it is clear that the location of breakdown is quite different, with reversed flow not being predicted for any of the slices. As stated in previous sections, the mean breakdown location was found to occur at approximately $x/c_r = 0.86$, which is downstream of the slices used in the experiment. The discrepancy of mean vortex breakdown location may be due to many factors. It was mentioned in the highlights of the RTO AVT-080 task group that this set of experimental data was affected by blockage and support interference effects, which may have caused up to $2-3^o$ of upwash. It was stated that this upwash may have caused breakdown to occur earlier on the wing than would have been expected for this configuration. Other factors include, imperfections on the experimental model due to the sting fitting, the differences in freestream velocity between the experiment and computation as it was noted by Mitchell that with an increase in freestream velocity that the breakdown location moved downstream, or the levels of turbulent eddy viscosity predicted in the computational results. From both the grid study and time step study it was shown that the predicted location of breakdown did not change significantly with any change in grid density or time step refinement, thus the DES calculations are consistent. Further consideration of the prediction of vortex breakdown location will be given in the following chapter. This discrepancy of location should also be kept in mind when considering the unsteady nature of the flow, which will be discussed later in this section.

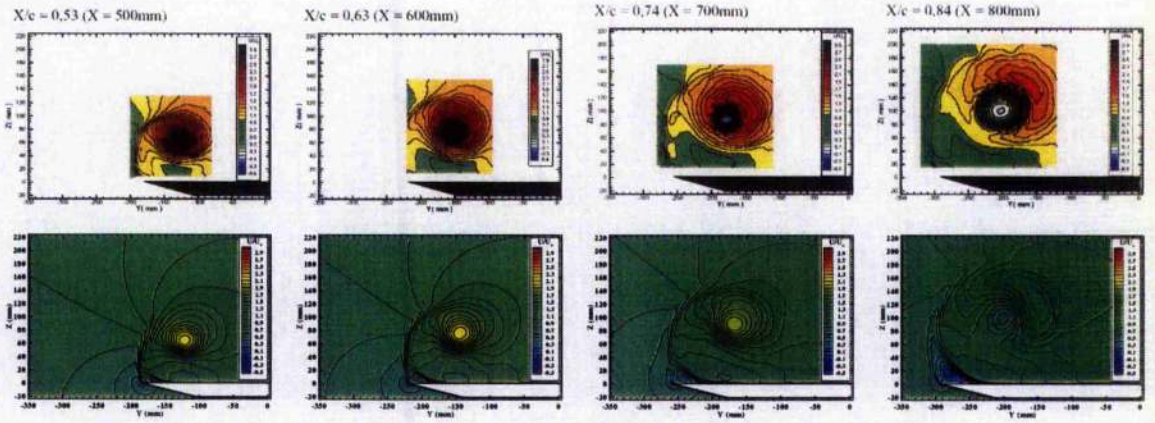

(a) u velocity

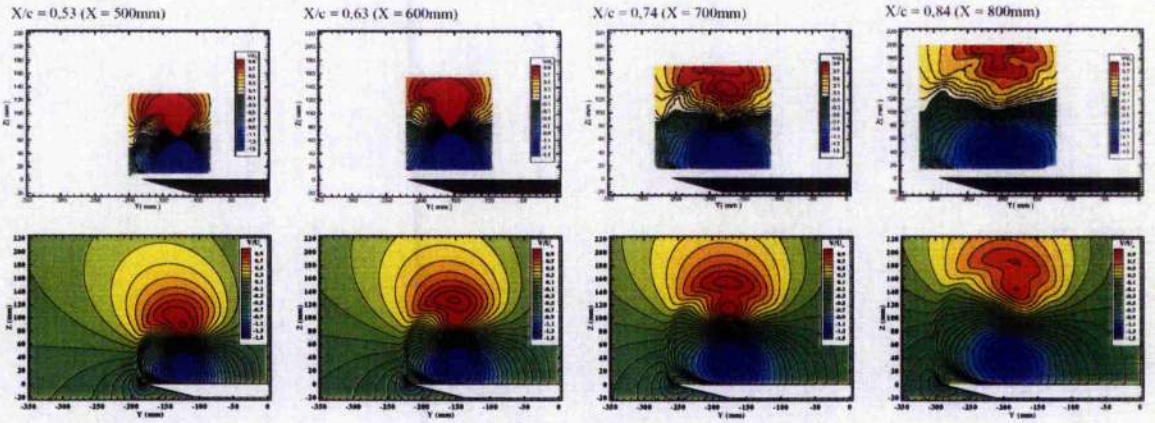

(b) v velocity

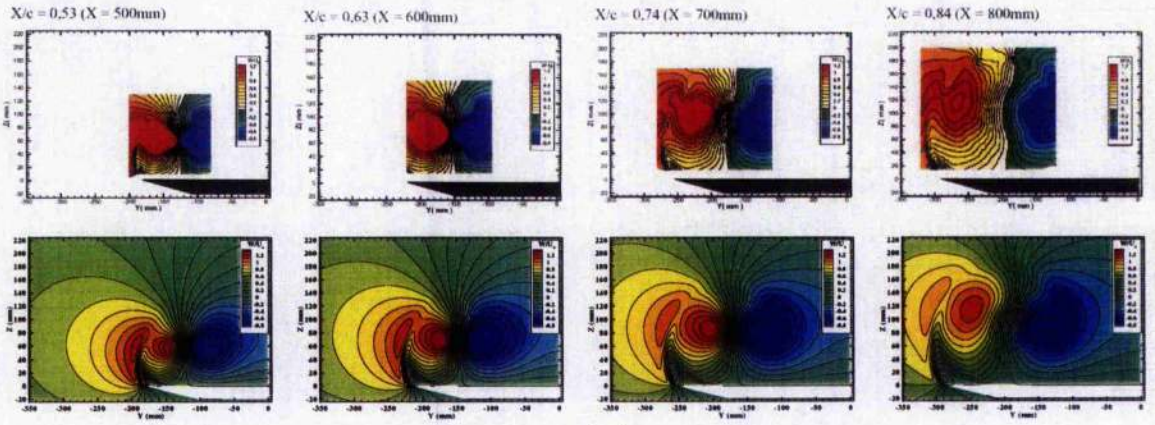

(c) w velocity

Figure 4.37: Time averaged velocity results from Mitchell's experiment compared to mean computational results

From the contours of u velocity, it is also found that the maximum axial velocity of the vortex core prior to breakdown was approximately $4U_\infty$. The mean predicted value from the current results, is found to be considerably less and is given as approximately $2.2U_\infty$. This is consistent with the findings of the AVT-080 task group, where a number of calculations were performed for this test case using various CFD solvers, techniques and grids. The axial velocity was not found to be accurately predicted for any of the cases and it was concluded that the grid refinement at the vortex core was not sufficient. Considering the v and w velocity contours, however, it is clear that the agreement between the experimental and computational solutions is very good with the magnitude and shape of the velocity contours being predicted well, despite the differences in breakdown location.

Contours of x vorticity were also considered and the comparisons are shown in Figure 4.38. In the experimental plots, it is clear that there are small vortical substructures in the shear layer. However, these structures are not found in the computational results for these contour levels, despite the unsteady probe data providing evidence of oscillations associated with such phenomenon. Evidence of these structures is found by changing the contour levels, however this shows that the predicted behaviour is weak. As with all the other experimental contour plots, the boundary layer region is not captured due to the experimental techniques used, which cannot resolve the flow close to walls. However, there is a suggestion of a secondary vortex in the bottom left corner of each contour plot. This is also shown in the computational results, with the location of both the secondary and primary vortices being predicted well.

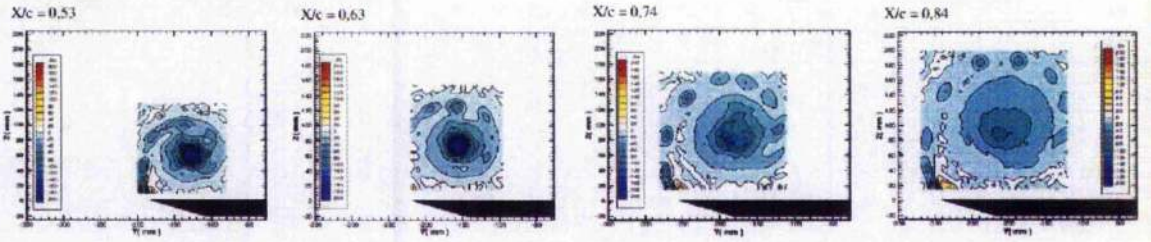

(a) Experiment [13]

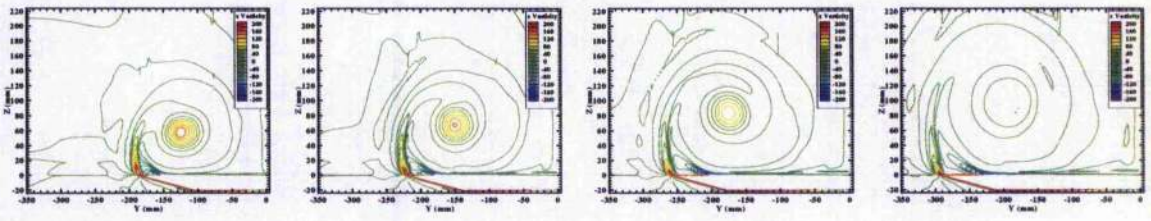

(b) Current Results

Figure 4.38: Time averaged x vorticity results from Mitchell's experiment compared to mean computational results

Comparisons can also be made with the experimental surface pressure coefficients obtained from steady pressure transducers on the surface of the wing at the same chordwise locations. Figure 4.39 shows these comparisons for the current results. Also included is data from two investigations carried out as part of the AVT-080 task group, from the USAFA [30], as detailed in the previous section and from work carried out at NLR on a structured grid using a URANS $k-\omega$ model with a modification for vortical flows [31]. It is clear that although the computational results are in good agreement there is a consistent under-prediction of the pressure coefficient compared to the experimental results. For the current results, this corresponds to a difference of 24% for the $x/c_r = 0.53$ peak. For the USAFA and NLR results it was reported that the difference was 24% and 22.4% respectively. Other computational results from the AVT-080 task group, using both DES and URANS methods, were also found to exhibit these discrepancies with the experimental data and differences at $x/c_r = 0.53$ of 23.8% were reported [165, 196]. As all the computational results were in good agreement and factors such as grid refinement, transition and turbulence model had no effect, it was determined that the differences may have been due to a scaling issue with the experimental data.The current results scaled by 24% are also shown in Figure 4.39 to allow a broad comparison with the computational results. This shows that generally the agreement is good when all streamwise results are scaled by this factor. However, due to the blockage and support interference effects mentioned previously, this straight-forward scaling can not account for all the physical differences in the flow and should be considered with care.

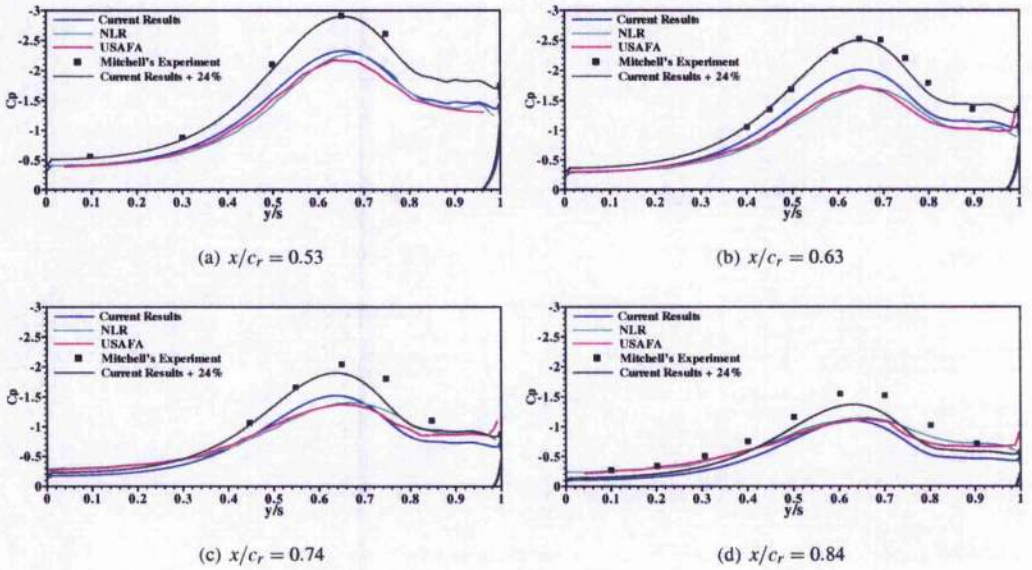

(a) $x/c_r = 0.53$ (b) $x/c_r = 0.63$

(c) $x/c_r = 0.74$ (d) $x/c_r = 0.84$

Figure 4.39: Surface pressure coefficient data for both experimental and computational results [13, 30, 31]

To consider the unsteady nature of the flow behaviour pressure readings were taken from Kulite^{TM} pressure transducers on the surface of the wing as detailed in Table 4.3. The numbering and location of each of the probes to be compared are shown schematically in Figure 4.40. The resulting unsteady pressure time histories are shown in Figure 4.41. Also shown are the corresponding time histories for 12 of the transducer locations taken from the unsteady probe data on the surface of the wing.

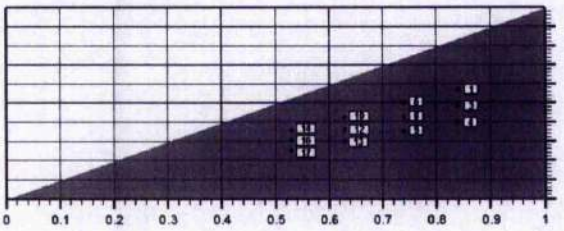

Figure 4.40: Location of unsteady probes used for comparison with Mitchell's data

It is clear from these traces that the mean pressure decreases with outboard movement on the wing. This suggests that the vortex core sits either above or close to the $y/s = 0.7$ position. In the computational results, the vortex core is also found to be close to this location. The mean computational pressure coefficients have been scaled by the 24% factor discussed previously to aid in the comparison and it is clear that they are in reasonably good agreement. The highly unsteady nature of the flow is obvious, both up- and downstream of breakdown, with reasonably large amplitude oscillations occurring at many frequencies. The length of the corresponding signals should be considered before any comparisons can be made, with the experimental data being captured over 2 seconds and the total computed time being equivalent to approximately 0.2 seconds. The corresponding computational time is marked on the experimental plots for comparison. However, despite this difference, qualitative and quantitative comparisons can be made. It is clear that the amplitude of the unsteady fluctuations of almost all the probes are in good agreement, with the most obvious exception being Probe 1 at $x/c_r = 0.84$. In the experimental data, the signal from this probe exhibits some rather strange behaviour with the pressure coefficient decreasing significantly in what appears to be a random pattern. This was noticed by Mitchell, who decided that it was the response of a faulty transducer, thus this signal will not be considered for comparison.

To consider the frequency content of the signals, PSD were calculated from each signal. These are shown in Figure 4.42, again with similar plots for the current results. The plots taken from Mitchell's work have been altered slightly to show the corresponding non-dimensional frequencies for comparison. From the experimental plots, upstream of breakdown at $x/c_r = 0.53$ and 0.63, the flow behaviour is dominated by a low frequency oscillation, which occurs at approximately 2Hz ($St = 0.08$). There is evidence of some higher frequency broadband content,

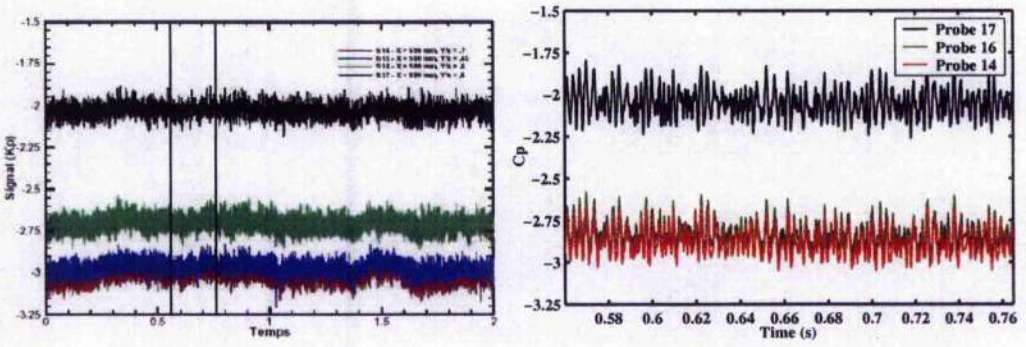

(a) $x/c_r = 0.53$

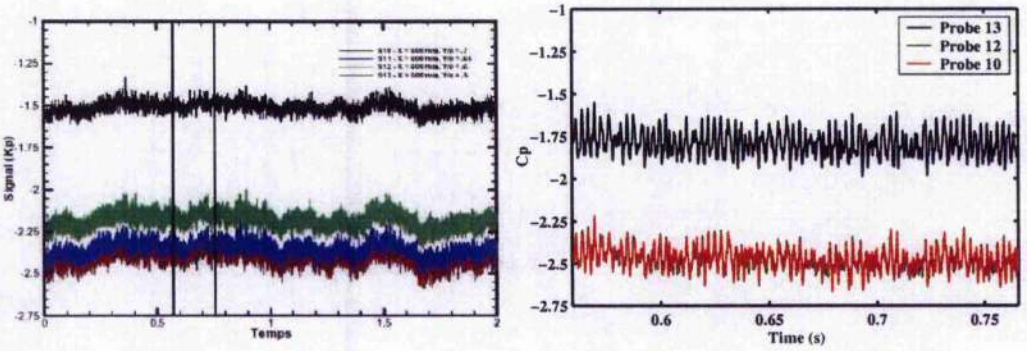

(b) $x/c_r = 0.63$

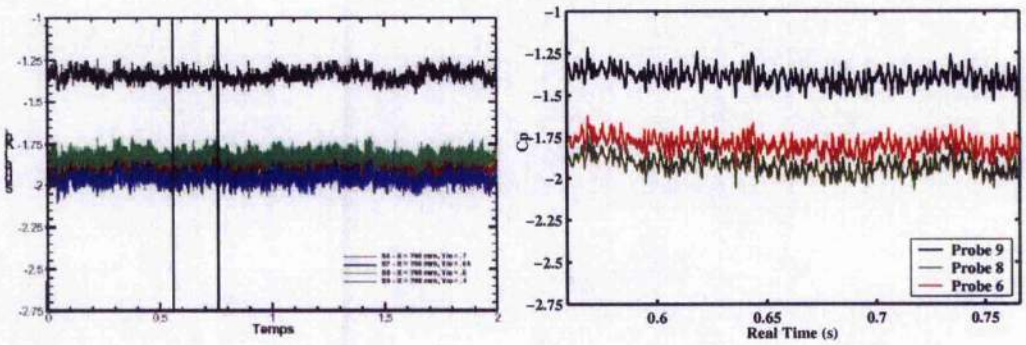

(c) $x/c_r = 0.74$

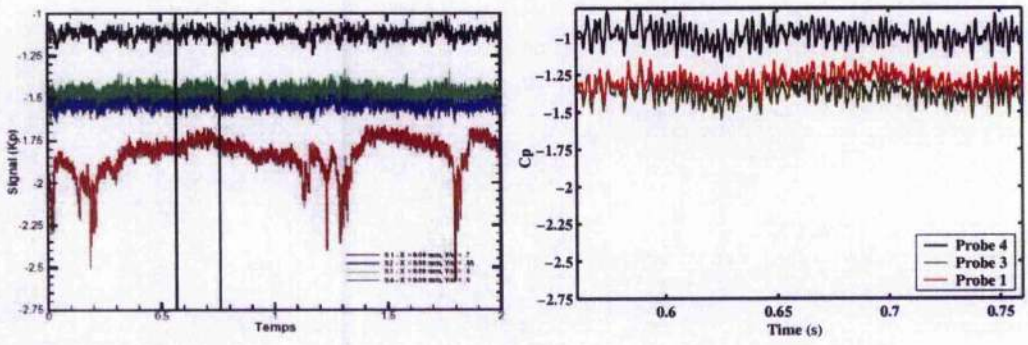

(d) $x/c_r = 0.84$

Figure 4.41: Time histories of unsteady pressure probe data [13]

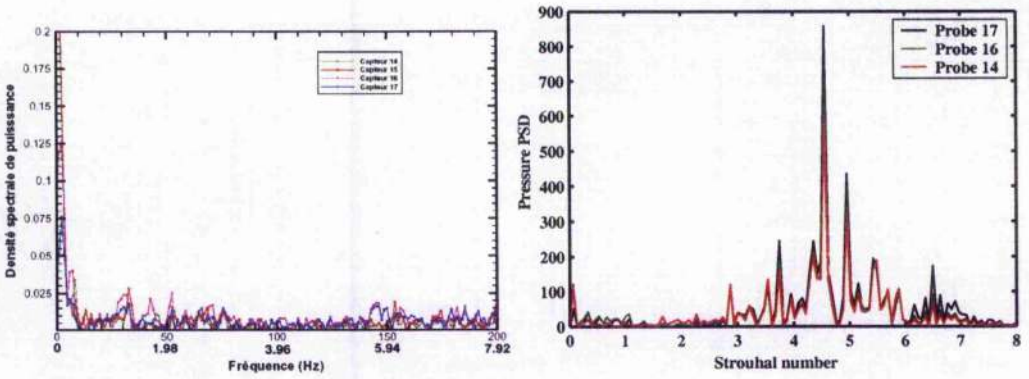

(a) $x/c_r = 0.53$

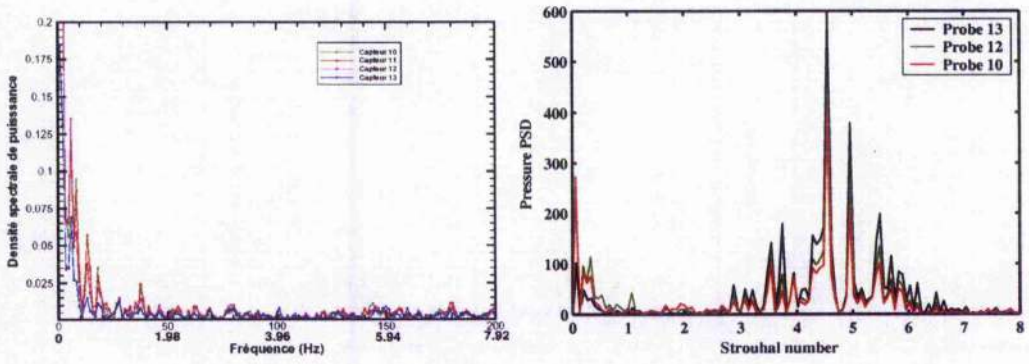

(b) $x/c_r = 0.63$

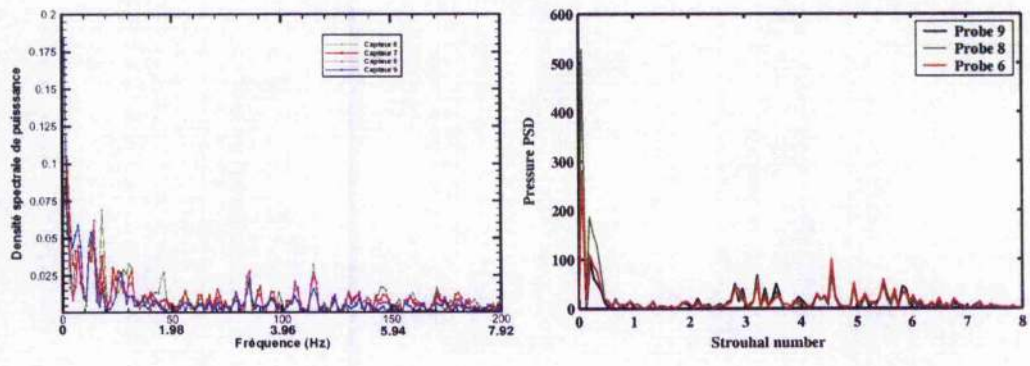

(c) $x/c_r = 0.74$

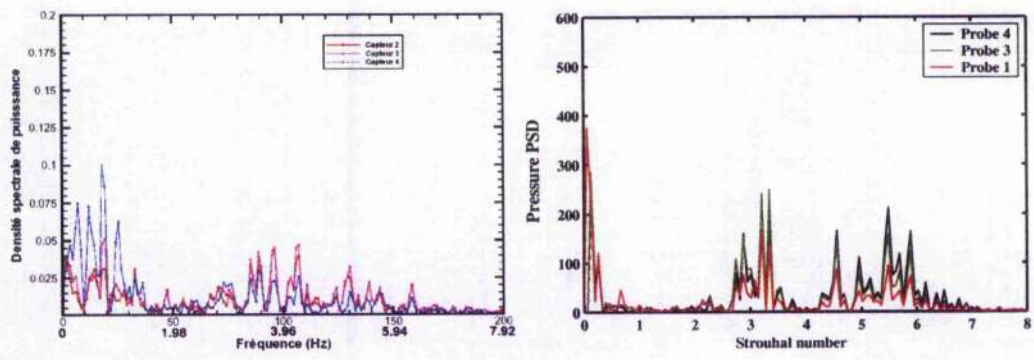

(d) $x/c_r = 0.84$

Figure 4.42: Power spectral density plots of unsteady pressure probe data [13]

however this has relatively low power in comparison. Downstream of breakdown, many more frequencies occur, although the low frequency content is still dominant. Definite peaks occur in the range $15-50Hz$ ($St = 0.5-2$), around 100Hz ($St \approx 4$) and around $130Hz$ ($St \approx 5$). Due to the difference in location of vortex breakdown it may not be possible to make direct comparisons between the frequency responses for a given chordwise location. Indeed, from comparing the experimental and computational results at $x/c_r = 0.53$ it is clear that although the low frequency content is predicted well at $St \approx 0.07$, the dominant behaviour of the flow at this location in the computational results appears at approximately $St = 4.5$. This is also true for $x/c_r = 0.63$, but this behaviour does not occur in the experiments. However, if the non-dimensional distance from the breakdown location is considered, the agreement between the results is much better. As the mean breakdown location is $x/c_r = 0.65$ in the experiments, the $x/c_r = 0.53$ station is $0.15c_r$ upstream and the $x/c_r = 0.63$ station is $0.02c_r$ upstream of this location. Similarly, for the computational results, the $x/c_r = 0.74$ station is $0.14c_r$ upstream and the $x/c_r = 0.84$ station is $0.04c_r$ upstream of breakdown. If these two locations are compared, the agreement is significantly improved, with the low dominant frequency occurring close to $St = 0.07$ in both results and the higher frequency content focusing around $St = 3-5$.

In the unsteady analysis performed on the current results in previous sections, it was determined that the low frequency response found in the flow, close to breakdown, was due to the unsteady oscillation of the breakdown location. As a similar frequency was found for the experimental data, the behaviour of the unsteady location of breakdown should be considered. Figure 4.43 shows the time traces of vortex breakdown location for both the experimental and computational results. The computational results shown were created by considering the location of breakdown in the flow domain for every 100 time steps. Due to the computational expense of the calculation, it was only possible to consider a total time of 0.2 seconds. This makes a comparison with the experimental data difficult as the lowest frequency which could be captured would be approximately $St = 0.069$ and the dominant frequency captured for this phenomenon in the experiment is $St = 0.043$. Considering the amplitude of the oscillations it is clear that the vortex breakdown location oscillates with an amplitude of approximately 15% root chord. This corresponds to a location $x/c_r = 0.6-0.75$ for the left hand side and $x/c_r = 0.65-0.8$ for the right hand side vortex. Comparatively, the computational results predict an oscillation with an amplitude of approximately 6% root chord. This under-prediction of the amplitude may be due to the symmetric assumption as in the experiment there may be interaction between the behaviour of the two leading edge vortices.

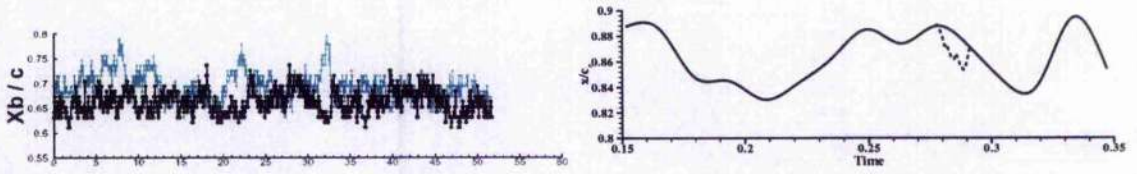

(a) Experimental Results, Black - Left, Cyan - Right; (Scanned - Poor Quality)

(b) Current Results

Figure 4.43: Comparison of unsteady vortex breakdown results

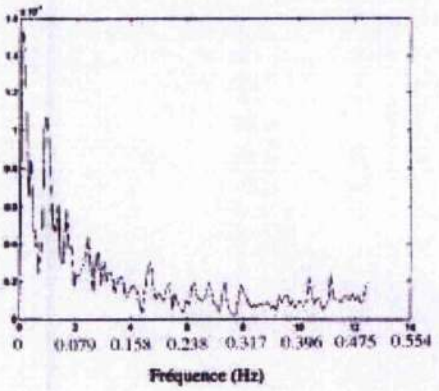

Figure 4.44: PSD plot of unsteady vortex breakdown results from Mitchell's experiment for left hand side [13] $\alpha = 27^o$ $U_\infty = 0.24$ (Scanned - Poor Quality)

From the computational signal, it appears that there are approximately two low frequency oscillations over the 0.2 seconds. This corresponds to a non-dimensional frequency of $St = 0.139$. This is higher than the frequency which was assumed to be the vortex breakdown location in previous sections. However, as the signal length is short the lower frequency may not be detected. From a PSD analysis of the experimental data, shown in Figure 4.44, it is clear that there are a number of frequencies present in the experimental signal. Thus, it may be suggested that the frequency captured by the computation is consistent with the higher frequency content. This frequency is also in agreement with the unsteady breakdown oscillations witnessed from a similar plot for the USAFA DES results for the 65^o VFE-2 test case, which occurred for a frequency of approximately $St = 0.14$. Further higher frequency content is suggested by the trace of vortex breakdown location plotted at a much smaller sample rate of 100 time steps between non-dimensional times of $\tau = 50 - 51$, which is shown in Figure 4.43(b) as the dotted line.

4.7.2 Comparison to Other Unsteady Experimental Results

Further comparisons may be made by considering other experimental investigations from the literature summarised in Chapter 1. In the investigation carried out by Klute [6] and summarised in Klute *et al.* [55], the unsteady flow over a sharp leading edged, 75^o delta wing at an incidence of $\alpha = 40^o$ was considered using digital PIV techniques in a water tunnel. The model had a root chord of $0.141m$ and the freestream velocity was $0.32ms^{-1}$ which provided a Reynolds number of $Re = 4.5 \times 10^4$. This is low, particularly in comparison with the current configuration, however considering the non-dimensional behaviour of the flow, qualitative comparisons may be made. The purpose of the investigation was to consider the unsteady nature of the helical mode instability of vortex breakdown and to consider its evolution with time. Therefore, a large database of images and temporal information was gathered in the post-breakdown flow region. The digital PIV was set up to record an image 500 times a second, which corresponds to a sample time step of approximately $\Delta\tau = 0.004$ and data was gathered over a period of 4 seconds ($\tau = 9.08$).

In this case, due to the relatively high angle of incidence, vortex breakdown occurred at approximately $x/c_r = 0.5$ on the wing. From the DPIV data, the unsteady velocity signals at a number of points on a measurement plane $30\%c_r$ downstream of the breakdown location at $x/c_r = 0.8$ were isolated and considered using a PSD analysis and it is with this data that comparisons will be made with the current results. Figure 4.45(a) shows the instantaneous post-breakdown region on a plane through the vortex core at a time $\tau = 0.101$. This plane shows the velocity vectors and corresponding streamlines for the helical mode, with the vortical regions caused by the spiral breakdown intersecting the plane. The locations of the two points which correspond to probes within the computational domain are highlighted in red, their precise locations are given as non-dimensional distances, 0.108, (which will be referred to as point A) and 0.158 (point B) above the wing surface. Figure 4.45(b) shows the corresponding instantaneous vortex core streamline behaviour at $\tau = 50$. The corresponding probe locations for the computational results are also shown.

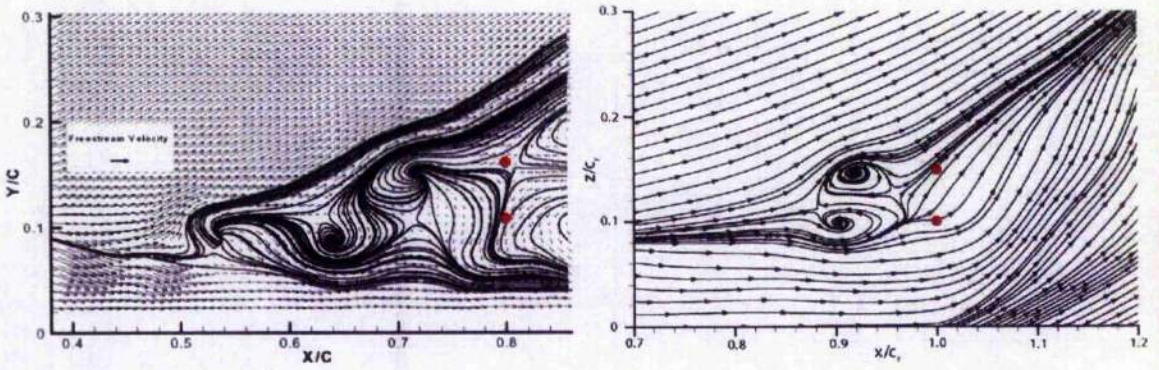

(a) DPIV results showing velocity vectors and corresponding streamlines (Adapted from Ref. [6])

(b) Current DES results showing streamlines

Figure 4.45: Instantaneous vortex breakdown regions for experimental and computational results. Also shown are the locations of the data points from which the time histories of u velocity were taken.

The behaviour of the vortex breakdown flow structure may be considered from the streamline plots. It is clear that the locations where the helical mode winding pass through the analysis plane for the experimental results, are more spread out than for the current results. This suggests that the overall pitch of the helix is much larger

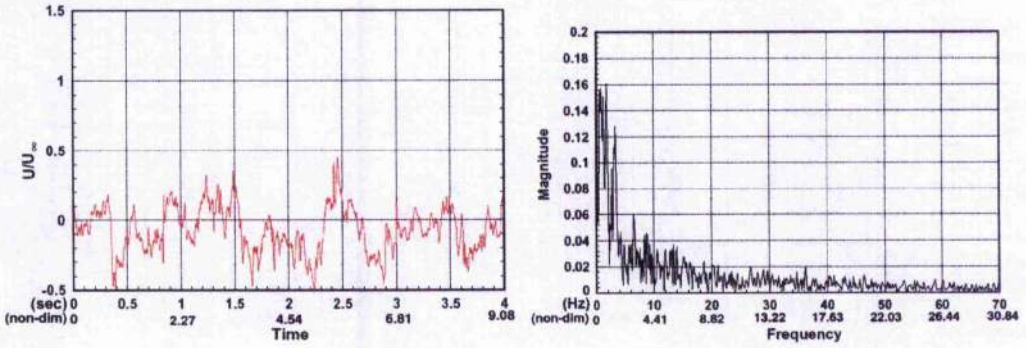

(a) Experimental results (Adapted from Ref. [6])

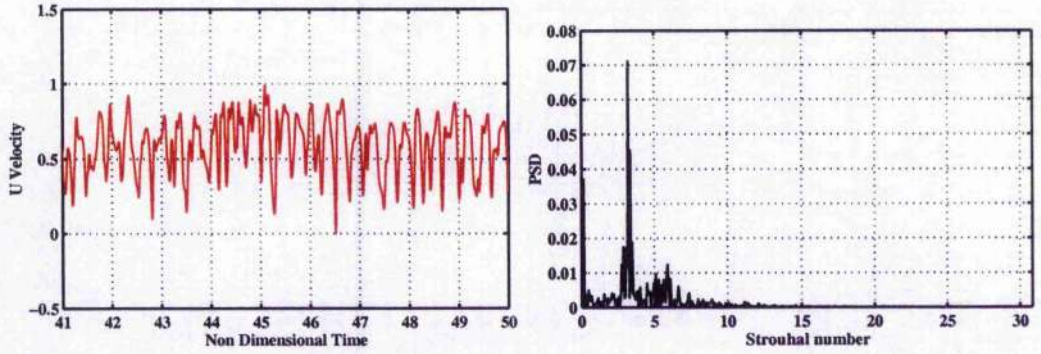

(b) Computational results

Figure 4.46: Time histories and PSD analyses of u velocity for Point A

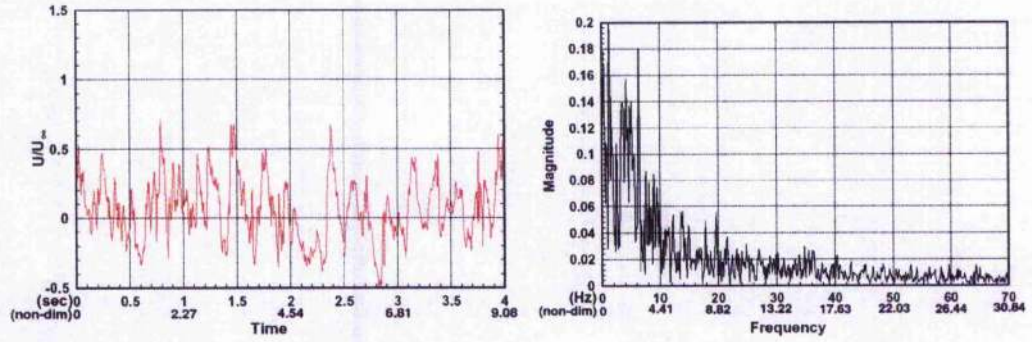

(a) Experimental results (Adapted from Ref. [6])

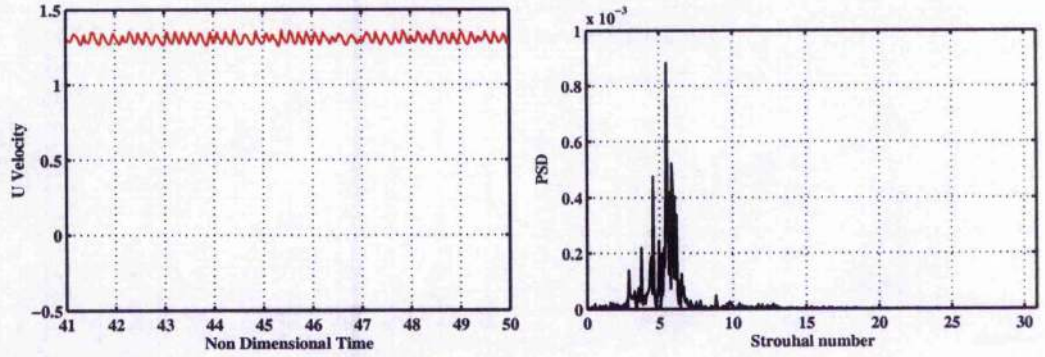

(b) Computational results

Figure 4.47: Time histories and PSD analyses of u velocity for Point B

and the effect of the breakdown is greater on the wing surface. It may also be suggested that the difference in helical pitch is due to the proximity of the vortex breakdown location to the trailing edge in the computational solutions. However, further analysis at higher angles of incidence would be needed to state this conclusively. In the experimental results, the locations of these intersections were tracked with time and it was found that these structures were convected downstream toward the trailing edge. With this downstream motion, the spiral of the helical mode winding stretched and the diameter increased. Coupled to this increase in diameter is a reduction in dominant non-dimensional frequency. However, considering the evolution of the computational results over a time $\tau = 1$ it was found that there was only a slight downstream motion of the structures on the vortex core plane and the diameter of the helical structure did not increase significantly. This diameter is relatively small in comparison with the experimental results, which would suggest a higher non-dimensional dominant frequency. The behaviour of the structures in the experiments at or close to the trailing edge was not mentioned. However, for the current results, the helical winding appeared to dissipate. As discussed in Section 4.5 this is likely to be due to the rapidly decreasing resolution of the grid downstream of the trailing edge. However, it is unclear what effect the trailing edge has on the coherent vortex breakdown structures. Keeping all these differences in mind, the u velocity traces at point A and B can be considered and compared to the probe locations shown in Figure 4.45(b).

It is clear from Figure 4.45 that the non-dimensional distance between the vortex breakdown location and the probe positions is greater for the experimental results. Thus, only a qualitative comparison may be made. However, comparing the results shown in Figures 4.46 and 4.47 it is clear that there are both similarities and differences between the two sets of results. Considering Point A and the corresponding computational probe at a nominal distance $0.1c_r$ from the wing surface. It is evident that the amplitude of the time histories of u velocity are comparable at this location. However, the mean velocity is much lower for the experimental results, and the flow is found to reverse for large periods of the time history. In the computational results the flow does not reverse at any point in the time period shown. Also, the level of fluctuations of the velocity are found to be less in the computational results, but not significantly so. The frequency content is also quite different. The dominant peaks in the PSD analysis for the experimental results occur for $St < 2$ whereas for the computational results, the main peak occurs at approximately $St = 3.5$. This increase is likely to be due to the differences in the helical winding discussed before. In the experiment, there is also considerably more energy in the higher frequencies. Whereas for the computational results there is some content at frequencies, $St < 10$, but this reduces rapidly with increasing frequency. The energy in the high frequencies of the experimental results also decays but at a much reduced rate. The presence of this high frequency energy relates back to the observation that there are more small scale fluctuations in the experimental time history and suggests the presence of smaller scale structures and a turbulent behaviour. However, this behaviour is secondary to the helical model instability and so the flow has not broken down into full scale turbulence at this location. It may be suggested that a fully turbulent flow, with the breakdown of the helical mode instability into smaller structures, does not occur until downstream of the trailing edge. A similar conclusion may also be made from the USAFA results for the 65^o VFE-2 wing discussed in Section 4.6 and shown in Figure 4.48 for a similar probe location to Probe A. For this case, the probe is also approximately $30\%c_r$ downstream of the vortex breakdown location. This shows that despite greater overall grid refinement, the results are again very similar, with the dominant frequencies occurring for $St < 10$. There is little frequency content above this frequency.

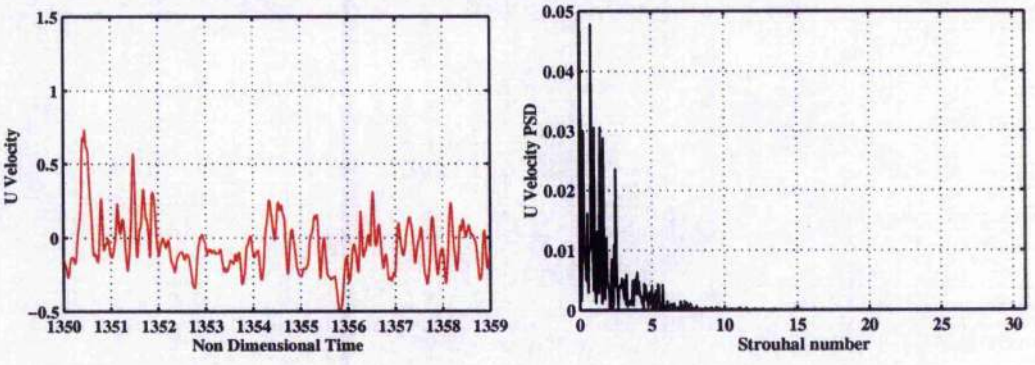

Figure 4.48: Time histories and PSD analyses of u velocity USAFA results for 65^o delta wing at location on vortex core plane, $x/c_r = 1.0$, $z/c_r = 0.1$

At point B, the experimental results exhibit a similar behaviour to Point A, with many scales of fluctuations being evident from the time trace of u velocity. However, the PSD analysis of the signal shows that the frequency of the dominant peaks has increased and there is an overall increase in the energy of the signal. Compared to a probe in the computational flow domain situated at $z/c_r = 0.15$ above the wing surface, it is clear that the behaviour

is quite different. The mean velocity is much greater, in fact it becomes slightly higher than the freestream and the amplitude of the signal is greatly reduced. Considering the frequency content, it is clear that the increase of frequency compared to Point A has been captured, but the content is very different. These differences between the experimental and computational results are likely to be due to a difference in location of the measurement point within the post-breakdown region. This region is much larger for the experimental results and the measurement point sits well within this region. However, for the computational result, this probe location is close to the edge of the region and closer to the freestream flow.

From consideration of these comparisons and particularly from the experimental results it is evident that the helical mode structure is dominant downstream of breakdown for at least $30\%c_r$ and it is likely that this structure remains coherent until at least the trailing edge. Although there is evidence from the experimental results of high frequency content in the post-breakdown flow, which suggests the presence of turbulence, it is clear that this is not dominant. At some location, the coherent structure of the helical mode instability will breakdown and the flow will become fully turbulent, at which point the frequency content will exhibit a broadband response, however this has not been found to occur in the experiments. There is also little evidence of small scale structures in the streamline plot of Figure 4.45(a). This suggests that turbulence does not become dominant until downstream of the trailing edge, with the flow over the wing, post-breakdown being dominated by coherent structures. The level of small scale fluctuations within the experimental signals, does not appear to be significantly greater than the computational results (particularly in view of the under-resolution of the grid discussed previously).

4.8 Discussion

4.8.1 The Role of Turbulence in Vortical Flows

As shown in the previous section, it is clear that the unsteady flow immediately downstream of vortex breakdown is not dominated by turbulence. Although small scale turbulence does exist, as is evident from the low energy response at high frequencies in the experimental data from Figures 4.46(a) and 4.47(a). In this investigation, the ability of the DES turbulence treatment to predict this flow behaviour was analysed and particularly the role of turbulence in the prediction of breakdown and other dominant flow features was considered in a number of ways.

From the grid refinement study, it was shown that although the streamwise refinement improved the resolution of the unsteady flow in the wake region, there was little overall effect on the mean flow behaviour, particularly upstream of the trailing edge. It was concluded from this study that an overall refinement was needed in this region, but that it may be likely that the prediction of the turbulence downstream of the trailing edge would have only a small effect on the upstream flow predictions. From comparisons with existing DES calculations it was shown that with overall refinement of the grid, smaller structures could be captured, both within the shear layer and downstream of breakdown, however, this did not appear to have a significant effect on the dominant unsteady flow frequencies captured. Indeed, from analysis of the turbulent behaviour on the grids, it was found that generally the behaviour was very similar. Therefore, it may be suggested that the level of grid refinement to capture the turbulence within the wake of a delta wing is considerably greater than that used in investigations to date.

However, it was shown from validation of the results with existing unsteady data, that the DES solutions were adequately predicting the dominant features of the flow. These included the helical mode instability of breakdown and the wandering of the vortex core due to the motion of breakdown. Evidence of shear layer structures were also found within the frequency data, although it is felt that further investigation on more refined grids is needed to confirm the behaviour and frequencies of these features. Therefore, it is clear that although the small scale turbulence of the post-breakdown flow is not adequately captured, this does not appear to have a significant effect on the ability of DES to predict the dominant flow features. Therefore, it may be concluded that the overall behaviour of vortical flows and vortex breakdown over slender delta wings is not dominated by turbulence.

4.8.2 The Role of μ_{SGS} in the DES Calculations

As mentioned, the structured grid used in this investigation is not sufficiently refined to capture small scale turbulence and the smallest eddy size resolved on the grid is approximately $5\%c_r$. This means that the level of turbulence captured on the grid, defined as ϕ in Section 4.5.2, is close to zero. The exact value of ϕ is difficult to quantify as the precise levels of turbulence in this region have not been quantified. However, as discussed above, it is found the low energy, high frequency, broadband response of small scale turbulence is missing from the DES results.

If ϕ is close to zero, this means that the turbulent fluctuations, u_i', are modelled by the subgrid scale model with only the mean flow being resolved on the grid. This results in the velocity decomposition as given by Equation 4.3.

$$u_i = \underbrace{\langle U_i \rangle + u_i''}_{\textit{Resolved on grid}} + \underbrace{u_i'}_{\textit{modelled by SGS}} \tag{4.3}$$

From the description of the URANS method in Chapter 2, it is evident that for an under-resolved DES calculation, the behaviour of the DES model is very similar to the URANS method with the turbulence predicted by a turbulence model, which in the case of the DES calculation is the subgrid scale Smagorinsky model. This means that the subgrid eddy viscosity, μ_{SGS}, behaves in the same way as the turbulent eddy viscosity, μ_T and will model the contribution of the turbulence to the flow. To consider this behaviour, contours of the subgrid eddy viscosity relative to the laminar viscosity were plotted on a plane through the vortex core region and are shown in Figure 4.49. From this plot, it is evident that the levels of Smagorinsky eddy viscosity predicted by the subgrid model increase in the vicinity of the vortex breakdown region and trailing edge. However, these values are low in comparison with values of turbulent eddy viscosity predicted for standard Boussinesq models, such as the Wilcox $k-\omega$ model discussed in Chapter 2, which can be of the order of 10^4. This is due to the fact that the subgrid eddy viscosity is scaled by the spatial filter length squared, Δ^2, as detailed in Equation 2.50, which for the DES implementation corresponds to the maximum cell size squared Δ_{max}^2. Thus, as the grid is refined, the level of μ_{SGS} will decrease and the value of ϕ will increase. It has been shown in this investigation that the magnitude of Δ_{max} through the grid is insufficient for ϕ to be greater than zero and thus the turbulence is modelled.

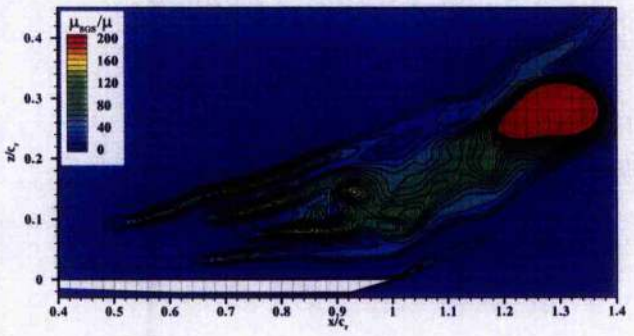

Figure 4.49: Slice through vortex core at $y/s = 0.7$ showing contours of sub-grid eddy viscosity relative to laminar viscosity created by the DES calculation

4.9 Conclusions

From consideration of DES calculations performed on a structured grid for a slender delta wing at moderate incidence, it was found that a number of low frequency, coherent unsteady features dominate the flow. Effects of both temporal and spatial refinement were examined and the ability of DES to predict the unsteady nature of the flow was considered, particularly in light of the prediction of turbulence in the post-breakdown region. Comparisons were made to other, similar DES calculations carried out by the USAFA and with experimental data to measure the validity of the results.

It is clear from this investigation that the DES calculations performed are under-resolved, with little turbulence being resolved on the grid within the LES region of the flow domain. From this analysis and the comparisons with existing DES results using unstructured grids, it is suggested that the grid requirements to capture the turbulent behaviour of the flow close to and downstream of breakdown are much larger than those described in this investigation. It was found that to fully capture the turbulent scales it would be necessary to refine the grid not only over the wing, but also in the region downstream of the trailing edge. How far downstream may not be proposed based on the results gained here, but based on the results of the investigation by Allan [144] who considered the effect of sting fairings downstream of the trailing edge on vortex breakdown, it is felt that a distance of at least one root chord length downstream is a good starting point . This will have a direct impact on the size of the grids used for DES for delta wing flows, increasing the computational expense of an already expensive turbulence method. This is particularly prohibitive for structured grids, which have the disadvantage compared to unstructured grids that any refinement needs to be taken to the farfield. However, this may be overcome by considering overset grids, hanging nodes and hybrid grids. Therefore, it may be concluded that the computational cost of the calculations needed to fully resolve the turbulent scales within a delta wing flow is still too high to make these calculations

accessible to the majority of CFD users.

However, the results of this investigation may also show that it is possible that these calculations are not necessary. From this study it was shown that although turbulence is present in the flow downstream of breakdown, it does not appear to have a significant effect on the prediction of the salient flow features and the validation with the experimental data was good, despite the under-resolution of the results. The dominant flow features were shown to be coherent, low frequency phenomenon, which could be assumed to be part of the mean flow. Therefore, it is suggested that traditional URANS models may be able to perform well and accurately predict the main features of the flow at a significantly reduced computational cost.

Chapter 5

Assessment of URANS for Predicting Vortex Breakdown

5.1 Introduction

From the study into the use of DES to capture the unsteady flow behaviour of the vortical flow and vortex breakdown over a slender delta wing, a number of conclusions were made. It was found that the resolution of the grid used was not adequate to resolve the turbulent scales and that further refinement, both above the wing and downstream of the trailing edge would be needed to improve the resolution of the flow. This would have the consequence of increasing the computational expanse of an already expensive calculation, particularly as the time steps involved may have to decrease with the increasing grid refinement. However, it was also found from comparisons with other DES solutions and with experimental data, that the flow behaviour in the region of interest, downstream of breakdown, was not initially highly turbulent in nature with the breakdown to turbulence not being found to occur until much further downstream. From the unsteady analysis of the DES results and from consideration of the literature, it is clear that the majority of the frequencies associated with the flow phenomena present above the wing occur for Strouhal numbers less than 20. Finally, it was concluded that these lower frequencies are within the grasp of more traditional URANS calculations and that these methods could capture the unsteady flow behaviour for a greatly reduced computational cost.

From the literature review in Chapter 1, it is clear that there have been many investigations into the ability of RANS models to predict the important features of vortex breakdown, with varying success. From work carried out for steady state calculations, it is clear that the standard linear Boussinesq turbulence models struggle to accurately predict vortex breakdown behaviour due to their inability to correctly model the turbulent behaviour within the vortex core. Due to this, a number of corrections have been proposed for these linear models, to account for the rotation of the flow and to improve the flow solutions. Some of these were discussed in Chapter 1 and have been found to give good agreement with experimental data. Non-linear eddy viscosity models have also been proposed and applied to the solution of delta wing flow and again also show improvement compared to linear models for steady state solutions. This is due to the addition of a dependence on the rotation of the flow in the calculation of turbulence. However, to date there has been little research into applying these models to unsteady flows and their ability to accurately predict the important flow phenomena and frequencies is largely unknown.

Therefore, to consider the ability of URANS methods to predict the unsteady behaviour of vortical flow and vortex breakdown, two turbulence models were used, one a linear Boussinesq model with a rotation correction for vortical flows and the other a non-linear model. The calculations were performed on the test case and conditions defined in the previous chapter to allow for the relative behaviour compared to the DES solutions to be considered. The turbulence models used are, the $k-\omega$ with P_ω Enhancer, which is the Wilcox $k-\omega$ two equation model with rotation correction for vortical flows [158], and a Non-Linear Eddy Viscosity model (NLEVM), which is also based on the $k-\omega$ model, but which uses an algebraic formulation for the eddy viscosity instead of the Boussinesq approximation [170]. Both models are detailed and discussed with respect to vortical flows in Chapter 2.

In order to fully consider all aspects of the URANS solutions, the effect of grid refinement and time step refinement are considered. The relative modelling approaches and results for each model are the considered before a full assessment of the ability of the URANS models to predict the unsteady behaviour and dominant frequencies is carried out and discussed with respect to the validated DES results presented in the previous chapter. Finally, the

results are discussed overall and conclusions made.

5.2 Effect of Grid Refinement

By their nature, URANS flow solutions are only dependent on grid refinement for numerical accuracy. As the the size of the cells in a grid decreases, the numerical accuracy of the solution should improve. Before considering the ability of the URANS models to predict the unsteady vortical flow behaviour, it is necessary to quantify the effect in the grid refinement for each of the models used. In order to consider this, calculations were performed for the coarse and fine grids described in Section 4.2.1 with the non-dimensional baseline time step of $\Delta\tau = 0.01$ using both models. Probes were put in the flow domain at the same locations as detailed before and, as far as possible, the resulting analyses have been kept consistent to facilitate the comparisons with the DES results.

5.2.1 $k-\omega$ model with P_ω Enhancer

As before, five probes on a plane through the vortex core region were analysed to allow comparisons to be made using both the mean and unsteady components of the flow. Figure 5.1 shows the location of these probes relative to the flow features, shown by slices of instantaneous u velocity and an isosurface of entropy which shows the winding downstream of breakdown, for both the fine and coarse grids. From these plots it is evident that the location of the vortex core with respect to the wing surface and the relative locations of the five probes is very similar for both grids.

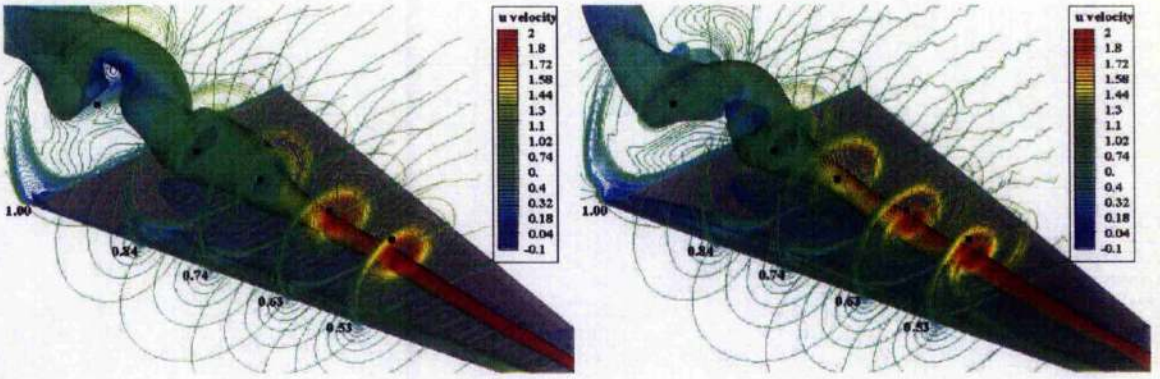

(a) Coarse Grid

(b) Fine Grid

Figure 5.1: Location of probes though vortex core region compared to instantaneous u velocity contours at each streamwise location and an isosurface of entropy at $\tau = 50$, coarse and fine grid comparisons for $k-\omega$ with P_ω Enhancer model

Further analysis of the flow behaviour, shows that the location of vortex breakdown is different for the two grids. The mean vortex breakdown location was determined, as before, from the average of instantaneous flow data at every 100 time steps. From this, the location of vortex breakdown was found to occur at approximately $x/c_r = 0.70$ for the coarse grid and $x/c_r = 0.83$ for the fine results. This difference in breakdown location, is most likely to be due to the differences in resolution of the vortex core behaviour. From comparison of the contours of u velocity, in Figure 5.1, it is clear that the vortex core behaviour is slightly different for the fine grid, with a tighter vortex core region and the appearance of a shear layer structure under the vortex. A tighter, more compact vortex core region may suggest a stronger vortex which may explain the downstream location of breakdown. The difference in breakdown location is also obvious both from the slice at $x/c_r = 0.74$, which clearly shows a high velocity region for the fine grid but a region of recirculation for the coarse grid and from the isosurface of entropy, which shows the differences in the winding behaviour downstream of breakdown. It is evident from this isosurface, that the winding for the coarse grid is more elongated, with a larger pitch angle than for the fine grid, which appears to be relatively compact in comparison.

The mean and RMS values of the velocity components are shown in Figure 5.2 for the five probes mentioned above. From the mean u velocity plot, the relative locations of breakdown are clear, with the vortex breakdown occurring upstream of the $x/c_r = 0.74$ location for the coarse grid. Both upstream and downstream of this location, the mean

values of both solutions are in good agreement. The agreement is also very good for the v and w components, with the plane of probes crossing the rotation axis at the same location. This is downstream of breakdown for the coarse grid and upstream for the fine grid solutions. As suggested from the u velocity contours before, the greatest difference in mean velocity occurs at $x/c_r = 0.74$, however, this does not seem to affect the agreement downstream. For the probes upstream of breakdown for both cases, it is evident that the spanwise and normal velocities are slightly greater for the fine grid, confirming a tighter vortex core region and suggesting a stronger vortex occurs for the fine grid solution.

Considering the RMS velocities and the differences in the behaviour of the two grids becomes more evident. Upstream of breakdown, the results are very similar for all three velocity components, however close to and downstream of vortex breakdown the solutions are quite different. It is clear from the RMS of u velocity that the level of unsteadiness at $x/c_r = 0.74$ is very similar for both grids, despite vortex breakdown having occurred upstream of this location for the coarse grid. Further downstream, the level of unsteadiness has increased for the fine grid solutions (as vortex breakdown has occurred), it levels off for the coarse grid. This is consistent for the v and w components of velocity, where the coarse grid predicts a higher unsteadiness than the fine grid at $x/c_r = 0.74$ due to breakdown. Downstream of this the levels drop off and it is clear that the fine grid exhibits greater unsteadiness in the post-breakdown region.

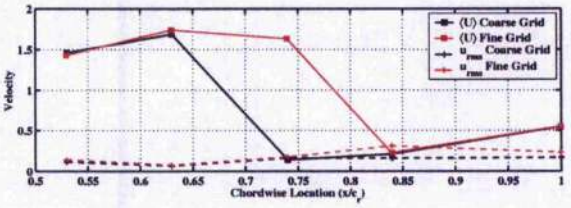

(a) u velocity

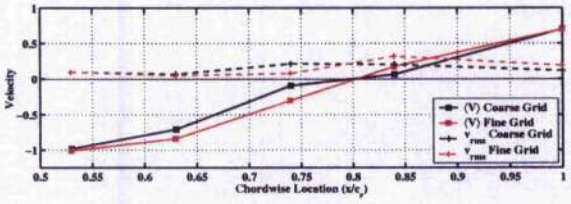

(b) v velocity

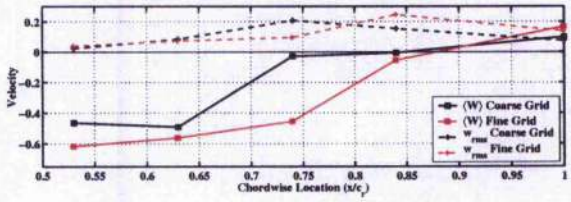

(c) w velocity

Figure 5.2: Mean and RMS velocity components through vortex core; coarse and fine grid comparisons for $k-\omega$ with P_ω Enhancer model

To further analyse the unsteadiness in the post-breakdown region, a single probe situated above the trailing edge is considered for both cases. It is clear from Figure 5.2 that at this location, the mean velocities are virtually identical for both grids, but that the RMS velocities and therefore the levels of unsteadiness are quite different. Figure 5.3 shows the time history and results from a PSD analysis of the u velocity signal. From the time history, the most noticeable difference is that the fine grid solution gives a signal with a greater amplitude than the coarse grid, in agreement with the RMS values discussed above. Considering the frequency content of the signals, it is clear that the behaviour is quite different. The coarse grid predicts two dominant frequencies at approximately $St = 2.6$ and 4.25 with a much smaller peak evident at $St \approx 5.2$ which is the harmonic of the first dominant peak. The fine grid, however, only predicts one dominant peak at approximately $St = 3.4$ and some higher frequency content at $St = 4.5 - 7$. For the fine grid, it may be suggested that the dominant frequency captured is associated with the helical mode instability as this is close to the frequency determined from the unsteady analysis of the DES results.

However, the source of the two peaks in the coarse grid results is not so obvious. It is possible that they are also related to the rotation of the vortex breakdown winding, but at a location much further downstream of breakdown. This was considered due to the results of the grid refinement study carried out for the DES results in Section 4.4 where two dominant frequencies were found in the wake flow further downstream of breakdown. However, the dominant peaks occurred at frequencies slightly lower than those predicted by the coarse grid URANS. It may be suggested that this predicted behaviour is similar, however, further experimental data in the wake downstream of breakdown is needed to confirm the occurrence of these two frequencies in the unsteady flow.

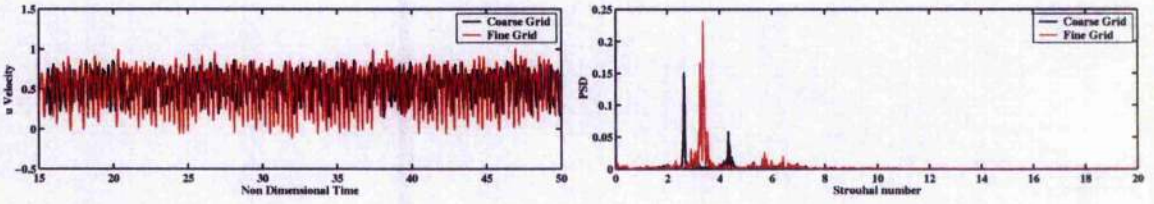

(a) Time history

(b) PSD vs. St

Figure 5.3: Time history and PSD analysis of u velocity signal situated above the trailing edge on the vortex axis at $z/c_r = 0.1$; coarse and fine grid comparisons for $k-\omega$ with P_ω Enhancer model

However, despite appearing to have reasonably predicted the unsteady nature of the flow, it is clear that the behaviour of the post-breakdown flow for the coarse grid is quite different to the fine grid as shown by the isosurface of entropy in Figure 5.1. This is confirmed from considering the behaviour of the flow on a slice through the vortex core, as shown in Figure 5.4. For the coarse grid, the location of vortex breakdown does not appear to be well defined and is very elongated in appearance. The stretched appearance of the winding is also evident and it is clear that it does not have a strong, clear structure at the trailing edge. Looking at the results for the fine grid, it is clear that in contrast, the location of vortex breakdown is well defined with clear evidence of an increase in vortex core diameter and helix pattern downstream. Smaller structures also exist at the trailing edge, which may cause the higher frequency content found in the u velocity signal. However, these are dissipated very quickly downstream of the trailing edge.

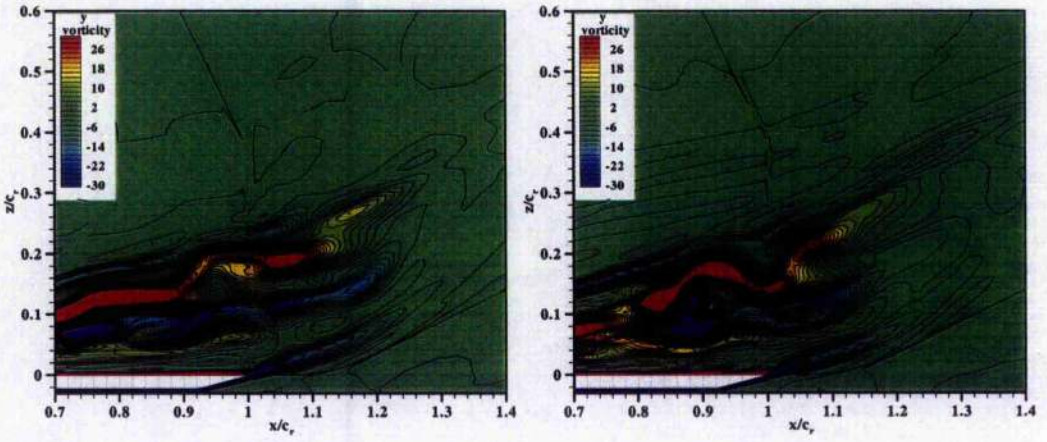

(a) Coarse

(b) Fine

Figure 5.4: Slice through vortex breakdown region, on a plane through vortex core, $y/s = 0.7$ showing instantaneous contours of y vorticity, coarse and fine grid comparisons for $k-\omega$ with P_ω Enhancer model

From this analysis, it is clear that the fine grid produces results with greater resolution of the flow features, particularly downstream of breakdown. The unsteady behaviour downstream of the breakdown also appears to be closer to the behaviour expected. Therefore, the fine grid results will be further analysed and compared to the DES results in a later section.

5.2.2 Non-Linear Eddy Viscosity Model

An identical analysis was carried out for the non-linear eddy viscosity model, using the same grids and computational set up. Figure 5.5 show the relative locations of the probes used for the analysis compared to the vortex

core location. From these plots the relative locations of the vortex core and probes appear to be similar for both solutions. The location of vortex breakdown is also clear from the isosurfaces, due to the expansion of the core, and with further analysis it was found that the mean location occurs at approximately $x/c_r = 0.77$ for the coarse grid and $x/c_r = 0.87$ for the fine grid results. The difference in location is similar to that found for the $k-\omega$ model with P_ω Enhancer discussed above, however the predicted breakdown is further downstream for both grids.

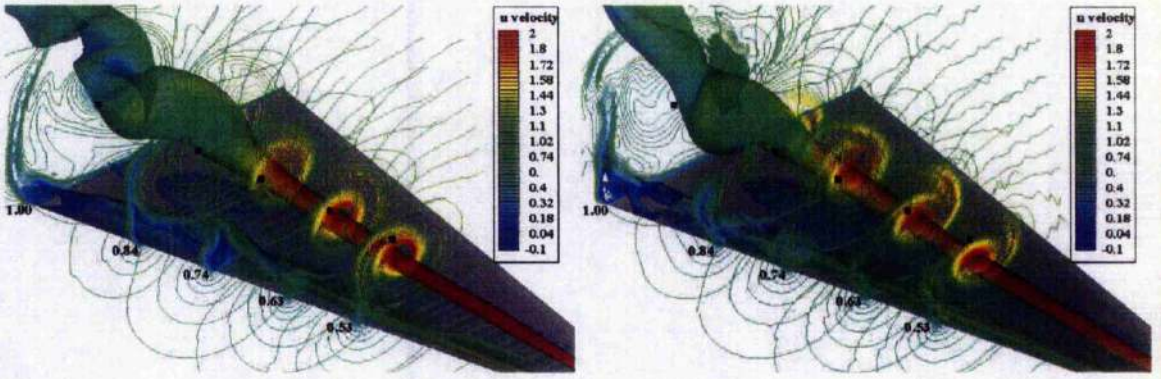

(a) Coarse Grid

(b) Fine Grid

Figure 5.5: Location of probes though vortex core region compared to instantaneous u velocity contours at each streamwise location and an isosurface of entropy at $\tau = 50$, coarse and fine grid comparisons for Non-Linear Eddy Viscosity model

From the instantaneous contours of u velocity, the improvement in vortex core resolution with grid refinement is clear. The vortex core appears to be more compact for the fine grid and again there is more evidence of a structure in the shear layer under the vortex core. Again, this may be the cause of the difference in breakdown location for the two grids. As with the $k-\omega$ model with P_ω Enhancer results discussed previously, the behaviour of the winding downstream of breakdown appears to be quite different. For the coarse grid the breakdown is less clear and the winding is elongated with a lazy helical form. For the fine grid, the behaviour is more compact and the winding appears to have a smaller pitch angle.

The mean and RMS values of the components of velocity are shown in Figure 5.6 through the vortex core region. However, unlike for the $k-\omega$ model with P_ω Enhancer model solutions, the mean velocities for the coarse and fine grid are quite different. From the mean u velocity, the reduction of the velocity as breakdown is approached is clear. However for the coarse grid this reduction starts much further upstream. Although the breakdown is further upstream for the coarse grid, it still appears that the onset of breakdown also occurs much earlier than for the fine grid results. This may be related to the size of the vortex core region in relation to the probe location. This was suggested by the contours of u velocity discussed above and is confirmed by comparison of the mean w velocity which shows that the plane of the probes crosses the vortex core axis at a point upstream of the fine grid results (the change in location from inboard to outboard is indicated by the change in sign of the mean velocity). As the vortex core region is larger it is likely that the u velocities predicted for a given location will be smaller. Downstream at the trailing edge the mean u velocity is almost identical.

Considering the RMS velocities, the unsteady behaviour on the two grids is evident. For the coarse grid, just prior to breakdown, the RMS u velocity increases significantly to a value almost five times that for the previous probe. This is also evident for the fine grid, but the increase in RMS velocity is not so pronounced. It is likely that this increase is due to the presence of the vortex breakdown oscillation in this region. Far upstream and downstream of the breakdown location the agreement is good between the grid results, although the fine grid consistently predicts a higher level of unsteadiness. For the v and w RMS velocities, it appears that the level of unsteady behaviour is very similar between the solutions. However, some slight differences are clear, particularly for the w RMS velocity, both upstream and downstream of breakdown.

The single probe in the post-breakdown flow was also considered for these cases and the resulting time histories and PSD analysis are shown in Figure 5.7. As mentioned before, both the mean and RMS velocities at this location were very similar for the two cases. Looking at the time histories, it is clear that the fine grid exhibits a signal with a slightly larger amplitude than the coarse grid. This is also apparent from the PSD frequency plot, which shows

the fine grid signal to have more power. The frequency content of the two signals are similar with dominant peaks occurring for the coarse grid around $St \approx 4$ and around $St \approx 3.6$ for the fine grid. These frequencies may both be attributed to the helical mode instability. There is also similar low frequency and high frequency content, although the coarse grid consistently predicts the peaks at lower frequencies than the fine grid.

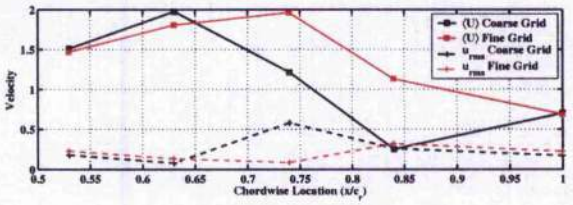

(a) u velocity

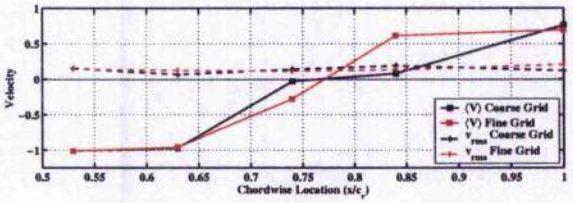

(b) v velocity

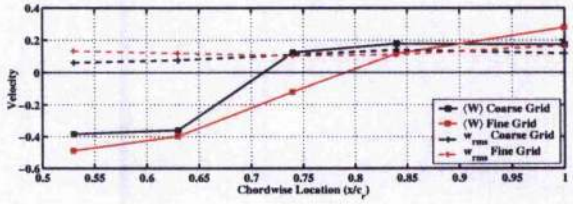

(c) w velocity

Figure 5.6: Mean and RMS velocity components through vortex core; coarse and fine grid comparisons for Non-Linear Eddy Viscosity model

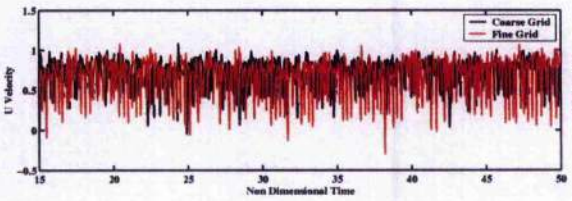

(a) Time history

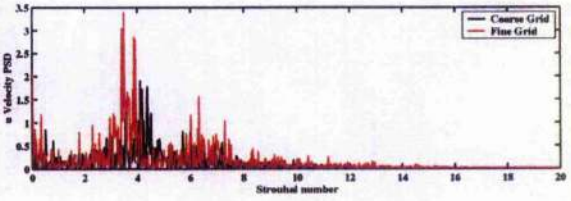

(b) PSD vs. St

Figure 5.7: Time history and PSD analysis of u velocity signal situated above the trailing edge on the vortex axis at $z/c_r = 0.1$; coarse and fine grid comparisons for Non-Linear Eddy Viscosity model

Despite the similarities in the unsteady u velocity signals between the two grids, there are still differences in the behaviour of the flow downstream of breakdown. Figure 5.8 shows the breakdown region using instantaneous contours of y vorticity on a plane through the vortex core. From this it is clear that the behaviour of the Non-Linear Eddy Viscosity model on the coarse grid is similar to that of the $k-\omega$ model with P_ω Enhancer discussed previously. The vortex winding downstream of the breakdown location is very stretched and elongated, as was shown by the isosurfaces of entropy in Figure 5.5. This is particularly obvious when compared to the fine grid results which show a defined breakdown region with a clear helical structure, upstream of the trailing edge. Again, some smaller structures are predicted for both cases, which will correspond to the higher frequencies in the signal.

As with the $k-\omega$ model with P_ω Enhancer, it is concluded that the fine grid results provide a better resolved flow solution in comparison to the coarse grid results and will, as a results be used for the remainder of this investigation.

However, it is clear that the coarse grid gave good approximations, particularly to the unsteady frequencies present in the flow, and this should be kept in mind when considering the relative cost of the calculations performed.

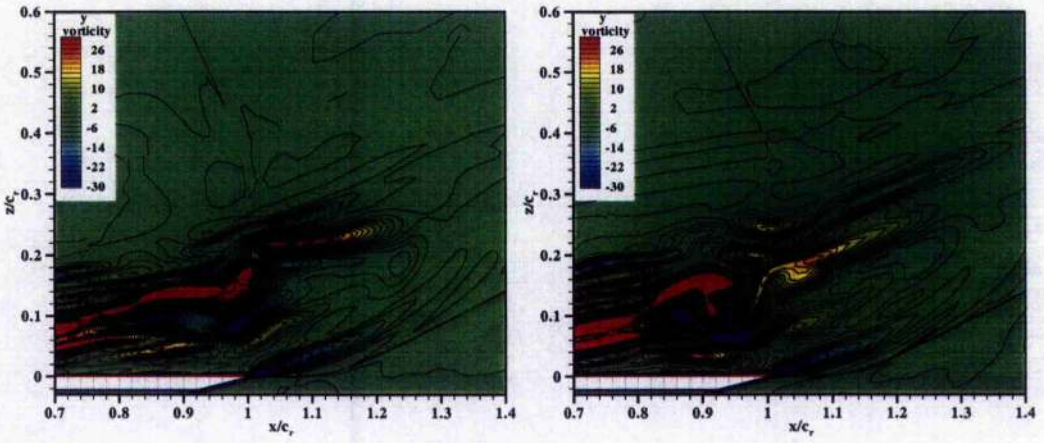

(a) Coarse (b) Fine

Figure 5.8: Slice through vortex breakdown region, on a plane through vortex core, $y/s = 0.7$ showing instantaneous contours of y vorticity, coarse and fine grid comparisons for Non-Linear Eddy Viscosity model

5.3 Effect of Time Step Refinement

Unlike DES calculations, the refinement of time step and grid size for URANS calculations are not inter-related. However, just as an increase in grid refinement improves the numerical accuracy of the solution, a refinement in time step will increase the resolution of the unsteady behaviour and increase the maximum flow frequency which can be captured. To consider the effect of this on the flow behaviour, the solutions obtained using the Non-Linear Eddy Viscosity model for the fine grid with the baseline time step of $\Delta\tau = 0.01$ were compared to similar results obtained with a time step of $\Delta\tau = 0.005$. An analysis similar to that used for the grid refinement study was performed to compare the results.

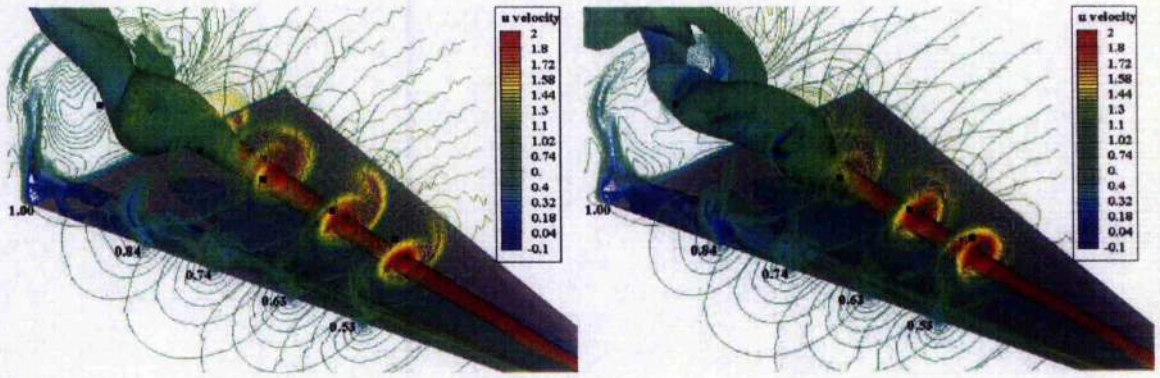

(a) $\Delta\tau = 0.01$ (b) $\Delta\tau = 0.005$

Figure 5.9: Location of probes though vortex core region compared to instantaneous u velocity contours at each streamwise location and an isosurface of entropy at $\tau = 50$, time step comparisons for Non-Linear Eddy Viscosity model

Figure 5.9 shows instantaneous u velocity contours and an isosurface of entropy, as before, for both solutions. From these plots it is clear that there are a number of differences in the flow solutions. The overall location of the vortex core appears to be very similar, however the size of the core region, the behaviour of the shear layer and the vortex breakdown location are all quite different. With a reduction in time step, the size of the vortex core appears to increase as suggested by the contours of u velocity, although the maximum axial velocity is not found to increase

significantly. Also evident is a difference in the strength of the shear layer structure found inboard of the vortex core region, this is not as clearly defined for the $\Delta\tau = 0.005$ time step results. Considering the mean location of breakdown, it was found that with a decrease in time step size the location of breakdown moves upstream from $x/c_r = 0.87$ for $\Delta\tau = 0.01$ to $x/c_r = 0.81$ for $\Delta\tau = 0.005$. This may again be attributed to the change in vortex core behaviour as a compact vortex core suggests a stronger vortex core and thus a delay in breakdown. For the grid refinement study, these differences were attributed to the improved grid resolution of the vortex core region. However, these results suggest that the level of unsteadiness of the flow is also important for the prediction of the vortex core behaviour and vortex breakdown. The difference in the location of breakdown and the winding of the helical mode instability in the post-breakdown region are also shown from the isosurfaces of entropy in Figure 5.9. From this comparison, it is clear that the winding is more elongated for the finer time step in a similar manner to the coarse grid results shown in the previous section, particularly in comparison to the $\Delta\tau = 0.01$ results.

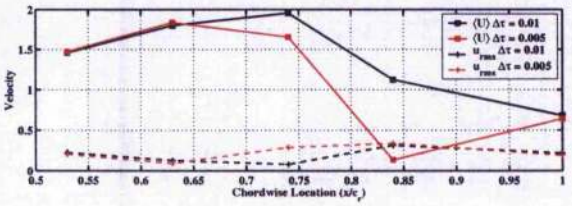

(a) u velocity

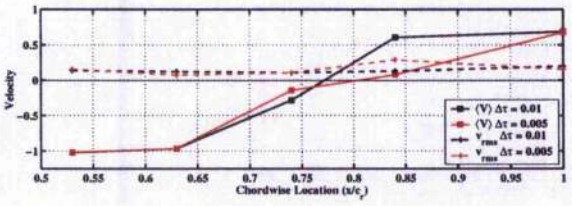

(b) v velocity

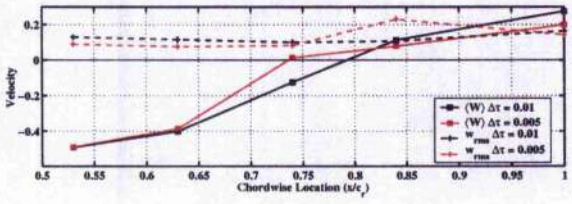

(c) w velocity

Figure 5.10: Mean and RMS velocity components through vortex core; time step comparisons for Non-Linear Eddy Viscosity model

For all mean velocity components it is clear that far upstream of the breakdown at $x/c_r = 0.53$ and 0.63, the solutions are in very good agreement. Closer to the breakdown region at $x/c_r = 0.74$ the agreement between the solutions reduces, due to the differences in vortex breakdown location. Further downstream, the finer time step results exhibit a greater reduction of velocity at $x/c_r = 0.84$ than the coarse time step results. However, by the trailing edge region, as found for all the other comparisons, the mean velocities are, again, in agreement. This is also the case for the other components of velocity. The largest differences are at $x/c_r = 0.84$ for the mean v velocity and $x/c_r = 0.74$ for the mean w velocity. As before these differences are most likely to be associated with the relative difference in location of breakdown and the size and strength of the vortex core region.

Considering the RMS velocities, it is clear that reducing the time step has a significant effect on the unsteady nature of the flow, as expected. Upstream of breakdown, there is an overall reduction in all the RMS velocity components for the fine time step. However, as the flow approaches the vortex breakdown location there is much greater excitation of the flow than for the $\Delta\tau = 0.01$ results. For the u RMS velocity, it is clear that the level of unsteadiness increases upstream of the breakdown location at $x/c_r = 0.74$, which may be due to the influence of the motion of the vortex breakdown location. This level increases again just downstream of breakdown to a level greater than with $\Delta\tau = 0.01$, despite its increased distance from the location of breakdown. Then it reduces to a value less than the coarse time step results at the trailing edge. The behaviour of the spanwise and normal RMS velocities are very similar, with an increase of unsteadiness downstream of breakdown, before a reduction to a level below coarse

time step results. If the location of breakdown is considered relative to the levels of unsteadiness of each case, it may be suggested that unsteadiness in the post-breakdown flow for the fine time step remains higher for a greater distance downstream.

Before discussing the unsteady behaviour predicted from the probe data for each case, it is important to consider the expected levels of temporal resolution for each case. As discussed in Section 2.6, the maximum frequency which can be captured in the flow is determined by the time step (or sample rate) of the signal based on a number of criteria. The baseline time step of $\Delta\tau = 0.01$ was used as an example and it was determined that the maximum non-dimensional frequency would be $St = 10$ for this case. Applying the same method to the $\Delta\tau = 0.005$ time step and the maximum frequency increases to $St = 20$. It is important to remember that this is grid independent for URANS. It was shown for the DES results that a maximum Strouhal number of 40 should have been obtainable but that the grid refinement limited this to approximately $St = 10$. Therefore, the comparison between the unsteady behaviour of the two solutions is very interesting and it is expected that the finer time step will exhibit higher frequency content than the coarse time step.

To consider this expectation, two probe locations were considered. These were close to breakdown for both cases at $x/c_r = 0.84$ and downstream, above the trailing edge. Figure 5.11 shows the time histories and PSD analysis of the u velocity signals at these two locations. The increase in unsteadiness for the $\Delta\tau = 0.005$ solution at $x/c_r = 0.84$ can be considered further and it is clear that the finer time step results not only contain low frequency content associated with the oscillation of breakdown location, but are also influenced by the helical mode winding, which will cause an increase in unsteadiness in the RMS velocity. However, downstream the content of the two signals is very similar, and it is surprising to note that there is similar energy in the higher frequencies at this location for both solutions. For both locations the lower frequency content is almost identical for the two cases, indicating that the behaviour of the vortex breakdown oscillation is unchanged with time step size. The expected higher frequency content for the finer time step is not apparent and for both solutions there is virtually no energy in the solutions above approximately $St = 14$ for either case. It is clear from this comparison that, as for the DES results in the previous chapter, the majority of the dominant flow features in the post-breakdown flow occur at Strouhal numbers less than 10 and are not greatly affected by the decrease in time step size.

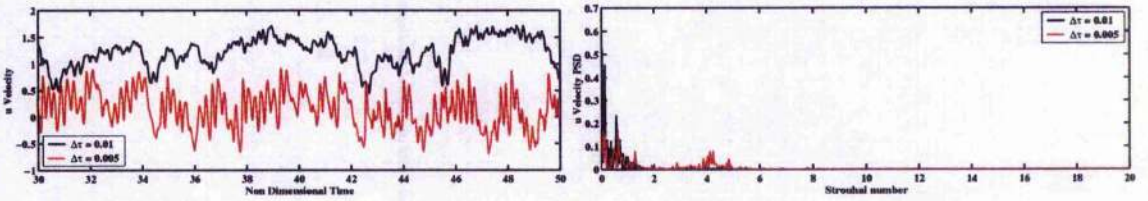

(a) $x/c_r = 0.84$

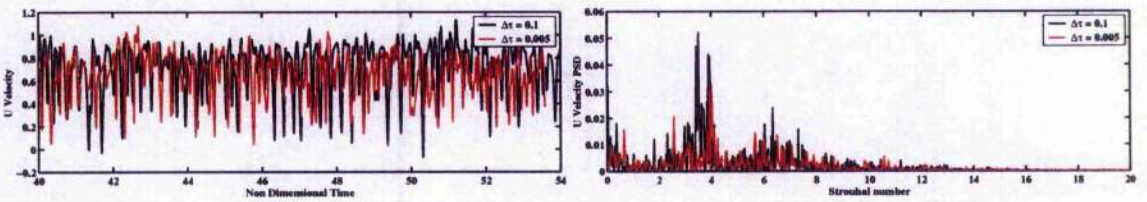

(b) $x/c_r = 1.00$

Figure 5.11: Time history and PSD analysis of u velocity signals for two probes situated on the vortex axis at $z/c_r = 0.1$ above the wing surface; time step comparisons for Non-Linear Eddy Viscosity model

The structure of the vortex breakdown region is shown in Figure 5.12 using contours of instantaneous y vorticity on the probe plane through the vortex core region. From this comparison, it is clear that the behaviour downstream of breakdown is very similar for the two cases. However, there does appear to be slightly more smaller vortical structures in the flow for the $\Delta\tau = 0.005$ solution. Therefore, the resolution of the expected break up of the flow into smaller structures downstream of breakdown has only been marginally improved for this case. As with all other results this behaviour does not appear to continue downstream of the trailing edge and this is likely to be due to the rapid reduction in grid resolution in this region for the fine grid as discussed for the DES results in Section 4.4.

From this analysis of the effect of time step on the Non-Linear Eddy Viscosity model URANS results, it is clear that the flow behaviour is sensitive to the level of predicted unsteadiness in the flow such that the strength of the vortex and the location of breakdown changes. However, the frequencies of the unsteady phenomena in the flow do not appear to be affected. The increase in time refinement has allowed the URANS turbulence model to capture a few more small structures in the flow, however, this does not correspond to an increase in the presence of higher flow frequencies. Therefore, it may be concluded that for this type of flow a time step of $\Delta\tau = 0.01$ is adequate to capture the important frequencies of the flow.

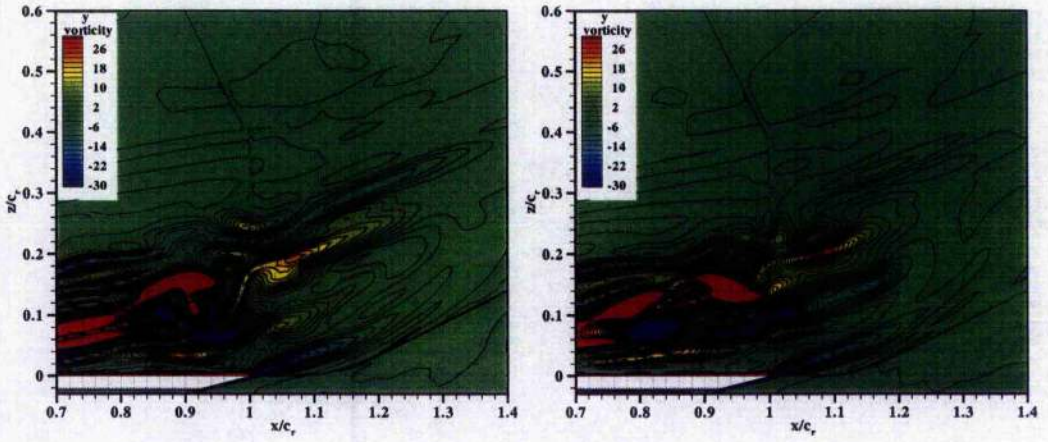

(a) $\Delta\tau = 0.01$ (b) $\Delta\tau = 0.005$

Figure 5.12: Slice through vortex breakdown region, on a plane through vortex core, $y/s = 0.7$ showing instantaneous contours of y vorticity; time step comparisons for Non-Linear Eddy Viscosity model

5.4 Comparison between Non-Linear Eddy Viscosity Model and $k-\omega$ with P_ω Enhancer Model

Before making comparisons with the DES results from the previous chapter, it is necessary to consider the relative behaviour of the two URANS models. Comparisons of the solutions from the two models, the $k-\omega$ with P_ω Enhancer and the Non-Linear Eddy Viscosity model on the fine grid are shown. The comparisons were made using the baseline time step, $\Delta\tau = 0.01$. Figure 5.13 shows the comparisons of the mean and RMS velocity components for the five probes in the vortex core region detailed in the previous sections. The vortex breakdown locations for these results are $x/c_r = 0.83$ for the $k-\omega$ with P_ω Enhancer model and $x/c_r = 0.87$ for the Non-Linear Eddy Viscosity model. Comparison of the vortex core behaviour is shown in Figures 5.1(b) and 5.5(b). From the contours of instantaneous u velocity it is clear that the vortex core region for the Non-Linear Eddy Viscosity model is much more compact than the $k-\omega$ with P_ω Enhancer model. It also appears that the probes sit closer to the vortex core axis in the spanwise direction for the $k-\omega$ with P_ω Enhancer model results. The behaviour of the shear layer emanating from the leading edge is also quite different and does not appear to curve upward to form the vortex, instead an inflection point is evident outboard of the leading edge where the shear layer suddenly changes direction inboard to create the roll up into the primary vortex. This is accompanied by a larger and stronger secondary vortex in this region, which is also suggested from the entropy isosurface.

Considering the behaviour of the mean velocity components, it is clear that the location of breakdown is the cause of the greatest differences. For the mean u velocity this shows that the level of axial velocity does not decrease as significantly for the Non-Linear Eddy Viscosity model for the probes downstream of breakdown as for the $k-\omega$ with P_ω Enhancer model. However, upstream of breakdown and at the trailing edge, the behaviour is very similar. The mean velocity in the spanwise and normal directions also exhibit similar behaviour. Emphasis of the relative size and location of the vortex cores are obtained by consideration of the mean w velocity. The Non-Linear Eddy Viscosity model predicts consistently lower mean values, suggesting that the probe is further from the core axis and that the vortex is weaker. This means that the vortex core is further inboard for the Non-Linear Eddy Viscosity model, however the locations are similar in the normal direction. A further appreciation of the differences between the solutions predicted by each model may be obtained from analysis of the RMS velocities in the vortex core region. It is evident that the velocity fluctuations in the spanwise and normal directions are greater upstream of breakdown for the Non-Linear Eddy Viscosity model, but much less in the downstream region.

However, further downstream at the trailing edge, the level of unsteadiness is similar for the two models. For the streamwise velocity fluctuations, indicated by u_{rms}, the solutions exhibit similar behaviour at $x/c_r = 0.84$ although this location is downstream of breakdown for the $k-\omega$ with P_ω Enhancer model and upstream for the Non-Linear Eddy Viscosity model solution. Despite the differences in breakdown location, it is clear that the effect of the vortex breakdown at this location is the same for each case. This is due to this probe being within the oscillating region of breakdown for both cases. Upstream of breakdown, it is again clear that the level of unsteadiness is greater for the Non-Linear Eddy Viscosity model solution.

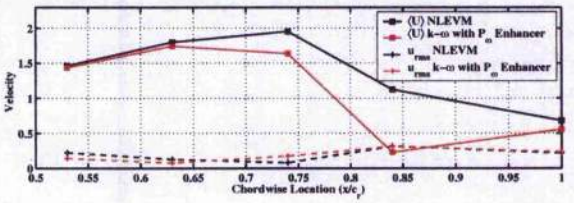

(a) u velocity

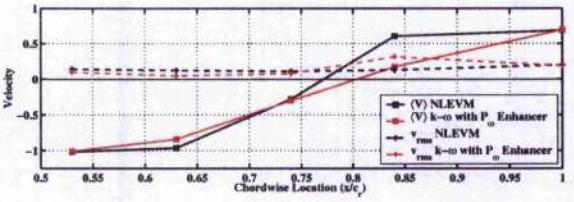

(b) v velocity

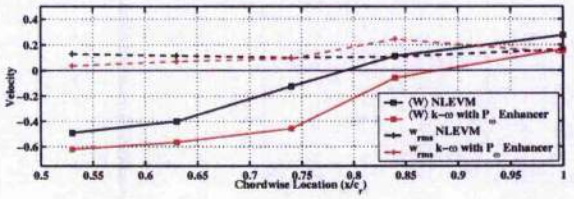

(c) w velocity

Figure 5.13: Mean and RMS velocity components through vortex core; comparison of $k-\omega$ with P_ω Enhancer, $\Delta\tau = 0.01$, and Non-Linear Eddy Viscosity model, $\Delta\tau = 0.01$, for the fine grid

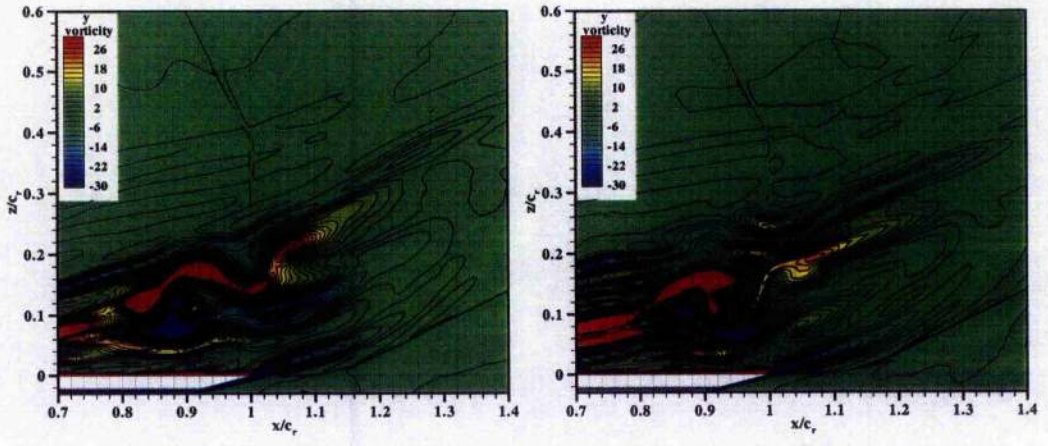

(a) $k-\omega$ with P_ω Enhancer (b) NLEVM

Figure 5.14: Time history and PSD analysis of u velocity signals for two probes situated on the vortex axis at $z/c_r = 0.1$ above the wing surface; Comparison of $k-\omega$ with P_ω Enhancer and NLEVM models for the Fine grid at $\Delta\tau = 0.01$

To further consider the post-breakdown flow behaviour, a slice through the vortex core region in the plane of the probes is taken and instantaneous contours of y vorticity are analysed as before. Figure 5.14 shows these results for both turbulence models. At this instant in time, $\tau = 50$, it appears that the location of breakdown is in agreement for the two solution and it is evident that the winding of the spiral breakdown is clear in each case. From the three-dimensional flow behaviour, shown by the isosurfaces of entropy, this behaviour also appeared to be very similar. However from these plots, a number of small differences in the post-breakdown flow behaviour are evident. The onset of breakdown and the change from a clear vortex to the breakdown spiral appears to be more pronounced for the $k-\omega$ with P_ω Enhancer model and the post-breakdown region for the Non-Linear Eddy Viscosity model solution appears to be smaller in extent in the normal direction. However, the location above the wing is the same. The streamwise extent of the flow behaviour is also smaller for the Non-Linear Eddy Viscosity model solution, however both cases clearly show the effect of the decrease in grid refinement downstream of the trailing edge and the resulting decrease in numerical accuracy in this region. Further consideration of the relative behaviour of the two URANS models can be obtained from analysis of the unsteady behaviour in the vortex core region in a similar manner to the DES results described previously in Section 4.5.

5.4.1 Unsteady Behaviour predicted by URANS Solutions

Figures 5.15 and 5.16 show the unsteady flow behaviour at each probe location considered above, for the $k-\omega$ with P_ω Enhancer and Non-Linear Eddy Viscosity models respectively. Considering the unsteady behaviour of the $k-\omega$ with P_ω Enhancer model in the first instance. For this case, it is found that the probes at $x/c_r = 0.53, 0.63$ and 0.74 are upstream of breakdown, with all probes sitting above the vortex core axis. The probe at $x/c_r = 0.53$ sits within the shear layer and the probe at $x/c_r = 0.63$ sits in the region between the vortex core and the shear layer. As breakdown occurs at $x/c_r = 0.83$, the probes at $x/c_r = 0.84$ and 1.0 are within the post-breakdown region.

Considering the flow behaviour in the streamwise direction, the u velocity traces show that, upstream of breakdown, the unsteady oscillations of the velocity have relatively low amplitude, particularly in comparison with the behaviour downstream of breakdown. At $x/c_r = 0.53$, the trace exhibits a slightly larger amplitude and higher frequency than for the probes closer to the vortex core, due to its location in the shear layer. This is likely to be due to the presence of shear layer instabilities. At $x/c_r = 0.84$, the velocity time history shows a large amplitude, low frequency oscillation consistent with the fluctuation of vortex breakdown location and it is evident that the breakdown location passes over this position at a number of instances in the time trace as the velocity decreases below zero, suggesting recirculating flow. A higher frequency clearly exists in this signal also. Further downstream, at the trailing edge, the low frequency behaviour appears to have disappeared and a higher frequency remains. Considering the spanwise and normal velocity behaviour and it is evident that these trends are similar for each component of velocity. However, larger amplitude oscillations are found to occur in the $x/c_r = 0.84$ signal as the breakdown moves upstream of the probe location.

From analysis of the frequency content of the time traces, a number of dominant flow frequencies can be identified. For the streamwise velocity, it is evident that there are two dominant frequencies in the probes used in this investigation. At $x/c_r = 0.84$, the dominant frequencies in the signal appear to be centred around $St = 0.07$, which has previously been identified with the oscillation of vortex breakdown location. A second smaller peak is also evident at approximately $St = 3.25$ and is associated with the helical mode instability and winding. This is the higher frequency mentioned above. Further downstream of breakdown, this frequency is also dominant, however appears to have more energy. With a closer look at the u velocity PSD analysis, further frequencies may be determined in the signals upstream of breakdown. It was found that the effect of the oscillation of breakdown location was also mildly felt upstream of breakdown at $x/c_r = 0.74$. At $x/c_r = 0.53$, the higher frequencies associated with the time trace described before were found to correspond to $St \approx 5-8$, which is within the possible frequency range for shear layer instabilities.

For the spanwise velocity, the helical mode winding frequency dominates the PSD analysis occurring at $St \approx 3.25$ as before, but with a slightly broader frequency peak. This frequency is most dominant at $x/c_r = 0.84$, with the energy at this frequency close to the trailing edge being significantly less. Also present at $x/c_r = 0.84$ is evidence of a spanwise oscillation of the vortex breakdown location with a frequency peak again centred at $St = 0.07$. Upstream of breakdown, similar low energy frequencies are present in the range $St \approx 5-8$. This pattern is also evident for the normal velocity, w, with the same frequencies appearing. However, the effect of the vortex breakdown location, although present, is not as significant. It also appears that the signal at the trailing edge has some content at similar frequencies as that found for the probe within the shear layer, $St \approx 5-7$.

A similar analysis can be carried out for the Non-Linear Eddy Viscosity model results. Consideration was given

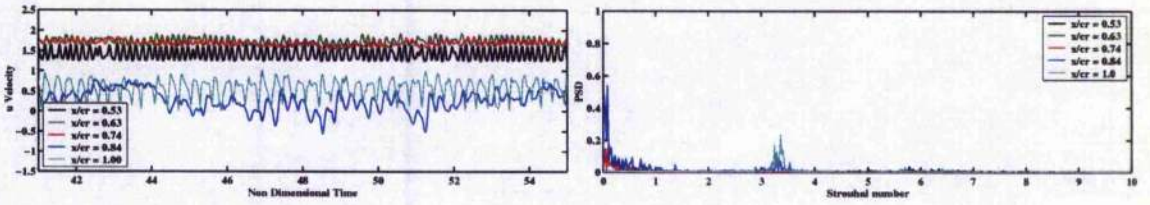

(a) u velocity

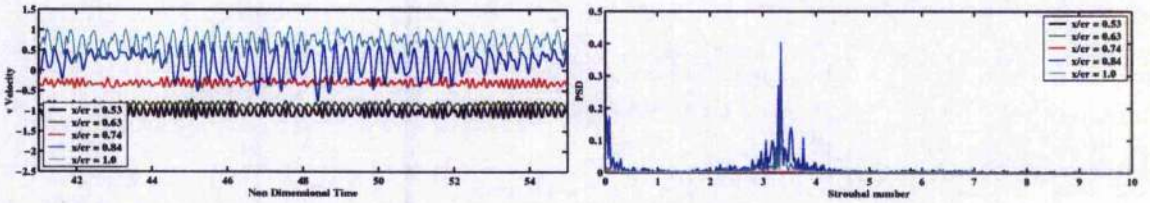

(b) v velocity

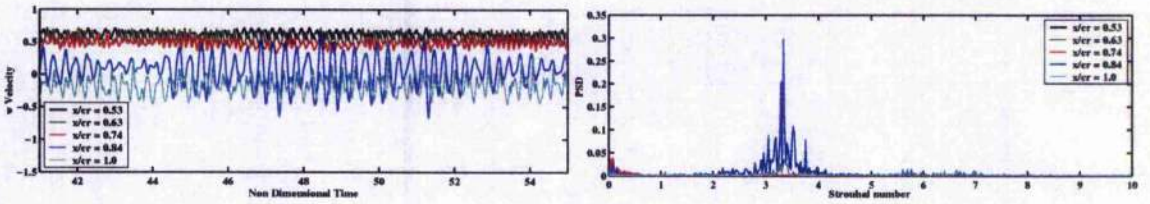

(c) w velocity

Figure 5.15: Unsteady behaviour of non-dimensional velocity components at probes through vortex core region shown by time histories and PSD frequency plots for $k-\omega$ with P_ω Enhancer model, $\Delta\tau = 0.01$

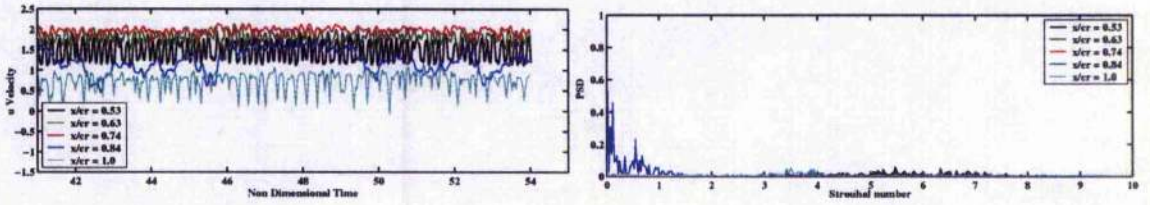

(a) u velocity

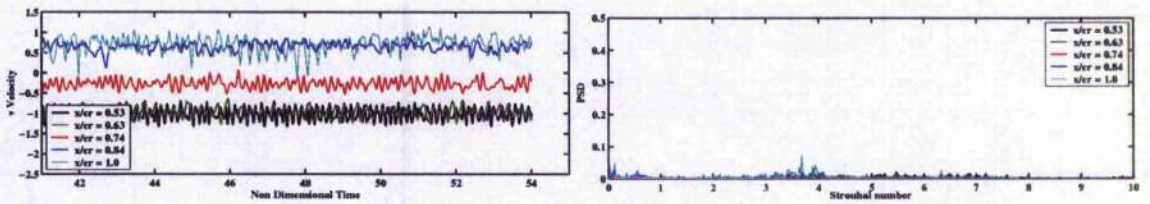

(b) v velocity

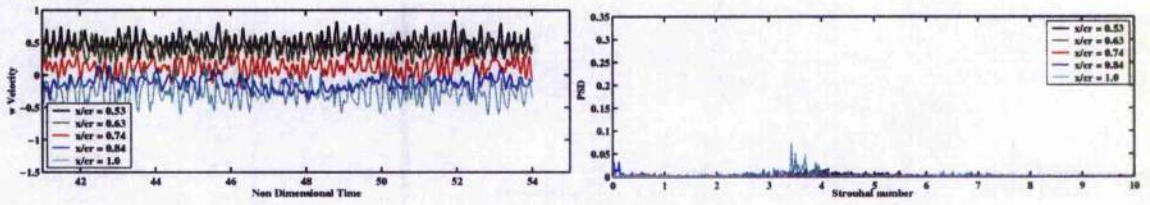

(c) w velocity

Figure 5.16: Unsteady behaviour of non-dimensional velocity components at probes through vortex core region shown by time histories and PSD frequency plots for NLEVM, $\Delta\tau = 0.01$

to the location of the probes with respect to the vortex core location and it was determined that the probes at $x/c_r = 0.53$, 0.63 and 0.74 are all in similar locations to those for the $k-\omega$ with P_ω Enhancer model, upstream of breakdown and above the vortex core. However, as the mean location of breakdown was found to be further downstream for this case, the probe at $x/c_r = 0.84$ is upstream of breakdown. The probe at $x/c_r = 1.0$ is in the post-breakdown flow as before. Considering the u velocity time traces, it is evident that there are both similarities and differences compared to the $k-\omega$ with P_ω Enhancer model results. Upstream of breakdown, at $x/c_r = 0.53$ the behaviour is similar to the $k-\omega$ with P_ω Enhancer results, however the amplitude and frequency of the signal appears to be larger. This is also true for the probes at $x/c_r = 0.63$ and 0.74. The trend of amplitudes between the upstream probe locations is, however, the same as before. As before, at $x/c_r = 0.84$ the behaviour is quite different with a high amplitude, low frequency oscillation being present, superimposed on to a smaller amplitude, higher frequency fluctuation. This is in agreement with the $k-\omega$ with P_ω Enhancer model results. However, from the signal, it is clear that the breakdown location does not oscillate over this probe position. This indicates the effect of the vortex breakdown location on the vortex core properties upstream of breakdown, which is not evident from the $k-\omega$ with P_ω Enhancer model results. Downstream of breakdown, a higher frequency is again found in the time history at the trailing edge and the amplitude appears to be of a similar size to the $k-\omega$ with P_ω Enhancer model results.

Differences in the flow behaviour are also apparent from the spanwise and normal velocity time traces. Upstream of breakdown, the behaviour is similar to the $k-\omega$ with P_ω Enhancer model results, however as before, the amplitudes of the signals are larger. This is particularly true for the w velocity traces, which have amplitudes which appear to be 2 to 3 time larger than the corresponding signals from the $k-\omega$ with P_ω Enhancer model solution. Close to breakdown, however, the behaviour of the unsteady flow appears to be quite different. In the $k-\omega$ with P_ω Enhancer model results, the amplitude of the signal from the $x/c_r = 0.84$ probe exhibited an amplitude modulation as the breakdown location was found to move over the probe location. Clearly, as this does not occur for the Non-Linear Eddy Viscosity results, there is no modulation and it is found that the amplitude is considerably less. At the trailing edge, the behaviour of the time traces appear to show the best agreement with the $k-\omega$ with P_ω Enhancer model solutions, although the frequency of the fluctuations does appear to be higher.

As before, the frequency content of these signals was considered from PSD analyses of the time traces. Considering the frequency content of the u velocity signals, it is again evident that a number of dominant frequencies are present. Low frequencies associated with the fluctuations of vortex breakdown location are evident, for the signal at 0.84. In this case, it appears that there are two dominant frequencies, one centred at $St \approx 0.07$ and a second occurring at $St \approx 0.6$. There does not appear to be much energy at higher frequencies at this location, however, there is a slight indication of frequencies in the range $St \approx 3.5-4$. Downstream of the breakdown location at $x/c_r = 1.0$ this higher frequency range $St \approx 3.5-4$ is much more dominant, however it has a much reduced energy level than that found in the $k-\omega$ with P_ω Enhancer model results. This is likely to be the frequency associated with the helical mode winding as it occurs at a similar frequency as found before. Closer analysis of the probes upstream of breakdown, show that there is also little energy in the probes at $x/c_r = 0.63$ and 0.74, although evidence of a very small upstream effect of the helical mode winding and vortex breakdown location is found at $x/c_r = 0.74$, by changing the scale of the plot. At $x/c_r = 0.53$, energy within the signal is greater with dominant frequencies occurring in the range $St = 4-7$. This is in good agreement with the $k-\omega$ with P_ω Enhancer model results however, the energy at these frequencies is slightly greater. Similar frequencies are also found in the $x/c_r = 0.63$ signal, but at a much reduced level. Overall it is found that, with the exception of the frequencies found within the shear layer region, the frequencies predicted for this case are consistently higher than those found for the $k-\omega$ with P_ω Enhancer model.

As before, the spanwise and normal velocities show similar frequency content, however there are, again, some differences compared to the $k-\omega$ with P_ω Enhancer results. The most striking difference is the omission of the large dominant peak for the $x/c_r = 0.84$ probe at the frequency associated with the helical mode winding. This is again due to the location of breakdown not moving upstream of this point in the unsteady solution. For the v velocity, it also appears that there is no evidence of a spanwise motion of the vortex breakdown oscillation at this location. However, a small peak is clear in the w velocity PSD plot. Downstream of breakdown, however, this frequency content is clear for the v velocity but not for the w velocity signal. The frequency content for the helical mode winding, however, occurs for both cases and appears to have a similar level of energy compared to the $k-\omega$ with P_ω Enhancer model results. Very low energy frequency content is also found for the probes upstream of breakdown, $x/c_r = 0.53$ and 0.63, at the frequencies mentioned for the u velocity, with the dominant frequencies appear to be higher for the v velocity PSD analysis than the w velocity, these frequencies are $St = 4-7$ and $St = 3-5$ respectively. As before, these frequencies are likely to be associated with the shear layer behaviour.

5.4.2 Effect of Eddy Viscosity Treatment

In order to further understand the comparisons and differences between these flow solutions, it is necessary to consider the differences in formulation of each model. Both models used in this investigation modify the linear Boussinesq based Wilcox $k-\omega$ model to account for the rotation present in the flow due to the leading edge vortices. The $k-\omega$ with P_ω Enhancer model applies a modification which accounts for vortical flows. This modification enhances the production of the dissipation in order to reduce the turbulence and the eddy viscosity in the vortex core. Whereas the Non-Linear Eddy Viscosity model uses an approach derived from a explicit algebraic Reynolds stress model, which models the Reynolds stresses using both strain rate and rotation tensors. This adds extra terms to the calculation of the Reynolds stress tensor and results in a non-linear formulation. Further detail of each model was given in Chapter 2.

Before considering the relative behaviour of each model used in this investigation, it is important to consider the turbulent behaviour of the baseline model, the Wilcox $k-\omega$ model. A similar unsteady calculation was performed to allow this comparison. Instantaneous contours of the ratio of turbulent eddy viscosity to the laminar viscosity are shown in Figure 5.17 for these results. In the discussion of the Wilcox $k-\omega$ model in Section 2.4.1, it was stated that the main issue with standard Boussinesq models for vortical flows is that there is an overproduction of turbulence within the vortex core region. This is due to the linear dependence of the Reynolds stress tensor on the strain rate tensor with no accounting for the rotation of the flow. As a result, the levels of eddy viscosity are large due to its dependence on k and ω (See Equation 2.58). It is clear from Figure 5.17 that the levels of eddy viscosity are indeed very high in the vortex region above the wing surface and that there is no distinction between the core region, shear layer or breakdown region. As discussed before, this generally results in the prediction of a very weak vortex system, which is sensitive to instabilities in the flow. The over-prediction of turbulence also causes the unsteadiness of the flow to be dissipated due to an increase in turbulent mixing and the solution becomes unrealistically steady in nature.

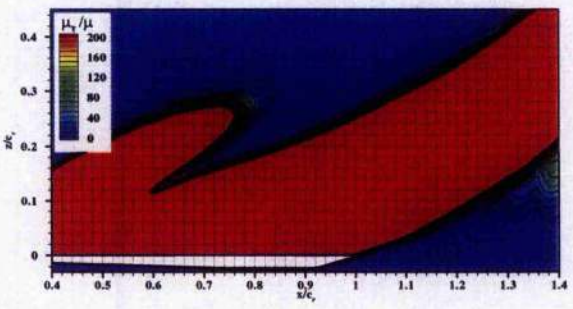

Figure 5.17: Slice through vortex breakdown region, on a plane through vortex core, $y/s = 0.7$ showing instantaneous contours of μ_T/μ for Wilcox $k-\omega$ model

Figure 5.18 shows similar contours of the turbulent behaviour through the vortex core for the $k-\omega$ with P_ω Enhancer and Non-Linear Eddy Viscosity models. Also shown are contours of instantaneous turbulent kinetic energy for comparison. With the P_ω Enhancer applied to the $k-\omega$ model, the levels of eddy viscosity are found to reduce in the vortex core. This is due to the enhancement of ω in regions of high rotation as described in Section 2.4.2, reducing the production of turbulence. The eddy viscosity is calculated in the same way as the Wilcox $k-\omega$ model, thus as ω is increased and k is reduced, the eddy viscosity also reduces. It is clear from Figure 5.18(a), that comparably high regions of turbulence still exist within the shear layer region and downstream of the vortex breakdown location. However, even in these regions the levels of turbulence are reduced by two orders of magnitude compared to the standard Wilcox $k-\omega$ model. This is evident from the comparison of the eddy viscosity contours in these regions.

Considering the turbulent contours for the Non-Linear Eddy Viscosity model, it is clear that the overall behaviour is quite different. Upstream of the trailing edge, there is little evidence of turbulence in the flow, with both the ratio of turbulent eddy viscosity to laminar viscosity and the turbulent kinetic energy exhibiting values close to zero in this region. It appears that the levels of these variables only increase in the shear layer region of the flow downstream of the trailing edge. As stated previously, breakdown is found to occur at approximately $x/c_r = 0.87$ and it would be expected that the flow would be turbulent downstream of this location. However, this clearly does not occur immediately. However, despite this, the vortex core region is laminar, which is the most important factor in the prediction of the flow behaviour, as described previously. The reduction of the eddy viscosity and turbulence in the vortex region was expected from the formulation of the model. The extra anisotropy term of the Reynolds

stress equation reduces the production of turbulence in the flow and the eddy viscosity of the model is reduced, particularly in the vortex core regions, due to the dependency of the C_μ^{eff} term on the rotation of the flow. However, it appears that this non-linear modification of the model provides a virtually laminar solution throughout the entire vortex region.

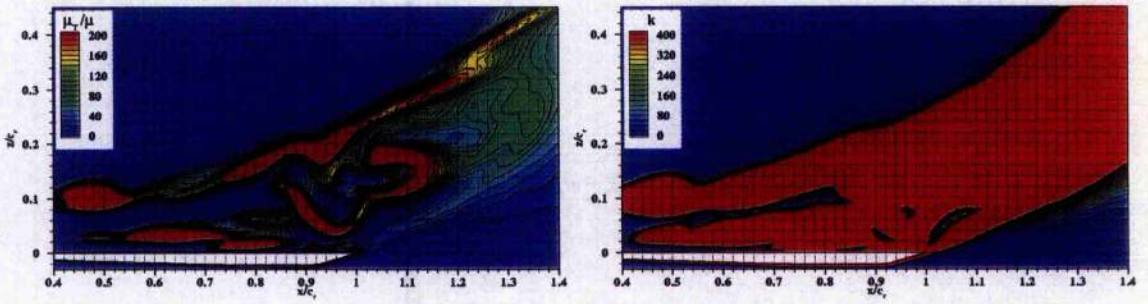

(a) $k-\omega$ with P_ω Enhancer

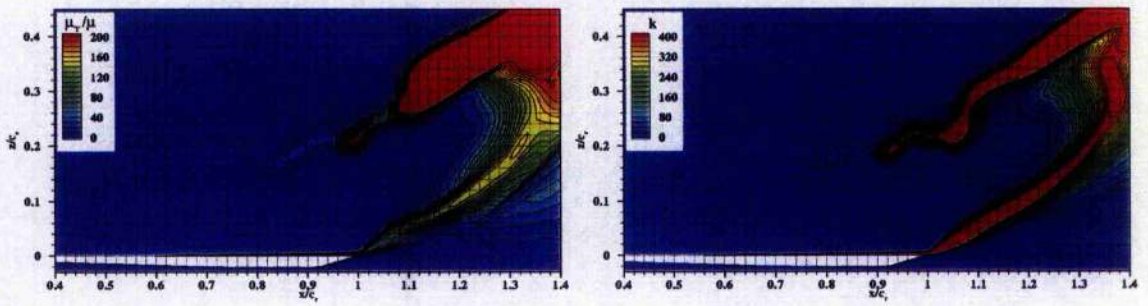

(b) NLEVM

Figure 5.18: Slice through vortex breakdown region, on a plane through vortex core, $y/s = 0.7$ showing instantaneous contours of μ_T/μ and turbulent kinetic energy for both URANS models, fine grid, $\Delta\tau = 0.01$

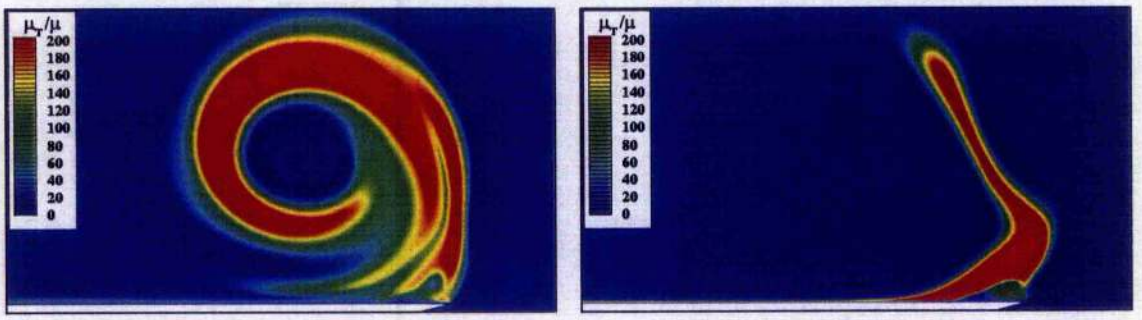

(a) $k-\omega$ with P_ω Enhancer

(b) NLEVM

Figure 5.19: Slice through vortex region at $x/c_r = 0.84$ showing instantaneous contours of μ_T/μ for both URANS models, fine grid, $\Delta\tau = 0.01$

To further consider the turbulent behaviour through the vortex region and particularly to consider if there are regions of turbulence apparent in the Non-Linear Eddy Viscosity model solution, a slice was taken through the vortex at $x/c_r = 0.84$. Figure 5.19 shows this slices with instantaneous contours of μ_T/μ, as before. This plane is just downstream of breakdown for both solutions. For the $k-\omega$ with P_ω Enhancer model, the widened laminar vortex core region is clear with higher levels of eddy viscosity found in the shear layer and a smaller low viscosity region evident which corresponds to the secondary vortex core region. For the Non-Linear Eddy Viscosity model solution, the behaviour is again very different, however it is clear that turbulence exists in the solution, in the shear layer close to the leading edge and within the secondary vortex region. However, this does not extend around the vortex

region and the flow is virtually laminar in all other regions.

Returning to the comparisons between the two models discussed previously and the fact that the Non-Linear Eddy Viscosity model is predicting a very laminar flow may explain some of the differences witnessed between the two solutions. For example, it was found that the location of the primary vortex was further inboard for the Non-Linear Eddy Viscosity model solution than for the $k-\omega$ with P_ω Enhancer results. This is due to the larger secondary vortex also noted in the previous section. The larger, stronger secondary vortex occurs as a result of the laminar behaviour within the boundary layer and the secondary separation caused by an adverse pressure gradient. As mentioned before, Hummel [48] showed that a laminar separation causes a larger and stronger secondary vortex than a turbulent separation. Further evidence of this behaviour can be obtained from consideration of the surface streamlines, as shown in Figure 5.20. As stated in the description of the calculations given in Chapter 4 a forced transition was set on the grid at a streamwise location of approximately $x/c_r = 0.36$ and therefore it is assumed that transition will occur just downstream of this location where the turbulence model is active. Considering the surface streamlines for the $k-\omega$ with P_ω Enhancer model, it is clear that this is the case. This is indicated by the outboard inflection of the secondary separation line, as separation will occur earlier for a laminar boundary layer for a given adverse pressure gradient. However, for the Non-Linear Eddy Viscosity model results, this inflection of the secondary separation line does not occur until approximately $x/c_r = 0.64$. This suggests that the increase of μ_T in the flow is too gradual, resulting in a delayed transition to turbulent flow. The strong secondary vortex is also evident from the surface pressure coefficient contours shown.

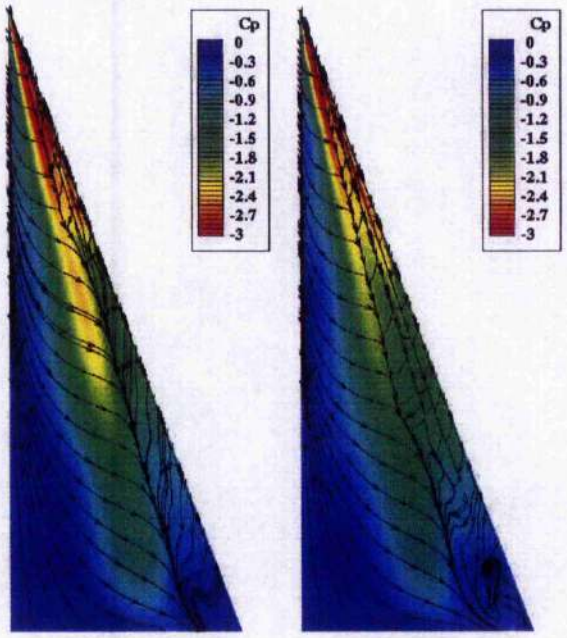

(a) $k-\omega$ with P_ω Enhancer (b) NLEVM

Figure 5.20: Surface streamlines showing comparable behaviour of secondary separation line after transition to turbulence at $x/c_r \approx 0.36$ for both URANS models, fine grid, $\Delta\tau = 0.01$

Reconsidering the unsteady behaviour of the solutions, some of the differences in the predictions may also be attributed to the levels of turbulence within the vortex region. It was found that the vortex breakdown oscillation predicted by the Non-Linear Eddy Viscosity model exhibits a greater upstream influence on the flow behaviour than for the $k-\omega$ with P_ω Enhancer model. This is likely to be due to the decrease in dissipation and mixing which comes with a laminar flow, resulting in the effects of a disturbance to be felt further upstream than for a turbulent flow. Thus, the eddy viscosity of the $k-\omega$ with P_ω Enhancer model dissipates these fluctuations. This increase in influence results in a higher energy of the peak predicted by the PSD analysis for the dominant frequency of breakdown. However, downstream of breakdown the behaviour changes and the levels of energy in the dominant peaks reduce compared to the $k-\omega$ with P_ω Enhancer model solutions. This may also be due to the levels of turbulence in the flow solution. For low levels of eddy viscosity and turbulence, there will be much less turbulence mixing compared to the $k-\omega$ with P_ω Enhancer model solutions. This acts to smooth the gradients of the mean flow fluctuations, resulting in a lower energy for these frequencies.

However, despite the largely laminar behaviour of the flow and the differences compared to the $k-\omega$ with P_ω Enhancer model described, the Non-Linear Eddy Viscosity model exhibits reasonable results, with similar dominant frequencies and behaviours. This further confirms the suggestion that the level of turbulence predicted is not a significant factor in predicting the major flow phenomenon downstream of vortex breakdown. However, it may serve to show that with a better resolution of the turbulence in the flow, the dominant frequencies will be lower. However, further investigation would be needed to state this conclusively.

From these comparisons and the discussion of the performance of each model it may be concluded that for this investigation that the $k-\omega$ with P_ω Enhancer model has predicted the flow behaviour more accurately. These solutions will now be compared with the DES results detailed in the previous Chapter to asses the ability of the model to predict the unsteady vortex flow.

5.5 Comparison of URANS and DES

Having made comparisons with other URANS models and concluded that the behaviour of the solution using the $k-\omega$ with P_ω Enhancer model on the fine grid with a time step of $\Delta\tau = 0.01$ is reasonable, it may now be compared to the results of the DES investigation detailed in the previous Chapter. This comparison will provide a measure of the applicability of this linear URANS model with rotation correction to unsteady delta wing vortical flows. The DES calculations discussed in detail in Chapter 4 were performed using the fine grid with refined trailing edge region, as it was found in Section 4.4 that an increase in refinement in the trailing edge region slightly improved the resolution of the turbulence and unsteady behaviour of the flow. However, for the URANS calculations, this refinement is not necessary, as the solutions are only numerically dependent on the grid refinement. Therefore, as stated in the previous sections, all URANS calculations were performed using the fine grid. To allow for a fair comparison and to keep the grid consistent, the DES solution on the fine grid will be used in this section for comparison.

Figure 5.21 shows the comparison of the mean and RMS velocity components for the two turbulence treatments in the same manner as before. It is clear from these plots that overall the solutions are in reasonable agreement. Considering the mean u velocity, it is clear that the $k-\omega$ with P_ω Enhancer model predicts values which are lower than the DES results for all probe locations. It is also evident that the mean location of breakdown is predicted to be slightly further upstream, which is likely to be due to the prediction of a lower core velocity upstream of breakdown. The mean breakdown location for the $k-\omega$ with P_ω Enhancer model solution is approximately $x/c_r = 0.83$ and for the fine grid DES results it is approximately $x/c_r = 0.85$. The RMS u velocity shows good agreement for all probe locations except the probe closest to breakdown at $x/c_r = 0.84$. It is clear that there is considerably more unsteadiness in the flow for the DES solution at this location. This may be due to greater fluctuations of the vortex breakdown location in the streamwise direction for the DES solution.

The mean and RMS spanwise velocity show very good agreement between the two solutions, showing that the location above the wing is the same for each solution. However, there is a consistent difference in the mean w velocity predictions. This shows that the $k-\omega$ with P_ω Enhancer model predicts a higher normal velocity suggesting that either the core region is larger than for the DES results or that the vortex sits slightly further inboard. As this difference is consistent both upstream and downstream of the breakdown location, it may be suggested that it is the location of the vortex core which is different. The RMS w velocity shows that there is more unsteadiness predicted for the DES model upstream of breakdown in this direction, but that close to breakdown the $k-\omega$ with P_ω Enhancer model results exhibit a higher unsteadiness. Downstream of breakdown, the levels appear to be the same for all RMS velocity components.

To consider the relative post-breakdown behaviour, instantaneous contours of y vorticity are shown in Figure 5.22 through the vortex core region. It is clear that at the instant compared, the location of breakdown is very similar for the two solutions. This occurs at approximately $x/c_r = 0.80$ for the $k-\omega$ with P_ω Enhancer model solution and just upstream of this location for the DES solution. The breakdown appears to be similar in form for both solutions with a sudden change in the behaviour of the vortex core. Downstream of breakdown, the behaviour is also very similar with the vortex core winding evident in both solutions. However further downstream it is clear that more smaller structures exist in the DES solution. Whereas the $k-\omega$ with P_ω Enhancer model results show some structures, however these appear to be smeared across the grid in the trailing edge region. It is also evident that the shear layer is clearer in the DES solution both upstream and further downstream of the trailing edge. However, the area covered by the breakdown region is the same for each solution.

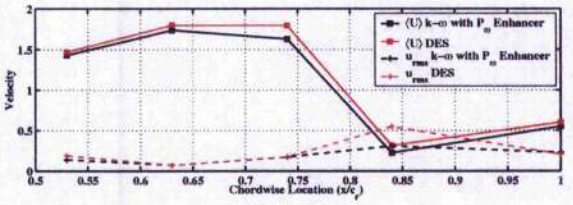

(a) u velocity

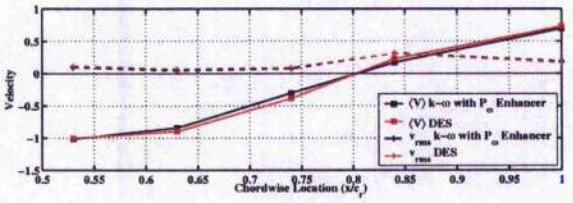

(b) v velocity

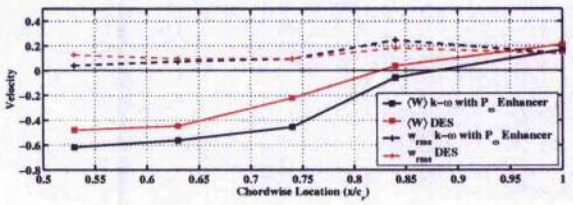

(c) w velocity

Figure 5.21: Mean and RMS velocity components through vortex core; URANS $k-\omega$ with P_ω Enhancer model compared to DES solutions

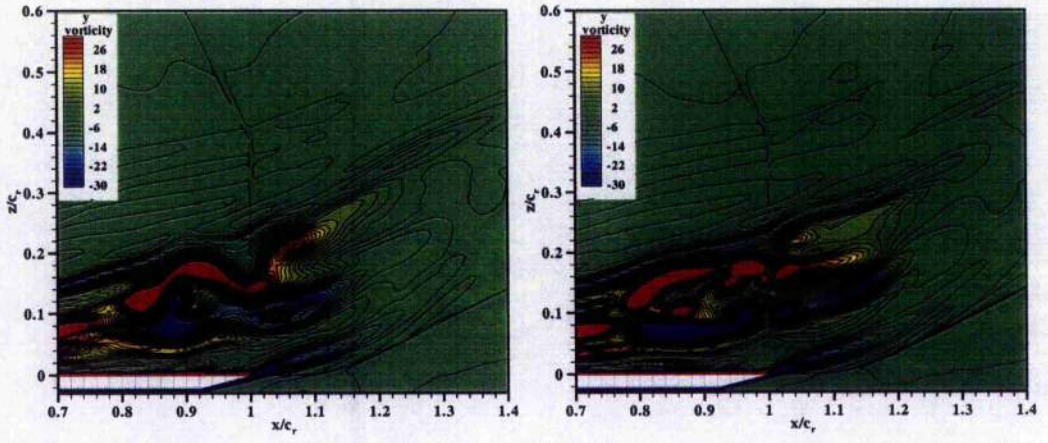

(a) $k-\omega$ with P_ω Enhancer $\Delta\tau = 0.01$

(b) DES $\Delta\tau = 0.0025$

Figure 5.22: Slice through vortex breakdown region, on a plane through vortex core, $y/s = 0.7$ showing instantaneous contours of y vorticity at $\tau = 50$, for URANS $k-\omega$ with P_ω Enhancer model and DES

5.5.1 Comparison of Unsteady Flow Behaviour Prediction

Figures 5.23 and 5.24 show the time histories and PSD analyses for the $k-\omega$ with P_ω Enhancer model and DES solutions, respectively. Considering the time histories initially, the amplitude and the unsteady behaviour of each component of velocity can be considered. It is clear that upstream of breakdown, at $x/c_r = 0.53$, 0.63 and 0.74 probe locations that the amplitude and oscillation of all three components of velocity are very similar for each model. However, at $x/c_r = 0.74$ for the u velocity, it is clear that for the DES solution, the oscillation of breakdown appears to have a more significant effect than for the $k-\omega$ with P_ω Enhancer model. The behaviour at

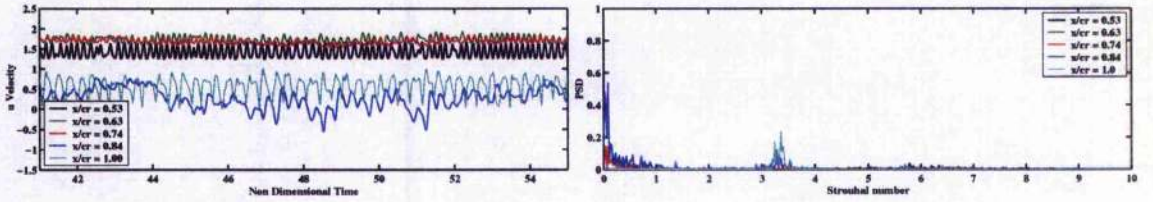

(a) u velocity

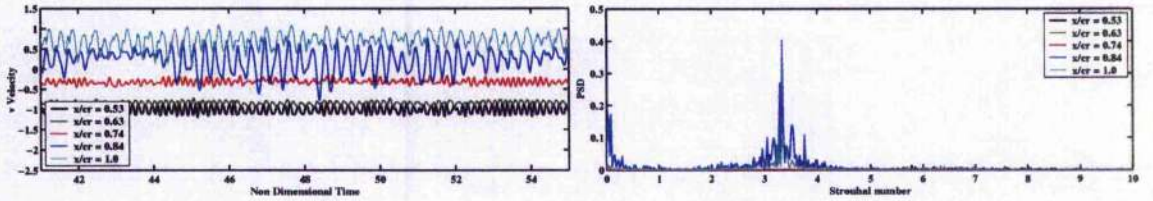

(b) v velocity

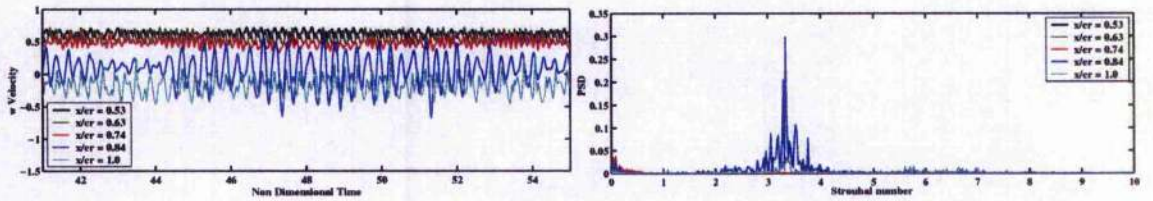

(c) w velocity

Figure 5.23: Unsteady behaviour of non-dimensional velocity components at probes through vortex core region shown by time histories and PSD frequency plots for $k-\omega$ with P_ω Enhancer model, $\Delta\tau = 0.01$

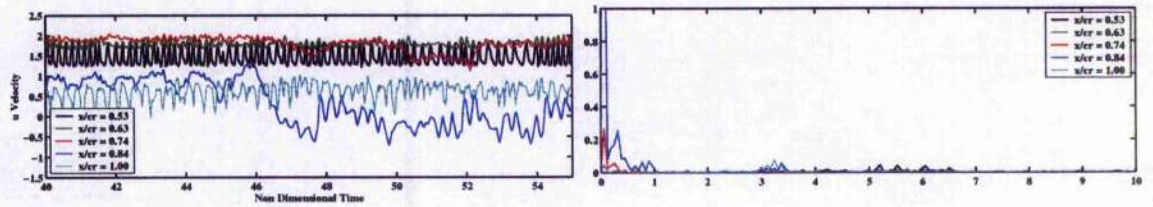

(a) u velocity

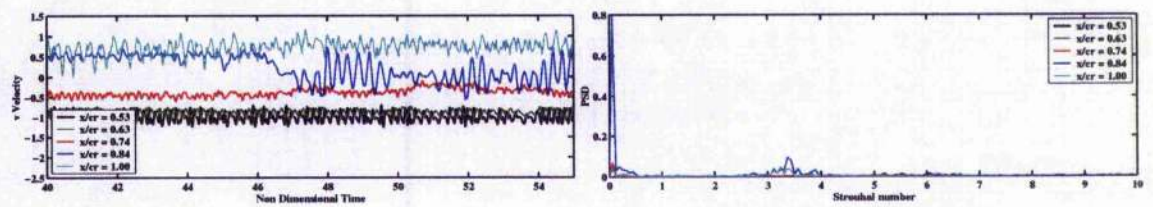

(b) v velocity

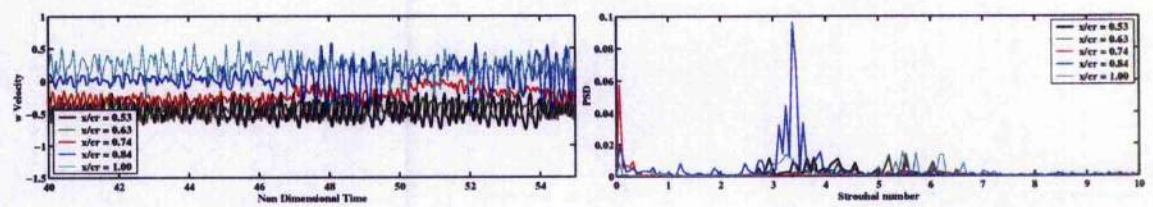

(c) w velocity

Figure 5.24: Unsteady behaviour of non-dimensional velocity components at probes through vortex core region shown by time histories and PSD frequency plots for DES, $\Delta\tau = 0.0025$

$x/c_r = 0.84$ is also slightly different for the DES solution with the location of breakdown clearly sitting downstream of the probe location for almost half of the signal, then it moves upstream and seems to oscillate over the probe location as the velocity appears to oscillate about zero. For the $k-\omega$ with P_ω Enhancer model solution, breakdown appears to oscillate over the probe location for the whole signal length, although it is clear that this is not the mean location. The change in behaviour for the DES solution also appears for the v and w velocity traces, with an increase in amplitude evident. The results from the $k-\omega$ with P_ω Enhancer model calculation exhibits this larger amplitude for a larger portion of the signal, which appears to occur when breakdown is close to or upstream of the probe location. Downstream at the trailing edge the behaviour is again very similar.

Considering the frequency content of the probe signals for the two models, it is clear that the magnitude of the frequencies are very similar. The PSD analyses of the velocity components show that the oscillation of the breakdown location and the frequency associated with the helical mode winding are both present. These occur at $St = 0.07$ and $St = 3.25$, respectively for both models. However, the power of these frequencies within the signals are quite different. The energy in the oscillation of breakdown frequency is much larger for the DES solution compared to the $k-\omega$ with P_ω Enhancer model results. For the u velocity, the energy of the DES oscillation is almost ten times larger. However, the energy of the helical mode instability frequency is consistently larger for the $k-\omega$ with P_ω Enhancer model solutions. Higher frequency content at $St = 5-7$ is also present in both solutions. The agreement between the solutions can be seen more clearly by directly comparing the signal from a single probe in the flow. Figure 5.25 shows the u velocity time histories and PSD analysis from the probe above the trailing edge for each solution. These plots further confirm the discussion given above. The time histories show that although the signals behave differently with time, it is clear that the amplitude and oscillation of the signals are very similar. Considering the PSD analysis, this highlights that the frequencies present in the signals are almost identical, with the main differences being due to the relative energy of each frequency. It is clear that the energy of the higher frequencies are the same.

From this unsteady analysis and the analysis of the mean flow behaviour, it is evident that the URANS model is capable of predicting the same dominant flow features and frequencies as the DES model.

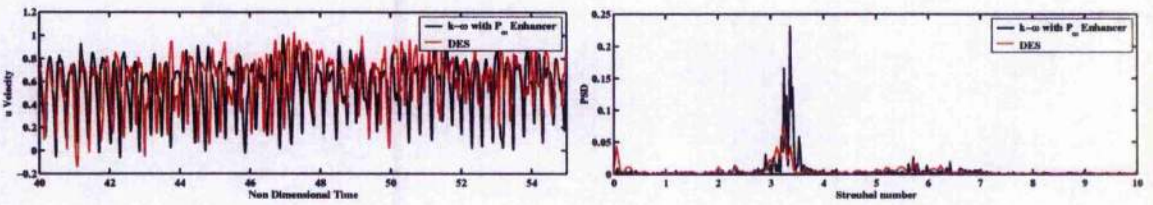

(a) (b)

Figure 5.25: Time history and PSD analysis of u velocity signals for a probe situated on the vortex axis at $z/c_r = 0.1$ above the wing surface for URANS $k-\omega$ with P_ω Enhancer and DES solutions

5.5.2 Effect of Eddy Viscosity Treatment

The relative behaviour of the solutions can also be considered in light of the turbulence treatment of each model. In order to consider the relative prediction of the turbulent behaviour by each model, the eddy viscosity in the vortex region was analysed. Figure 5.26 shows instantaneous contours of the ratio of eddy viscosity to laminar viscosity for both turbulence treatments. Due to the under-resolution of the turbulence for the DES solution, as discussed in Chapter 4, the behaviour of the subgrid scale eddy viscosity will be very similar to the URANS turbulent eddy viscosity and so a comparison is valid.

It is clear from Figure 5.26 that the distribution through the vortex region is quite different for the two solutions. The behaviour of the eddy viscosity of the $k-\omega$ with P_ω Enhancer model was described in Section 5.4 and similarly the role of the subgrid eddy viscosity in the DES calculations was discussed in Section 4.8.2. It is clear that in comparison that the DES model predicts much lower eddy viscosity in the vortex region, although the pattern of the contours is very similar. This reduction, as discussed previously is due to the dependence of the subgrid eddy viscosity on the grid dimensions. The region of high viscosity downstream of the trailing edge is, therefore, due to the reduction of the grid refinement in that region. Both models predict higher levels of viscosity in the shear layer and predict a laminar vortex core region. Downstream of breakdown, the behaviour is also quite similar, with an increase in eddy viscosity levels in the post-breakdown flow. This is widespread for the DES solution, however the

$k-\omega$ with P_ω Enhancer model predicts more localised regions of high viscosity.

The higher levels of viscosity predicted by the $k-\omega$ with P_ω Enhancer model may explain the increased energy of the helical mode frequency discussed above since an increase in eddy viscosity comes an increase in turbulent production and therefore turbulent mixing, which will smooth out fluctuations on the unsteady mean flow. Therefore, more energy will exist for the mean flow oscillations. However, the converse is true for the vortex breakdown oscillations, which are shown to have more energy in the DES solutions. This is likely to be due to the reduction of eddy viscosity in this region, which means that the effects of the breakdown fluctuations will be felt more strongly. However, it is important to note that despite the differences in eddy viscosity distributions and levels through the vortex region and in the post-breakdown flow, the frequencies and behaviour predicted are very similar for both solutions.

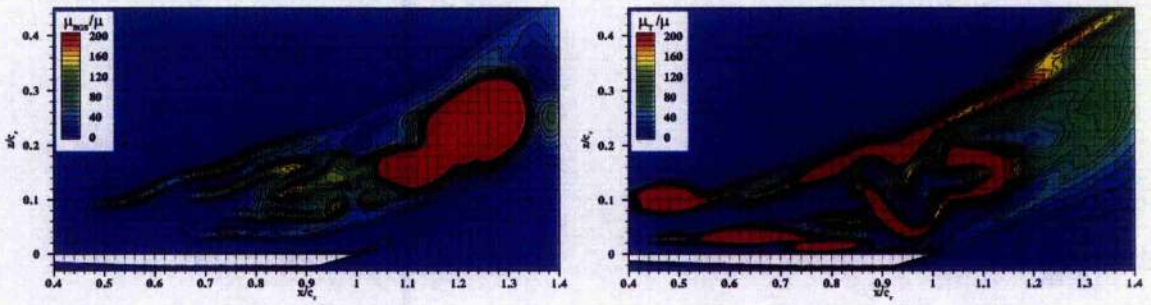

(a) DES, $\Delta\tau = 0.0025$

(b) $k-\omega$ with P_ω Enhancer model, $\Delta\tau = 0.01$

Figure 5.26: Slice through vortex breakdown region, on a plane through vortex core, $y/s = 0.7$ showing instantaneous contours of μ_T/μ for URANS $k-\omega$ with P_ω Enhancer model and DES

5.6 Discussion

Before discussing the ability of URANS to predict the unsteady behaviour of delta wing vortical flows it is necessary to review the turbulent features of vortical flows. In Chapter 2 the application of each turbulence model used in this investigation was discussed with reference to delta wing flows. It was stated that it was necessary that each model was able to predict a laminar vortex core region with higher turbulence production occurring in the shear layer and downstream of the vortex breakdown. Unfortunately, limited data exists to quantify the exact levels of turbulence within this type of flow, therefore it is difficult to exactly measure the ability of each model to accurately predict the turbulence. However, from the formulation of each model and the predicted solution, it is possible to determine the relative behaviour of each model and qualitatively assess the ability to predict the turbulent behaviour accurately. This is further aided by validation of the predictions with available experimental data as performed for the DES solution in Chapter 4.

From the discussion of the formulation of the linear Boussinesq Wilcox $k-\omega$ model and the contours of turbulent eddy viscosity shown in Figure 5.17, it is evident that this model over-predicts the turbulence within the vortex region and particularly through the vortex core. This has the effect of creating a weak vortex, which has a significantly increased susceptibility to breakdown. Also, with the increased turbulence, the ability to capture the unsteady behaviour is diminished. This is due to the significant increase in dissipation of the unsteady fluctuations of the mean flow, which causes the flow to become steady in nature. To reduce the turbulence within this model, rotation corrections may be applied to sensitise the model to the rotation of the vortex flow. This was explained in Chapter 2 for the $k-\omega$ with P_ω Enhancer model. Similarly, a non-linear model can be formulated, which provides a more general improvement to the Wilcox $k-\omega$ model by including further terms to the calculation of the Reynolds stress anisotropy based on both the rotation and strain-rate tensors. Both methods reduce the turbulence within the flow and result in reduced dissipation of the unsteady behaviour, improving the prediction of the vortex system.

Having considered all URANS solutions and the comparison with the validated DES results from the previous Chapter, it is possible to discuss the ability of URANS to predict the vortex flow system over the wing. It is clear from the comparisons shown in the previous section, that the $k-\omega$ with P_ω Enhancer model adequately

predicts the mean flow unsteady behaviour as defined in Chapter 4 for the DES. This includes predicting the vortex breakdown oscillation and helical mode frequencies accurately compared to the DES solution for the same grid. It is also evident from the comparison between the two URANS models that the Non-Linear Eddy Viscosity model also predicts these frequencies. However, it is clear from analysis of the mean properties of the flow that the predicted location of breakdown is different for each turbulence treatment, This is also true in comparison with the DES solutions. To consider this further, the mean breakdown locations for each calculation considered in this investigation are summarised in Table 5.1.

Turbulence Treatment	*Grid*	$\Delta\tau$	*Mean VBD location,* x/c_r
$k-\omega$ with P_ω Enhancer	Fine	0.01	0.83
NLEVM	Fine	0.01	0.87
NLEVM	Fine	0.005	0.81
DES	Fine	0.01	0.88
DES	Fine	0.005	0.84
DES	Fine	0.0025	0.85
DES	Refined TE Grid	0.0025	0.86

Table 5.1: Location of mean vortex breakdown for each unsteady calculation performed in this investigation

It is clear from Table 5.1, for both the URANS and DES solutions, that with a decrease in time step size, there is an upstream shift in mean breakdown location. This suggests that the location of breakdown is dependent on the resolution of the temporal behaviour of the flow. However, from the DES results it is evident that the location will converge to a constant value as the time step is reduced. Although this value, for the DES solutions is dependent on the grid refinement, it may be suggested that a similar behaviour would be exhibited by the URANS models for further decreases in time step size. It was also found that an increase in grid refinement had the opposite effect for the URANS solutions and moved the location of breakdown further downstream. This is also the case for the DES solution with refinement in the trailing edge region, although the change in the mean location is small. This suggests that with an increase in the spatial resolution of the flow, both upstream and downstream, the mean breakdown location moves downstream. The effect of the turbulence treatment is a little harder to consider. Figure 5.27 shows the instantaneous ratio of eddy viscosity to laminar viscosity through the vortex core for each model at the instant $\tau = 50$. From this plot, it is clear that each model keeps the eddy viscosity close to zero through the vortex core region upstream of breakdown, however at the location of breakdown the turbulence in the flow increases. It is clear that the $k-\omega$ with P_ω Enhancer model predicts the largest eddy viscosity values downstream of breakdown and the furthest upstream breakdown location, similarly the Non-Linear Eddy Viscosity model predicts the lowest eddy viscosity ratio, but the furthest downstream mean breakdown location. This suggests that there is a link between the turbulence predicted downstream of breakdown and the location of breakdown. However, from the values of mean breakdown location given in Table 5.1 it is clear that the differences in predicted mean breakdown location between each solution in this investigation is only approximately $7\%c_r$. Therefore, it may be suggested that provided the vortex core is predicted as being laminar, the levels of turbulence predicted in the flow downstream has some effect on the location of the mean location of breakdown but little effect on the unsteady behaviour of the post-breakdown flow.

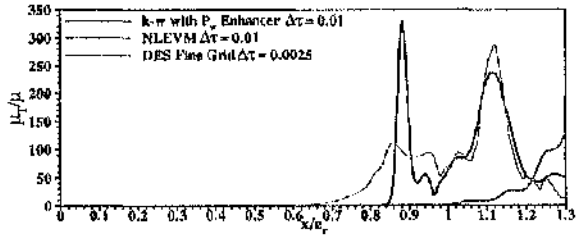

Figure 5.27: Distribution of μ_t through vortex core for all turbulence models used in this investigation

One of the factors driving the use of URANS for unsteady vortical flows, which was mentioned in the introduction of this chapter and has been mentioned in previous discussions is the relative computational expense of the calculations in comparison with DES methods. Table 5.2 shows the length of the calculations required to simulate one second of real time for each calculation carried out in this investigation. From this data, it is clear that the URANS calculations are at a minimum four times cheaper than the DES calculations for the same grid on half as many processors. The reason that the Non-Linear Eddy Viscosity model is more expensive than the $k-\omega$ with P_ω Enhancer model is due to the requirement of a reduced unsteady convergence limit, thus increasing the work unit of the calculation, which is defined as the non-dimensional time taken to reach convergence for one time step of

the calculation. It is important at this point to also note that it was concluded in the previous chapter, that the DES calculations were under-resolved. Therefore, to fully resolve the turbulent scales of the flow, the computational resources required would be significantly larger. This clearly shows the advantage of using URANS to capture the flow details.

Turbulence Treatment	*Grid*	$\Delta\tau$	*No. of Processors*	*Total No. of* $\Delta\tau$	*Work Units*	*Approx. Total Run Time (hrs)*
$k-\omega$ with P_m Enhancer	Fine	0.01	24	7,158	40,228 (5.62)	500
NLEVM	Fine	0.01	24	7,158	60,843 (8.50)	1000
NLEVM	Fine	0.005	24	14,316	121,686 (8.50)	2000
DES	Fine	0.0025	48	28,632	161,485 (5.64)	8000
DES	Refined TE	0.0025	48	28,632	161,199 (5.63)	8000

Table 5.2: Length of calculations for each turbulence treatment used in this investigation to predict a total time of one second. Work units in brackets denote unit for one time step

5.7 Conclusions

It may be concluded from this investigation that URANS turbulence models perform well in predicting the necessary features of the unsteady vortical flow and vortex breakdown provided the turbulence in the vortex core is kept low. It is clear from these results that the majority of the frequencies and phenomena predicted by each URANS model is in good agreement, although the mean location of breakdown is found to change. The effect of grid and time step resolution was considered, and it was found that the mean behaviour of the flow is more sensitive to these issues than the unsteady phenomena. Comparing the linear model with the rotational correction to the DES solutions from the previous chapter shows that the predicted unsteady behaviour is again very similar, with the majority of the differences occurring in the mean location of breakdown. Therefore, due to the validation of the DES solutions, it may be suggested that the URANS model is capturing the flow behaviour well with all the main dominant frequencies being present in the solutions. It was shown in the previous chapter that the DES solutions were not well resolved spatially, however it was also shown that the resolution of the turbulent scales was not important to the prediction of the main flow features. This investigation shows that due to this the URANS models were able to predict the main features of the flow.

It was found that the mean behaviour of the flow is more sensitive to the turbulence treatment, grid and time step size than the frequencies of the unsteady oscillations. However, from analysis of the mean breakdown location, it was found that this difference was limited to $7\%c_r$, which is relatively small. Therefore, it may be concluded that it is more important to accurately predict the turbulent behaviour in the vortex core than downstream of breakdown. The resolution of the post-breakdown flow does have a small effect on the mean breakdown location but does not appear to impact the frequency of oscillation of breakdown in the flow or the frequency of the helical mode winding.

Overall, it may be concluded that URANS is suitable for use in capturing the unsteady behaviour of delta wing flows at moderate incidence where vortex breakdown occurs, provided the core behaviour is modelled accurately. It has also been shown that this may be performed at considerably less computational expense than DES methods and thus is a promising tool for industrial use in the prediction of vortical flows.

Chapter 6

Conclusions and Future Work

The main conclusions drawn from this investigation are now summarised and recommendations for future research given.

6.1 Conclusions

Within the transonic regime it has been found that shocks interact with the leading edge vortices. Vortex breakdown is found to occur in an abrupt nature and this can have a significant effect on the aerodynamic performance. Due to this, one of the aims of this project was to consider the behaviour of vortex breakdown within a transonic flow and to consider the predictive ability of RANS methods. Steady state calculations were compared to experimental data which showed very good agreement for the pre-breakdown flow. However, for a larger incidence a discrepancy between the CFD and experimental results appeared due to the premature occurrence of vortex breakdown in the computational results.

Analysis of the flow behaviour resulted in the identification of a number of shocks which could be classified into two main shock types, cross-flow and normal. The locations and behaviour of these shocks was found to agree with observations in the literature. The normal shocks, which occurred normal to the wing surface and symmetry plane, were found to interact with the vortex core and were determined to cause the sudden appearance of breakdown. A sensitivity study was performed to consider the effect of a number of factors on the predicted behaviour. These included, grid refinement, turbulence model, solution convergence and time accuracy. However, it was found that breakdown was consistently predicted and was not significantly affected by any of these factors. Comparisons were also made with other structured grid results from participants within the VFE-2, but again the solutions were found to be comparable.

From consideration of the interaction between the normal shocks and the vortex core, it was suggested that a critical limit must exist where breakdown will occur. This limit was concluded to be dependent on the strength of the vortex and the interacting normal shock. Using this argument of a critical limit for breakdown, it was concluded that the premature breakdown behaviour of the computations was due to under-predicting the vortex core axial velocity accurately most likely due to grid refinement issues in this region. However, overall it was found that the computational results were adequately predicting the transonic behaviour of the vortex flow.

The unsteady behaviour of the flow is a second aspect of delta wing flows which requires further investigation. At moderate angles of incidence where breakdown occurs on the wing, the flow becomes highly unsteady and interactions between the flow and aircraft structures have been found to occur. To avoid aeroelastic issues, it is necessary to have a greater understanding of the unsteady phenomena which occur. This is becoming increasingly important with the emergence of UAV technologies. The second aim of this thesis was to consider the ability of CFD to predict the main unsteady behaviour of the flow. In Chapter 4 the use of DES to predict the unsteady flow behaviour associated with the flow upstream and downstream of breakdown was considered for the ONERA 70° delta wing geometry at a moderate incidence within the subsonic regime. Before the predicted unsteady behaviour was considered, the effect of time step and grid refinement at the trailing edge were analysed. This determined the optimum time step for use in the calculations and that there was only a small influence of grid refinement in the trailing edge on the mean flow behaviour.

From analysis of the unsteady flow behaviour and consideration of the level of turbulence captured in the unsteady signals, it was determined that the solutions obtained in the investigation were spatially under-resolved.

This resulted in the conclusion that the spatial and temporal requirements of a fully resolved DES calculation of the post-breakdown flow are significantly larger than those used in this investigation and that further refinement downstream of the trailing edge would be needed to capture all the turbulent behaviour in the post-breakdown flow. This would have the effect of increasing the computational expense of an already expensive calculation.

However, from comparison of the results with other DES solutions on finer grids, it was determined that the unsteady vortex breakdown behaviour was not dominated by turbulence with the dominant frequency occurring for less than $St = 10$, which is low. It was also found that the results were in good agreement with corresponding experimental results. Therefore, despite the under-resolution of the turbulent flow, the salient features of the flow were being captured well. As the main unsteady phenomena were found to occur at low frequencies, and turbulence was not found to be dominant in the flow, it was concluded that URANS turbulence models should be able to adequately predict this behaviour for a considerably reduced computational cost.

To investigate this conclusion, the ability of URANS to predict the unsteady flow behaviour was evaluated in Chapter 5. Two URANS turbulence models were considered for this investigation, a linear Boussinesq model with a rotation correction and a Non-Linear Eddy Viscosity model, both based on the Wilcox $k-\omega$ model. The effect of grid refinement and time step refinement were considered and it was concluded that with an overall increase in grid refinement, the solutions were found to improve, however the coarse grid results were adequate for an approximation of the flow at low computational expense. From the time step refinement study, it was found that the increase in temporal resolution did not have a significant effect on the unsteady behaviour predicted, despite an upstream movement of the mean breakdown location. Higher frequencies were also not found to occur with a decrease in time step and so it was concluded that the baseline time step of $\Delta\tau = 0.01$ was suitable for URANS calculations.

Comparisons were then made between the URANS models and the relative behaviour of each model in predicting the unsteady flow frequencies was analysed. This was also considered in light of the formulation of the models and the treatment of the turbulence in the vortex core region. From this comparison it was concluded that both models were adequate in reducing the eddy viscosity in the vortex core and that similar unsteady behaviour was predicted. The model with the rotation correction was then compared to the DES results discussed in Chapter 4 to evaluate the mean and unsteady behaviour of the solutions. From this comparison, it was clear that the majority of the dominant frequencies of the vortex flow were captured by the URANS model and the agreement with the DES solutions was very good. From this analysis it was concluded that the URANS model had predicted all the important unsteady features of the flow and was, therefore, suitable for use in predicting the unsteady nature of vortical flows.

It was also determined from this investigation that the mean behaviour of the flow, such as the mean location of breakdown, is far more dependent on the turbulence treatment of the models used that the unsteady behaviour. All turbulence treatments used predicted similar dominant frequencies and unsteady phenomenon. However, the mean location of breakdown was found to be different for each case. This difference was found to be approximately $7\%c_r$, which was considered relatively small. Therefore, it was concluded that provided the core region of the vortex flow is modelled as laminar, the turbulent treatment of the model used does not have a significant influence on the overall flow behaviour. If this is considered in the context of the computational expense of each model used, it is clear that URANS can predict the main features of the flow for a significant reduction in computational cost.

Overall, from this investigation, it can be concluded that CFD is a very useful tool for the prediction of vortex flows and vortex breakdown over slender delta wings and that it is capable of predicting complex flow behaviour, such as transonic vortex breakdown and the unsteady nature of the flow. In this study both RANS/URANS and DES methods were considered and it is clear that both methods can be used to predict the flow accurately. However, some limitations of these methods have also been highlighted.

6.2 Future Work

Throughout this project a number of potential avenues for further work have presented themselves.

From Chapter 3, the main avenue for further work would be to consider the flow for different configurations and flow conditions to attempt to define a limit for vortex breakdown based on the Rossby number of the vortex and the shock strength. Further experimental data is also required to validate this limit and this would require measurements taken across shocks and through the vortex core for a range of flow conditions. This would also allow further validation of the location and strength of the shocks in the flow, improve their prediction and therefore improve the understanding of their behaviour. Further work is also needed to consider the conclusion that the under-prediction

of the vortex core axial velocity is the cause of the premature prediction of breakdown for this case. This could be performed by systematically refining the vortex core region and determining any link with the location and onset of vortex breakdown.

With regards to the use of DES to predict the unsteady behaviour of the vortex flow, a number of possibilities are clear. Firstly, further refinement of the grid could be carried out to analyse the behaviour of a solution with more turbulent scales simulated on the grid and to consider the effect of this on the predicted behaviour of the flow - particularly on the mean breakdown location. This could also include a further refinement of the trailing edge region to capture the breakdown of the helical mode winding into turbulence downstream of the trailing edge. This may not be important for the flow at this incidence, however it is unclear whether this turbulent region would effect the unsteady flow behaviour over the wing as the incidence was increased. Therefore, it would also be interesting to consider the flow for a incidence at which breakdown is much further upstream, such as $\alpha = 35^o - 40^o$ for this wing. The use of overset or hybrid grids may also be interesting to consider to reduce the cost of structured grid DES calculations, this would allow refinement and accuracy of the solution in the vortex region but without unnecessary grid points in the farfield region of the flow domain.

Further unsteady experimental data is also greatly needed to improve the understanding of this subject and to aide in the validation of such investigations. Unsteady point probe data, similar to that shown in this investigation through the vortex region, for all components of velocity would be highly beneficial to the development and validation of CFD in the future, and in particular for URANS models. Further work is needed to understand the relation between the mean location of vortex breakdown and the turbulence downstream of the breakdown location. Finally, this work could be extended by considering the unsteady forces which are incident on the wing surface as a result of the unsteadiness, the phenomena which cause this forcing and the possible structural response that this may cause.

Appendix A

Turbulence Models

The full form of each main turbulence model used in the investigation will be detailed in this section.

A.1 Wilcox $k-\omega$

The Kinematic Eddy Viscosity is calculated from,

$$\mu_T = \rho \frac{k}{\omega} \tag{A.1}$$

Where the turbulent kinetic energy, k and specific dissipation rate, ω are calculated from the partial differential equations,

$$\rho \frac{\partial k}{\partial t} + \frac{\partial \rho k U_j}{\partial x_j} = \frac{\partial}{\partial x_j}\left[(\mu + \sigma^* \mu_T)\frac{\partial k}{\partial x_j}\right] - P_k - \beta^* \rho k \omega \tag{A.2}$$

and

$$\rho \frac{\partial \omega}{\partial t} + \frac{\partial \rho \omega U_j}{\partial x_j} = \frac{\partial}{\partial x_j}\left[(\mu + \sigma \mu_T)\frac{\partial \omega}{\partial x_j}\right] + P_\omega - \beta \rho \omega^2 \tag{A.3}$$

In the equations above the production terms of k and ω, P_k and P_ω respectively, are defined as,

$$P_k = \tau_{ij}^R \frac{\partial U_i}{\partial x_j} \quad \text{and} \quad P_\omega = \alpha \frac{\omega}{k} P_k \tag{A.4}$$

The rate of dissipation, ε and the length scale of the model are given by,

$$\varepsilon = \beta^* k \omega \quad and \quad \ell = \frac{k^{1/2}}{\omega} \tag{A.5}$$

The closure coefficients for the model are defined in Table A.1.

α	β	β^*	σ	σ^*
5/9	0.075	0.09	0.5	0.5

Table A.1: Model constants for the Wilcox $k-\omega$ turbulence model [34]

A.2 NLEVM

In an explicit algebraic Reynolds Stress model (EARSM), the anisotropic term of the Reynolds stresses is described as a function of the normalised mean strain-rate, $\mathbf{S}$ and rotation, $\mathbf{\Omega}$ tensors. Based on the Cayley-Hamilton theorem [167], this means that the anisotropy can be described by a series of ten independent, symmetric, deviatoric functions of $\mathbf{S}$ and $\mathbf{\Omega}$ or a linear combination of these ten. For the model specified in [170] this results in the relationship,

$$\begin{aligned}\mathbf{a} = {} & \beta_1 \mathbf{S} + \beta_2 \mathbf{S}^2 - \frac{1}{3} II_S \mathbf{I} + \beta_3 \mathbf{\Omega}^2 - \frac{1}{3} II_\Omega \mathbf{I} + \beta_4 (\mathbf{S\Omega} - \mathbf{\Omega S}) + \beta_5 (\mathbf{S}^2\mathbf{\Omega} - \mathbf{\Omega S}^2) + \beta_6 \left(\mathbf{S\Omega}^2 - \mathbf{\Omega}^2\mathbf{S} - \frac{2}{3} IV\, \mathbf{I}\right) \\ & + \beta_7 \left(\mathbf{S}^2\mathbf{\Omega}^2 - \mathbf{\Omega}^2\mathbf{S}^2 - \frac{2}{3} V\, \mathbf{I}\right) + \beta_8 (\mathbf{S\Omega S}^2 - \mathbf{S}^2\mathbf{\Omega S}) y + \beta_9 \left(\mathbf{\Omega S\Omega}^2 - \mathbf{\Omega}^2\mathbf{S\Omega}\right) + \beta_{10} \left(\mathbf{\Omega S}^2\mathbf{\Omega}^2 - \mathbf{\Omega}^2\mathbf{S}^2\mathbf{\Omega}\right)\end{aligned} \tag{A.6}$$

The coefficients β_n are functions of the five independent invariants of the normalised mean strain-rate and rotation tensors, $\mathbf{S}$ and $\mathbf{\Omega}$, which can be written as

$$II_S = tr\left\{\mathbf{S}^2\right\}, \quad II_\Omega = tr\left\{\mathbf{\Omega}^2\right\}, \quad III_S = tr\left\{\mathbf{S}^3\right\}, \quad IV = tr\left\{\mathbf{S}\mathbf{\Omega}^2\right\}, \quad V = tr\left\{\mathbf{S}^2\mathbf{\Omega}^2\right\} \tag{A.7}$$

where $tr\{\}$ is the trace of the second order tensors and the turbulent time scale is given by,

$$\tau = max\left\{\frac{1}{\beta^*\omega}, C_\tau\sqrt{\frac{\mu}{\beta^* k\omega}}\right\} \tag{A.8}$$

For the non-linear eddy viscosity model, this relationship for the anisotropy is reduced to a few terms and the Reynolds stress tensor formulation becomes,

$$\overline{u_i'u_j'} = k\left(\frac{2}{3}\delta_{ij} - 2C_\mu^{\text{eff}}S_{ij} - a_{ij}^{(\text{ex})}\right) \tag{A.9}$$

where,

$$\mathbf{a}^{(\text{ex})} = \beta_3\left(\mathbf{\Omega}^2 - \frac{1}{3}II_\Omega\,\mathbf{I}\right) + \beta_6\left(\mathbf{S}\mathbf{\Omega}^2 + \mathbf{\Omega}^2\mathbf{S} - II_\Omega\mathbf{S} - \frac{2}{3}IV\mathbf{I}\right) + \beta_9\left(\mathbf{\Omega}\mathbf{S}\mathbf{\Omega}^2 - \mathbf{\Omega}^2\mathbf{S}\mathbf{\Omega}\right) \tag{A.10}$$

The turbulent eddy viscosity is calculated from,

$$\mu_T = C_\mu^{\text{eff}}\rho k\tau \tag{A.11}$$

where,

$$C_\mu^{\text{eff}} = -\frac{1}{2}f_1\left(\beta_1 - II_\Omega\beta_6\right) \tag{A.12}$$

As mentioned above, the β_n coefficients are derived from the invariants of the strain-rate and rotation tensors and are defined fort his model as,

$$\beta_1 = -\frac{N\left(2N^2 - 7II_\Omega\right)}{Q}, \quad \beta_3 = -\frac{12N^{-1}IV}{Q}, \quad \beta_4 = -\frac{2\left(N^2 - 2II_\Omega\right)}{Q}, \quad \beta_6 = -\frac{6N}{Q}, \quad \beta_9 = \frac{6}{Q} \tag{A.13}$$

with

$$Q = \frac{5}{6}\left(N^2 - 2II_\Omega\right)\left(2N^2 - II_\Omega\right) \tag{A.14}$$

and

$$N_c = \begin{cases} \frac{c_1'}{3} + \left(P_1 - \sqrt{P_2}\right)^{1/3} + sign\left(\left(P_1 - \sqrt{P_2}\right)|P_1 - \sqrt{P_2}|^{1/3}\right), & P_2 \geq 0 \\ \frac{c_1'}{3} + 2\left(P_1^2 - P_2\right)^{1/6} cos\left(\frac{1}{3}cos^{-1}\left(\frac{P_1}{\sqrt{P_1^2 - P_2}}\right)\right), & P_2 < 0. \end{cases} \tag{A.15}$$

where,

$$P_1 = \left(\frac{c_1'^2}{27} - \frac{9}{20}III_S - \frac{2}{3}II_\Omega\right)c_1'^2, \quad P_2 = P_1^2 - \left(\frac{c_1'^2}{9} + \frac{9}{10}II_S + \frac{2}{3}II_\Omega\right)^3 \quad \text{and} \quad c_1' = \frac{9}{4}\left(c_1 - 1\right) \tag{A.16}$$

Therefore,

$$N = N_c + \frac{162\left(\phi_1 + \phi_2 N_c^2\right)}{D} \tag{A.17}$$

with,

$$\phi_1 = IV^2, \quad \phi_2 = V - \frac{II_S II_\Omega}{2} \quad \text{and} \quad D = 20N_c^4\left(N_c - \frac{1}{2}c_1'\right) - II_\Omega\left(10N_c^3 - 15c_1'N_c^2\right) + 10c_1'II_\Omega^2 \tag{A.18}$$

For the model implimented in PMB there is no damping or low Reynolds number correction applied, thus the coefficients are defined $f_1 = 1.0$, $C_\tau = 6.0$ and $c_1 = 1.8$

A.3 Spalart-Allmaras

The kinematic turbulent eddy viscosity is calculated from

$$\mu_T = \rho \tilde{\nu} f_{v1} \tag{A.19}$$

where,

$$f_{v1} = \frac{\chi^3}{\chi^3 + c_{v1}^3} \quad \text{and} \quad \chi = \frac{\tilde{\nu}}{\nu} \tag{A.20}$$

In equation A.19, $\tilde{\nu}$ is the working variable of the transport equation of the model, which is given by

$$\frac{\partial \tilde{\nu}}{\partial t} + \frac{\partial (\tilde{\nu} u_j)}{\partial x_j} = c_{b1} \tilde{S} \tilde{\nu} - c_{w1} f_w \left(\frac{\tilde{\nu}}{d}\right)^2 + \frac{1}{\sigma} \frac{\partial}{\partial x_k} \left[(\nu + \tilde{\nu}) \frac{\partial \tilde{\nu}}{\partial x_k} \right] + \frac{c_{b2}}{\sigma} \frac{\partial \tilde{\nu}}{\partial x_k} \frac{\partial \tilde{\nu}}{\partial x_k} \tag{A.21}$$

where $\tilde{S}$ is the modified vorticity given by

$$\tilde{S} = S + \frac{\tilde{\nu}}{\kappa^2 d^2} f_{v2} \quad \text{and} \quad f_{v2} = 1 - \frac{\chi}{1 + \chi f_{v1}}; \tag{A.22}$$

where d is the distance to the closest wall and S is the magnitude of vorticity,

$$S = |\omega| = |\nabla \times (u\hat{i} + v\hat{j} + w\hat{k})| \tag{A.23}$$

Similarly, in the destruction/near wall term, the function f_w in Equation A.21 is given by

$$f_w = g \left[\frac{1 + c_{w3}^6}{g^6 + c_{w3}^6} \right]^{1/6}, \quad g = r + c_{w2} \left(r^6 - r \right), \quad r = \frac{\tilde{\nu}}{\tilde{S} \kappa^2 d^2} \tag{A.24}$$

These functions take the presence of a wall into account and satisfy the wall boundary conditions where $\tilde{\nu} = 0$. As r increases, f_w tends to an asymptote, therefore values of r are generally truncated to about 10. In the freestream region, it is also best to use $\tilde{\nu} = 0$, provided that numerical errors do not cause $\tilde{\nu}$ to become negative close to the edge of the boundary layer - the exact solution cannot become negative. Generally, values less than $\nu/10$ are acceptable. This also applies to the initial conditions. The model coefficients are given in Table A.2.

c_{b1}	c_{b2}	c_{v1}	c_{w1}	c_{w2}	c_{w3}	σ	κ
0.1355	0.622	7.1	3.239	0.3	2.0	2/3	0.41

Table A.2: Model constants for the Spallart-Allmaras turbulence model [35], where $c_{w1} = \frac{c_{b1}}{\kappa^2} + \frac{(1+c_{b2})}{\sigma}$

Appendix B

Probe Analyser Tool

B.1 Probe Analyser

In the course of the investigation into unsteady flows, the unsteady behaviour was considered through use of a series of point probes applied to the flow domain. These point probes were applied to the computational grid through specification of coordinates at the outset of the calculations and the flow variables were saved at each point for every time step of the calculation. This results in a number of files being created which contain the time histories of each flow variable. However, these files are not immediately usable and require reorganisation into a form which is more practical. To alter the form of these files and to allow analysis of the resulting time histories in an easy and efficient manner, a program was created using *Matlab*, which combines all the analytical and statistical analyses into one interface allowing consistent analysis and easy comparison and cross-plotting of data. This program, *Probe Analyser*, was originally designed to analyse acoustical data from pressure signals for cavity flows and was created by Lawrie [178]. Further work was carried out by Nayyar [179] who added further analyses and created a similar program for turbulent analysis.

At the start of this project, *Probe Analyser* was only able to perform statistical analyses on the pressure time histories from the point probe files. However, to fully consider the unsteady behaviour over delta wings it was necessary to be able to consider all flow variables in a similar manner. It was also important to be able to consider the unsteady forces acting on the wing and therefore the ability to process the integrated loads files was also added. As mentioned, the program was originally designed for cavity flows, therefore the length scales and plots were specific to the character of these flows, these were changed to make the program more specific to delta wings. Further work was carried out to improve the ability of the program to quickly cross-plot data, this involved adding the ability to process multiple probes and multiple probe files and to plot these on the same graphs. To reduce the size of the data sets, in order to reduce the memory requirements of the program, a facility to split the large data files into smaller subfiles was added. This had the effect of further increasing the ease of comparison of multiple signals. The turbulent analyses created by Nayyar were also incorporated into the main *Probe Analyser* program to create a single program which was capable of fully analysing the unsteady data. The ability to time average the signals was also added, as was the ability to consider non-stationary turbulence.

Probe Analyser has the ability to perform many more analyses than were used in this investigation. The main analyses which were used are the calculation of the mean and RMS values, the power spectral density (PSD), the time average of the signals and the calculation of turbulent kinetic energy. Explanations of each of these methods will be given in a later section. However, analyses such as the probability density function (PDF), auto-correlation, calculation of the Reynolds stresses and further turbulent correlations are also available. These will not be discussed in detail in this Appendix. The graphical user interface (GUI) of the program is shown in Figure B.1. This shows all the analyses available and the overall format of the program. This GUI comes from the Windows interface, however the program can be used on the Linux operating system and a start up command allows this to be specified. The left hand side of the GUI mainly deals with the input of the files, the specification of the important flow parameters and the selection of the probes to be considered. The right hand side allows the selection of the analysis and the specification of the resulting plots through drop-down menus. The initial manipulation of the probe data files, created from the CFD calculation, into a usable format, as mentioned above, is done through a secondary program accessed through the "Locate Probes" button on the top left of the GUI.

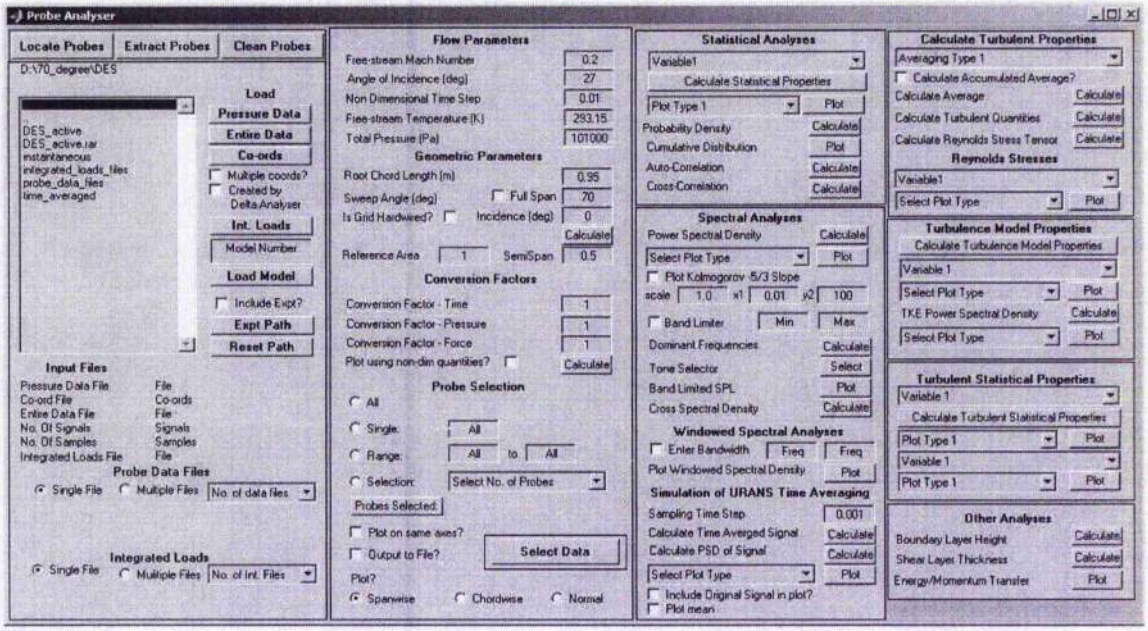

Figure B.1: Graphical User Interface for probe analyser program

B.2 Application of Statistical Methods

Probe Analyser was initially created in *Matlab* as it allowed the use of some existing mathematical functions and made the creation of the GUI easier through use of the *Matlab* add-on package *Guide*. This program automatically sets up the links between the GUI and the underlying code, greatly reducing the complexity of the programming task. The underlying code for the *Probe Analyser* program is large with many subroutines and will not be reproduced here, however the initial code of the program can be found in Ref. [178]. As mentioned above, the main analyses used in this investigation are the calculation of the mean, RMS, PSD, time average and turbulent kinetic energy of the specified signal or signals. In this section each of these methods will be described. In all cases, with the exception of the turbulent kinetic energy which is calculated using the velocity vector, the general variable, Φ, will be used as these analyses can be carried out on the signals of any of the flow variables. It should be noted that only the mean, RMS and PSD analysis are able to be carried out on the integrated loads signals.

B.2.1 Mean and Root Mean Square Values

The mean of the time varying signals is calculated from a straight forward average of the data points such that,

$$\langle \Phi \rangle = \frac{\Sigma \Phi}{N} \tag{B.1}$$

where N is the number of samples in the signal.

The RMS value is a statistical measure of the deviance of a signal from the mean and therefore a measure of the intensity of the fluctuations of the unsteady signal. It is calculated by

$$\Phi_{rms} = \sqrt{\frac{\left(\Sigma \left(\Phi - \langle \Phi \rangle\right)\right)^2}{N}} \tag{B.2}$$

Within the *Probe Analyser* program, both these values can be plotted against location on the wing, in the spanwise, chordwise or normal directions depending on the probes selected for analysis. They provide an excellent way to compare results, particularly for multiple solutions as up to four files can be entered into probe analyser for analysis at any one time.

B.2.2 Power Spectral Density

The behaviour of an unsteady time dependent random variable, such as the flow variables in this investigation, can be though of as the superposition of multiple oscillations at different frequencies. This can be mathematically described as a trigonometric series of harmonic waveforms. This series is known as the Fourier series and is defined as

$$\Phi(t) = a_o + \sum_{k=1}^{\infty} \left(a_k cos\frac{2\pi kt}{T} - b_k sin\frac{2\pi kt}{T} \right) \tag{B.3}$$

where the Fourier coefficients are given by

$$a_o = \frac{1}{T}\int_{\frac{T}{2}}^{-\frac{T}{2}} \Phi(t)dt, \quad a_k = \frac{2}{T}\int_{\frac{T}{2}}^{-\frac{T}{2}} \Phi(t)cos\frac{2\pi kt}{T}dt, \quad b_k = \frac{2}{T}\int_{\frac{T}{2}}^{-\frac{T}{2}} \Phi(t)sin\frac{2\pi kt}{T}dt \tag{B.4}$$

and

$$\omega_k = \frac{2\pi k}{T} \tag{B.5}$$

The Fourier series, therefore, describes the signal within the frequency domain instead of the time domain. A similar series can be formed for fluctuations in space, i.e $\Phi(x)$, which provides a description of the signal in wave number space, κ. To transform between the time and frequency domains (or space and wave number domains) the Fourier Transform of the signal is used. This is derived from the Fourier series and for a given time dependent variable, $\Phi(t)$ is defined as

$$\Phi(\omega) = \mathscr{F}\{\Phi(t)\} = \frac{1}{2\pi}\int_{-\infty}^{\infty} \Phi(t)e^{-i\omega t}dt \tag{B.6}$$

and its inverse is

$$\Phi(t) = \mathscr{F}^{-1}\{\Phi(\omega)\} = \int_{-\infty}^{\infty} \Phi(\omega)e^{i\omega t}d\omega \tag{B.7}$$

The power spectral density function is defined as the Fourier transform of the auto-correlation function of the time dependent variable and provides information of the frequency distribution and power of a signal in the frequency domain. It is defined mathematically as

$$PSD_{\Phi(t)} = \mathscr{F}\{R_\Phi(\tau)\} = \frac{1}{2\pi}\int_{-\infty}^{\infty} R_\Phi(\tau)e^{-i\omega\tau}d\tau \tag{B.8}$$

where the auto-correlation function of the variable is defined as the mean of the product of the variable at time t and the variable at time $t+\tau$, such that

$$R_\Phi(\tau) = \frac{\sum(\Phi(t)\Phi(t+\tau))}{N} \tag{B.9}$$

As the signals obtained from the CFD calculation are discrete, finite in length this form of the Fourier series cannot be applied directly. A computationally efficient form of a method known as the discrete Fourier transform (DFT) is used instead. The DFT merely allows the transform to be applied to sampled signals and redefines the Fourier transform as

$$\Phi(\omega) = \frac{1}{N}\sum_{r=0}^{N-1} \Phi_r(t)e^{-i\left(\frac{2\pi kr}{N}\right)} \tag{B.10}$$

The form of this method used, is known as the fast Fourier transform (FFT) which is a computationally efficient method of calculating Fourier transforms for signal processing. This method is used by *Matlab* in a number of available standard PSD functions. The PSD is calculated in *Probe Analyser* by using the `periodogram` function. This function applies a rectangular window (equivalent to no window) to the signal and calculates the PSD using a standard periodogram. The periodogram calculates the PSD by taking the square of the magnitude of the FFT and dividing it by the number of samples, such that

$$PSD^{Periodogram}_{\Phi(t)} = \frac{1}{N}|\Phi(\omega)|^2 \tag{B.11}$$

Further detail of this function and its use can be obtained from the *Matlab* Documentation [201]. The function outputs the PSD and the frequency data, which can then be plotted to determine the frequency content of the signal. The PSD magnitude is dependent on the length of the signal and whether the variables used are dimensional or non-dimensional, therefore in this investigation, only the relative values of the PSD have been considered. In *Probe Analyser* a number of plotting options are available and the PSD can be plotted against both dimensional and non-dimensional frequency (Strouhal number) and period. The area under the PSD - frequency plot should be equal to the square of the RMS value of the signal. This has been used as a check to the validity and accuracy of this method within the investigation.

B.2.3 Time Averaging

The time average of the signal can be defined as,

$$\bar{\Phi} = \frac{1}{T}\int_{t-\frac{T}{2}}^{t+\frac{T}{2}} \Phi dt \tag{B.12}$$

where T is defined as the sample rate of the averaging process, which is specified by the user in *Probe Analyser*. This value must be a multiple of the time step of the calculation, $\Delta\tau$. As with the Fourier transform, this form cannot be applied to a discrete signal and so the integral is approximated to a summation over each interval, T in turn,

$$\bar{\Phi} = \frac{1}{T}\sum_{n=0}^{n=\frac{T}{\Delta\tau}} \Phi\Delta\tau \tag{B.13}$$

The mid point of each interval is also calculated by a similar averaging technique to determine the time at which the new point occurs. The resulting series of new data points creates the time averaged signal for the specified sample rate. This new signal can then be evaluated in a similar manner to the original signal by using the PSD analysis and the results can be plotted to determine the effect of time averaging. The location of the stationary mean can also be plotted for comparison. Currently, this can only be performed on a single probe at a time. For non-stationary process this method also allows the non-stationary mean to be determined for a specified sample rate. This can then be used to determine the turbulent properties of the signal.

B.2.4 Turbulent Kinetic Energy

As mentioned, the calculation of the turbulent kinetic energy is only one of a number of turbulent properties which can be calculated in *Probe Analyser*. Before any of the turbulent properties can be calculated, it is necessary to calculate the fluctuating variables of the flow. This is done simply by subtracting the mean from the unsteady signal. Either the stationary mean described in Section B.2.1 or the non-stationary mean calculated from the time averaging process can be selected. The turbulent kinetic energy is calculated from the fluctuating velocities, u', v' and w' by

$$k = \frac{1}{2}\left(u'^2 + v'^2 + w'^2\right) \tag{B.14}$$

The resulting signal can then be considered, as before, by calculation of the mean and RMS values and by calculation of the PSD.

References

[1] Anderson J.D. *Fundamentals of Aerodynamics*. McGraw-Hill International Editions, 2nd edition, 1991.

[2] Nelson R.C and Pelletier A. The unsteady aerodynamics of slender wings and aircraft undergoing large amplitude manoeuvers. *Progress in Aerospace Sciences*, 39:185–248, 2003.

[3] Pagan D and Solignac J.L. Experimental study of the breakdown of a vortex generated by a delta wing. *Recherche Aerospatiale*, 3:197–219, 1986.

[4] Lambourne N.C and Bryer D.W. The bursting of leading edge vortices - some observations and discussion of the phenomenon. Report and Memorandum No. 3282, Aircraft Research Council, April 1961.

[5] Görtz S. *Realistic Simulations of Delta Wing Aerodynamics Using Novel CFD Methods*. PhD thesis, Aeronautics and Vehicle Engineering, KTH, June 2005.

[6] Klute S.M. *The Development and Control of Axial Vortices over Swept Wings*. PhD thesis, Virginia Polytechnic Institute and State University, August 1999.

[7] Wentz W.H and Kohlman D.L. Vortex breakdown on slender sharp edged wings. *Journal of Aircraft*, 8(3):156–161, March 1971.

[8] Huang X.Z and Hanff E.S. Unsteady behaviour of spiral leading edge vortex breakdown. In *AIAA Atmospheric Flight Mechanics Conference*. AIAA Paper 1996-3408, July 1996.

[9] Lee M and Ho C-M. Lift force of delta wings. *Applied Mechanics Review*, 43(9):209–221, September 1990.

[10] Visbal M.R. Computed unsteady structure of spiral vortex breakdown on delta wings. In *27th AIAA Fluid Dynamics Conference*. AIAA Paper 96-2074, June 1996.

[11] Gursul I and Xie W. Physics of buffeting flows over delta wings. In *36th AIAA Aerospace Sciences Meeting and Exhibit*. AIAA Paper 98-0688, January 1998.

[12] Riley A.J and M.V Lowson. Development of a three-dimensional free shear layer. *Journal of Fluid Mechanics*, 369:49–89, 1998.

[13] Mitchell A.M. *Caractérisation et Contrôle de L'éclatement Tourbillonnaire sur une Aile Delta aux Hautes Incidences*. PhD thesis, L'Universite Paris 6, July 2000.

[14] Visbal M.R and Gordnier R.E. On the structure of the shear layer emanating from a swept leading edge at angle of attack. In *33rd AIAA Fluid Dynamics Conference and Exhibit*. AIAA Paper 2003-4016, June 2003.

[15] Menke M, Yang H, and Gursul I. Experiments on the unsteady nature of vortex breakdown over delta wings. *Experiments in Fluids*, 27:262–272, 1999.

[16] Miller D.S and Wood R.M. Leeside flows over delta wings at supersonic speeds. *Journal of Aircraft*, 21(9):680–686, September 1984.

[17] Donohoe S.R and Bannink W.J. Surface reflective visualisations of shock-wave/vortex interactions above a delta wing. *AIAA Journal*, 35(10):1568–1573, October 1997.

[18] Elsenaar A and Hoeijmakers H.W.M. An experimental study of the flow over a sharp-edged delta wing at subsonic and transonic speeds. In *AGARD Conference Proceedings "Vortex Flow Aerodynamics"*, pages 15.1–15.19. AGARD-CP-494, July 1991.

[19] Kameda M, Tabei T, Nakakita K, Sakaue H, and Asai K. Image measurements of unsteady pressure fluctuation by a pressure sensitive coating on porous anodized aluminium. *Measurement Science and Technology*, 16:2517–2524, 2005.

[20] Chu J and Luckring J.M. Experimental surface pressure data obtained on a 65° delta wing across Reynolds number and Mach number ranges: Volume 1 - sharp leading edge. NASA Technical Memorandum 4645, NASA Langley Research Centre, February 1996.

[21] Kourath R. Private communication.

[22] Agrawal S, Barnett R.M, and Robinson B.A. Numerical investigation of vortex breakdown on a delta wing. *AIAA Journal*, 30(3):584–591, March 1992.

[23] Görtz S. Time accurate Euler simulations of a full span delta wing at high incidence. In *21st AIAA Applied Aerodynamics Conference*. AIAA Paper 2003-4304, June 2003.

[24] Morton S.A, Forsythe J, Mitchell A.M, and Hajek D. Detached eddy simulation and Reynolds averaged Navier-Stokes simulations of delta wing vortical flow fields. *Journal of Fluids Engineering*, 124:924–932, December 2002.

[25] Mary I. Large eddy simulation of vortex breakdown behind a delta wing. *International Journal of Heat and Fluid Flow*, 24(4):596–605, August 2003.

[26] Wilcox D.C. *Turbulence Modelling for CFD*. DCW Industries Inc,, 1993.

[27] Lovely D and Haimes R. Shock detection from computational fluid dynamics results. In *14th AIAA Computational Fluid Dynamics Conference*. AIAA Paper 99-3285, June/July 1999.

[28] Kalkhoran I.M and Smart M.K. Aspects of shock wave-induced vortex breakdown. *Progress in Aerospace Sciences*, 36:63–95, 2000.

[29] Mitchell A.M, Morton S.A, and Forsythe J.R. Analysis of delta wing vortical substructures using detached eddy simulation. In *32nd AIAA Fluid Dynamics Conference*. AIAA Paper 2002-2968, June 2002.

[30] Morton S.A. High reynolds number DES simulations of vortex breakdown over a 70° delta wing. In *21st AIAA Applied Aerodynamics Conference*. AIAA Paper 2003-4217, June 2003.

[31] Soemarwoto B.I and Boelens O.J. Simulation of vortical flow over a slender delta wing experiencing vortex breakdown. In *21st AIAA Applied Aerodynamics Conference*. AIAA Paper 2003-4215, June 2003.

[32] Görtz S and Le Moigne Y. Time accurate detached eddy simulations of a full span delta wing at high incidence. In *21st AIAA Applied Aerodynamics Conference*. AIAA Paper 2003-4216, June 2003.

[33] Spalart P.R. Strategies for turbulence modelling and simulations. *International Journal of Heat and Fluid Flow*, 21(3):252–263, June 2000.

[34] Wilcox D.C. Reassessment of the scale determining equation for advanced turbulence models. *AIAA Journal*, 26(11):1299–1310, November 1988.

[35] Spalart P.R and Allmaras S.R. A one equation turbulence model for aerodynamic flows. In *30th AIAA Aerospace Science Meeting and Exhibit*. AIAA Paper 1992-0439, January 1992.

[36] Earnshaw P.B. An experimental investigation of the structure of a leading edge vortex. RAE Technical Note No. Aero. 2740, Royal Aeronatical Establisment, March 1961.

[37] Flynn G.A, Morrison J.F, and Mabey D.G. Buffet alleviation on swept and unswept wings at high incidence. *Journal of Aircraft*, 38(2):368 – 378, March - April 2001.

[38] Gad-el-Hak M and Blackwelder R.F. The discrete vortices from a delta wing. *AIAA Journal*, 23(6):961–962, June 1985.

[39] Lowson M.V. Visualisation measurements of vortex flows. *Journal of Aircraft*, 28(5):320–327, May 1991.

[40] Gad-el-Hak M and Blackwelder R.F. Control of the discrete vortices from a delta wing. *AIAA Journal*, 25(8):1042–1049, August 1987.

[41] Payne F.M, Ng T.T, Nelson R.C, and Schiff L.B. Visualisation and flow surveys of the leading edge vortex structure on delta wing planforms. In *24th AIAA Aerospace Sciences Meeting*. AIAA Paper 1986-0330, January 1986.

[42] Payne F.M. *The Structure of Leading Edge Vortex Flows Including Vortex Breakdown*. PhD thesis, University of Notre Dame, Notre Dame, IN, 1987.

[43] Hemsch M.J and Luckring J.M. Connection between leading edge sweep, vortex lift and vortex strength for delta wings. *Journal of Aircraft*, 27(5):473–475, May 1990.

[44] O'Neil P.J, Roos F.W, Kegelman J.T, Barnett R.M, and Hawk J.D. Investigation of flow characteristics of a developed vortex. NADC-89114-60, McDonnell Aircraft Company, P.O. Box 516, St. Louis, MO 63166, May 1989.

[45] Elle B.J. An investigation at low speed of the flow near the apex of thin delta wings with sharp leading edges. Reports and Memorandum No. 3176, Aircraft Research Council, January 1958.

[46] Rusak Z and Lamb D. Prediction of vortex breakdown in leading-edge vortices above slender delta wings. *Journal of Aircraft*, 36(4):659–667, 1999.

[47] Jupp M.L, Coton F.N, and Green R.B. A statistical analysis of the surface pressure distribution on a delta wing. *The Aeronautical Journal*, 103(1025):349–357, July 1999.

[48] Hummel D. On the vortex formation over a slender wing at large incidence. In *AGARD CP-247 Paper No. 15*. NATO AGARD, January 1979.

[49] Délery J.M. Aspects of vortex breakdown. *Progress in Aerospace Sciences*, 30(1):1–59, 1994.

[50] Hall M.G. Vortex breakdown. *Annual Review of Fluid Mechanics*, 4:195–218, 1972.

[51] Visser K.D and Nelson R.C. Measurements of circulation and vorticity in the leading edge vortex of a delta wing. *AIAA Journal*, 31(1):104–111, January 1993.

[52] Polhamus E.C. Prediction of vortex lift characteristics by a leading edge suction analogy. *Journal of Aircraft*, 8(4):193–199, 1971.

[53] Faler J.H and Leibovich S. Disrupted states of vortex flow and vortex breakdown. *Physics of Fluids*, 20(9):1385–1400, September 1977.

[54] Payne F.M, Ng T.T, and Nelson R.C. Experimental study of the velocity field on a delta wing. In *19th AIAA Fluid Dynamics, Plasma Dynamics and Lasers Conference*. AIAA paper 1987-1231, June 1987.

[55] Klute S.M, Vlachos P.P, and Telionis D.P. High-speed digital-particle-image-velocimtery study of vortex breakdown. *AIAA Journal*, 43(3):642–650, March 2005.

[56] Özgören M, Sahin B, and Rockwell D. Vortex structure on a delta wing at high angle of attack. *AIAA Journal*, 40(2):285–292, February 2002.

[57] Towfighi J and Rockwell D. Instantaneous structure of vortex breakdown on a delta wing via particle image velocimetry. *AIAA Journal*, 31(6):1160–1162, June 1993.

[58] Escudier M. Vortex breakdown: Observations and explanations. *Progress in Aerospace Sciences*, 25:189–229, 1988.

[59] Spall R.E, Gatski T.B, and Grosch C.E. A criterion for vortex breakdown. *Physics of Fluids*, 30(11):3434-3440, November 1987.

[60] Robinson B.A, Barnett R.M, and Agrawal S. Simple numerical criterion for vortex breakdown. *AIAA Journal*, 32(1):116–122, January 1994.

[61] Ashley H, Katz J, Jarrah M A, and Vaneck T. Survey of research on unsteady aerodynamic loading of delta wings. *Journal of Fluids and Structures*, 5:363–390, 1991.

[62] Mitchell A.M and Delery J.M. Research into vortex breakdown control. *Progress in Aerospace Sciences*, 37(4):385–418, 2001.

[63] Brown G.L and Lopez J.M. Axisymmetric vortex breakdown, Part II: Physical mechanisms. *Journal of Fluid Mechanics*, 221:553–576, December 1990.

[64] Jumper E.J, Nelson R.C, and Cheung K. A simple criterion for vortex breakdown. In *31st AIAA Aerospace Science Meeting and Exhibit*. AIAA Paper 93-0866, January 1993.

[65] Sarpkaya T. Effect of the adverse pressure gradient on vortex breakdown. *AIAA Journal*, 12(5):602–607, May 1974.

[66] Ericsson L.E. Effect of fuselage geometry on delta wing vortex breakdown. *Journal of Aircraft*, 35(6):898–904, November - December 1998.

[67] Ericsson L.E. Multifaceted influence of fuselage geometry on delta wing aerodynamics. *Journal of Aircraft*, 40(1):204–206, January - February 2003.

[68] Lowson M.V and Riley A.J. Vortex breakdown control by delta wing geometry. *Journal of Aircraft*, 32(4):832–838, July-August 1995.

[69] Srigrarom S and Kurosaka M. Shaping of delta wing planform to suppress vortex breakdown. *AIAA Journal: Technical Notes*, 38(1):183–186, January 2000.

[70] Allan M.R, Badcock K.J, Barakos G.N, and Richards B.E. Wind tunnel interference effects on delta wing aerodynamics computational fluid dynamics investigation. *Journal of Aircraft*, 42(1):189–198, January-February 2005.

[71] Allan M.R, Badcock K.J, Barakos G.N, and Richards B.E. Wind-tunnel interference effects on a 70^o delta wing. *The Aeronautical Journal*, pages 505–513, October 2004.

[72] Jobe C.E. Vortex breakdown location over 65^o delta wings empiricism and experiment. *Aeronautical Journal*, pages 475–482, September 2004.

[73] Gursul I. Criteria for vortex breakdown location over delta wings. *Aeronautical Journal*, pages 194–196, May 1995.

[74] Johari H and Moreira J. Direct measurement of delta wing vortex circulation. *AIAA Journal*, 36(12):2195–2203, December 1998.

[75] Earnshaw P.B and Lawford J.A. Low-speed wind-tunnel experiments on a series of sharp edged delta wings. Reports and Memoranda No. 3424, Aircraft Research Council, March 1964.

[76] Mabey D.G. Beyond the buffet boundary. *The Aeronautical Journal*, pages 201–215, April 1973.

[77] Garg A.K and Leibovich S. Spectral characteristics of vortex breakdown flowfields. *Physics of Fluids*, 22(11):2053–2064, November 1979.

[78] Singh P.I and Uberoi M.S. Experiments on vortex stability. *Physics of Fluids*, 19(12):1858–1863, December 1976.

[79] Gursul I. Unsteady flow phenomena over delta wings at high angle of attack. *AIAA Journal*, 32(2):225–231, February 1994.

[80] Lowson M.V. Some experiments with vortex breakdown. *Journal of the Royal Aeronautical Society*, 68:343–346, May 1964.

[81] Mitchell A.M, Barberis D, Molton P, and Délery J. Oscillation of vortex breakdown location and blowing control of time averaged location. *AIAA Journal*, 38(5):793–803, May 2000.

[82] Lambert C and Gursul I. Insensitivity of unsteady vortex interactions to Reynolds number. *AIAA Journal*, 38(5):937–939, May 2000.

[83] Ayoub A and McLachlan B.G. Slender delta wing at high angles of attack - a flow visualisation study. In *19th AIAA Fluid Dynamics, Plasma Dynamics and Lasers Conference*. AIAA Paper 87-1230, June 1987.

[84] Portnoy H. Unsteady motion of vortex breakdown positions on delta wings. In *International Council of the Aeronautical Sciences Congress*. ICAS, August-September 1988.

[85] Helin H.E and Watry C.W. Effects of trailing edge jet entrainment on delta wing vortices. *AIAA Journal*, 32(4):802–804, April 1994.

[86] Gursul I and Yang H. On fluctuations of vortex breakdown. *Physics of Fluids*, 7(1):229–231, January 1995.

[87] Menke M and Gursul I. Unsteady nature of leading edge vortices. *Physics of Fluids*, 9(10):2960–2969, October 1997.

[88] Gursul I and Xie W. Origin of vortex wandering over delta wings. *Journal of Aircraft*, 37(2):348–350, 2000.

[89] Rediniotis O.K, Stapountzis H, and Telionis D.P. Vortex shedding over delta wings. *AIAA Journal*, 28(5):944–946, May 1990.

[90] Rediniotis O.K, Stapountzis H, and Telionis D.P. Periodic vortex shedding over delta wings. *AIAA Journal*, 31(9):1555–1562, September 1993.

[91] Gursul I and Xie W. Buffeting flows over delta wings. *AIAA Journal*, 37(1):58–65, January 1999.

[92] Winant C.D and Browand F.K. Vortex pairing: the mechanism of turbulent mixing-layer growth at moderate Reynolds number. *Journal of Fluid Mechanics*, 63:237–255, 1974.

[93] Gordnier R.E and Visbal M.R. Unsteady vortex structure over a delta wing. *Journal of Aircraft*, 31(1):243–248, January 1994.

[94] Gordnier R.E and Visbal M.R. Unsteady Navier-Stokes solutions for a low aspect ratio delta wing. AIAA Paper 90-1538, June 1990.

[95] Gursul I. Review of unsteady vortex flows over slender delta wings. *Journal of Aircraft*, 42(2):299–319, March-April 2005.

[96] Gordnier R.E and Visbal M.R. Instabilities on the shear layer of delta wings. In *26th AIAA Fluid Dynamics Conference*. AIAA Paper 95-2281, June 1995.

[97] Washburn A.E and Visser K.D. Evolution of vortical structures in the shear layer of delta wings. In *25th AIAA Fluid Dynamics Conference*. AIAA Paper 94-2317, June 1994.

[98] Shan H, Jiang L, and Liu C. Direct numerical simulation of three-dimensional flow around a delta wing. In *38th AIAA Aerospace Sciences Meeting and Exhibit*. AIAA Paper 2000-0402, January 2000.

[99] Mitchell A.M, Molton P, Barberis D, and Délery J. Vortical substructures in the shear layers forming leading edge vortices. In *19th AIAA Applied Aerodynamics Conference*. AIAA Paper 2001-2424, June 2001.

[100] Mitchell A.M and Molton P. Vortical substructures in the shear layers forming leading edge vortices. *AIAA Journal*, 40(8):1689–1692, September 2002.

[101] Honkan A and Andreopoulos J. Instantaneous three-dimensional vorticity measurements in vortical flow over a delta wing. *AIAA Journal*, 35(10):1612–1620, October 1997.

[102] Gursul I. Recent developments in delta wing aerodynamics. *Aeronautical Journal*, pages 437–452, September 2004.

[103] Furman A and Breitsamter C. Investigation of flow phenomena on generic delta wing. In *25th International Congress of the Aeronautical Sciences*. ICAS, 2006.

[104] Lee Y.L and Gursul I. An investigation of unsteady interactions of a vortex pair over delta wings. In *41st AIAA Aerospace Sciences Meeting and Exhibit*. AIAA Paper 2003-0423, January 2003.

[105] Lowson M.V. The three dimensional vortex sheet structure on delta wings. In *Fluid Dynamics of Three Dimensional Turbulent Shear Flows and Transition*, pages 11.1–11.16. AGARD CP-438, October 1988.

[106] Renac F, Barberis D, and Molton P. Control of vortical flow over a rounded leading edge delta wing. *AIAA Journal*, 43(7):1409–1418, July 2005.

[107] Taylor G.S and Gursul I. Unsteady vortex flows and buffeting of a low sweep delta wing. In *42nd AIAA Aerospace Sciences Meeting and Exhibit*. AIAA Paper 2004-1066, January 2004.

[108] Woppowa S and Grosche F.R. Unsteady vortex flow over a combat aircraft configuration at high angles of incidence. In *Unsteady Aerodynamics*. Royal Aeronautical Society, July 1996.

[109] Yaniktepe B and Rockwell D. Flow structure on a delta wing of low sweep angle. *AIAA Journal*, 42(3):513–523, March 2004.

[110] Yavuz M.M, Elkhoury M, and Rockwell D. Near surface topology and flow structure on a delta wing. *AIAA Journal*, 42(2):332–340, February 2004.

[111] Cummings R.M, Morton S.A, and Siegel S.G. Computational simulation and experimental measurements for a delta wing with periodic suction and blowing. *Journal of Aircraft*, 40(5):923–931, September-October 2003.

[112] Cummings R.M, Morton S.A, and Seigel S.G. Computational simulation and PIV measurements of the laminar vortical flowfield for a delta wing at high angle of attack. In *41st AIAA Aerospace Sciences Meeting and Exhibit*. AIAA Paper 2003-1102, January 2003.

[113] Gordnier R.E and Visbal M.R. Higher-order compact difference scheme applied to the simulation of a low sweep delta wing flow. In *41st AIAA Aerospace Sciences Meeting and Exhibit*. AIAA-2003-0620, January 2003.

[114] Gordnier R.E and Visbal M. Compact difference scheme applied to simulation of low sweep delta wing flow. *AIAA Journal*, 43(8):1744–1752, August 2005.

[115] Wolfe S, Lin J.C, and Rockwell D. Buffeting at the leading edge of a flat plate due to a streamwise vortex: Flow structure and surface pressure loading. *Journal of Fluids and Structures*, 9:359–370, 1995.

[116] Morton S.A, Steenman M, Cummings R.M, and Forsythe J.R. DES grid resolution issues for vortical flows on a delta wing and an F-18C. In *41st AIAA Aerospace Sciences Meeting and Exhibit*. AIAA Paper 2003-1103, January 2003.

[117] Erickson G.E and Rogers L.W. Experimental study of the vortex flow behaviour on a generic fighter wing at subsonic and transonic speeds. In *19th AIAA Fluid Dynamics, Plasma Dynamics and Lasers Conference*. AIAA Paper 87-1262, June 1987.

[118] Erickson G.E, Schreiner J.A, and Rogers L.W. Multiple vortex and shock interactions at subsonic, transonic and supersonic speeds. In *8th AIAA Applied Aerodynamics Conference*. AIAA Paper 90-3023, August 1990.

[119] Stanbrook A and Squire L.C. Possible types of flow at swept leading edges. *The Aeronatical Quarterly*, 15:72–82, 1964.

[120] Yenga Narayan K and Seshadri S.N. Types of flow on the lee side of delta wings. *Progress in Aerospace Sciences*, 33:167–257, 1997.

[121] Longo J.M.A. Compressible inviscid vortex flow of a sharp edge delta wing. *AIAA Journal*, 33(4):680–687, April 1995.

[122] Donohoe S.R, Houtman E.M, and Bannink W.J. Surface reflective visualization system study to vortical flow over delta wings. *Journal of Aircraft*, 32(6):1359–1366, November-December 1995.

[123] Kandil O.A, Kandil H.A, and Liu C.H. Shock-vortex interaction over a 65-degree delta wing in transonic flow. In *24th AIAA Fluid Dynamics Conference*. AIAA Paper 93-2973, July 1993.

[124] Kandil O.A, Kandil H.A, and Liu C.H. Supersonic vortex breakdown over a delta wing in transonic flow. In *11th AIAA Applied Aerodynamics Conference*. AIAA Paper 93-3472-CP, August 1993.

[125] Visbal M.R and Gordnier R.E. Compressibility effects on vortex breakdown onset above a 75-degree sweep delta wing. *Journal of Aircraft*, 32(5):936–942, September-October 1995.

[126] Hoeijmakers H.W.M. Modelling and numerical simulation of vortex flow in aerodynamics. In *AGARD Conference Proceedings "Vortex Flow Aerodynamics"*, pages 1.1–1.46. AGARD-CP-494, July 1991.

[127] Squire L.C. Leading edge separations and cross-flow shocks on delta wings. *AIAA Journal*, 23(3):321–325, 1985.

[128] Muylaert J.M. Effect of compressiblity on vortex bursting on slender delta wings. Project report 1980-21, Von Karman Institute for Fluid Dynamics, Rhode St, Genese, Belgium, July 1980.

[129] Houtman E.M and Bannink B.J. Experimental and numerical investigation of the vortex flow over a delta wing at transonic speeds. In *AGARD Conference Proceedings "Vortex Flow Aerodynamics"*, pages 5.1–5.11. AGARD-CP-494, July 1991.

[130] Thomer O, Schröder W, and Krause E. Normal shock vortex interaction. In *Proceedings of the RTO-AVT Symposium on "Advanced Flow Management: Part A - Vortex Flows and High Angle of Attack for Military Vehicles" - RTO-MP-069(I)*, pages 18.1–8.10. NATO RTO, 2001.

[131] Smart M.K and Kalkhoran I.M. Flow model for predicting normal shock wave induced vortex breakdown. *AIAA Journal*, 35(10):1589–1596, October 1995.

[132] Chu J and Luckring J.M. Experimental surface pressure data obtained on a 65^o delta wing across Reynolds number and Mach number ranges: Volume 2 - small radius leading edge. NASA Technical Memorandum 4645, NASA Langley Research Centre, February 1996.

[133] Chu J and Luckring J.M. Experimental surface pressure data obtained on a 65^o delta wing across Reynolds number and Mach number ranges: Volume 3 - medium radius leading edge. NASA Technical Memorandum 4645, NASA Langley Research Centre, February 1996.

[134] Chu J and Luckring J.M. Experimental surface pressure data obtained on a 65^o delta wing across Reynolds number and Mach number ranges: Volume 4 - large radius leading edge. NASA Technical Memorandum 4645, NASA Langley Research Centre, February 1996.

[135] Luckring J.M. Reynolds number and leading edge bluntness effects on a 65^o delta wing. In *40th AIAA Aerospace Sciences Meeting and Exibit*. AIAA Paper 2001-0907, January 2002.

[136] Luckring J.M. Transonic Reynolds number and leading edge bluntness effects on a 65^o delta wing. In *41st Aerospace Sciences Meeting and Exhibit*. AIAA-2003-0753, January 2003.

[137] Luckring J.M. Compressibility and leading edge bluntness effects for a 65^o delta wing. In *42nd Aerospace Sciences Meeting and Exhibit*. AIAA-2004-0765, January 2004.

[138] Luckring J.M. Reynolds number, compressibility and leading edge bluntness effects on delta wing aerodynamics. In *24th International Congress of the Aeronautical Sciences*, pages 1–14. ICAS, 2004.

[139] Schrader K.F, Reynolds G.A, and Novak C.J. Effects of Mach number and Reynolds number on leading edge vortices at high angles of attack. In *26th AIAA Aerospace Sciences Meeting*. AIAA Paper 88-0122, January 1988.

[140] Konrath R, Klein C, Engler R.H, and Otter D. Analysis of PSP results obtained for the VFE-2 65^o delta wing configuration at sub- and transonic speeds. In *44th AIAA Aerospace Sciences Meeting and Exhibit*. AIAA Paper 2006-60, January 2006.

[141] Konrath R, Schröder A, and Kompenhans J. Analysis of PIV results obtained for the VFE-2 65^o delta wing configuration at sub- and transonic speeds. In *24th AIAA Applied Aerodynamics Conference*. AIAA Paper 2006-3003, June 2006.

[142] Schröder A, Agocs J, Frahnert H, Otter D, Mattner H, Kompenhans J, and Konrath R. Application of stereo PIV to the VFE-2 65^o delta wing configuration at sub- and transonic speeds. In *24th AIAA Applied Aerodynamics Conference*. AIAA Paper 2006-3486, June 2006.

[143] Cummings R.M, Forsythe J.R, Morton S.A, and Squires K.D. Computational challenges in high angle of attack flow prediction. *Progress in Aerospace Sciences*, 39(5):369–384, July 2003.

[144] Allan M. *A CFD Investigation of Wind Tunnel Interference on Delta Wing Aerodynamics*. PhD thesis, University of Glasgow, October 2002.

[145] Newsome R.W. Euler and Navier-Stokes solutions for flow over a conical delta wing. *AIAA Journal*, 24(4):552 -561, April 1986.

[146] Murman E.M and Rizzi A. Applications of Euler equations to sharp edged delta wings with leading edge vortices. In *AGARD CP-412 Paper 15*. Applications of Computational Fluid Dynamics in Aeronautics, November 1986.

[147] Rizzi A and Muller B. Comparison of Euler and Navier-Stokes solutions for vortex flow over a delta wing. *Aeronautical Journal*, 92(914):145–153, April 1988.

[148] Tsai H.M, Leck C.L, Guarino L, and Lee K.M. Euler/Navier-Stokes analysis of vortical flow about rounded leading edge delta wing. In *13th AIAA Applied Aerodynamics Conference*, pages 703 – 713. AIAA Paper 95-1847, June 1995.

[149] Agrawal S, Barnett R.M, and Robinson B.A. Numerical investigation of vortex breakdown on a delta wing. *AIAA Journal*, 30(3):584–591, March 1992.

[150] Kegelman J.T and Roos F.W. Effects of leading edge shape and vortex burst on the flowfield of a 70 degree sweep delta wing. In *27th AIAA Aerospace Sciences Meeting*. AIAA-1989-0086, January 1989.

[151] Roos F.W and Kegelman J. An experimental investigation of sweep angle influence on delta wing flows. In *28th AIAA Aerospace Sciences Meeting*. AIAA Paper 90-0383, January 1990.

[152] Kumar A. On the structure of vortex breakdown. In *Proceedings of the Royal Society of London, Series A (Mathematical, Physical and Engineering Sciences)*, pages 89–110. Royal Society of London, January 1998.

[153] Kumar A. Role of flow-consistent grid in CFD. *Computers and Fluids*, 28:265–280, 1999.

[154] Kumar A. Accurate development of leading edge vortex using an embedded conical grid. *AIAA Journal*, 34(10):2038–2046, October 1996.

[155] Strohmeyer D, Orlowski M, Longo J.M.A, Hummel D, and Bergmann A. An analysis of vortex breakdown predicted by the Euler equations. In *ICAS Conference*, pages 1189–1200. ICAS-96-1.6.3, 1996.

[156] Gordnier R.E. Numerical simulation of a 65^o delta wing flowfield. *Journal of Aircraft*, 34(4):492–499, 1997.

[157] Gordnier R.E. Computational study of a turbulent delta wing flowfield using two-equation turbulence models. In *27th AIAA Fluid Dynamics Conference*. AIAA Paper 96-2076, June 1996.

[158] Brandsma F.J, Kok J.C, Dol H.S, and Elsenaar A. Leading edge vortex flow computations and comparison with DNW-HST wind tunnel data. In *Proceeds of the RTO/AVT Symposium on Vortex Flows and High Angle of Attack*. NATO RTO/AVT, 2001.

[159] Dol H.S, Kok J.C, and Oskam B. Turbulence modelling for leading edge vortex flows. In *40th AIAA Aerospace Sciences Meeting and Exhibit*. AIAA Paper 2002-0843, January 2002.

[160] Bartels R.E and Gatski T.B. Prediction of transonic vortex flows using linear and non-linear turbulent eddy viscosity models. NASA-TM-2000-210282, NASA Langely Research Center, May 2000.

[161] Morton S.A, Forsythe J, Mitchell A.M, and Hajek D. DES and RANS simulations of delta wing vortical flows. In *40th AIAA Aerospace Sciences Meeting and Exhibit*. AIAA Paper 2002-0587, January 2002.

[162] Mitchell A.M, Molton P, Barberis D, and Délery J. Characterization of vortex breakdown by flow field and surface measurements. In *38th AIAA Aerospace Science Meeting and Exhibit*. AIAA Paper 2000-0788, January 2000.

[163] Morton S.A, Forsythe J.R, Squires K.D, and Wurtzler K.E. Assessment of unstructured grids for detached-eddy simulation of high Reynolds number separated flows. In *8th International Conference on Numerical Grid Generation in Computational Field Simulations*, June 2002.

[164] Mitchell A.M, Morton S.A, Forsythe J.R, and Cummings R.M. Analysis of delta wing vortical substructures using detached eddy simulation. *AIAA Journal*, 44(5):964–972, May 2006.

[165] Görtz S. Detached-eddy simulation of a full-span delta wing at high incidence. In *21st AIAA Applied Aerodynamics Conference*. AIAA Paper 2003-4216, June 2003.

[166] de Cock K.M.J, Kok J.C, van der Ven H, Soemarwoto B.I, Boelens O.J, and Oskam B. Extra large eddy simulation for delta wings and space launchers. In *24th International Congress of the Aeronautical Sciences*. ICAS, 2004.

[167] Pope S.B. *Turbulent Flows*. Cambridge University Press, 2000.

[168] Favre A. Equations des gaz turbulents compressibles. *Journal de Mecanique*, 4(3):361–390, 1965.

[169] Ferziger J.H. Large eddy simulation. In Gatski T.B, Hussaini M.Y, and Lumley J.L, editors, *Simulation and Modelling of Turbulent Flows*, pages 109–154. ICASE/LaRC Series in Computational Science and Engineering, Oxford University Press, 1996.

[170] Wallin S and Johansson A. An explicit algebraic Reynolds stress model for incompresible and compressible turbulent flows. *Journal of Fluid Mechanics*, 403:89–132, January 2000.

[171] Spalart P.R, Jou W-H, Strelets M, and Allmaras S.R. Comments on the feasibility of LES for wings and on a hybrid RANS/LES approach. In *Advances in DNS/LES, 1st AFSOR International Conference on DNS/LES*. AFOSR, August 1997.

[172] Shur M, Spalart P.R, Strelets M, and Travin A. Detached eddy simulation of an airfoil at high angle of attack. In *4th International Symposium Engineering Turbulence modelling and Measurements*, May 1999.

[173] Badcock K.J, Richards B.E, and Woodgate M.A. Elements of computational fluid dynamics on block structured grids using implicit solvers. *Progress in Aerospace Sciences*, 36:351–392, 2000.

[174] Roe P.L. Approximate riemann solvers, parameter vectors and difference schemes. *Journal of Computational Physics*, 43:357–372, 1981.

[175] Osher S and Solomon F. Upwind difference schemes for hyperbolic systems of conservation laws. *Mathematics of Computing*, 38:339–374, 1982.

[176] Jameson A. Time dependent calculations using multigrid with applications to unsteady flows past airfoils and wings. In *10th Computational Fluid Dynamics Conference*. AIAA Paper 91-1596, June 1991.

[177] Spalart P.R. Young person's guide to detached-eddy simulation grids. NASA/CR-2001-211032, NASA Langley Research Centre, July 2001.

[178] Lawrie D. *Investigation of Cavity Flows at Low and High Reynolds Numbers using Computational Fluid Dynamics*. PhD thesis, Department of Aerospace Engineering, University of Glasgow, January 2004.

[179] Nayyar P. *CFD Analysis of Transonic Turbulent Cavity Flows*. PhD thesis, Department of Aerospace Engineering, University of Glasgow, August 2005.

[180] Délery J.M. Physics of vortical flows. *Journal of Aircraft*, 29(5):856–876, September - October 1992.

[181] Elsenaar A, Hjemberg L, Bütefisch K-A, and Bannink W.J. The international vortex flow experiment. In *Validation of Computational Fluid Dynamics - AGARD-CP-437 Volume 1*, pages 9.1–9.23. AGARD, 1988.

[182] Hummel D and Redeker G. A new vortex flow experiment for computer code validation. In *Proceedings of the RTO-AVT Symposium on "Advanced Flow Management: Part A - Vortex Flows and High Angle of Attack for Military Vehicles" - RTO-MP-069(I)*, pages 8.1–8.32. NATO RTO, 2001.

[183] Hummel D. Effects of boundary layer formation on the vortical flow above slender delta wings. In *RTO-MP-AVT-111*, pages 30.1–30.22. NATO, October 2004.

[184] Boelens O.J. Private communication.

[185] Görtz S and Rizzi A. Computing the high alpha aerodynamics of delta wings - evaluation and analysis. In *39th AIAA Aerospace Sciences Meeting and Exhibit*. AIAA Paper 2001-0115, January 2001.

[186] Görtz S. Steady and unsteady CFD simultations of vortex breakdown over delta wings. Master's thesis, Royal Institute of Technology, Stockholm, Sweden, 2002.

[187] Görtz S, Rizzi A, and Munukka K. Computational study of vortex breakdown over swept delta wings. In *17th AIAA Applied Aerodynamics Conference*. AIAA Paper 99-3118, June/July 1999.

[188] Schiavetta L.A, Boelens O.J, and Fritz W. Analysis of transonic flow on a slender delta wing using CFD. In *24th AIAA Applied Aerodynamics Conference*. AIAA Paper 2006-3171, June 2006.

[189] *FLOWer, Installation and User Handbook*.

[190] Kok J.C. Mathematical physical model of ENSOLV version 3.20; a flow solver for 3D Euler/Navier-Stokes equations in arbitrary multi-block domains. NLR-CR-2000-621, Nationaal Lucht- en Ruimtevaartlaboratorium, NLR, 2000.